Ministry of Education and Science of the Russian Federation
Saint Petersburg National Research University of Information
Technologies, Mechanics, and Optics

NANOSYSTEMS:

PHYSICS, CHEMISTRY, MATHEMATICS

2016, volume 7(6)

Наносистемы: физика, химия, математика

2016, том 7, № 6

NANOSYSTEMS:

PHYSICS, CHEMISTRY, MATHEMATICS

ADVISORY BOARD MEMBERS

Chairman: V.N. Vasiliev *(St. Petersburg, Russia)*,
V.M. Buznik *(Moscow, Russia)*; V.M. Ievlev *(Voronezh, Russia)*, P.S. Kop'ev*(St. Petersburg, Russia)*, N.F. Morozov *(St. Petersburg, Russia)*, V.N. Parmon *(Novosibirsk, Russia)*, A.I. Rusanov *(St. Petersburg, Russia)*,

EDITORIAL BOARD

Editor-in-Chief: I.Yu. Popov *(St. Petersburg, Russia)*

Section Co-Editors:
Physics – V.M. Uzdin *(St. Petersburg, Russia)*,
Chemistry, material science –V.V. Gusarov *(St. Petersburg, Russia)*,
Mathematics – I.Yu. Popov *(St. Petersburg, Russia).*

Editorial Board Members:
V.M. Adamyan *(Odessa, Ukraine)*; O.V. Al'myasheva *(St. Petersburg, Russia)*; A.P. Alodjants *(Vladimir, Russia)*; S. Bechta *(Stockholm, Sweden)*; J. Behrndt *(Graz, Austria)*; M.B. Belonenko *(Volgograd, Russia)*; V.G. Bespalov *(St. Petersburg, Russia)*; J. Brasche *(Clausthal, Germany)*; A. Chatterjee (*Hyderabad, India)*; S.A. Chivilikhin *(St. Petersburg, Russia)*; A.V. Chizhov *(Dubna, Russia)*; A.N. Enyashin *(Ekaterinburg, Russia)*, P.P. Fedorov *(Moscow, Russia)*; E.A. Gudilin *(Moscow, Russia)*; V.K. Ivanov *(Moscow, Russia)*, H. Jónsson *(Reykjavik, Iceland)*; A.A. Kiselev *(Madison, USA)*; Yu.S. Kivshar *(Canberra, Australia)*; S.A. Kozlov *(St. Petersburg, Russia)*; P.A. Kurasov *(Stockholm, Sweden)*; A.V. Lukashin *(Moscow, Russia)*; V.A. Margulis *(Saransk, Russia)*; I.V. Melikhov *(Moscow, Russia)*; G.P. Miroshnichenko *(St. Petersburg, Russia)*; I.Ya. Mittova *(Voronezh, Russia)*; H. Neidhardt *(Berlin, Germany)*; K. Pankrashkin *(Orsay, France)*; A.V. Ragulya *(Kiev, Ukraine)*; V. Rajendran *(Tamil Nadu, India)*; A.A. Rempel *(Ekaterinburg, Russia)*; V.Ya. Rudyak *(Novosibirsk, Russia)*; D Shoikhet *(Karmiel, Israel)*; P Stovicek *(Prague, Czech Republic)*; V.M. Talanov *(Novocherkassk, Russia)*; A.Ya. Vul' *(St. Petersburg, Russia)*; A.V. Yakimansky (*St. Petersburg, Russia*), V.A. Zagrebnov *(Marseille, France).*

Editors:
I.V. Blinova; A.I. Popov; A.I. Trifanov; E.S. Trifanova *(St. Petersburg, Russia),*
R. Simoneaux *(Philadelphia, Pennsylvania, USA).*

Address: University ITMO, Kronverkskiy pr., 49, St. Petersburg 197101, Russia.
Phone: +7(812)232-67-65, **Journal site:** http://nanojournal.ifmo.ru/,
E-mail: popov1955@gmail.com

AIM AND SCOPE

The scope of the journal includes all areas of nano-sciences. Papers devoted to basic problems of physics, chemistry, material science and mathematics inspired by nanosystems investigations are welcomed. Both theoretical and experimental works concerning the properties and behavior of nanosystems, problems of its creation and application, mathematical methods of nanosystem studies are considered.

The journal publishes scientific reviews (up to 30 journal pages), research papers (up to 15 pages) and letters (up to 5 pages). All manuscripts are peer-reviewed. Authors are informed about the referee opinion and the Editorial decision.

CONTENT

PHYSICS

CHEMISTRY AND MATERIAL SCIENCE

NANOSYSTEMS: PHYSICS, CHEMISTRY, MATHEMATICS, 2016, 7 (6), P. 906–910

Effect of the removal of the barrier layer period in productive process for anodic alumina membrane

M. Ahmadi Daryakenari[1], M. Zohrabi[2], A. Ahmadi Daryakenari[3]

[1]Kazan National Research Technological University, 68 K. Marksa Str, Kazan, Russia

[2]Kazan Federal University, 18 Kremlin Str, Kazan, Russia

[3]The University of Tokyo, 7-3-1 Hongo, Bunkyo-ku, Tokyo, 113–8656, Japan

dariakenari@gmail.com

DOI 10.17586/2220-8054-2016-7-6-906-910

An anodic alumina membrane (AAM) is produced using two-step anodizing by using various types of acidic electrolytes, such as sulfuric acid, phosphoric acid and oxalic acid. Holes are characterized by hexagonal structure with diameters ranging from 40 to 420 nm. Heat and chemical stability also regular formed holes are made the membranes appropriate for using in gas separating process, drug delivery and applicant for fuel cell membrane. Detaching of membrane from the aluminum base is the most important stage of the membrane production process. In this research, initially, the aluminum base layer was removed with the use of $CuSO_4$ and HCl. In secondary step, barrier layer at the end of the holes were removed with phosphoric acid solution. The aim of this work is to analyze the effect of time on the barrier layer removal process.

Keywords: alumina, nanopore, anodizing, phosphoric acid.

Received: 26 April 2016

Revised: 10 July 2016

1. Introduction

The use of anodized aluminum began only in the last century. The anodic behavior of aluminum was intensively investigated to obtain protective and attractive films on its surface. Currently, anodizing is defined as an electrochemical process of converting metal (usually aluminum) to metal oxide on the metal's surface. The electrochemical cell of anodizing consists of cathode, anode (the metal substrate to be converted to metal oxide) and direct current (DC) power supply. The anodic aluminum oxide thin film starts to grow at the anode (aluminum surface) as the anodic current or voltage is applied [1,2].

An anodic alumina membrane (AAM) can provide a simple template for deposition and the growth of various materials with ordered structures. A new two-step anodization method for the synthesis of porous aluminum oxide having regular structure in oxalic acid was invented by H.Masuda in 1995 [3]. After this invention, scientists have tried to discover new ways to synthesize this material with different characteristics.

The success of AAM is due to its attractive physical and chemical properties: its ceramic temperament involves high thermal strength (up to several hundred degrees) and excellent chemical insensitivity in many environments (from pH's ranging from 5-9). It has highly-ordered nanopores with controllable and uniform dimensions arranged in a close-packed hexagonal footprint. AAM's with pore diameters ranging from 4-420 nm, density as high as 10^{11} pores/cm^2, and film thickness variable from 0.1–300 μm have been obtained using two-step anodization or nanoimprint methods. These materials can be synthesized in slightly soluble electrolytes, such as sulfuric, phosphoric and oxalic acids [4,5].

The synthesis of nanomaterials such as polymeric nanowire, metallic nanowire [6] , 3D nanodots [7], polymeric- [8] and metallic nanotubes [9], etc have given many research directions to anodic alumina membrane also because it can be used as membrane in various applications such as gas separation [10], drug delivery [11], in solid acid fuel cells [12] and solar cells [13].

A key difficulty encountered in the above-mentioned applications is how to attain through-hole porous anodic alumina which was previously produced on an alumina barrier layer covering aluminum substrate in the anodization process. Wet chemical etching founded on H_3PO_4 is commonly considered the most reliable method for custom pore opening of AAM [14,15]. The difficulty of this method is that the process of pore opening is controlled by the etching time, usually from 50–90 minutes. Different etching conditions, e.g. the concentration of H_3PO_4 (5–10 wt %), temperatures (25–50 °C) have been reported for pore opening of AAM, but there are no details on how these variations affect the pore diameters of AAM [14,15]. The aim of this work is to analyze the effect of time on the barrier layer removal process. The morphological modifications were monitored by Scanning Electron Microscopy (SEM).

2. Experimental procedures

AA1057 aluminum (diameter 14 mm, thickness 0.3 mm) was used as the starting material. Active surface diameter of the samples was 10 mm. The samples were disc-shaped to minimize both the uneven electric field during electropolishing (EP) and anodizing, and the undesirable effects of heat treatment such as remaining stress. Before anodizing, the aluminum was degreased with acetone and then annealed at 450 °C for 15 min. During the EP, the aluminum specimens were electropolished in a mixture of ethanol- hydrochloric acid solution (1:4) at 35 V for 1 min. To speed up the anodizing process, a polyethylene chemical reactor was designed which permitted the anodization of 4 specimens simultaneously. The temperature of the electrolyte was maintained at 17±0.1 °C by means of isotherm Lauda circular bath (RE106). AAM's were prepared in a two-step anodizing process. In the first step, aluminum specimens were anodized in 0.3 M oxalic acid ($C_2H_2O_4$) electrolyte 40 V and 17 °C. After 15 h of anodization, the specimens were immersed in a mixture of 0.5 wt% H_3PO_4 and 0.2 wt% H_2CrO_4 at 70 °C for 6 h to remove the alumina layers. The aluminum specimens were then anodized again for 24 h under the same anodization conditions used in the first step. The Current-Time diagram of the 2-nd anodizing at 40 V, was drawn using multi-meter (Loutron 801) software. The film thickness was measured using a scanning electron microscope (SEM, XL30, Philips company). Since the layers are fragile, they are deeply cracked when curved. Hence, the thickness of oxide layer will be observed more easily and carefully using Scanning Electron Microscopy. X-Ray Diffraction (XRD) patterns of AAM were obtained by Philips PW1140 system. A saturated solution of copper sulfate and hydrochloric acid was used for dissolving the metallic base. Then, the membrane was immersed in 100 mL of 5.00 wt% phosphoric acid at 30.0 °C for different periods of time (30 min, 60 min and 90 min).

3. Result and discussion

3.1. Model of anodic alumina membrane

The model of an AAM nanopore is shown in Fig. 1 by following a literature reference [16]. As indicated in the figure, C is the cell dimension (pore-to-pore distance) with cell wall thickness, w and P is the pore diameter, and A is the center of curvature that moves continuously during anodization toward the bottom. The active layer during nanopore growth is the barrier layer with thickness (d). There are two active interfaces associated with the barrier layer. The outer one is associated with oxidation of aluminum to aluminum cation (Al $\rightarrow$ Al^{3+}), and the inner one is associated with O^{2-} migration that leads to the formation of alumina (Al_2O_3), as well as dissolution and deposition of alumina to and from the etching solution. The whole process is driven by the local electric field (E), which is defined by the current applied (I) over conductivity (σ) and the surface area of the spherical bottom ($\frac{\omega}{4\pi} \cdot 4\pi b^2$), where ω is the solid angle of the active barrier area and b radius of curvature:

$$E = \frac{J}{b} = \frac{I}{b\sigma\omega_2}.$$

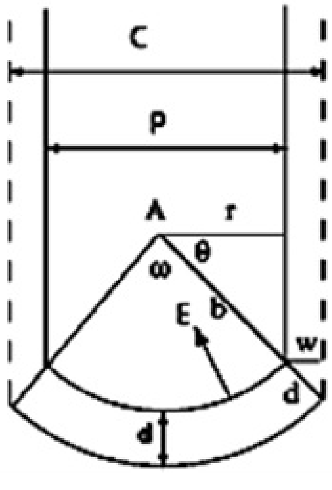

FIG. 1. Schematic drawing of the cross section a nanopore

3.2. Current – time diagram

As shown in Fig. 2, the current drastically decreases as the anodizing duration increases. The reduction is due to the formation of a barrier layer with high electric resistance on the aluminum surface. As the thickness of the layer increases, the voltage approaches its minimum value. Then, the oxide layer is partially cracked, leading to a voltage increment (Fig. 2). The cracks made on barrier layer are responsible for pore formation. On the other hand, the cracks themselves are formed after dissolution of areas of barrier layer having physical and/or chemical defects. When no more cracks are going to be created, the current reaches a steady state (Fig. 2, the horizontal lines at $t > 50$ s) in which the pore growth initiates. In two-step anodizing, all pores grow in the same direction. This is because of the reaction related to the oxide layer formation and its dissolution simultaneously in myriads of pores, leading to an equilibrium state. In fact, there is a uniform electric area in all pores which arranges the pores in an equidistant arrangement from each other.

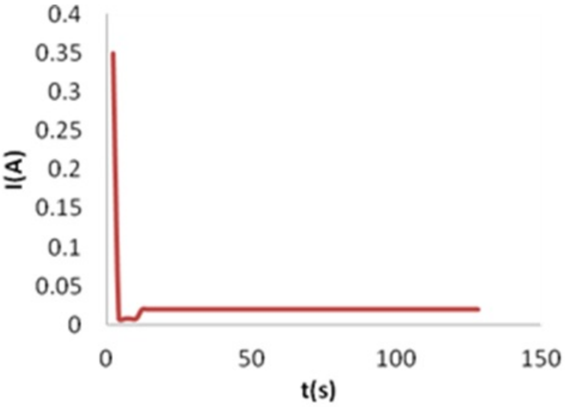

FIG. 2. Current density–time curve of the second anodic oxidation process at 40 V and 0.3 M $H_2C_2O_4$ at 17°C

3.3. Barrier layer opening

The SEM images of the anodic alumina generated by anodization at 40 V are shown in Fig. 3a. The average pore diameters at this voltage were calculated to be 62 nm. The SEM pattern also shows that the thickness of the oxide layer under these conditions was about 80.9 μm (Fig. 3b).

To investigate structural changes that occurred during the pore opening process, a series of SEM images of the barrier oxide layer were taken at different time intervals representing different stages of barrier layer dissolution, and these are presented in Fig. 4.

The SEM image (Fig. 4b) of the barrier layer after about 30 minutes of etching did not show morphological differences in comparison with structures prior to etching (Fig. 4a). After 60 min of etching, the barrier layer is finally breached by the acid (Fig. 4c). Note that the initial opening is uneven across the surface. The majority of the cells have an opening of 57 nm, while a few of the cells remain closed. The structure of the barrier layer after 90 minutes of etching, is completely removed (Fig. 4d).

The XRD patterns for the anodic alumina generated by anodization at 40 V are shown in Fig. 5. There is no peak for nanoporous alumina except the peak of aluminum basis and the amorphous oxide layer. The oxide layer is fragile (ruptured) owing to its amorphous structure.

4. Conclusion

In this work, it has been shown that through a highly-controlled process, the chemical etching of the AAM barrier layer can be performed in such a way as to achieve nanometer scale control of the pore opening. The time resolved dissolution of the barrier oxide film was characterized by SEM. This method has the potential to significantly improve existing pore opening procedures based on time-controlled etching and to improve the reproducibility in the fabrication of AAM membranes having desired pore diameters, particularly when AAM is synthesized using different anodization conditions.

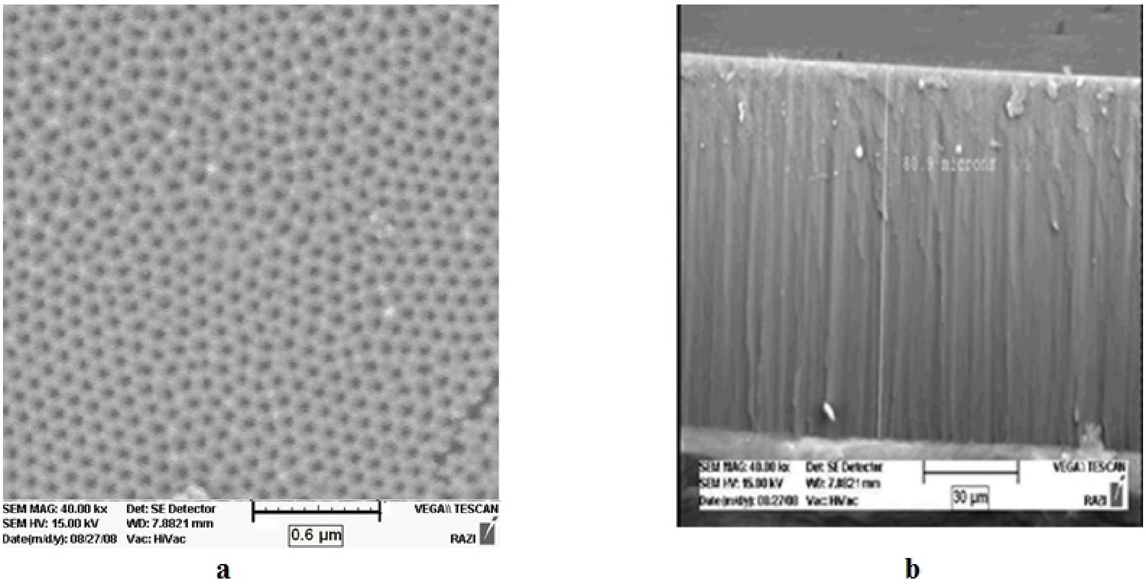

FIG. 3. SEM images of surface (a) and cross section b) of anodic alumina at anodizing conditions of 40 V, 0.3 M $H_2C_2O_4$, 17 °C, 24 hours

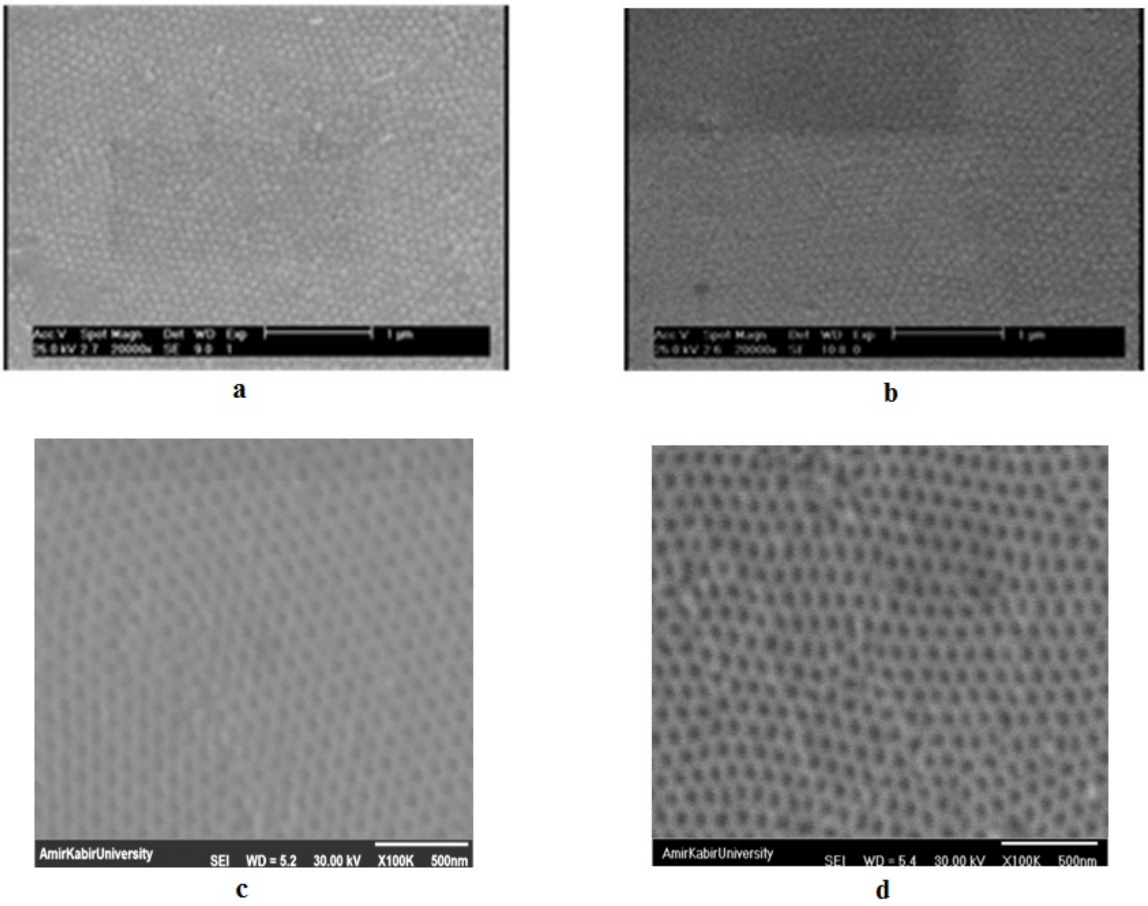

FIG. 4. Bottom surfaces of specimens after barrier layer removal for different processing times. a) 0 min b) 30 min c) 60 min d) 90 min

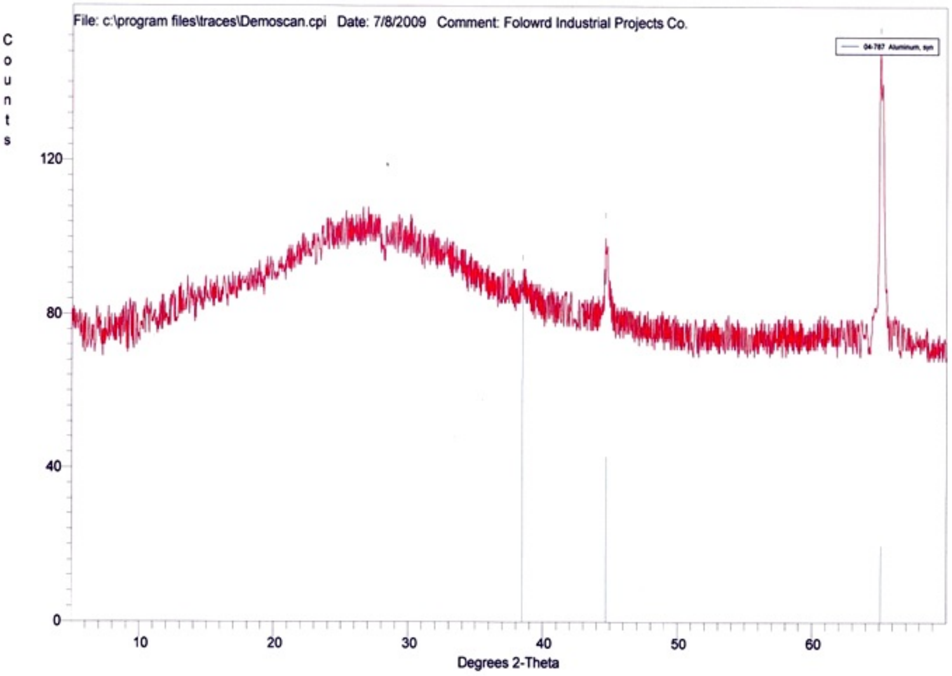

FIG. 5. X-ray diffraction patterns of alumina formed by two step anodizing process

References

[1] Reidenbach F. *Surface Engineering*. ASM International, Ohio, 2007, p. 124.

[2] Itaya K., Sugawara S., Arai K., and Saito S. Properties of porous anodic aluminum oxide films asmembrances. *Journal of Chemical Engineering of Japan*, 1984, **17**(6), P. 514–520.

[3] Masuda H., Yada K. and Osaka A. Self-Ordering of Cell Conguration of Anodic Porous Aluminawith Large-Size Pores in Phosphoric Acid Solution. *Japanese Journal of Applied Physics*, 1998, **37**, P. 212–219.

[4] Keller F., Hunter M.S., Robinson D.L. Structural Features of Oxide Coatings on Aluminum. *The Electrochemical Society*, 1953, **100**(9), P. 411–419.

[5] Crouse D., Lo Y.H., Miller A.E., Crouse M. Self-ordered pore structure of nodized aluminum on silicon and pattern transfer. *Appl. Phys. Lett*, 2000, **76**(1), P. 49–51.

[6] Qin D., Lu M., Li. H. Magnetic force microscopy of magnetic domain structure in highly ordered Conanowire arrays. *Chem. Phys. Lett*, 2001, **350**, P. 51–56.

[7] Imai T., Nomura S. Quantum dot arrays prepared with self-organized nanopore and its photoluminescence spectra. *Physica E: Low-dimensional Systems and Nanostructures*, 2004, **21**, P. 1093–1097.

[8] Steinhart M., Wehrspohn R.B., Gosele U., Wendor J. Nanotubes by Template Wetting: A Modular Assembly System. *Chem. Int. Ed.*, 2004, **43**, P. 1334–344.

[9] J. Justin Gooding. Nanostructuring electrodes with carbon nanotubes: A review on electrochemistry and applications for sensing. *Electrochim. Acta*, 2005, **50**, P. 3049–3060.

[10] Gong D., Yadavalli V., Paulose M., Pishko M., Grimes C. Controlled molecular release using nanoporous alumina, Biomed. *Microdevices*, 2003, **5**, P. 75–80.

[11] Darder M., Aranda P., Hernandez-Velez M., Manova E., Ruiz-Hitzky E. Encapsulation of enzymes in alumina membranes of controlled pore size. *Thin Solid Films*, 2005, **495**, P. 321–326.

[12] Bocchetta P., Ferraro R., F. Di Quarto. Advances in anodic alumina membranes thin film fuel cell: CsH_2PO_4 pore-filler as proton conductor at room temperature. *Power Sources*, 2009, **187**, P. 49–56.

[13] Zheng M.J., Zhang L.D., Li G.H., Shen W.Z. Fabrication and optical properties of large-scale uniformzinc oxide nanowire arrays by one-step electrochemical deposition technique. *Chemical Physics Letters*, 2002, **363**, P. 123–128.

[14] Lee W., Ji R., Gosele U., Nielsch K. Fast fabrication of long-range ordered porous alumina membranesby hard anodization. N*ature Materials*, 2006, **5**, P. 741-747.

[15] Vrubevsky I., Parkoun V., Schreckenbach J., Marx G. Study of porous oxide film growth on aluminum in oxalic acid using a re-anodizing technique. *Applied Surface Science*, 2004, **227**, P. 282–292.

[16] O'Sullivan J.P. and Wood G.C. The Morphology and Mechanism of Formation of Porous Anodic Films on Aluminium. *Proceeding of the Royal Society*, 1970, P. 511–544.

NANOSYSTEMS: PHYSICS, CHEMISTRY, MATHEMATICS, 2016, 7 (6), P. 911–918

The anisotropic properties of a terbium-based liquid crystal complex

L. A. Dobrun[1], A. S. Sakhatskii[1], A. P. Kovshik[1], E. I. Ryumtsev[1], W. Haase[2],
Yu. G. Galyametdinov[3], A. S. Krupin[3], A. A. Knyazev[3]

[1]Saint Petersburg State University, Universitetskaya nab. 7/9, Saint Petersburg, 199034, Russia

[2]Technical University Darmstadt, Alarich-Weiss-Str 4, Darmstadt, D 64284, Germany

[3]Kazan National Research Technological University, Karl Marks street 68, Kazan, 420015, Russia

l.dobrun@spbu.ru

DOI 10.17586/2220-8054-2016-7-6-911-918

The dielectric properties of a paramagnetic terbium-containing liquid crystal have been studied. The magnitude and the sign of the dielectric of the liquid crystalline complex have been determined. The relaxation processes (modes) characterizing the dispersion of the principal values of the sample's dielectric permittivity has been studied. The relaxation times, activation energy and the dipole moment of the complex could be evaluated.

Keywords: lanthanidomesogens, dielectric permittivity, dielectric anisotropy.

Received: 14 October 2016

Revised: 20 November 2016

1. Introduction

Lanthanide containing compounds are widely used in various optical electronic devices, organic light-emitting diodes of different colors, flat-panel and flexible displays, optical waveguides, hybrid lasers, solar cells, etc [1–3]. Synthesizing and studying the molecular and macroscopic properties of liquid crystalline coordination compounds of lanthanides (lanthanidomesogens) is an important physicochemical problem. Paramagnetic complexes of lanthanides with organic ligands combined highly effective luminescence with abnormally large values of magnetic susceptibility anisotropy, allowing the easy alignment under the influence of an external magnetic field [4]. The technical characteristics of the lanthanidomesogens depend essentially on their physical properties.

Some important physical parameters that determine the effectiveness of the orientation of the lanthanidomesogens under the magnetic or electric field are the anisotropy of magnetic susceptibility and of dielectric anisotropy, respectively. Physical characteristics of lanthanide coordination compounds are determined by the central ion and its surrounding ligands [5]. Therefore, studying the relationship between molecular and macroscopic properties of lanthanidomesogens is an important task of physical chemistry of the lanthanides.

In recent years, a number of lanthanide complexes that include Lewis bases and -diketones serving as ligands have been synthesized [6–10]. Rare examples of these compounds have a stable enantiotropic nematic phase within a wide temperature range, which was demonstrated by methods of differential scanning calorimetry and polarizing optical microscopy [11, 12]. It was found that magnetic properties of lanthanidomesogens are strongly dependent upon the nature of the lanthanide ion and on the structure of the coordination center [13, 14]. The first study of the dielectric properties of lanthanidomesogens - tris[1- (4- (4-propylcyclohexyl) phenyl) octane-1,3-dion]-[5,5'-diheptadecyl-2,2'-bipyridine] ytterbium ($\mathrm{Yb(CPDk_{3-5})_3\ Bpy_{17-17}}$) is presented in [15, 16]. The frequency dependence of the components of the dielectric permittivity tensor has been obtained in the range between 100 Hz–5 MHz. The magnitude and the sign of the dielectric anisotropy, the relaxation time, the activation energy, and the dipole moment have been determined.

The aim of this study is to investigate the influence of the central ion on dielectric properties of nematic lanthanidomesogens, and, in particular, on the magnitude and the sign of dielectric anisotropy.

2. Material

The object of the study was a liquid crystal complex tris[1-(4-(4-propylcyclohexyl)phenyl)octane-1,3-dion]-[5,5'-di(heptadecyl)-2,2'-bipyridine] terbium ($\mathrm{Tb(CPDk_{3-5})_3Bpy_{17-17}}$), containing ligands similar to the previously studied lanthanidomesogens $\mathrm{Yb(CPDk_{3-5})_3Bpy_{17-17}}$ [15,16]. The synthetic schemes for the investigated materials are shown in Fig. 1.

Quantum-chemical simulation of the equilibrium geometry of $\mathrm{Yb(CPDk_{3-5})_3Bpy_{17-17}}$ complexes was performed using the Prird 06 software by the DFT method with the PB exchange correlation functional (Fig. 2).

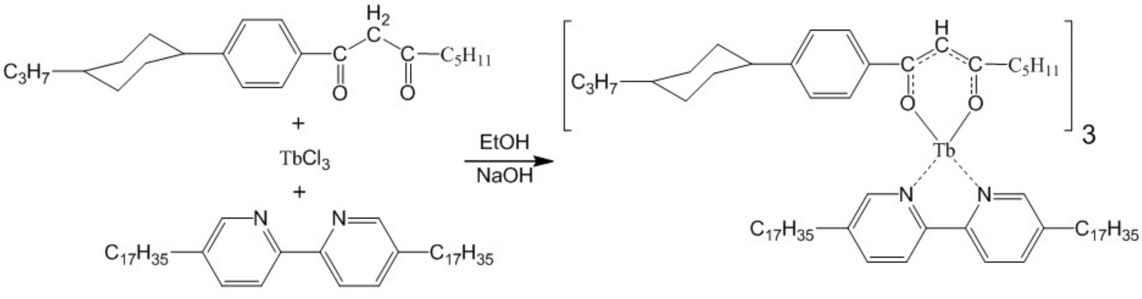

FIG. 1. Synthesis and chemical structure of the investigated terbium-based liquid crystalline complex

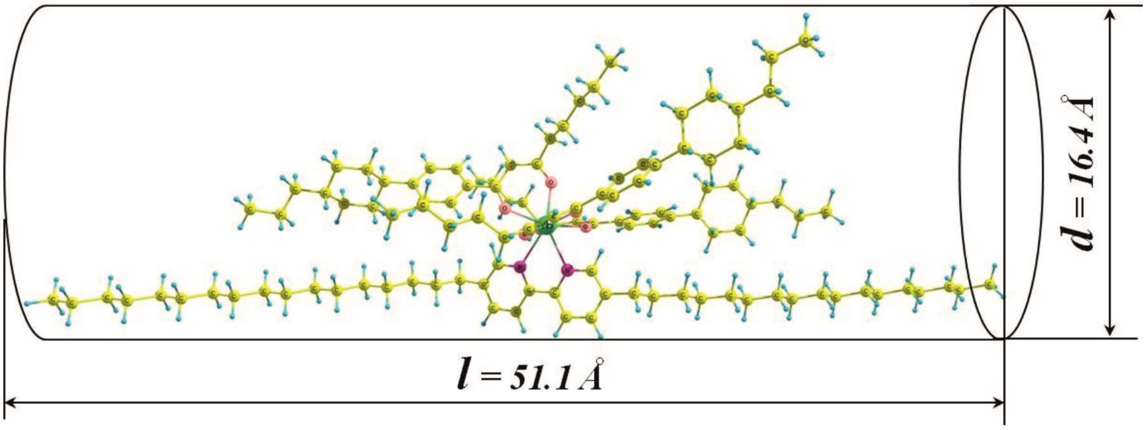

FIG. 2. Optimized structure and geometry parameters of Tb(CPDk$_{3-5}$)$_3$Bpy$_{17-17}$ complexes

For synthesizing Tb(CPDk$_{3-5}$)$_3$Bpy$_{17-17}$, an alcoholic solution of 0.031 g (0.083 mM) TbCl$_3$6·H$_2$O, while stirring, was slowly poured into a hot solution, containing 0.085 g (0.25 mM) of β-diketone (1-(4-(4-propylcyclohexyl)phenyl)octane-1,3-dion), 0.053 g (0.083 mM) 5,5'-diheptadecyl-2,2'-bipyridine and 0.015 g (0.25 mM) EOH. The deposited yellow precipitate was filtered off while hot, under stirring, washed with alcohol and dried in vacuo. Yield: 0.078 g (52 %). Formula: C$_{113}$H$_{175}$N$_2$O$_6$Tb; Found, %: C, 74.68; H, 9.84; N, 1.51; Tb, 8.72. Calculated, %: C, 74.71; H, 9.71; N, 1.54; Tb, 8.75. IR spectrum, ν, cm^{-1}: 1590, 1492 (C=N, Phen); 1542, 1465, 1437, 938 (C=O); 1394, 1348, 1024 (CH$_3$); 1172, 784, 765 ((CH$_2$)n); 1254 (C=C), 1218, 1103 (C$_6$H$_4$); 729, 654, 634, 602, 512 (Tb-O); 728 ((CH$_2$) n-O). CHN elemental microanalysis was performed with the analyzer CE Instruments EA-1110, X-ray fluorescence analysis – with the universal spectrometer "SUR-02 "Renom FV". IR Specta of the sample in KBr were registered with ALPHA FT-IR spectrometer. The terbium complex Tb(CPDk$_{3-5}$)$_3$Bpy$_{17-17}$ forms a nematic liquid crystalline phase within the temperature range 100–160°C.

The anisotropy of the magnetic susceptibility of the complex $\Delta\chi = \chi_{||} - \chi_{\perp}$ ($\chi_{||}$ and χ are values of the magnetic susceptibility of the liquid crystal in the directions parallel and perpendicular to the axis of preferential orientation of molecules, respectively) was measured using the Faraday method [17]. The sign of $\Delta\chi$ was via optical birefringence measurements in a magnetic field (Cotton-Mouton effect) [13].

The obtained value $\Delta\chi$, that equals -12690×10^{-6} cm^3/mol, is one of the largest absolute values among the compounds using the same type of ligand environment but various lanthanide ions [13].

3. Dielectric measurements

The measurement of the dielectric permittivity is a powerful tool for characterizing the structure and physical properties of liquid crystalline materials [18] Investigations of the terbium complex were carried out using the analyzer HIOKI-3532 operating within the frequency range 100 Hz to 5 MHz. A titanium plane capacitor with the 200 μm distance between electrodes (electrical capacity 12 pF) was used as a sample cell. The macroscopic alignment of the liquid crystal sample in the cell was provided by a magnetic field of up to 5000 Oe. As probing voltage U we used 1V because the dielectric permittivity ε do not depend on U between 0.5 V and 2.0 V (Fig. 3). In this range the electric field does not affect the orientation of the complex.

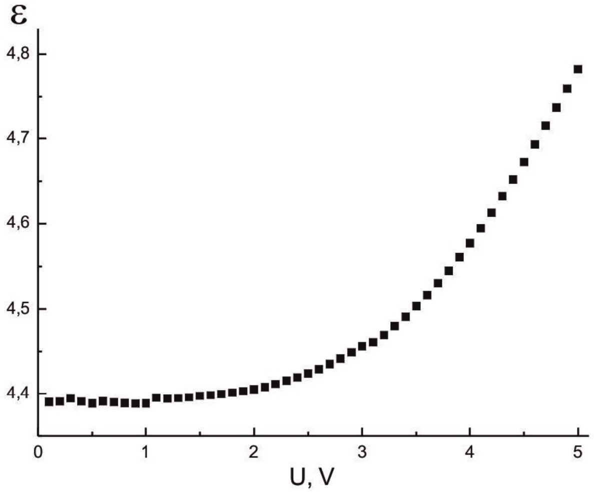

FIG. 3. The dielectric permittivity ε of the sample versus the probing voltage U (frequency $f = 10$ kHz, $T = 130$ °C)

X-ray diffraction pattern of a number of paramagnetic lanthanidomesogens oriented throughout a magnetic field showed that, unlike diamagnetic liquid crystal, the director (the preferred direction of orientation of the molecular long axes) can vary by several degrees from the direction of the highest value of the magnetic susceptibility χ [17]. The difference of 10 degrees between the directions of the axes of the highest value of the magnetic susceptibility χ and the highest value of the dielectric permittivity ε, has been found in the study of the dielectric properties of Yb(CPDk$_{3-5}$)$_3$Bpy$_{17-17}$ using the orienting magnetic field [16]. Therefore, in this study we measured the dielectric permittivity Tb(CPDk$_{3-5}$)$_3$Bpy$_{17-17}$ at different angles φ between the directions of the probing electric field **E** ($f = 10$ kHz) and the orienting magnetic field (**H**=5000 Oe). The dependence of ε on φ at 130 ° is shown in Fig. 4.

It can be seen the dielectric permittivity reaches a maximum value at angle $\varphi = 0$ °, i.e. the directions of the electric and magnetic fields, respectively, coincide (**E**$||$**H**). The minimum value of the dielectric permittivity corresponds to the angle $\varphi = 90$ °, if the direction of the electric field is orthogonal to the magnetic field (**E**$\perp$**H**). Consequently, the maximum of the magnetic susceptibility coincides with the maximum of the dielectric permittivity. That is why the measurement of the components of the dielectric permittivity Tb(CPDk$_{3-5}$)$_3$Bpy$_{17-17}$ was carried out for **E**$||$**H** and **E**$\perp$**H**.

The orientation of the nematic liquid crystal molecules in the plane sample cell relative to the direction of the orienting magnetic field **H** and the probing electric field **E** is shown schematically in Fig. 5.

In the case of a positive sign of the magnetic susceptibility anisotropy $\Delta\chi > 0$, the long axes of the mesogenic molecules are homogeneously aligned along the direction of the magnetic field (Fig. 6a,b). The paramagnetic complex under study, as noted above, has a negative sign of the macroscopic anisotropy of the magnetic susceptibility [13]. In this case the long axes of the molecules Tb(CPDk$_{3-5}$)$_3$Bpy$_{17-17}$ are perpendicular to the orienting magnetic field (Fig. 5c,d). However, the magnetic field does not provide a homogeneous orientation (same direction) rather a planar one of the long molecular axes throughout the sample (Fig. 5c,d). Fig. 5 shows that for **E**$||$**H** the electric field direction is perpendicular to the long axes of the molecules. Then it seems evident that the measured component $\varepsilon_{(\mathbf{E}||\mathbf{H})}$ is the transverse component of the dielectric permittivity $\varepsilon_\perp$. The reorientation around the short molecular axes is at lower frequencies, probably hidden under the conductivity part.

The measurement of the dielectric permittivities over frequency range of 100 Hz to 5 MHz indicated the presence of the dispersion within the temperature range of the nematic phase and in the isotropic liquid state ε_{is}. To illustrate it, Fig. 6 showed the dependencies of $\varepsilon_{(\mathbf{E}||\mathbf{H})} = \varepsilon_\perp$ and $\varepsilon_{(E\perp H)}$ on $\lg f$ at 130 °C, and also ε_{is} at 160 °C.

First, it can be seen from Fig. 6 that within the 100 Hz–100 kHz frequency range the anisotropy $\varepsilon_{(\mathbf{E}\perp\mathbf{H})} - \varepsilon_\perp$ has a negative sign and changes the sign to positive at the highest frequencies (the insert in Fig. 6). The increase of all components $\varepsilon_\perp$, $\varepsilon_{(\mathbf{E}\perp\mathbf{H})}$ and ε_{is} at frequencies below 5 kHz is due to contribution of conductivity to the

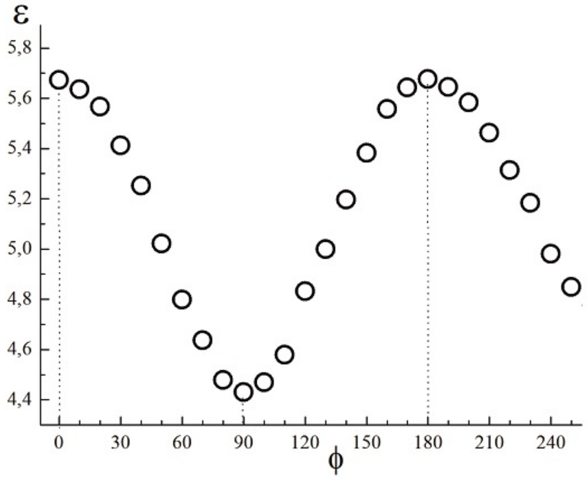

FIG. 4. The dielectric permittivity ε of the sample versus the angle φ between the directions of the probing electric field **E** ($f = 10$ kHz) and the direction of orienting magnetic field (**H**=5000 Oe), $T = 130$ °C

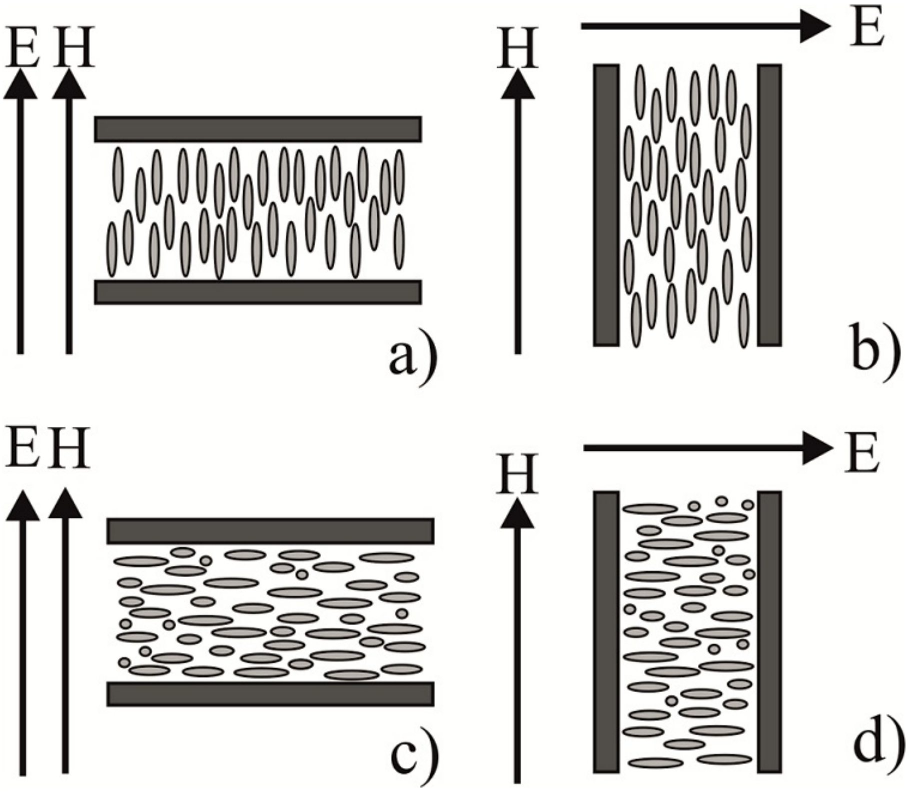

FIG. 5. The orientation of nematic liquid crystal molecules in the sample cell under the influence of the magnetic field **H** relative to the direction of the probing electric field **E**: a) and b) – nematic liquid crystal with a positive magnetic anisotropy **E**||**H** and **E**⊥**H** respectively; c) and d) – nematic liquid crystal with a negative magnetic anisotropy **E**||**H** and **E**⊥**H** respectively

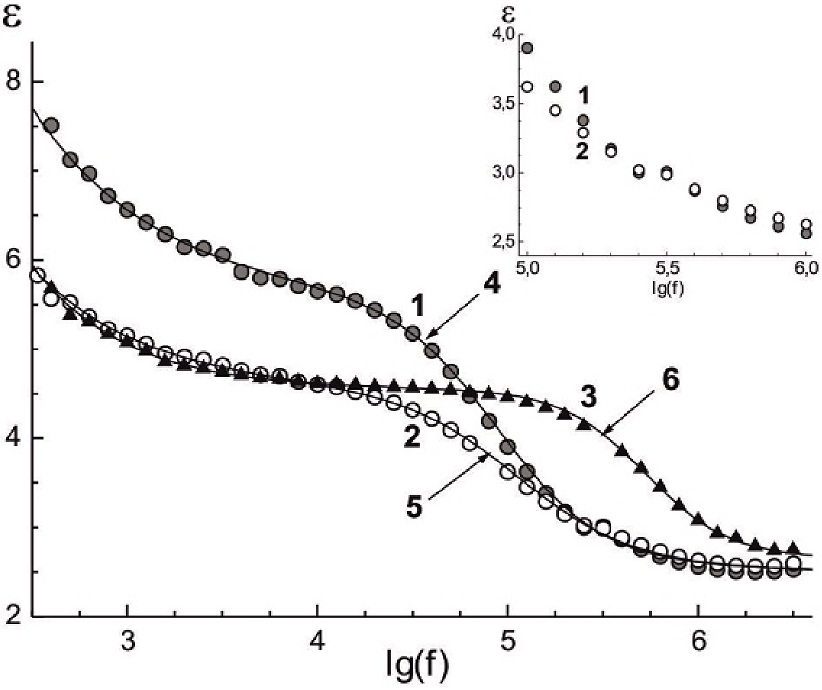

FIG. 6. The dependence of the components of dielectric permittivity on the electric field frequency. Experimental points: 1 – $\varepsilon_{(\mathbf{E}||\mathbf{H})} = \varepsilon_{\perp}$; 2 – $\varepsilon_{(\mathbf{E}\perp\mathbf{H})}$; 3 – ε_{is}; Theoretical curves calculated using the Cole-Cole equation: 4 – $\varepsilon_{(\mathbf{E}||\mathbf{H})} = \varepsilon_{\perp}$; 5 – $\varepsilon_{(\mathbf{E}\perp\mathbf{H})}$; 6- ε_{is}

effective value of the dielectric permittivity. From the given data it also follows that the dispersion is realized within the same frequency range 10 kHz – 1 MHz. The values $\varepsilon_{\perp} = 2.496$ and $\varepsilon_{(\mathbf{E}\perp\mathbf{H})} = 2.564$ at highest frequency $f = 5$ MHz differ slightly from the values $n_o^2 = 2.256$ and $n_e^2 = 2.522$, that was measured using the prism method [19] at wavelength $\lambda = 632$ nm). This means that the dipole part is almost completely excluded from the dielectric polarization of the complex at frequencies above 5 MHz. Perhaps the small contribution ($\varepsilon_{\perp}$- n_o^2) and ($\varepsilon_{(\mathbf{E}\perp\mathbf{H})}$- n_e^2) to the dielectric polarization by intramolecular rotation of polar groups remains. In order to understand the observed phenomenon, it is useful to consider the well-known dipole mechanisms of dielectric polarization of nematic liquid crystals [20–22]. In the presence of the longitudinal and transverse components of the molecular dipole moment these mechanisms are: the rotation of molecules around short molecular axes, the rotation around the long axes and the rotational motion about the long axis of the precessing molecule. It should be noted that the rotation of molecules around the short transverse axis requires overcoming a potential barrier responsible for a long-range order in the liquid crystal phase, while the rotation of molecules around the longitudinal molecular axes and the cone is less hindered. Therefore, parts of the dipole polarization $\varepsilon_{\perp}$ and $\varepsilon_{||}$ are excluded from the polarization at much higher frequencies than the dipole part of polarization $\varepsilon_{||}$ determined by the first mechanism. Therefore, it can be claimed that the experimentally observed coincidence of dispersion areas of the permittivity $\varepsilon_{\perp}$and $\varepsilon_{(\mathbf{E}\perp\mathbf{H})}$ of Tb(CPDk$_{3-5}$)$_3$Bpy$_{17-17}$ (Fig. 6) indicates that the dipole parts of the dielectric polarization of the complex $\varepsilon_{\perp}$ is associated with the rotation of the polar molecules around the longitudinal axes and across to the cone surface. Reorientation around the short molecular axes was not seen. Perhaps this mechanism of the complex dielectric polarization is realized at frequencies below 100 Hz and may be hidden under the conductivity part.

The experimental frequency dependences of the dielectric permittivities given in Fig. 6 are approximated by the Cole-Cole equation taking into account the contribution of the sample's conductivity:

$$\varepsilon = \varepsilon_{\infty} + \frac{\varepsilon_0 - \varepsilon_{\infty}}{1 + (i2\pi f \tau)^{1-\alpha}} + \frac{B}{f^N}, \tag{1}$$

where, ε_0 is a quasi-static dielectric permittivity; ε_{∞} is a high-frequency value of the dielectric permittivity; τ is average time of the dielectric relaxation; α is a parameter characterizing the distribution of relaxation times; B and $N \leq 1$ are numerical coefficients. The best agreement between theoretical curves and experimental points for the components of the dielectric permittivity was obtained under the following parameters: for $\varepsilon_{\perp}$($\varepsilon_0 = 5.6$; $\varepsilon_{\infty} = 2.5$;

$\alpha = 0.1$; $\tau = 1.7 \times 10^{-6}$; $B = 100$; $N = 0.67$), for $\varepsilon_{(\mathbf{H}\perp\mathbf{E})}$ - ($\varepsilon_0 = 4.6$; $\varepsilon_\infty = 2.5$; $\alpha = 0.15$; $\tau = 1.4 \times 10^{-6}$; $B = 100$; $N = 0.75$), and for ε_{is} ($\varepsilon_0 = 4.55$; $\varepsilon_\infty = 2.65$; $\alpha = 0.01$; $\tau = 1.4 \times 10^{-6}$; $B = 100$; $N = 0.75$). In Fig. 6 theoretical curves are represented by solid lines 4,5,6. The above parameters are also determined for other temperatures in the nematic and isotropic phases.

The dependencies of quasi-static values $\varepsilon_{0\perp}= \varepsilon_{0(\mathbf{E}||\mathbf{H})}$, and ε_{0is} on the temperature are shown in Fig. 7, where the lower scale presents temperature; and the upper scale presents the relative temperature ΔT.

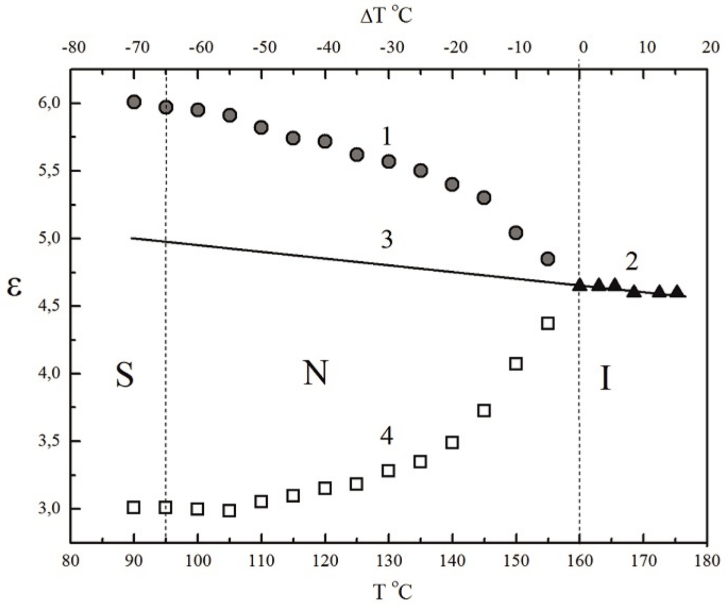

FIG. 7. The dependence of the quasi-static dielectric permittivity components on the temperature:1 – $\varepsilon_{o\perp}$; 2 – ε_{ois}; 3 – $<\varepsilon>$; 4 – $\varepsilon_{o||}$

The value $\varepsilon_{||}$ can be calculated using the Maier-Meier theory of liquid crystal dielectric polarization [23] and experimental data showing that the average value of the dielectric permittivity $<\varepsilon>= (\varepsilon_{||} + 2\varepsilon_{\perp})/3$ equals ε_{is} or is only a few percent different from it at the transition temperature from an isotropic phase to a mesomorphic state. The extrapolation of the temperature dependence ε_{ois} to the area of the mesophase existence allows one to obtain the dependency of $<\varepsilon>$ on the temperature (Fig. 7) and calculating $\varepsilon_{||}$ at different temperatures. Thus determined values of $\varepsilon_{o||}$ are presented in Fig. 7 (dependence 4). The value of the dielectric anisotropy of the complex Tb(CPDk$_{3-5}$)$_3$Bpy$_{17-17}$ $\Delta\varepsilon = \varepsilon_{||} - \varepsilon_{\perp}$, calculated on the basis of the data shown in Fig. 7 varies from -0.5 to -2.15 within the temperature ΔT from -5 °C to -25 °C For the studies in the paper [6], the ytterbium-based coordination compound Yb(CPDk$_{3-5}$)$_3$Bpy$_{17-17}$ with similar ligands in the same interval of temperatures ΔT the dielectric anisotropy $\Delta\varepsilon$ varies from -0.4 to -2.4. We can conclude that the dielectric anisotropies of the discussed liquid crystal complexes, found within the same frequency range, are identical in sign and close in magnitude.

During the analysis of the dispersion of the dielectric permittivities of the studied complex $\varepsilon_\perp$ and $\varepsilon_{(\mathbf{E}\perp\mathbf{H})}$ the relaxation times for different temperatures were determined. The dependencies of relaxation times $\tau_\perp\tau_{(\mathbf{E}\perp\mathbf{H})}$ and τ_{is} on the reciprocal temperature $1/T$ are shown in Fig. 8.

From the slopes of the lines according to the Arrhenius equation:

$$\tau = \tau_0 \exp\left(\frac{W}{kT}\right), \tag{2}$$

we obtained the activation energy of the molecular mechanisms responsible for the dipole polarization in the studied frequency range in the mesophase and isotropic state. The values W$_{||}$ and W$_{(\mathbf{E}\perp\mathbf{H})}$ are identical within experimental error, and equal to 80 kJ/mol. The activation energy in the isotropic phase was greater U$_{is}$ = 105 kJ/mol. This can be explained by the fact that the rotation of the molecules around the long axis in the isotropic phase is more hindered than in the nematic phase. As an example this was confirmed by experimental data for 4,4'-di-n-heptyloxyazoxybenzene [24].

The significant difference between the values of quasi-static dielectric permittivity $\varepsilon_{||}\varepsilon_\perp\varepsilon_{is}$ and refractive indices n_e, n_o and n_{is}, and also the presence of dispersion $\varepsilon_{(\mathbf{E}\perp\mathbf{H})}$, $\varepsilon_\perp$, ε_{is} suggests that the studied paramagnetic

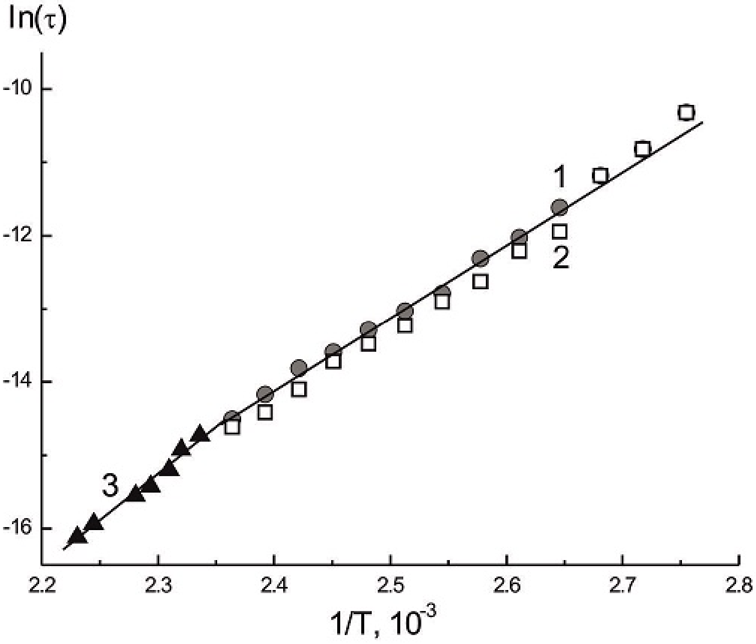

FIG. 8. The dependence of relaxation times on the temperature. 1 – $\tau_{\perp}$; 2 – $\tau_{(\mathbf{E}\perp\mathbf{H})}$; 3 – τ_{is}

complex is a polar substance. The value of the permanent dipole moment of the complex $\mu = 6.4$ D was determined using the dielectric permittivity $\varepsilon_{is} = 4.7$, the refractive index of the isotropic phase $n = 1.522$ and the Onsager's formula:

$$\frac{9\left(\varepsilon_{is} - n^2\right)\left(2\varepsilon_{is} + n^2\right)}{\varepsilon_{is}\left(n^2 + 2\right)^2} = \frac{4\pi N_A \rho \mu^2}{MkT}, \tag{3}$$

where N_A – Avogadro's number, $\rho \approx 1$ g/cm^3 – complex density, $M = 1814$ – molecular weight. The true value of the dipole moment of the complex μ can be higher than the obtained one, as the Onsager's formula is valid only for weakly polar substances. In addition, the presence of the longitudinal component of the dipole moment, that has not manifested itself during the polarization within the 100 Hz – 5 MHz electric field frequency range, can also increase μ.

4. Conclusion

Dispersions of the dielectric permittivity components of Tb(CPDk$_{3-5}$)$_3$Bpy$_{17-17}$ and Yb(CPDk$_{3-5}$)$_3$ Bpy$_{17-17}$ are realized within the same frequency range and are associated with the rotation of the polar molecules around the longitudinal axes and across to the cone's surface. Dispersion associated with reorientation around the short molecular axes was not seen. The value dielectric anisotropies of the discussed liquid crystal complexes are identical in sign and close in magnitude, therefore it can be concluded that variation of the central ion has a weak influence dielectric properties of lanthanidomesogens with the same ligand environment.

Acknowledgements

L. A. Dobrun, A. P. Kovshik, A. S. Sakhatskii thank grant SPbU No 11.37.161.2014 for support of the investigation of the dielectric properties of the terbium-based complex.

E. I. Ryumtsev thanks grant SPbU No 11.37.145.2014 for support of the investigation of the optical properties of the terbium-based.

A. S. Krupin, A. A. Knyazev, Yu. G. Galyametdinov thank grant RSF14-13-00758 for support of the synthesis of the terbium-based.

References

[1] Feng J., Zhang H. Hybrid materials based on lanthanide organic complexes: a review. *Chemical Society Reviews*, 2013, **42**, P. 387–410.

[2] Kalyani N.T, Dhoble S.J. Novel materials for fabrication and encapsulation of OLEDs. *Renewable and Sustainable Energy Reviews*, 2015, **44**, P. 319–347.

[3] Xu H., Sun Q., An Z., Wei Y., Liu X. Electroluminescence from europium (III) complexes. *Coordination Chemistry Reviews*, 2015, **293**, P. 228–249.

[4] Knyazev A.A., Molostova E.Yu., Krupin A.S., Heinrich B., Donnio B., Haase W., Galyametdinov Yu.G. Mesomorphic behaviour and luminescent properties of mesogenic-diketonate lanthanide adducts with 5,5′-di(heptadecyl)-2,2′-bipyridine. *Liquid Crystals*, 2013, **40**, P. 857–863.

[5] Binnemans K. Lanthanidomesogens. *Handbook on the Physics and Chemistry of Rare Earths*, 2013, **43**, P. 1–158

[6] Binnemans K. Luminescence of metallomesogens in the liquid crystal state *Journal of Materials Chemistry*, 2009, **19**, P. 448–453.

[7] Goossens K., Bruce D.W., Van Deun R., Binnemans K., Cardinaels Th. Nematogenic tetracatenar lanthanidomesogens. *Dalton Transactions*, 2012, **41**, P. 13271–13273.

[8] Terazzi E., Suarez S., Torelli S., Nozary H., Imbert D., Mamula O., Rivera J.-P., Guillet E., Bénech J.-M., Bernardinelli G., Scopelliti R., Donnio B., Guillon D., Bünzli J.-C., Piguet C. Introducing Bulky Functional Lanthanide Cores into Thermotropic Metallomesogens: A Bottom-Up Approach. *Advanced Functional Materials*, 2006, **16**, P. 157–168.

[9] Binnemans K., Lodewyckx K., Parac-Vogt T.N., R.Van Deun, Goderis B., Tinant B., K. Van Hecke, L. Van Meervelt. Adducts of Schiff Bases with Tris (β-diketonato) lanthanide(III) Complexes: Structure and Liquid-Crystalline Behaviour. *European Journal of Inorganic Chemistry*, 2003, P. 3028–3033.

[10] Knyazev A.A., Krupin A.S., Molostova E.Yu, Romanova K.A., Galyametdinov Yu.G. Influence of Structural Anisotropy on Mesogenity of Eu (III) Adducts and Optical Properties of Vitrified Films Formed on their Base. *Inorganic Chemistry*, 2015, **54**, P. 8987–8993.

[11] Galyametdinov Yu.G., Knyazev A.A., Dzhabarov V.I., Cardinaels T., Driesen K.S., Görller-Walrand C., Binnemans K. Polarized luminescence from aligned samples of nematogenic lanthanide complexes. *Advanced materials*, 2008, **20**, P. 252–257.

[12] Dzhabarov V.I., Knyazev A.A., Strelkov M.V., Molostova E.Yu., Schustov V.A., Haase W., Galyametdinov Yu.G. Tris (β-diketonates) lanthanum nematic adducts. *Liquid Crystals*, 2010, **37**, P. 285–291.

[13] Dzhabarov V.I., Knyazev A.A., Nikolaev V.F., Galyametdinov Yu.G. Anisotropy of the magnetic susceptibility of mesogeneous lanthanide complexes. *Russian Journal of Physical Chemistry A*, 2011, **85**, P. 1450–1453.

[14] Mironov V.S., Galyanetdinov Yu.G., Ceulemans A., Gorller-Walrand C., Binnemans K. Influence of crystal-field perturbations on the room-temperature magnetic anisotropy of lanthanide complexes, *Chem. Phys. Lett.*, 2001, **345**, P. 132-140.

[15] Dobrun L.A., Sakhatskii A.S., Kovshik A.P., Ryumtsev E.I., Knyazev A.A., Galyametdinov Yu.G. Dielectric Properties of an Ytterbium-Based Nematic Liquid-Crystal Complex. *JETP Letters*, 2014, **99**, P. 133–135.

[16] Dobrun L.A., Sakhatskii A.S., Kovshik A.P., Ryumtsev E.I., Kolomiets I.P., Knyazev A.A., Galyametdinov Yu.G. Dielectric and Magnetic Anisotropy of a Nematic Ytterbium Complex. *JETP*, 2015, **147**, P. 1064–1067.

[17] Galyametdinov Y.G., Haase W., Goderis B., Moors D., Driesen K., R. van Deun, Binnemans K. Magnetic alignment study of rare-earth-containing liquid crystals. *Journal of Physical Chemistry B*, 2007, **111**, P. 13881–13885.

[18] Haase W., Wróbel S. Relaxation phenomena: liquid crystals, magnetic systems, polymers, high-Tc superconductors, metallic glasses. Springer Science & Business Media, 2013.

[19] Kovshik A.P., Krainyukov E.S., Kovshik S.A., Knyazev A.A., Galyametdinov Yu.G., Ryumtsev E.I. Optical Anisotropy of Liquid Crystal Lanthanide Complexes. *Optics and Spectroscopy*, 2014, **116**, P. 56–61.

[20] Nordio P.L., Rigatti G., Serge U. Dielectric relaxation theory in nematic liquids. *Molecular physics*, 1973, **25**, P. 129–136.

[21] Tsvetkov V.N., Ryumtsev E.I., Polushin S.G., Kovshik A.P. Molecular mechanisms of polarization and its relaxation in nematic liquid-crystals. *Acta physica polonica A*, 1979, **56**, P. 871–878.

[22] Clark M.G. Macroscopic Properties of Liquid Crystals. *Molecular Crystals and Liquid Crystals*, 1985, **127**, P. 141.

[23] Maier W., Meier G. Eine einfache Theorie der dielektrischen Eigenschaften homogen orientierter kristallinflüssiger Phasen des nematischen Typs. *Z. Naturforschg*, 1961, **16a**, P. 262267.

[24] Nguyen X.P., Urban S., Wrobel S., Kresse H. *Acta physica polonica*, 1978, **A54**(5), P. 617–623.

NANOSYSTEMS: PHYSICS, CHEMISTRY, MATHEMATICS, 2016, 7 (6), P. 919–924

Macroscopic thermoelectric efficiency of carbon nanocomposites

E. D. Eidelman[1,2], A. P. Meilakhs[1]

[1]1Ioffe Physical Technical Institute, 26 Politekhnicheskaya, 194021 Saint Petersburg, Russia

[2]Saint Petersburg State Chemical-Pharmaceutical Academy, 14 Professora Popova,
197376 Saint Petersburg, Russia

eidelman@mail.ioffe.ru, mejlaxs@mail.ioffe.ru

PACS 84.60.Rb, 85.80.Fi **DOI 10.17586/2220-8054-2016-7-6-919-924**

The subject of this study is the thermoelectric efficiency (Z) and the thermoelectric parameter (ZT) of carbon nanocomposites, namely, the structures consisting of graphite-like (gr) and diamond-like (d) regions made of sp^2 and sp^3 hybridized carbon atoms, respectively. The impact of heat transfer across the boundary between sp^2 and sp^3 areas is analyzed for the first time. It is shown that the interfacial thermal resistance (Kapitza resistance) is not lower than the thermal resistance in the macroscopic gr region. The influence of various factors on the Kapitza resistance is analyzed. The value of $ZT \approx 3.5$ at room temperature, taking into account the interfacial thermal resistance, is significantly higher than it would be in gr films ($ZT \approx 0.75$).

Keywords: carbon nanostructures, thermoelectricity.

Received: 28 October 2016

1. Introduction

In recent years, a lot of attention has been paid to the influence of size on transport phenomena in solids and, in particular, on thermoelectric effects [1–5]. Currently, attention is focused on the creation of new materials with the highest possible thermoelectric figure of merit (quality factor) Z, which makes it possible to use this material in refrigerators or generators [2,5]: $Z = S^2\sigma/\chi$. Here, S is the thermoelectric coefficient or the Seebeck coefficient (V/K), σ is the conductivity ratio ((Ohm·m) -1), and χ is the thermal conductivity (J/(m·s·K)).

The higher the value of the parameter ZT (where T is the temperature in Kelvin) is for any material, the more useful this material is for thermoelectric conversion. Therefore, ZT is used as a dimensionless quantity that characterizes thermoelectric materials.

Serious efforts were made to increase Z, both by selecting an appropriate semiconductor and by determining its optimal layer thickness [3, 4]. To the best of the authors' knowledge, the highest value ZT = 2.6 at room temperature is reported in [6] for SnSe crystals.

Part of this effort is the study of thermoelectric phenomena in carbon nanostructures [3–5]. In these nanostructures, hybridized carbon atoms coexist. The coexistence of regions with very different electrical and thermal properties at such small distances from each other is a unique feature of these structures. The gr areas are semimetallic with a high electrical conductivity but a relatively low thermal conductivity. The d areas are wide bandgap semiconductors, dielectrics in fact, but with a high thermal conductivity. The corresponding kinetic coefficients differ in value by many orders of magnitude.

The article deals with the Z values of the composite produced from 4 nm diamond nanoparticles generated by detonation synthesis. Such diamond nanoparticles were prepared by milling [7–9] and before long by purification techniques [10, 11] from agglomerates about 100 nm in size. Then, solid composite was produced from 4 nm particles by sintering at high pressure and high temperature (HPHT). Regions with sp^3 hybridization, as determined by areas of coherence, reached sizes of up to 4-12 nm. The composite consists of such particles with a d core, which can be covered by up to four layers of the sp^2 phase, but may have no coating at all. The composite is completely free from the separate gr phase. The average particle size becomes 4-35 nm [12]. Then, the size of gr regions can be assumed at an average of $\mathrm{l} \approx$ 10–30 nm. The thermoelectric effect and mechanisms that contribute to the increase in the thermoelectric coefficient S, the main component of the Z, were discussed in [13, 14] for carbon nanostructures.

As for the ratio of electrical and thermal conductivity coefficients σ/χ being part of Z, it is always considered to be proportional to the temperature according to the Wiedemann - Franz law (see, e.g., [15] §78). Of course, there may be limitations associated with the possible flow of heat in the gr areas. Let us further assume that the percolation threshold (see, eg, [16]) is reached [9], but the heat carried by electrons is small compared with the lattice vibrations heat transfer.

It was recently shown that the presence of borders between the gr and d regions greatly influences the thermal conductivity of carbon nanostructures [17,18]. In this paper, we examine the effect of borders on the thermoelectric efficiency.

2. Statement of the problem of heat transfer through the interface between phases

Let us assume that the gr area is heated or cooled on one side and contacts with a d area on the other side. In this case, the gr phonons migrate into d or d phonons migrate into gr. In accordance with Fourier's law, this heat source lowers or raises the temperature of the gr lattice. The heat of the electron gas from the gr area is not directly transferred to the d area. However, the electrons can heat or cool the crystal lattice in gr. An increase in the phonon flux component takes place, and then the heat is transferred from this component to the d area. This nonlinear process occurs due to the temperature difference between the electronic and phonon subsystems in gr. It appears as a result of presence of the boundary with d. The ideal structure would be the one with plane borders perpendicular to the direction of heat propagation. Any possibility of heat flow bypassing the border increases the thermal conductivity, and thus reduces the thermoelectric efficiency Z.

The temperature at the border undergoes a jump ΔT, which is proportional to the heat flux q (W/m^2). Such dependence makes it possible to use the electrothermal analogy. The proportionality coefficient r (m^2·K/W) between the ΔT and q is called interfacial thermal resistance (Kapitza resistance). The Kapitza resistance is a characteristic of the interface; in the heat transfer theory the reciprocal value of $1/r$ is called the heat transfer coefficient.

The process being considered is a special case of heat transfer through the metal – dielectric boundary. The Kapitza resistance at the metal-dielectric interface has been widely studied (see, e.g., [17]). It was found that the Kapitza resistance, as calculated considering the nonlinearity of the process, does not depend on the dielectric characteristics and is fully determined by the properties of the metal. This thesis was experimentally confirmed in [19].

In fact, each subsystem in gr is characterized by its set of values: electron T_e; q_e: χ_e, and phonon T_{ph}, q_{ph}, χ_{ph}. Each triplet of values is related according to the Fourier law.

The interaction coefficient θ (W/(m^3·K)) characterizes the efficiency of heat transfer between subsystems and relates the heat flux to the difference $T_e - T_{ph}$.

It should be noted that in experiments, the temperature is measured far away from the boundary. At this location, the temperature is $T_e = T_{ph} = T$, and the thermal conductivity $\chi = \chi_e + \chi_{ph}$ can be attributable to the general heat flow in gr: $q = q_e + q_{ph}$. In gr, it can be assumed that $\chi_e >> \chi_{ph}$ and heat transfer through the electronic subsystem dominates.

Only phonons can pass from gr to d, hence $q_{ph} = q$; $q_e = 0$ at the boundary.

According to [19], the problem is posed so that the properties of d do not affect the T_e and T_{ph} temperature in gr.

3. Temperature and thermal resistance alignment at the boundary between *gr* and *d*

The solution of the problem is completely similar to that provided in [17]. The result is that the characteristic distance λ, at which the temperatures of the electron and phonon subsystems in gr are actually aligned, is related to the system characteristics as:

$$\lambda = \sqrt{\frac{\chi_e \chi_{ph}}{\theta \chi}} \simeq \left(\chi_{ph}/\theta\right)^{1/2}. \tag{1}$$

The components of the thermal resistance are determined by the jumps of the subsystems temperatures, $T_e(0)$ and $T_{ph}(0)$, relative to the temperature T_d in d, which is equal to $T_d(0)$ at the boundary (Fig. 1). In the course of the experiment, the temperature gradient from a region far from the boundary is usually extrapolated linearly to the boundary. This temperature T_{gr} is considered to be the gr temperature; accordingly, it is $T_{gr}(0)$ at the border, and the temperature jump is considered equal to $\Delta T = T_{gr}(0) - T_d(0)$. However, almost always $T_{gr}(0) \approx T_e(0)$.

The Kapitza thermal resistance caused by the measured jump ΔT can be divided into r_{ph}, arising due to the temperature jump ΔT$_{ph}$ of phonons in gr and d areas, and r_r, arising because the electronic and phonon subsystems in gr are heated unequally near the border. Therefore, $r = r_{ph} + r_r$.

The thermal resistance (relative!) r_r arises due to the difference in temperature jumps of the electron ΔT_e and phonon ΔT_{ph} subsystems: $\Delta T_r = T_e - T_{ph} = \Delta T_e - \Delta T_{ph}$. In practice, the temperature in gr is determined by the electronic subsystem temperature. So, the measured jump $\Delta T \approx \Delta T_e$ and ΔT_r can be calculated as $\Delta T_r = \Delta T - \Delta T_{ph}$.

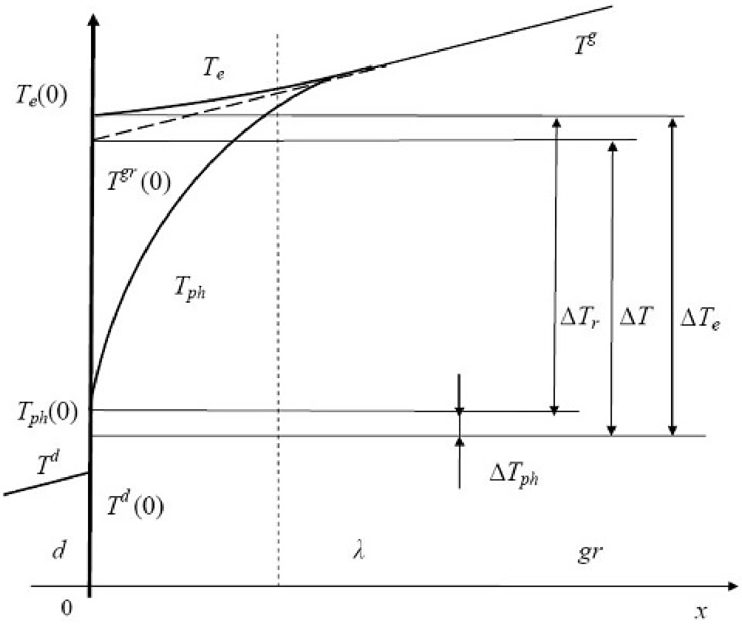

FIG. 1. This figure presents the temperatures in the graphite-like (gr) area T_{gr} (on the right) and the diamond-like (d) area T_d (on the left), near the boundary located at $x = 0$. At the boundary, the temperatures are, respectively, $T_{gr}(0)$, $T_d(0)$, $T_e(0)$ and $T_{ph}(0)$. Also shown are values of the corresponding temperature jumps ΔT_{ph} and ΔT_e at the border to the temperature $T^d(0)$. The jump $\Delta T = Tgr(0) - T^d(0)$ is measured experimentally. Finally, the temperature differences in gr subsystems were shown to be caused by the Kapitza resistance due to the presence of the boundary ΔT_r

The value of the jump ΔT_{ph} determines the proportion of phonons reflected from the boundary back into gr. This proportion was determined in [13] for a system very similar to the carbon nanocomposites under study. There, it was found to be usually small. Therefore, $\Delta T_{ph} << \Delta T_r$ and accordingly $r_{ph} << r_r$. This inequality is the major, roughest approximation that is used for the solution of the problem. The values in Fig. 1 are provided using this approximation.

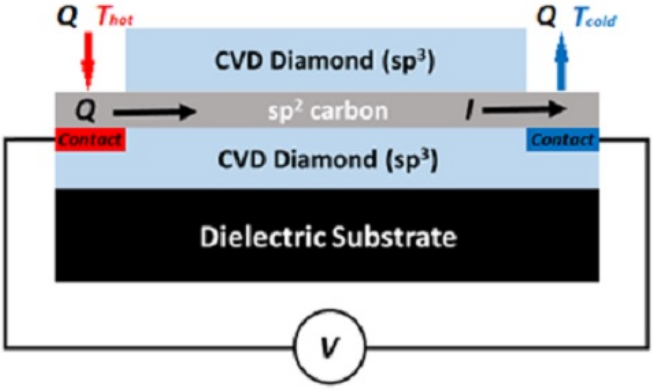

FIG. 2. A possible thermoelement design, where the heat Q and the temperature difference $T_{hot} - T_{cold}$ provide the conditions (see [13]) under which the quasi-ballistic drag of electrons by phonons prevails in the carbon nanostructure

Next, it will be assumed that the Kapitza resistance in carbon nanostructures and, in particular, carbon nanocomposites produced by HPHT, is determined by the relative temperature jump, which is approximately equal to the measured temperature jump $\Delta T_r \approx \Delta T$, and therefore, the thermal resistance is determined approximately by the relative thermal resistance $r \approx r_r$.

Then the solution obtained in [17] can be written for the simplest one-dimensional heat propagation as:

$$
\begin{aligned}
T^{gr} - T_e &= \frac{1}{\chi} qx + \frac{\lambda q}{\chi} e^{-x/\lambda};\\
T^{gr} - T_{ph} &= \frac{1}{\chi} qx - \frac{\lambda q}{\chi}\frac{\chi_e}{\chi_{ph}} e^{-x/\lambda}.
\end{aligned}
\tag{2}
$$

Then the thermal resistance:

$$
r \simeq= r_r = \frac{\lambda\chi_e}{\chi\chi_{ph}} \approx \frac{1}{\sqrt{\theta\chi_{ph}}}
\tag{3}
$$

is expressed in terms of the thermal conductivity of the phonon subsystem in gr and heat transfer efficiency between the electron and phonon subsystems in the same area.

4. Thermoelectric efficiency

The thermoelectric efficiency Z_b of the system at the boundary between gr and d can be represented now as:

$$
Z_b = \frac{S^2\sigma}{\chi_{ef}} \approx S^2\sigma\left(\frac{1}{\chi} + \frac{r}{l}\right).
\tag{4}
$$

This formula is stated using the electrothermal analogy. The magnitude of the thermoelectric efficiency is expressed through the effective thermal conductivity χ_{ef} of the system that takes into account the thermal conductivity in the gr area with the overall size of l, and the thermal resistance of the boundary.

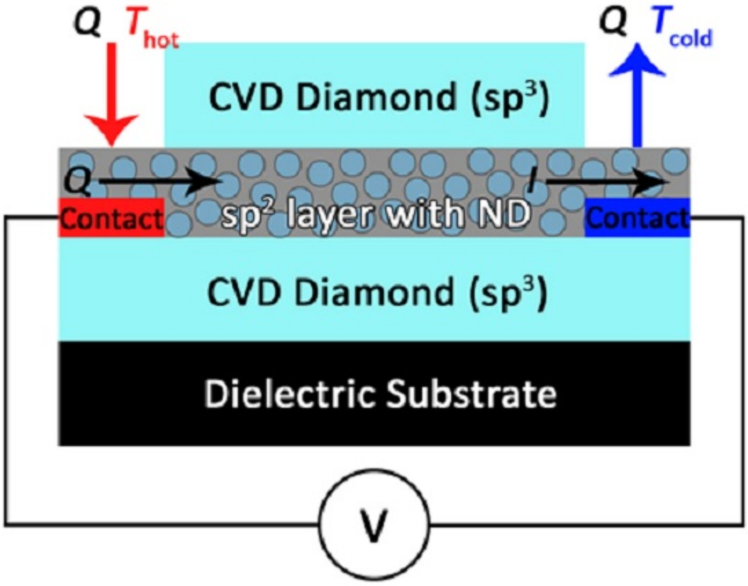

FIG. 3. A possible thermoelement design. In addition to the conditions corresponding to the structure shown in Fig. 2, the Wiedemann – Franz law is violated because of the introduction of diamond nanoparticles (ND). The thermal conductivity is determined by the Kapitza thermal resistance, i.e. by heat transfer at the interface of sp^2/sp^3 areas

Of course, even for macroscopic and microscopic samples, this formula provides the value Z mentioned in the Introduction. For small values of l << λ in nanosystems, the addition generated by a decrease in scattering due to heat transfer from the electron subsystem to the phonon subsystem, can significantly increase the thermoelectric efficiency.

Let us estimate, first of all, the value of θ, the efficiency coefficient of heat transfer between the subsystems. As the primary heat flux is carried by electrons, we can assume that energy is transmitted from them to the crystal lattice. It is clear that energy can be transmitted by quanta only and the characteristic energy of the quanta is determined by the temperature of phonons: T_{ph} when $T_{ph} < T_D$, or Debye temperature T_D in case $T_{ph} > T_D$. Of course, the temperature difference between the subsystems is small compared with each subsystem temperature, it may be a few tenths of a degree or a few degrees, but the heat transfer occurs with the phonon transition. The phonons have the specified temperature $T_{ph} \approx T_D$ in the sp^2 region. On the other hand, the gradient of the thermal flow of electrons is expressed in terms of the heat generated by the current, which would correspond to this heat flux. The result is:

$$\theta = a\frac{c^2e^2n_0^2}{\sigma T_D}. \tag{5}$$

Here, a is the order of unity factor, c $\approx 1.5 \cdot 10^3$ m/s is the speed at which the electrons move, because they captivate phonons, $n_0 \approx 10^{25}\text{m}^{-3}$ is the conduction electron density, $\sigma \approx 10^3$ (Om·m)$^{-1}$ is the conductivity coefficient, $T_D \approx 0.5 \cdot 10^3$ K, as already indicated, is the sp^2 region Debye temperature, and $e = 1.6 \cdot 10^{-19}$ Cl is the electron charge. The values of all variables, except, of course, the universal value of the electron charge, are given for graphite. All values are weakly dependent on the temperature and are borrowed from [20]. By substituting these values, we get $\theta \approx 10^{15}$ W/(m^3 K). Apparently, smaller values should be selected in reality. Of course, this assessment is by the order of magnitude.

In [21] and [22] the following values of graphite thermal conductivity versus temperature are given (see. Tab. 1).

TABLE 1. Graphite thermal conductivity versus temperature

χ_{gr}	Bt/(m·K)	114	86	61	47	40	34	25
T	K	293	473	873	1173	1473	1774	2073

Data for diamond $\chi_d = 1000$ W/(m·K) at T = 273 and 42 W/(m·K) at 4323 K are also provided. It is obvious that the thermal conductivity for gr must be somewhat intermediate. In [23,24] χ_{gr} values between 200 and 300 W/(m·K) are provided. On the other hand, the phonon part of thermal conductivity accounts for a small part of the total value. For further estimates, $\chi_{ph} \approx$5 - 10 W/(m·K) will be taken (see [25]).

According to the formula (1) it turns out that $\lambda \approx$100 nm, which confirms the above assumption on the size ratio of gr and the characteristic distance at which the temperatures of the electron and phonon subsystems can be regarded as being equal. Thus, the thermal conductivity in the carbon nanocomposites is no longer dependent on the size of the gr area, just like in the case where the interface is less than 4 nm thick (for oxides) the thermal conductivity is no longer dependent on the layer thickness [26–28].

Now, using the formulas (5) and (3) it is easy to estimate the thermal resistance. We obtain $r \approx 10^{-9}$ m^{2}K/W. The same value of the thermal resistance is derived with an entirely different reasoning in [24]. Finally, let us find the relative thermoelectric efficiency:

$$\frac{Z_{ef}}{Z} - 1 = \frac{r\chi^{gr}}{l}. \tag{6}$$

As stated above (see Introduction), we can assume that if the size of the graphite-like area is on the order of l $\approx 10 - 30$ nm, it turns out that the thermoelectric efficiency of carbon nanocomposites is ten times higher than that of graphite. At room temperature, the thermoelectric parameter is 5-20 times higher than that of graphite.

5. Conclusion

As is known (see, for example, [20]), the Seebeck coefficient of graphite depends on its purity, but it is of the order of $S = 2 - 3\mu$V/K. Thus, the graphite-like layer, whose surfaces have the temperature difference 100 K, produces the voltage of 0.3 mV. This value does not depend on the layer thickness, but the layer geometry affects the conditions of heating and heat dissipation and, consequently, the thermoelectric efficiency. At the surface with the lower temperature of 300 K, subject to the Wiedemann – Franz law, such a thermoelement would have the thermoelectric parameter $ZT = 3{\cdot}10^{-4}$. Materials from carbon nanostructures have $S = 10 - 20\mu$V/K [28] and they could produce the voltage of 1-2 mV with $ZT = 3 \cdot 10^{-2}$ with the same temperature differences. However, if such conditions are provided under which the quasi-ballistic drag of electrons by phonons prevails in the carbon nanostructure [13], it would be possible to obtain 5-10 mV and $ZT = 0.75$ (Fig. 2). In nanocomposites with the quasi-ballistic drag, in which the Wiedemann – Franz law is not fulfilled, namely, the thermal conductivity is determined by the Kapitza thermal resistance, it is possible to achieve the thermoelectric parameter 3.5 (Fig. 3).

Acknowledgement

The authors are grateful to Professor Dieter Gruen who pointed to the existence of the efficiency problem for the engineering of generators and refrigerators operating on the thermoelectric effect. We would like to acknowledge A.Ya. Vul' for his attention, which enabled us to complete this work. We are also thankful to F.M. Shakhov for fruitful discussions and the design of the figures. This work was supported by RSF grant No. 16-19-00075.

References

[1] Heremans J.P. Thermoelectricity: The ugly duckling. *Nature*, 2014, **508**, P. 327–328.

[2] Enhanced thermoelectric power in bismuth nanocomposites. Patent 6670.539 United States. Joseph Pierre Heremans, Cristofer Mark Thrush, Donald T. Morecli, 2003.

[3] Wang Y., Jaiswal M., Lin M., Saha S., Ozyilmaz B., Loh K.P. Electronic properties of nanodiamond decorated graphene. *ACS Nana*, 2012, **6**(2), P. 1018–1025.

[4] Vul' A., Reich K., Eidelman E., Terranova M.L., Ciorba A., Orlanducci S., Sessa V., Rossi M. A Model of Field Emission from Carbon Nanotubes Decorated by Nanodiamons. *Advanced Science Letters*, 2010, **3**, P. 1–8.

[5] The thermoelectric element. Invention. Patent 2,376,681 Russia. Vul A.Ya., Eidelman E.D. The legal owner of Physics – Technical Institute. AF Ioffe RAS, 2008.

[6] Zhao L.-D., Lo S-H., Zhang Y., Sun H., Tan G., Uher C., Wolverton C., Dravid V.P., Kanatzidis M.G. Ultralow thermal conductivity and high thermoelectric figure of merit in SnSe crystals. *Nature*, 2013, **508**, P. 373–377.

[7] Krueger A., Kataoka F., Ozawa M., Fujino T., Suzuki Y., Aleksenskii A.E., Vul'A.Ya., Osawa E. Unusually tight aggregation in detonation nanodiamond: identification and disintegration. *Carbon*, 2005, **43**, P. 1722–1726.

[8] Eydelman E.D., Siklitsky V.I., Sharonova L.V., Yagovkina M.A., Vul' A.Ya., Takahashi M., Inakuma M., Ozawa M., Osawa E. A stable suspension of single ultrananocrystalline diamond particles. *Diamond and Related Materials*, 2005, **14**, P. 1765–1769.

[9] Vul' A.Ya., Eidelman E.D., Inakuma M., Osawa E. Correlation between viscosity and absoption of electromagnetic waves in an aqueous UNCD suspension. *Diamond and Related Materials*, 2007, **16**, P. 2023–2028.

[10] Williams O., Hees A., Dieker C., Jager W., Kirste L, Nebel C. Size-dependent reactivity of diamond nanoparticles. *ACS Nano*, 2010, **4**, P. 4824–4830.

[11] Aleksenskii A., Eydelman E., Vul' A.Ya. Deaglomeration of detonation nanodiamonds. *Nanosci. Nanotechnol. Lett.*, 2011, **3**, P. 68–74.

[12] Kidalov S.V., Shakhov F.M., Lebedev V.T., Orlova D.N., Grushko Y.S. Small-angle neutron scattering study of high-pressure sintered detonation nanodiamonds. *Crystallogr. Rep.*, 2011, **56**(7), P. 1181–1185.

[13] Eidelman E., Vul' A.Ya. The strong thermoelectric effect in nanocarbon generated by the ballistic phonon drag of electrons. *Journal of Physics: Condensed Matter*, 2007, **19**, P. 1–8.

[14] Koniakhin S.V., Eidelman E.D. Phonon drag thermopower in graphene in equipartition regime. *EuroPhysLett.*, 2013, **103**(8), P. 1–6.

[15] Lifshitz E.M., Pitaevskii L.P. *Physical kinetics*. Pergamon International Library of Science, Technology, Engineering and Social Studies. 2008, 482 p.

[16] Efros A.L. *Physics and Geometry of Disorder*. Percolation Theory. Imported Pubn, 2004, 256 p.

[17] Meilakhs A.P., Eidelman E.D. Overheating or overcooling of electrons in a metal because of the effect of an interface with an insulator. *JETP. Lett.*, 2014, **100**(2), P. 81–85.

[18] Eidelman E.D. Estimation of the contact area of solids by electrothermal analogy. *Nanosystems: Physics, Chemistry, Mathematics*, 2015, **6**(4), P. 547–550.

[19] Costescu R.M., Wall M.A., Cahill D.G. Thermal conductivity of thin films. Measurements and understanding. *Phys. Rev B.*, 2003, **67**, P. 054302-1-8.

[20] Prut V.V., *IFE Working Paper*, 2007, **30**, P. 6462.

[21] *Properties and Characteristics of Graphite*. Entegris, Inc., 2013, 38 p.

[22] Levinshtein M., Rumyantsev S., Shur M. *Handbook series on Semiconductor Parameters*. World Scientific, Singapore, 2007, 219 p.

[23] Kidalov S.V., Shakhov F.M., Vul' A.Ya. Thermal conductivity of nanocomposites based on diamonds nanodiamonds. *Diamond and Related Materials*, 2007, **17**, P. 844–847.

[24] Kidalov S.V., Shakhov F.M., Vul' A.Ya. Thermal conductivity of sintered nanodiamonds and microdiamonds. *Diamond and Related Materials*, 2008, **17**, P. 844–847.

[25] Kidalov S.V., Shakhov F.M., Vul' A.Ya., Ozerin A.N. Grain-boundary heat conductance in nanodiamond composites. *Diamond and Related Materials*, 2010, **19**, P. 976–980.

[26] Cahill D.G., Ford W.K., Goodson K.E., Mahan G.D., Majumdar A., Maris H.J., Merlin R., Phillpot S. R. Nanoscale thermal transport. *Journal of Applied Physics*, 2003, **93**, P. 793–798.

[27] Losego M.D., Grady M.E., Sottos N.R., Cahill D.G., Braun P.V. Effects of chemical bonding on heat transport across interfaces. *Nature materials*, 2012, **11**, P. 502–506.

[28] Cahill D.G., Braun P.V., Chen G., Clarke D.R., Fan S., Goodson K.E., Keblinski P., King W.P., Mahan G.D., Majumdar A., Maris H.J., Phillpot S.R., Pop E., Shi L. Nanoscale thermal transport. II. 2003-2012. *Applied physics reviews*, 2014, **1**, P. 011305-1-45.

[29] Zolotukhin I.V., Golev I.M., Markova A.E., Panin Yu.V., Sokolov Yu.V., Tkachev A.G., Negrov V.L. Some properties of solid fractal structures in carbon nanofibers. *Technical Physics Letters*, 2006, **32**(3), P. 199–200.

NANOSYSTEMS: PHYSICS, CHEMISTRY, MATHEMATICS, 2016, 7 (6), P. 925–935

Minimum energy path calculations with Gaussian process regression

O-P. Koistinen[1], E. Maras[2], A. Vehtari[1], H. Jónsson[2,3]

[1]Helsinki Institute for Information Technology HIIT,
Department of Computer Science, Aalto University, Finland

[2]Department of Applied Physics, Aalto University, Finland

[3]Faculty of Physical Sciences, University of Iceland, 107 Reykjavík, Iceland

hj@hi.is

DOI 10.17586/2220-8054-2016-7-6-925-935

The calculation of minimum energy paths for transitions such as atomic and/or spin rearrangements is an important task in many contexts and can often be used to determine the mechanism and rate of transitions. An important challenge is to reduce the computational effort in such calculations, especially when *ab initio* or electron density functional calculations are used to evaluate the energy since they can require large computational effort. Gaussian process regression is used here to reduce significantly the number of energy evaluations needed to find minimum energy paths of atomic rearrangements. By using results of previous calculations to construct an approximate energy surface and then converge to the minimum energy path on that surface in each Gaussian process iteration, the number of energy evaluations is reduced significantly as compared with regular nudged elastic band calculations. For a test problem involving rearrangements of a heptamer island on a crystal surface, the number of energy evaluations is reduced to less than a fifth. The scaling of the computational effort with the number of degrees of freedom as well as various possible further improvements to this approach are discussed.

Keywords: minimum energy path, machine learning, Gaussian process, transition mechanism, saddle point.

Received: 2 December 2016

1. Introduction

The task of predicting the rate and identifying the mechanism of transitions involving some rearrangements of atoms in or on the surface of solids shows up in many different applications, for example diffusion, crystal growth, chemical catalysis, nanotechnology, etc. At a finite temperature, the thermal fluctuations in the dynamics of atoms can lead to rearrangements from one stable configuration to another, but these are rare events on the time scale of atomic vibrations, so direct dynamics simulations cannot in most cases be used for these types of studies. The separation of time scales typically amounts to several orders of magnitude and a direct simulation would take impossibly long time. Instead, algorithms based on statistical mechanics as well as classical dynamics and focusing on the relevant rare events need to be applied [1–3]. Typical transitions involve not just one or a few atoms but rather a large number of atoms so the challenge is also to deal with multiple degrees of freedom. One way of looking at the problem is to characterise the motion of the system on a high dimensional energy surface where the number of degrees of freedom is easily more than a hundred. A key concept is the reaction coordinate which usually is taken to be a minimum energy path (MEP) on the energy surface connecting one minimum to another. The rate of transitions in solids is usually evaluated within harmonic transition state theory which is based on a quadratic expansion of the energy surface at the initial state minimum and at the highest maximum along the MEP, which is a first order saddle point on the energy surface [4]. For given initial and final states, the task is to determine the MEP and identify the saddle point(s) as well as possible unknown, intermediate minima [5]. The discussion here has been in terms of rearrangements of atoms, but similar considerations apply to reorientations of magnetic moments [6–9].

The nudged elastic band (NEB) method is commonly used to find MEPs for atomic rearrangements [5,10,11]. An analogous method, referred to as the geodesic NEB, has been developed for magnetic transitions [12]. In NEB calculations, some initial path is constructed between two local minima on the energy surface and the path is represented by a discrete set of replicas of the system. The replicas are referred to as images of the system. They consist of some set of values for all degrees of freedom in the system. The NEB algorithm then optimises iteratively the location of the images that are between the endpoint minima so as to obtain a discrete representation of the MEP. Initially, the method was mainly used in combination with analytical potential energy functions, but today the method is used extensively in combination with electronic structure calculations. A large amount of computer time is used in these calculations. Each calculation typically involves 100 evaluations of the energy and force (the negative gradient of the energy) for each one of the images and the path is typically represented by 5 to 10 images. Since a typical electronic structure calculation takes on the order of tens of CPU minutes or more, these calculations can be heavy. Also, several different possible final states usually need to be tested and the NEB calculation therefore repeated. In light of the widespread use and large amount of CPU time used in NEB calculations, it is of great practical importance to find ways to accelerate the calculations. The goal should be to use the information coming from all the computationally intensive electronic structure calculations in an optimal way so as to reduce as much as possible the number of iterations needed to reach the MEP.

It has recently been shown that a machine learning algorithm based on neural networks can be used to significantly reduce the computational effort in NEB calculations [13]. An approximate representation of the energy surface is constructed from the calculations using a machine learning approach and the MEP calculated using the NEB method on this approximate surface. Then, additional evaluations are made of the true energy surface, the approximate model surface refined, etc., until convergence on the MEP of the true energy surface has been reached. The number of function evaluations was shown to drop dramatically by applying such an approach [13].

We present here an initial step in the development of a similar approach to accelerated MEP calculations based on Gaussian process regresssion [14–17]. This approach could have some advantages over neural networks for such applications. Neural networks have a large number of weights which can have multimodal distributions making the search for global optimum difficult and leading to possible dependence on the initial values of the parameters [13]. Also, the handling of uncertainties in GP theory is easier than in neural networks since the prediction equations are analytical and integration over the parameter space can be carried out more easily. It is, therefore, of interest to test the efficiency of the GP approach in MEP calculations. We report in this article initial feasability studies. More extensive testing and comparison with other approaches such as neural networks is left for future work.

The article is organized in the following way: The methodology is presented in the next section, followed by a section on applications, both a simple two-dimensional system and a larger test problem involving rearrangements of a heptamer island on a crystal surface. The article concludes with a discussion section.

2. Methods

The method presented here for finding the minimum energy paths can be viewed as an acceleration of a NEB calculation by making use of Gaussian process theory. Previously calculated data points are used to construct an approximate model of the energy surface and the MEP is found for this approximate surface before additional calculations of the true energy are carried out. This gives an interpolation between the calculated points and also provides an extrapolation that can be used to explore the energy surface with larger moves. The savings in computational effort are based on the fact that several computationally light iterations can be made for the approximate surface in between the computationally demanding evaluations of the true energy function. A brief review of the NEB method is first given, then a description of the Gaussian process regression, and finally a detailed algorithm describing how the calculations were carried out in the present case.

2.1. Nudged elastic band method

Given two local minima on the energy surface, the task is to find an MEP connecting the two. The definition of an MEP is that the gradient has zero component perpendicular to the path tangent at each point along the path. The NEB method needs to be started with some initial path between the two minima that is represented by a set of images. Most often, a straight line interpolation between the minima is used to generate the initial path [11], but a better approach is to start with a path that interpolates as closely as possible the changes distances between atoms [18].

The key aspect of the NEB algorithm is the nudging, a force projection which is used to decouple the displacements of the images perpendicular to the path towards the MEP from the displacements that affect their distribution along the path. In order to make this projection, an estimate of the local tangent to the path at each of the images is needed. A numerically stable choice involves finding the line segment from the current image to the adjacent image of higher energy [19].

Given this decoupling, there are several different options for distributing the images along the path. Some constraint is needed to prevent the images from sliding down to the minima at the two ends. In most cases an even distribution is chosen, but one can also choose to have, for example, higher density of images where the energy is larger [20]. An attractive spring force is typically introduced between adjacent images to control the spacing between images and this also prevents the path from becoming arbitrarily long in regions of little or no force. The latter is important, for example, in calculations of adsorption and desorption of molecules at surfaces. For systems that can freely translate and rotate, such as nano-clusters in free space, it is important to remove the translational and rotational degrees of freedom. This is non-trivial because the system cannot be treated as a rigid body. A method for doing this efficiently based on quaternions has recently been presented [21].

The component of the force acting on each image perpendicular to the path is used to iteratively move the images from the initial path to the MEP. The force is the negative of the gradient and in most cases an evaluation of the energy delivers also the gradient vector at little or no extra expense. The largest amount of information from an evaluation of a point on the energy surface is, therefore, represented by the gradient. It is hower typically too expensive to evaluate second derivatives of the energy and iterative algorithms for moving the images towards the MEP are therefore based solely on the gradient and the energy at each point. A simple and numerically stable method that has been used extensively in NEB calculations will be used here. It is based on the velocity Verlet method where only the component of the velocity in the direction of the force is included and the velocity is zered of the its dot product with the force becomes negative [11]. A somewhat higher efficiency can be obtained by using a quadratically convergent algorithm such as conjugate gradients or quasi-Newton [22] but those can be less stable especially in the beginning of an NEB calculation. A linear interpolation between the initial state minima was used in all the calculations presented here and the number of images, N_p, chosen to be either 5 or 8. An equal distribution of the images along the path was chosen.

The focus here is on calculations where the energy and the gradient are obtained using some ab initio or density functional theory calculation. The computational effort in all other parts of the calculation is then insignificant in comparison and the computational effort is well characterised by simply the number of times the energy and force need to be evaluated in order to converge on the MEP. Below, we introduce a strategy to accelerate the MEP search with Gaussian process regression.

2.2. Gaussian processes regression

The general idea behind the strategy is similar to the one introduced by Peterson [13]. The idea is to use the calculations carried out so far to train an approximate model of the energy surface, and find the MEP with the conventional methods using the approximations of the energy and gradient based on this model. After converging to the MEP on the approximate energy surface, the true energy and force are evaluated again, showing whether or not the path has converged to the true MEP. If not, the model is updated with the new values of the true energy and force to get a more accurate approximation, and this is continued iteratively, until the true MEP has been found. Since the number of true energy and force evaluations is the measure of computational effort, basically any method can be used to optimise the path on the approximate energy surface, as long as it converges to an MEP.

Here, a Gaussian process (GP) is used as a probabilistic model for the energy surface. GPs provide a flexible framework for modelling multidimensional functions. Through the selection of the covariance function and its hyperparameters, smoothness properties of the function can easily be defined and those properties can also be learned from the data. It is also straightforward to both include derivative observations into the model and to predict the derivative of the modelled function. Analytical expressions for the posterior predictions conditional on the hyperparameters allow both fast predictions and reliable estimation of uncertainties. In cases where only a small number of observations are available, Gaussian processes have been shown to have good predictive performance compared to other machine learning methods [23].

A GP can be seen as a probability distribution over functions in a continuous domain, see, e.g., [14–17]. In a GP, the joint probability distribution of the function values $f(\mathbf{x}^{(1)}), f(\mathbf{x}^{(2)}), \ldots, f(\mathbf{x}^{(N)})$ at any finite set of input points $\mathbf{x}^{(1)}, \mathbf{x}^{(2)}, \ldots, \mathbf{x}^{(N)} \in \mathbb{R}^D$ is a multivariate Gaussian distribution. A GP is defined by a mean function $m(\mathbf{x})$ and a covariance function $k(\mathbf{x}^{(i)}, \mathbf{x}^{(j)})$, which determines the covariance between $f(\mathbf{x}^{(i)})$ and $f(\mathbf{x}^{(j)})$, e.g., based on the distance between $\mathbf{x}^{(i)}$ and $\mathbf{x}^{(j)}$.

Consider a regression problem $y = f(\mathbf{x}) + \epsilon$, where ϵ is Gaussian noise with variance σ^2, and a training data set $\{\mathbf{X}, \mathbf{y}\}$, where $\mathbf{X} \in \mathbb{R}^{N \times D}$ denotes a matrix of N input vectors $\mathbf{x}^{(1)}, \mathbf{x}^{(2)}, \ldots, \mathbf{x}^{(N)} \in \mathbb{R}^D$ and $\mathbf{y}$ is a vector of the corresponding N noisy observations. By choosing a Gaussian process to model function f, different prior assumptions can be made about the properties of the function, and after observing $\{\mathbf{X}, \mathbf{y}\}$, the posterior predictive probabilities for the function values at a set of new points can be calculated analytically as a multivariate Gaussian distribution. Here, the mean function is taken to be $m(\mathbf{x}) = 0$ and the covariance function is assumed to have the form

$$k(\mathbf{x}^{(i)}, \mathbf{x}^{(j)}) = c^2 + \eta^2 \exp\left(-\frac{1}{2}\sum_{d=1}^{D} \rho_d^{-2}(x_d^{(i)} - x_d^{(j)})^2\right),$$

where η^2 and $\boldsymbol{\rho} = \{\rho_1, \ldots, \rho_D\}$ are the hyperparameters of the GP model. The squared exponential covariance function is infinitely differentiable and thus favours smooth functions. The length scales $\boldsymbol{\rho}$ define how fast the function f can change, and η^2 controls the magnitude of the overall variation. The additional constant term c^2 has a similar effect as integration over an unknown constant mean function with a Gaussian prior distribution of variance of c^2. The posterior predictive distribution for a function value of the function at a new point $\mathbf{x}^*$, denoted as f^*, is described by a Gaussian distribution with mean

$$E[f^*|\mathbf{x}^*, \mathbf{y}, \mathbf{X}, \boldsymbol{\theta}] = K(\mathbf{x}^*, \mathbf{X})(K(\mathbf{X}, \mathbf{X}) + \sigma^2\mathbf{I})^{-1}\mathbf{y}$$

and variance

$$\mathrm{Var}[f^*|\mathbf{x}^*, \mathbf{y}, \mathbf{X}, \boldsymbol{\theta}] = k(\mathbf{x}^*, \mathbf{x}^*) - K(\mathbf{x}^*, \mathbf{X})(K(\mathbf{X}, \mathbf{X}) + \sigma^2\mathbf{I})^{-1}K(\mathbf{X}, \mathbf{x}^*),$$

where $\mathbf{I}$ is the identity matrix and the notation $K(\mathbf{X}, \mathbf{X}')$ represents a covariance matrix with entries $K_{ij} = k(\mathbf{x}^{(i)}, \mathbf{x}'^{(j)})$. The hyperparameter values $\boldsymbol{\theta} = \{\eta^2, \boldsymbol{\rho}\}$ are optimised by defining a prior probability distribution $p(\boldsymbol{\theta})$ and maximising the marginal posterior probability $p(\boldsymbol{\theta}|\mathbf{y}, \mathbf{X}) = p(\boldsymbol{\theta})p(\mathbf{y}|\mathbf{X}, \boldsymbol{\theta})$ after observing $\mathbf{y}$.

Since differentiation is a linear operation, the derivative of a Gaussian process is also a Gaussian process (see, e.g., [24, 25]), and this makes it possible to use observations of the derivative of the function and also to predict derivatives of the function f. The partial derivative observations can simply be included in the observation vector $\mathbf{y}$ and the covariance matrix correspondingly extended with the covariances between the observations and the partial derivatives and the covariances between the partial derivatives themselves. In the case of the squared exponential covariance function, these entries are obtained by

$$\begin{aligned}\mathrm{Cov}\left[\frac{\partial f^{(i)}}{\partial x_d^{(i)}}, f^{(j)}\right] =& \frac{\partial}{\partial x_d^{(i)}}\mathrm{Cov}\left[f^{(i)}, f^{(j)}\right] = \frac{\partial}{\partial x_d^{(i)}} k\left(\mathbf{x}^{(i)}, \mathbf{x}^{(j)}\right) \\ =& \eta^2 \exp\left(-\frac{1}{2}\sum_{g=1}^{D} \rho_g^{-2}(x_g^{(i)} - x_g^{(j)})^2\right)\left(-\rho_d^{-2}(x_d^{(i)} - x_d^{(j)})\right),\end{aligned}$$

and

$$\begin{aligned}\mathrm{Cov}\left[\frac{\partial f^{(i)}}{\partial x_{d_1}^{(i)}}, \frac{\partial f^{(j)}}{\partial x_{d_2}^{(j)}}\right] =& \frac{\partial^2}{\partial x_{d_1}^{(i)}\partial x_{d_2}^{(j)}}\mathrm{Cov}\left[f^{(i)}, f^{(j)}\right] = \frac{\partial^2}{\partial x_{d_1}^{(i)}\partial x_{d_2}^{(j)}} k\left(\mathbf{x}^{(i)}, \mathbf{x}^{(j)}\right) \\ =& \eta^2 \exp\left(-\frac{1}{2}\sum_{g=1}^{D} \rho_g^{-2}(x_g^{(i)} - x_g^{(j)})^2\right) \times \\ & \rho_{d_1}^{-2}\left(\delta_{d_1 d_2} - \rho_{d_2}^{-2}(x_{d_1}^{(i)} - x_{d_1}^{(j)})(x_{d_2}^{(i)} - x_{d_2}^{(j)})\right),\end{aligned}$$

where $\delta_{d_1 d_2} = 1$ if $d_1 = d_2$, and $\delta_{d_1 d_2} = 0$ if $d_1 \neq d_2$.

These same expressions are useful also when predicting values of the derivatives. The posterior predictive distribution of the partial derivative of function f with respect to dimension d at a new point $\mathbf{x}^*$ is a Gaussian distribution with mean

$$E\left[\frac{\partial f^*}{\partial x_d^*}\middle|\mathbf{x}^*, \mathbf{y}, \mathbf{X}, \boldsymbol{\theta}\right] = \frac{\partial K(\mathbf{x}^*, \mathbf{X})}{\partial x_d^*}(K(\mathbf{X}, \mathbf{X}) + \sigma^2\mathbf{I})^{-1}\mathbf{y}$$

and variance

$$\mathrm{Var}\left[\frac{\partial f^*}{\partial x_d^*}\middle|\mathbf{x}^*, \mathbf{y}, \mathbf{X}, \boldsymbol{\theta}\right] = \frac{\partial^2 k(\mathbf{x}^*, \mathbf{x}^*)}{\partial x_d^* \partial x_d^*} - \frac{\partial K(\mathbf{x}^*, \mathbf{X})}{\partial x_d^*}(K(\mathbf{X}, \mathbf{X}) + \sigma^2\mathbf{I})^{-1}\frac{\partial K(\mathbf{X}, \mathbf{x}^*)}{\partial x_d^*}.$$

In the present application, the vector $\mathbf{x}$ represents coordinates of the atoms and the function f the energy of the system. The observations $\mathbf{y}$ are the true values of the energy as well as the partial derivatives of the energy with respect to the coordinates of the atoms at the various sets of coordinates $\mathbf{x}^{(1)}, \mathbf{x}^{(2)}, \ldots, \mathbf{x}^{(N)}$. With this input, the Gaussian process model is used to predict the most likely value of energy f^* and its derivatives $\frac{\partial f^*}{\partial x_d^*}$ at a new set of atom coordinates $\mathbf{x}^*$ representing in this case an image in the discrete path representation between the initial and final state minima. Since the training data is assumed to be noiseless and include also derivative observations, the equations for the mean predictions can be presented as

$$E[f^*|\mathbf{x}^*, \mathbf{y}_{ext}, \mathbf{X}, \boldsymbol{\theta}] = K_{ext}^* K_{ext}^{-1}\mathbf{y}_{ext} \tag{1}$$

and

$$E\left[\frac{\partial f^*}{\partial x_d^*}\middle|\mathbf{x}^*, \mathbf{y}_{ext}, \mathbf{X}, \boldsymbol{\theta}\right] = \frac{\partial K_{ext}^*}{\partial x_d^*} K_{ext}^{-1}\mathbf{y}_{ext}, \tag{2}$$

where

$$\mathbf{y}_{ext}^* = \left[y^{(1)} \cdots y^{(N)}, \frac{\partial f^{(1)}}{\partial x_1^{(1)}} \cdots \frac{\partial f^{(N)}}{\partial x_1^{(N)}}, \frac{\partial f^{(1)}}{\partial x_2^{(1)}} \cdots \frac{\partial f^{(N)}}{\partial x_2^{(N)}}, \quad \cdots \quad, \frac{\partial f^{(1)}}{\partial x_D^{(1)}} \cdots \frac{\partial f^{(N)}}{\partial x_D^{(N)}}\right]^T,$$

$$K^*_{ext} = \begin{bmatrix} K(\mathbf{x}^*, \mathbf{X}) & \dfrac{\partial K(\mathbf{x}^*, \mathbf{X})}{\partial x_1} & \dfrac{\partial K(\mathbf{x}^*, \mathbf{X})}{\partial x_2} & \cdots & \dfrac{\partial K(\mathbf{x}^*, \mathbf{X})}{\partial x_D} \end{bmatrix},$$

and

$$K_{ext} = \begin{bmatrix} K(\mathbf{X}, \mathbf{X}) & \dfrac{\partial K(\mathbf{X}, \mathbf{X}')}{\partial x'_1} & \dfrac{\partial K(\mathbf{X}, \mathbf{X}')}{\partial x'_2} & \cdots & \dfrac{\partial K(\mathbf{X}, \mathbf{X}')}{\partial x'_D} \\ \dfrac{\partial K(\mathbf{X}, \mathbf{X}')}{\partial x_1} & \dfrac{\partial^2 K(\mathbf{X}, \mathbf{X}')}{\partial x_1 x'_1} & \dfrac{\partial^2 K(\mathbf{X}, \mathbf{X}')}{\partial x_1 x'_2} & \cdots & \dfrac{\partial^2 K(\mathbf{X}, \mathbf{X}')}{\partial x_1 x'_D} \\ \dfrac{\partial K(\mathbf{X}, \mathbf{X}')}{\partial x_2} & \dfrac{\partial^2 K(\mathbf{X}, \mathbf{X}')}{\partial x_2 x'_1} & \dfrac{\partial^2 K(\mathbf{X}, \mathbf{X}')}{\partial x_2 x'_2} & \cdots & \dfrac{\partial^2 K(\mathbf{X}, \mathbf{X}')}{\partial x_2 x'_D} \\ \vdots & \vdots & \vdots & \ddots & \vdots \\ \dfrac{\partial K(\mathbf{X}, \mathbf{X}')}{\partial x_D} & \dfrac{\partial^2 K(\mathbf{X}, \mathbf{X}')}{\partial x_D x'_1} & \dfrac{\partial^2 K(\mathbf{X}, \mathbf{X}')}{\partial x_D x'_2} & \cdots & \dfrac{\partial^2 K(\mathbf{X}, \mathbf{X}')}{\partial x_D x'_D} \end{bmatrix}.$$

2.3. Algorithm for GP-aided MEP search

Input: the coordinates, energy and its gradient at the two minima on the energy surface, the number of images representing the path (N_p), convergence limit (CL), step coefficient (k_{step}).

Output: minimum energy path represented by N_p images.

1. Place the initial N_p images equally spaced along a straight line between the two minima.
2. Repeat until convergence (outer iteration loop):
    - A. Evaluate the true energy and its gradient at the $N_p - 2$ intermediate images of the path, and add them to the training data.
    - B. Calculate the negative energy gradient (e.g., force) component perpendicular to the path (ngc) for each intermediate image, and denote the mean of their norms as M_{ngc}.
    - C. If $M_{ngc} < CL$, the path has converged to the true MEP.
    - D. Optimise the hyperparameters of the GP model based on the training data, and calculate the matrix inversion in equation 1.
    - E. Define CL_{relax} as $\frac{1}{10}$ of the smallest M_{ngc} so far, and repeat (relaxation phase):
        - I. Move the intermediate images according to any stable path optimisation algorithm.
        - II. Update the GP posterior mean energy and gradient at the new intermediate images using equations 1 and 2.
        - III. Calculate ngc for each image using the GP posterior mean gradient, and denote the mean of their norms as M^{GP}_{ngc}.
        - IV. If $M^{GP}_{ngc} < CL_{relax}$, or if M^{GP}_{ngc} is increasing, exit the relaxation phase (E).

The GP calculations make use of the GPStuff toolbox [26]. For the hyperparameter optimisation which is carried out after each evaluation of the true energy and force, the computational effort scales as $\mathcal{O}((N(D+1))^3)$, where N is the number of observations and D is the number of degrees of freedom (here coordinate of movable atoms). Since the hyperparameters and observations stay the same during a search for the MEP on the approximate energy surface, the matrix inversion in equation 1 needs to be computed only once for each such optimization of the path. Thus, the complexity of one inner iteration on the GP posterior energy surface is $\mathcal{O}(N(D+1))$.

The length of any one displacement of an image is restricted to be less than half of the initial interval between the images in order to prevent the path from forming loops. Convergence of the path to the MEP is determined from the norm of the force component perpendicular to the path at each of the intermediate images. The path is considered to be converged to the MEP, when the mean of the true values of these norms is less than 0.001 eV/Å. During the relaxations, norms based on the current GP model are monitored and the mean of these used as a convergence criterion. Since it is not necessary to find a path that is accurately converged on the MEP of the inaccurate, approximate energy surface, the convergence limit for each relaxation phase is defined as $\frac{1}{10}$ of the smallest true mean of norms evaluated so far. Higher convergence limits at early relaxation steps speed up the algorithm and they also make it more stable by preventing the path from escaping too far from the true observation points. For the same reason, the relaxation is stopped before convergence if the convergence criterion starts to increase.

3. Applications

The method described above has been applied to two test problems: A simple two-dimensional problem where the energy surface can be visualised, and a more realistic problem involving the rearrangements of atoms in a heptamer island on a crystal surface.

3.1. Two-dimensional test problem

The two-dimensional problem is formulated by coupling a degree of freedom representing the simultaneous formation and breaking of chemical bonds with a degree of freedom representing a harmonic oscillator solvent environment. The model along with the detailed equations is described in the appendix A.2 of reference [11]. Here, one additional repulsive Gaussian was added to shift the saddle point away from the straight line interpolation between the two minima. A contour graph of the energy surface is shown in Fig. 1.

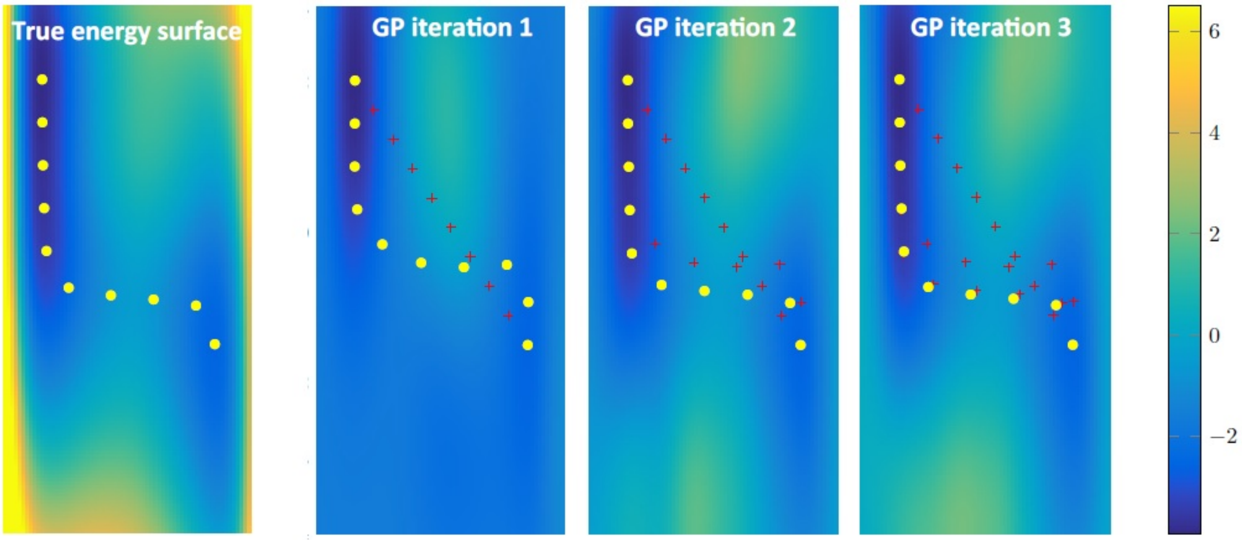

FIG. 1. The true and Gaussian process approximated energy surface and minimum energy path for a two-dimensional test problem. Far left: The true energy surface and points on the minimum energy path (yellow dots). Far right and intermediate figures: The approximate energy surface generated by the Gaussian process regression after one, two and three iterations, points ('images') on the estimated minimum energy path and points where the true energy and force have been calculated (red + signs) at each stage of the calculation the period is missing.

This example shows how the GP model of the energy surface is gradually built up and refined as more observations, i.e. calculations of the true energy and partial derivatives of the energy, are made. Here, $N_p = 10$ images are used to represent the path and the calculation is started by placing the images along a straight line between the two minima on the energy surface. The first observations are made at those points (see red + signs on the figure second from the left). Based on the energy and partial derivatives of the energy at those points, the GP model already shows some of the most important features of the energy surface close to the linear interpolation, but completely misses the increase in energy in the lower half of the figure. The relaxation of the images on this rough estimate of the energy surface does not, however, bring the images too far from the initial placement because of the condition that images cannot be moved in a single iteration by more than half the initial distance between the images. In the second GP iteration, observations are made at the position of the images at the end of the first GP iteration. When those data points are fed into the GP model, the energy surface is already showing the essential features around the MEP, but of course misses the steep increase in the energy far from the MEP. The relaxation of the images during the second GP iteration brings them quite close to the MEP. The addition of observations at those points at the beginning of the third GP iteration refines the model energy surface further. While a a total of six GP iteration are required to bring the images onto the MEP to within the tight tolerance of 0.001 eV/Å in the mean magnitude of the force component perpendicular to the path, no visible changes occur in the contour graph or the location of the images, so the results are not displayed in the figure.

3.2. Heptamer island on a crystal surface

A more realistic test problem which has been used in several studies of MEP and saddle point searches involves an island of 7 atoms on the (111) surface of a face centered cubic (FCC) crystal (see, for example, references [27, 28]). Roughly, this represents a metallic system, but the interaction between the atoms is described here with a simple Morse potential to make it easier to implement the benchmark calculation. The initial, saddle point and final configurations of the atoms for three possible rearrangements of the atoms is shown in Fig. 2. Several other transitions are possible (see reference [27]), but these three are chosen as examples.

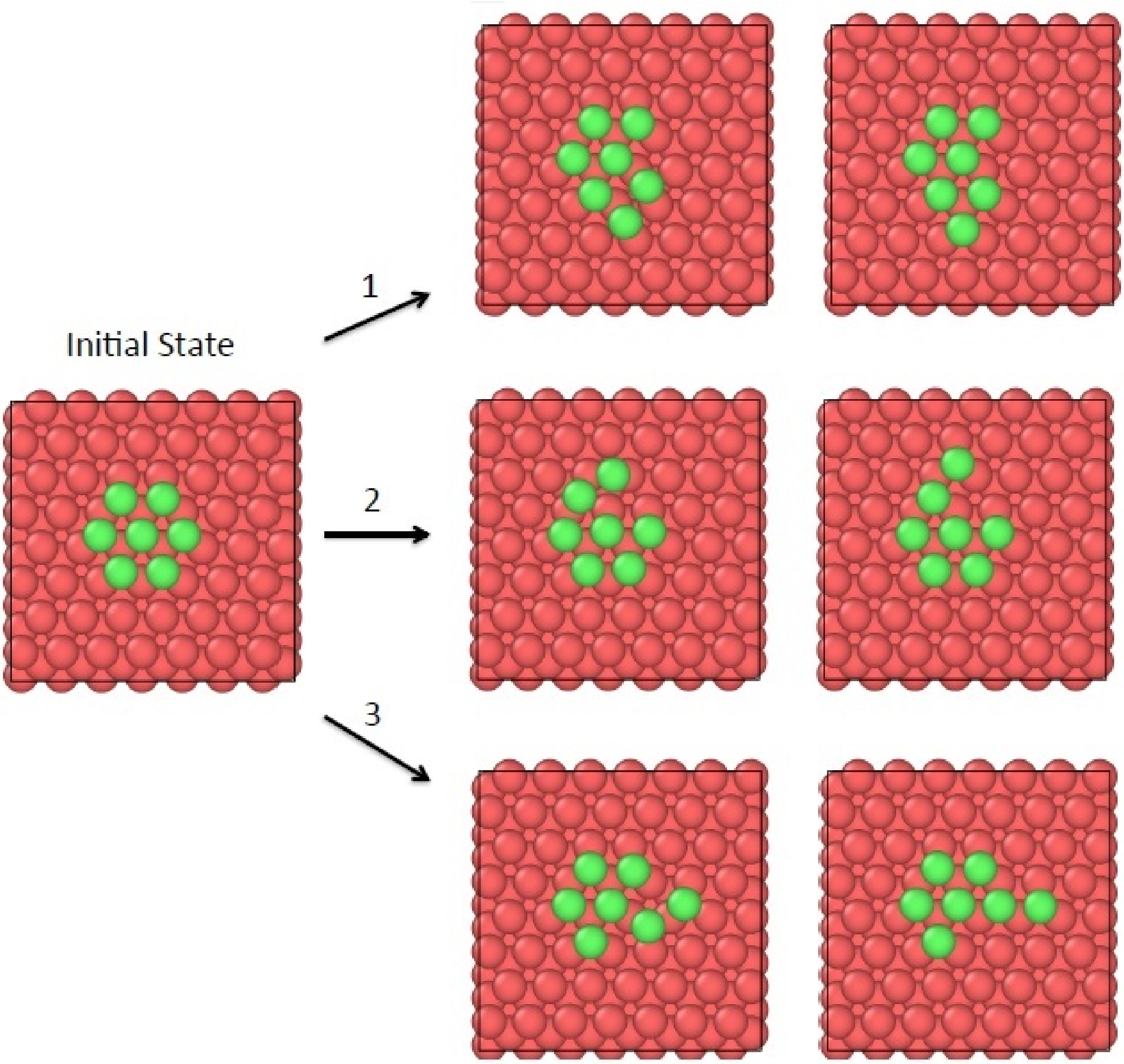

FIG. 2. On-top view of the surface and the seven atom island used to test the efficiency of the Gaussian process regression method. The initial state is shown to the left. The saddle point configurations and the final state configurations of three example transitions are also shown. Transition 1 corresponds to a pair of edge atoms sliding to adjacent FCC sites. In transition 2, an atom half way dissociates from the island. In transition 3, a pair of edge atoms moves in such a way that one of the atoms is displaced away from the island while the other atom takes its place. At the same time the other island atoms as well as some of the underlying atoms also move but in the end return to nearly the same position as they had initially.

The three examples chosen here represent three types of transitions that can occur in the shape of the island. In one case, a pair of edge atoms slides to adjacent FCC sites, in another an atom half way dissociates from the island, and in the third case pair of edge atoms moves in such a way that one of the atoms is displaced away from the island while the other atom takes its place.

The energy along the MEP for the transition 3 is shown in Fig. 3 as well as the energy of the $N_p = 7$ images at the end of GP iterations 1 to 7. After the first and second GP iteration, the estimates of the MEP is quite inaccurate and the energy rises along those paths by more than 3 eV, but already after the third GP iteration, the estimated energy barrier is not too far from the accurate value. After the fifth GP iteration, the shape of the energy curve is quite well reproduced, and after seven iterations the energy along the MEP of the approximate energy surface is nearly indistinguishable from the energy along the true MEP.

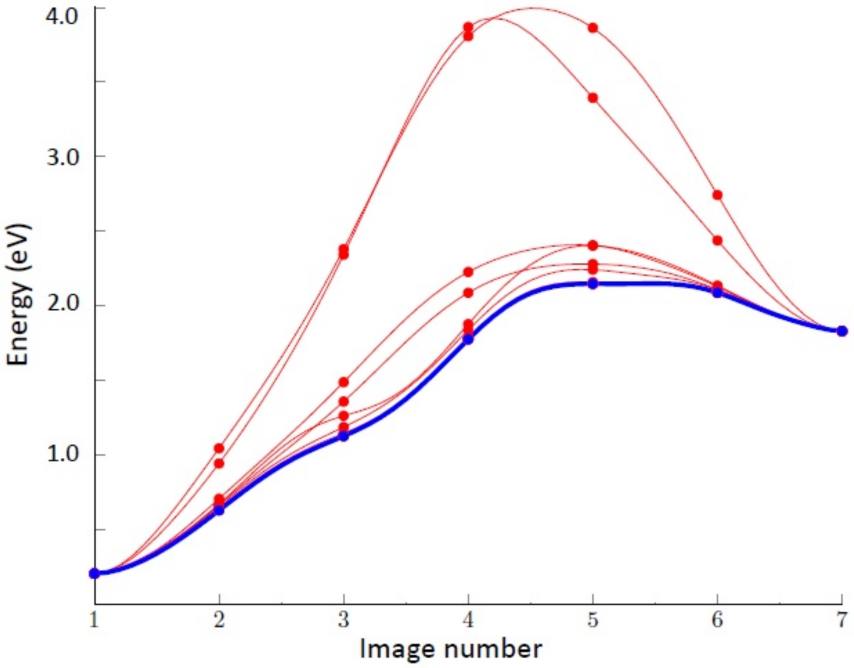

FIG. 3. Energy along paths for transition 3 shown in Fig. 2. The energy of images on the true MEP are shown in blue, but the energy of images on MEPs of approximate models of the energy surface obtained after 1 to 7 Gaussian process iterations are shown in red. After the first two Gaussian process iterations, the energy barrier for this transition is greatly overestimated, but already after three iterations the estimated energy barrier is quite close to the true value, and after 7 iterations an accurate estimate is obtained from the model energy surface.

The number of energy and force evaluations needed to converge the five intermediate images to the MEP in both a regular NEB calculation and in a GP aided calculation was found for varying number of degrees of freedom. The average for the three transitions depicted in Fig. 2 is shown in Fig. 4. The number of degrees of freedom varies from 21 (as only the island atoms are allowed to move while all the substrate atoms are kept immobile), to 42 (as seven of the closest substrate atoms are also allowed to move during the transition). The number of energy and force evaluations for the NEB method obtained here is similar to what has been reported earlier for this test problem, see references [27,28]. It is possible to use a more efficient minimisation scheme to relax the images in NEB calculations [22], but the difference is not large.

A large reduction in the number of energy and force evaluations is obtained by using the GP regression, as shown in Fig. 4. With the GP regression, the reduction is to less than a fifth as compared with the regular NEB calculation. In calculations involving *ab initio* or density functional theory evaluation of the energy and force, the computational effort is essentially proportional to this number of observations and the additional calculations involved in the GP regression is insignificant in comparison. This test problem, therefore, shows that the use of GP regression can significantly reduce the computational effort in, for example, calculations of surface processes.

4. Discussion

The results presented in this article indicate that GP regression is a powerful approach for significantly reducing the computational effort in calculations of MEPs for transitions. This is important since a great deal of computer time is used in such calculations, especially when *ab initio* or density functional theory calculations are used to evaluate the energy and atomic forces. The heptamer island test problem studied here indicates that the

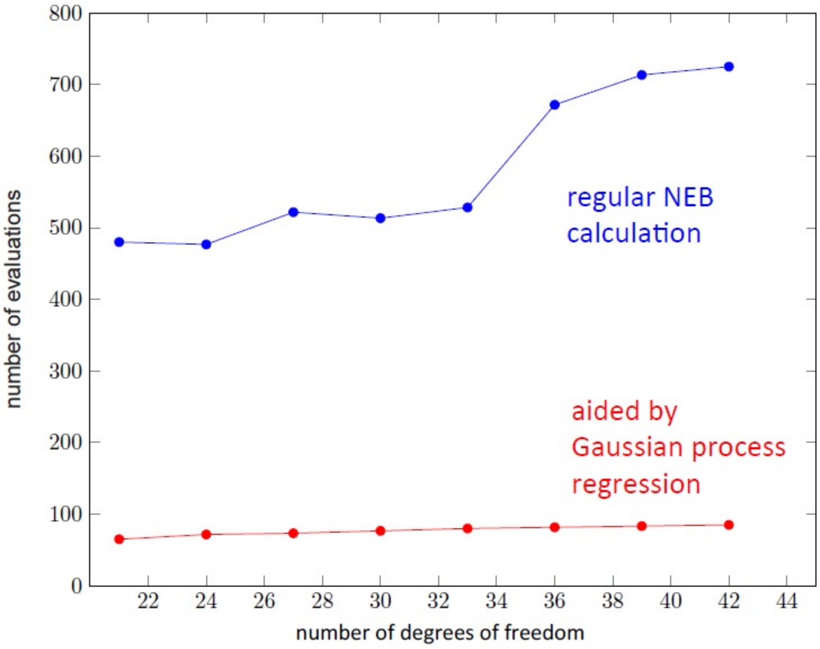

FIG. 4. The average number of energy and force evaluations needed to converge five intermediate images on the minimum energy paths of the three heptamer island transitions shown in Fig. 2 as a function of the number of degrees of freedom included in the calculations. The convergence tolerance is 0.001 eV/Å for the magnitude of the perpendicular component of the force on any one of the images. For the smallest number, 21, only the seven island atoms are allowed to move and all substrate atoms are immobile. For a larger number of degrees of freedom, some of the substrate atoms are also allowed to move during the transition. In the regular NEB calculations (blue dots), the minimization method for relaxing the images to the MEP is based on velocity Verlet algorithm, as described in reference [11]. In the Gaussian process regression calculations (red dots), the number of true energy and function evaluations is less than a fifth of what is needed in the regular NEB calculation. This illustrates well the large reduction in the computational effort that Gaussian process regression can provide in a typical surface process calculation.

computational effort can be reduced to less than a fifth. But, this study represents only an initial proof-of-principle demonstration of the GP regression in this context. There are several ways in which the implementation can be improved and made more efficient. One of the advantages of GP regression over, for example, neural networks is the availability of uncertainty estimates which can be used to make the observations more selective. In the present case, an observation (i.e., evaluation of the true energy and force) was made for all the images in each GP iteration. Alternatively, an observation may only be made for the image for which there is greatest uncertainty. This could target the calculations better and thereby reduce the total number of energy and force evaluations needed to converge to the true MEP.

While the whole path has to be converged well enough to provide an accurate estimate of the tangent, the part of the path that is most important for practical purposes is the region around the first order saddle point. In most cases, the MEP is needed mainly to find the highest energy point along the path, i.e. the first order saddle point on the energy surface that is required for evaluating the transition rate within harmonic transition state theory. The algorithm can be refined to take this into account by, for example, applying the climbing-image NEB [20] where one of the images is driven to the maximum energy along the path, and at the same time the tolerance for the convergence of other images can be increased.

In a typical case, the goal is to evaluate the transition rate using harmonic transition state theory. There, the second derivative matrix, the Hessian matrix, and the frequency of vibrational modes needs to be evaluated at the end points as well as at the (highest) first order saddle point. While the saddle point is not known until the MEP calculation has been carried out, the minima are, and the second derivative matrices at those points might as well be calculated right from the start. This would provide additional information that could be fed into the GP regression so as to improve the accuracy of the approximate energy surface right from first GP iteration. It remains an interesting challenge to extend the GP regression approach to include in some way such information on the second derivatives.

The test problems studied here are quite simple, and it will be important to test the method on more complex systems to fully assess its utility and to develop it further. One issue that can arise is that more than one MEP connects the two endpoint minima. Then, some kind of sampling of MEPs needs to be carried out [29]. Also, some energy surfaces have multiple local minima and highly curved MEPs, which can lead to convergence problems unless a large number of images is included in the calculation. The scaling of the GP regression approach to such more challenging problems needs to be tested. There will, however, clearly be a large set of important problems, such as calculations of catalytic processes, which often involve rather small molecules adsorbed on surfaces, where the complexity is quite similar to the heptamer island test probelm studied here, and where the GP regression is clearly going to offer a significant reduction in computational effort.

At low enough temperature, quantum mechanical tunneling becomes the dominant transition mechanism and the task is then to find the minimum action path [5,30,31]. Calculations of tunneling paths requires exploring the energy surface over a wider region than a calculation of MEPs and here again the GP regression approach can lead to a significant reduction in computational effort, even more than for MEP calculations since each iteration necessarily involves more observations and thereby more input for the modeling of the energy surface.

The discussion has focused here on atomic rearrangements, but it will, furthermore, be interesting to apply the GP regression approach to magnetic transitions where the evaluation of the magnetic properties of the system is carried out using computationally intensive *ab initio* or density functional theory calculations. There, the relevant degrees of freedom are the angles defining the orientation of the magnetic vectors and the task is again to find MEPs on the energy surface with respect to those angles [7–9].

Acknowledgements

HJ would like to thank Prof. Andrew Peterson at Brown University for helpful discussions. This work was supported by the Academy of Finland (FiDiPro program grant no. 263294) and by the Icelandic Research Fund.

References

[1] Wigner E. The Transition State Method. *Trans. Faraday Soc.*, 1938, **34**, P. 29.
[2] Kramers H.A. Brownian Motion in a Field of Force and the Diffusion Model of Chemical Reactions. *Physica*, 1940, **7**, P. 284.
[3] Keck J.C. Variational theory of reaction rates. *J. Chem. Phys.*, 1967, **13**, P. 85.
[4] Vineyard G.H. Frequency factors and isotope effects in solid state rate processes. *J. Phys. Chem. Solids*, 1957, **3**, P. 121.
[5] Jónsson H. Simulation of Surface Processes. *Proceedings of the National Academy of Sciences*, 2011, **108**, P. 944.
[6] Bessarab P.F., Uzdin V.M., Jónsson H. Harmonic transition state theory of thermal spin transitions. *Phys. Rev. B*, 2012, **85**, P. 184409.
[7] Bessarab P.F., Uzdin V.M., Jónsson H. Potential Energy Surfaces and Rates of Spin Transitions. *Z. Phys. Chem.*, 2013, **227**, P. 1543.
[8] Bessarab P.F., Uzdin V.M., Jónsson H. Calculations of magnetic states and minimum energy paths of transitions using a noncollinear extension of the Alexander-Anderson model and a magnetic force theorem. *Phys. Rev. B*, 2014, **89**, P. 214424.
[9] Bessarab P.F., Skorodumov A., Uzdin V.M., Jónsson H. Navigation on the energy surface of the noncollinear Alexander-Anderson model. *Nanosystems: Physics, Chemistry, Mathematics*, 2014, **5**, P. 757.
[10] Mills G., Jónsson H., Schenter G.K., Reversible work based transition state theory: Application to H_2 dissociative adsorption. *Surface Science*, 1995, **324**, P. 305.
[11] Jónsson H., Mills G., Jacobsen K.W. Nudged Elastic Band Method for Finding Minimum Energy Paths of Transitions. In "Classical and Quantum Dynamics in Condensed Phase Simulations", edited by B.J. Berne, G. Ciccotti, D.F. Coker, pages 385-404. World Scientific, 1998.
[12] Bessarab P.F., Uzdin V.M., Jónsson H. Method for finding mechanism and activation energy of magnetic transitions, applied to skyrmion and antivortex annihilation. *Comput. Phys. Commun.*, 2015, **196**, P. 335.
[13] Peterson A.A. Acceleration of saddle-point searches with machine learning. *J. Chem. Phys.*, 2016, **145**, P. 074106.
[14] O'Hagan A. Curve fitting and optimal design for prediction. *Journal of the Royal Statistical Society* (Series B), 1978, **40**, P. 1.
[15] MacKay D.J.C. Introduction to Gaussian processes. In "Neural Networks and Machine Learning", Editor C.M. Bishop, pages 133-166. Springer Verlag, 1998.
[16] Neal R.M. Regression and classification us- ing Gaussian process priors (with discussion). In "Bayesian Statistics 6", Editors J.M. Bernardo, J.O. Berger, A.P. Dawid, A.F.M. Smith, pages 475-501 (Oxford University Press, 1999).
[17] Rasmussen C.E., Williams C.K.I. *Gaussian Processes for Machine Learning*. MIT Press, 2006.
[18] Smidstrup S., Pedersen A., Stokbro K., Jónsson H. Improved initial guess for minimum energy path calculations. *J. Chem. Phys.*, 2014, **140**, P. 214106.
[19] Henkelman G., Jónsson H. Improved Tangent Estimate in the NEB Method for Finding Minimum Energy Paths and Saddle Points. *J. Chem. Phys.*, 2000, **113**, P. 9978.
[20] Henkelman G., Uberuaga B.P., Jónsson H. A Climbing-Image NEB Method for Finding Saddle Points and Minimum Energy Paths. *J. Chem. Phys.*, 2000, **113**, P. 9901.
[21] Melander M., Laasonen K., Jónsson H. Removing external degrees of freedom from transition state search methods using quaternions. *Journal of Chemical Theory and Computation*, 2015, **11**, P. 1055.
[22] Sheppard D., Terrell R., Henkelman G. Optimization methods for finding minimum energy paths. *J. Chem. Phys.*, 2008, **128**, P. 134106.

[23] Lampinen J., Vehtari A. Bayesian approach for neural networks – review and case studies. *Neural Networks*, 2001, **14**, P. 7.

[24] Solak E., Murray-Smith R., Leithead W.E., Leith D.J., Rasmussen C.E. Derivative observations in Gaussian process models of dynamic systems. In “Advances in Neural Information Processing Systems 15”, pages 1033–1040. MIT Press, 2003.

[25] Rasmussen C.E. Gaussian processes to speed up Hybrid Monte Carlo for expensive Bayesian integrals. In “Bayesian Statistics” **7**, pages 651-659. Oxford University Press, 2003.

[26] Vanhatalo J., Riihimäki J., Hartikainen J., Jylänki P., Tolvanen V., Vehtari A. GPstuff: Bayesian Modeling with Gaussian Processes. *Journal of Machine Learning Research*, 2013, **14**, P. 1175.

[27] Henkelman G., Jóhannesson G.H., Jónsson H. Methods for finding saddle points and minimum energy paths. In “Progress in Theoretical Chemistry and Physics”, ed. S. D. Schwartz, Vol. **5**, chapter 10, pages 269-300. Kluwer Academic, Dordrecht, 2000.

[28] Chill S.T., Stevenson J., Ruhle V., Shang C., Xiao P., Farrell J., Wales D., Henkelman G. Benchmarks for characterization of minima, transition states and pathways in atomic, molecular, and condensed matter systems. *J. Chem. Theory Comput.*, 2014, **10**, P. 5476.

[29] Maras E., Trushin O., Stukowski A., Ala-Nissila T., Jónsson H. Global transition path search for dislocation formation in Ge on Si(001). *Comput. Phys. Commun.*, 2016, **205**, P. 13.

[30] Mills G., Schenter G.K., Makarov D., Jónsson H. Generalized Path Integral Based Quantum Transition State Theory. *Chemical Physics Letters*, 1997, **278**, P. 91.

[31] Mills G., Schenter G.K., Makarov D. Jónsson H. RAW Quantum Transition State Theory. In “Classical and Quantum Dynamics in Condensed Phase Simulations”, editors B.J. Berne, G. Ciccotti and D.F. Coker, page 405. World Scientific, 1998.

NANOSYSTEMS: PHYSICS, CHEMISTRY, MATHEMATICS, 2016, 7 (6), P. 936–940

Three-dimensional extremely short optical pulses in graphene with coulomb impurities with taking into account inhomogeneity

N. N. Konobeeva[1], A. A. Polunina[1], M. B. Belonenko[1,2]

[1]Volgograd State University, 400062, Volgograd, Russia

[2]Volgograd Institute of Business, 400048, Volgograd, Russia

yana_nn@inbox.ru

DOI 10.17586/2220-8054-2016-7-6-936-940

Maxwell's equations were considered for the electromagnetic field propagating in doped graphene taking spatial inhomogeneity in the three-dimensional case. The electronic spectrum for the graphene subsystem was obtained from the model taking into account the Coulomb impurity. The effective equation for the vector potential of the electromagnetic field was solved numerically. A comparison of the forms of extremely short optical pulses is done for the case with recording inhomogeneities and one without.

Keywords: optical pulses, Coulomb impurities, inhomogeneity.

Received: 10 April 2016

Revised: 16 May 2016; 7 June 2016

1. Introduction

Recently interest in the study of extremely short optical pulses in different nanoobjects has increased, from both theoretical and practical viewpoints [1–7]. This is primarily due to the prospects of using such pulses to solve different kinds of problems which occur in modern nanoelectronics. In this paper, we will study features of the three-dimensional propagation of extremely short pulses (ESP) in doped graphene with consideration of its inhomogeneity. We mean that inhomogeneity is the region of high electron density. Random inhomogeneity of this field (due to the random arrangements of impurities) can result in interesting and unexpe [8] is related to the two-dimensional simulation of the propagation of ultrashort electromagnetic pulses in an array of CNTs (carbon nanotubes) with the inhomogeneity of the field along the axis (in this case, the field is not randomly inhomogenous, we assume that the inhomogeneity is given experimentally). In addition, in recent years authors conducted a comprehensive study of the last task in the 3D case, as a result of which, have demonstrated the possibility of bipolar propagation of electromagnetic breathers through an array of CNT with consideration of field inhomogeneities [9]. In this case, the electromagnetic pulse causes a significant redistribution of electron density in the sample for both 2D, and 3D systems. Besides field inhomogeneities that lead to a redistribution of the electrons, there are other natural inhomogeneities observed in experimental samples. This is especially important in the case where the inhomogeneities are caused by increased concentration regions of conduction electrons due to the presence of impurities. It is worth noting that the existence of different kinds of impurities and the nature of their interactions with graphene also requires the use of a variety of approaches. For example, in [10], the investigators considered the case of impurities in graphene with the disorder, where the spectrum of electrons was determined from the renormalization group approach.

In this paper, we will rely on a different approach [11], which is to consider the Coulomb charged impurities in graphene. In the cited paper, the effect of the gap, which is induced with impurities, was studied by using the Hartree-Fock method for the calculation of the Fermi velocity. This led to their own energy corrections to the polarization. The result is a renormalized Fermi velocity, which has a logarithmic dependency on the electron's energy.

2. The statement of the problem and basic equations

Consider the propagation of extremely short electromagnetic pulses in doped graphene with impurities, with consideration of the ultimate quasiparticle mass (i.e. with the gap in the spectrum). The vector-potential A is directed along the graphene sheet, the direction of the electric field propagation is perpendicular to the graphene sheet. Graphene is oriented in the plane XOY.

The dispersion relation for graphene can be found according to well-known relationship of charges speed and energy of electrons: $\nu_y = \dfrac{\partial\varepsilon\left(q_x, q_y\right)}{\partial q_y}$.

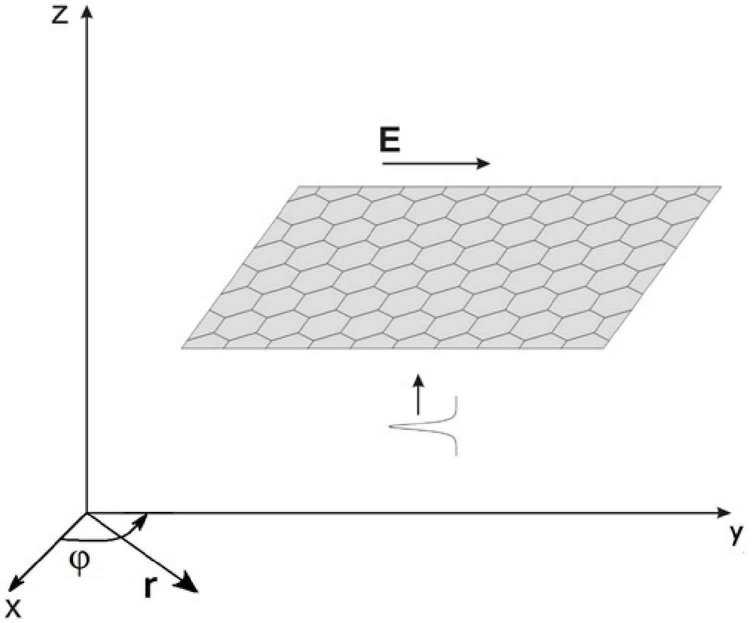

FIG. 1. Geometry of the problem

According to [9], we have:

$$\nu_y = \nu \left(1 + \frac{\alpha}{4} \ln \left(\frac{\Lambda + \sqrt{\Lambda^2 + m^2}}{\sqrt{q_x^2 + q_y^2} + \sqrt{q_x^2 + q_y^2 + m^2}} \right) \right), \tag{1}$$

Here, q_x, q_y - electron momentum component, m – gap in the spectrum (0.1 eV). It should be noted that the gap in the energy spectrum since graphene is considered with impurity.

As follows from the rules of quantum mechanics, in the presence of an external electric field of the **E** which for certainty is directed along the x-axis, and will be hereafter considered in the calibration: $\mathbf{E} = -\partial \mathbf{A}/c\partial t$, pulse needs to be replaced on the generalized pulse: $\mathbf{q} \to \mathbf{q} - e\mathbf{A}/c$ (is the electron charge).

We write the wave equation for the three-dimensional case in the cylindrical coordinate system:

$$A_{tt} = \frac{1}{r}\frac{\partial}{\partial r}\left(r\frac{\partial A}{\partial r} \right) + \frac{\partial^2 A}{\partial z^2} + \frac{1}{r^2}\frac{\partial^2 A}{\partial \phi^2} + 4\pi j\left(A \right) \tag{2}$$

Next, everywhere we believe that by virtue of the cylindrical symmetry: $\dfrac{\partial}{\partial \phi} \to 0$.

From the law of charge conservation, we have: $\rho \propto \tau \dfrac{j}{l_y}$ (here ρ is the charge density, j is the current density along y axis, τ is the electric field duration, l_y is the characteristic length of the electric field pulse along the y axis) shows that the duration of ESP has a significant impact on the accumulated charge, which creates an additional electric field. This electric field is interfering with the field of ESP. Previous estimates made by the authors (the stored charge is about 1-2% of the charge, giving contribution to the current) allow us to conclude that the charge accumulation effect for femtosecond pulses may be neglected. This is confirmed by numerical experiments for the case of carbon nanotubes and a pulse duration of tens of femtoseconds [8].

We write down the standard expression for the current density:

$$\mathbf{j} = e \sum_q v_y \left(\mathbf{q} - \frac{e}{c}\mathbf{A}(x,y,z,t) \right) \langle a_q^+ a_q \rangle, \tag{3}$$

where the brackets denote averaging with the non-equilibrium density matrix $\rho(t)$: $\langle B \rangle = Sp(B(0)\rho(t))$. Given that $[a_q^+ a_q, H] = [n_q, H] = 0$ (since the interaction with the external field is given by: $\varepsilon(\mathbf{q} - \frac{e}{c}\mathbf{A}(x,y,z,t))a_q^+ a_q$, $A = (0, A\left(x,y,z,t\right), 0)$, n_q is the number of particles) from the equations of motion for the density matrix immediately obtain that: $\left\langle a_q^+ a_q \right\rangle = \left\langle a_q^+ a_q \right\rangle_0$, where $\langle B \rangle_0 = Sp(B(0)\rho(0))$. Thus, in the expression for the current density, the number of particles can be used, which follows from the Fermi-Dirac distribution. Next, we consider the case of low temperatures, when only a small region in momentum space near the Fermi level gives a contribution to the sum (integral). Accordingly, we write the formula (3) as:

$$\mathbf{j} = e\int_{-\Delta}^{\Delta}\int_{-\Delta}^{\Delta} d\mathbf{q}_x dq_y v_y \left(q - \frac{e}{c}\mathbf{A}(x,y,z,t)\right). \tag{4}$$

The region of integration over the pulses in (6) is determined from the condition of equality the number of particles:

$$\int_{-\Delta}^{\Delta}\int_{-\Delta}^{\Delta} dq_x dq_y = \int_{ZB} dq_x dq_y \left\langle a^{+}_{qx,qy} a_{qx,qy}\right\rangle, \tag{5}$$

the integration of the right is carried out over the first Brillouin zone.

The equation on the distribution of extremely short pulses can be written as:

$$\begin{aligned} A_{tt} &= \frac{1}{r}\frac{\partial}{\partial r}\left(r\frac{\partial A}{\partial r}\right) + \frac{\partial^2 A}{\partial z^2} + \frac{1}{r^2}\frac{\partial^2 A}{\partial \varphi^2} + 4\pi\Phi\left(A\right)\cdot f\left(z\right), \\ f\left(z\right) &= 1 - \alpha\cdot\exp\left(-\left(\frac{z - z_0}{\delta}\right)^2\right), \end{aligned} \tag{6}$$

here $\Phi\left(A\right)$ is determined by integrating in (5), $f\left(z\right)$ is the function that determines the spatial inhomogeneity, α is the depth of spatial inhomogeneity (when α=0 – without inhomogenity), δ is the width of the spatial inhomogeneity, z_0 is the given position offset inhomogeneity.

3. Results of numerical simulation

Equation (6) was solved numerically [12]. The initial condition is chosen in the form:

$$\begin{aligned} A\left(z,r,0\right) &= Q\exp\left(-\left(\frac{z - z_0}{\gamma_z}\right)^2\right)\exp\left(-\left(\frac{r}{\gamma_r}\right)^2\right), \\ \frac{dA\left(z,r,0\right)}{dt} &= 2Qv_z\frac{z - z_0}{\gamma_z}\exp\left(-\left(\frac{z - z_0}{\gamma_z}\right)^2\right)\exp\left(-\left(\frac{r}{\gamma_r}\right)^2\right), \end{aligned} \tag{7}$$

where r is the radius, Q is the amplitude, γ_z, γ_r are the determine the pulse width, v_z is the initial pulse velocity along z-axis z_0 is the initial displacement of the pulse center. This initial condition corresponds to what is an extremely short pulse consisting of a single oscillation of the electric field applied to the sample. The values of energy parameters are expressed in units of Δ. It should be noted that time evolution is variable.

The arising evolution of the electromagnetic field during its propagation through each sample is shown in Fig. 2.

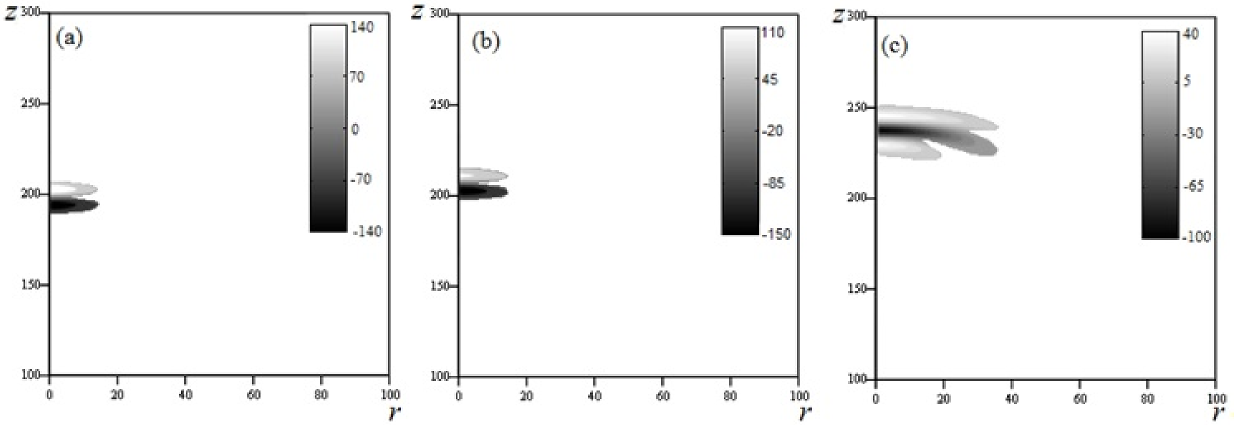

FIG. 2. The intensity of the three-dimensional electromagnetic pulse at different time points: (a) the initial pulse shape; (b) $t = 1.0\cdot 10^{-13}$ s; (c) $t = 5.0\cdot 10^{-13}$ s (unity along r and z corresponds to 5 nm)

This pulse behavior is associated with the nonlinearity in (6). There is a decline in pulse amplitude, as well as its spreading over time. This allows us to draw conclusions regarding the instability of pulses, which leads to the disruption of their structure.

Dynamics of a three-dimensional extremely short pulse considering inhomogeneity of the environment is shown in Fig. 3.

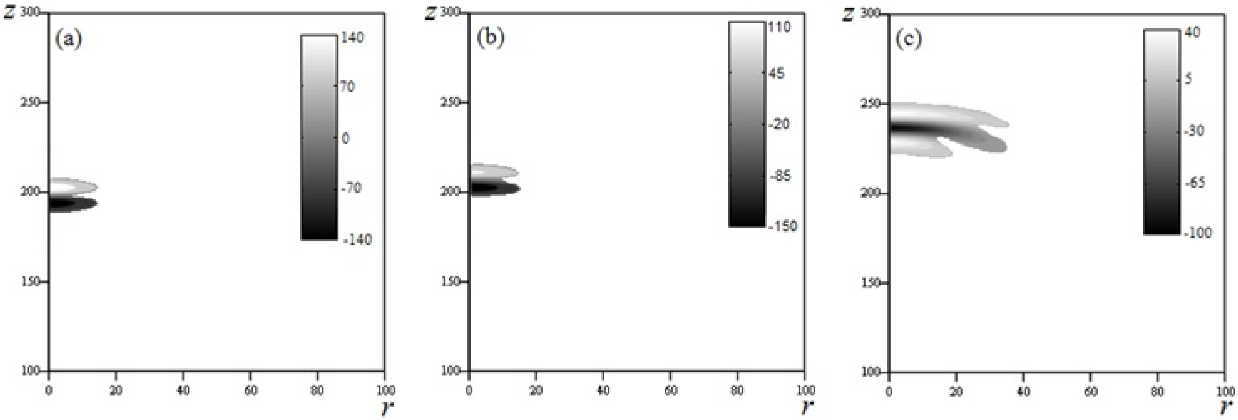

FIG. 3. The intensity of the three-dimensional electromagnetic pulse at different time points ($\alpha = 0.8$ r.u., $\delta = 5$ r.u.): (a) the initial pulse shape; (b) $t = 1.0 \cdot 10^{-13}$ s; (c) $t = 5.0 \cdot 10^{-13}$ s (unity along r and z corresponds to 5 nm)

As follows from Fig. 3, the introduction of spatial inhomogeneity does not preclude spreading of the pulse along the transverse coordinate.

Comparison of cases with consideration of the spatial inhomogeneity and without it is shown in Fig. 4.

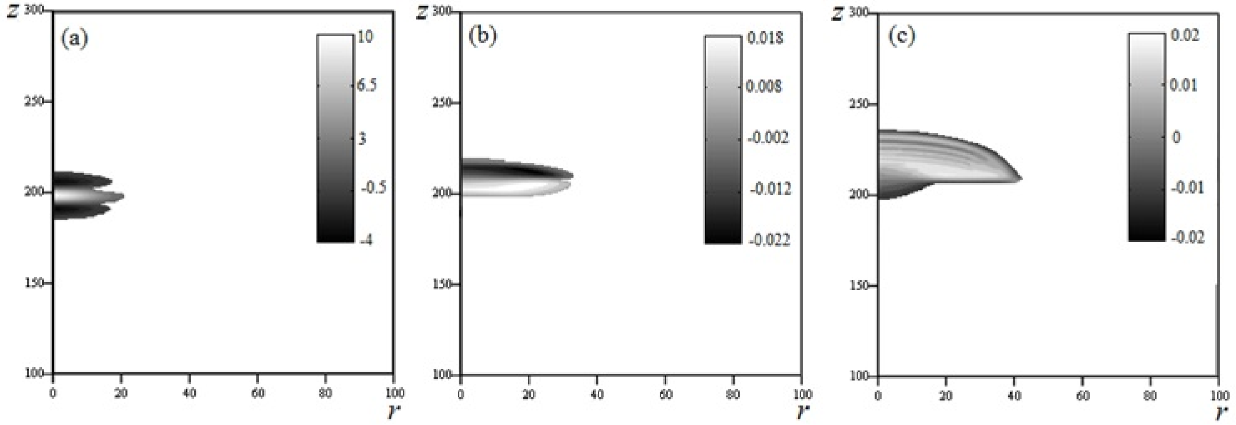

FIG. 4. The difference of the intensities of the three-dimensional electromagnetic pulse in the case of considering non-uniformity and without it: (a) the initial pulse shape; (b) $t = 1.0 \cdot 10^{-13}$ s; (c) $t = 5.0 \cdot 10^{-13}$ s (unity along r and z corresponds to 5 nm)

As is shown by the results of numerical calculations, with the passage of time, the difference between the pulse shape in the homogeneous recording case and without it becomes less noticeable. But, in the case for the introduction of spatial non-uniformity in the environment, the momentum in the amplitude is reduced by about 0.05% in comparison with the case of a homogeneous medium.

We also note that we studied the impact of inhomogeneity of parameters α and δ on the form of extremely short pulses. Numerical calculations have shown that the depth and width of the input inhomogeneity has little effect on the shape of the pulse.

Practical application of the methodology proposed in the article is the following: all the obtained nanotubes and graphene contain impurities that affect the propagation process of extremely short optical pulses due to electron density inhomogeneity. Thus, by examining the evolution of such pulse features, we can identify the characteristics of the impurities.

4. The conclusions

In conclusion, we will now formulate the main outcomes of this work:

(1) Three-dimensional extremely short optical pulses in doped graphene propagate unstably with violation of the pulse shape.
(2) Introduction of spatial inhomogeneities in the medium does not permit significant reduction of the pulse losses in amplitude in comparison with the case of a homogeneous medium.
(3) The depth and width of the spatial inhomogeneity does not seem to have much influence on the shape of the pulse.

Acknowledgements

This work was supported by the Russian Foundation for Basic Research under project No. 16-32-00230, by the Ministry of Education and Science of the Russian Federation project no. MK-4562.2016.2.

References

[1] Akhmanov S.A., Vysloukhy V.A., Chirikin A.S. *Optics of femtosecond laser pulses*. New York, AIP, 1992.
[2] Belonenko M.B., Demushkina E.V., Lebedev N.G. Electromagnetic soliton in bundles of carbon nanotubes. *Physics of the Solid State*, 2008, **50**, P. 383–389.
[3] Yanyushkina N.N., Belonenko M.B., Lebedev N.G., Zhukov A.V., Paliy M. Extremely Short Optical Pulses in Carbon Nanotubes in Dispersive Nonmagnetic Dielectric Media. *Int. J. Mod. Phys. B*, 2011, **25**, P. 3401–3408.
[4] Belonenko M.B., Popov A.S., Lebedev N.G., Pak A.V., Zhukov A.V. Extremely short optical pulse in a system of nanotubes with adsorbed hydrogen. *Phys. Lett. A*, 2011, **375**, P. 946–952.
[5] Belonenko M.B., Fedorov E.G. Extremely short electromagnetic pulses in an array of carbon nanotubes with a longitudinal field inhomogeneity. *Physics of the Solid State*, 2013, **55**, P. 1333–1337.
[6] Belonenko M.B., Nevzorova Ju.V., Galkina E.N. Few cycle pulses in the Bragg medium containing carbon nanotubes. *Nanosystems: physics, chemistry, mathematics*, 2014, **5**(5), P. 644–649.
[7] Konobeeva N.N., Belonenko M.B. Propagation of femtosecond pulses in carbon nanotubes. *Nanosystems: physics, chemistry, mathematics*, 2014, **5**(1), P. 91–97.
[8] Zhukov A.V., Bouffanais R., Fedorov E.G., Belonenko M.B. Three-dimensional electromagnetic breathers in carbon nanotubes with the field inhomogeneity along their axes. *J. Appl. Phys.*, 2013, **114**, P. 143106.
[9] Suzuura H., Ando T. Crossover from symplectic to orthogonal class in two-dimensional honeycomb lattice. *Phys. Rev. Lett.*, 2002, **89**, P. 266603.
[10] Belonenko M.B., Konobeeva N.N. Ultrashort Electromagnetic Pulses in Graphene with Disorder. *Optics and Spectroscopy*, 2015, **119**(2), P. 82–85.
[11] Kotov V.N., Pereira V.M., Uchoa B. Polarization charge distribution in gapped graphene: Perturbation theory and exact diagonalization analysis. *Phys. Rev. B*, 2008, **78**, P. 075433.
[12] Bahvalov N.S. *Numerical methods (analysis, algebra, ordinary differential equations*. Moscow, Nauka, 1975, 632 p.

NANOSYSTEMS: PHYSICS, CHEMISTRY, MATHEMATICS, 2016, 7 (6), P. 941–970

High-temperature superconductivity: From macro- to nanoscale structures

A. N. Kovalenko

Ioffe Institute, St. Petersburg, Russia

ras-kan@mail.ru

DOI 10.17586/2220-8054-2016-7-6-941-970

The analysis of achievements, problems and prospects of high-temperature superconductivity (HTSC) in the macro- and nanostructured materials has been given. The main experimental results and theoretical models describing the physical mechanisms of the superconductivity appearance at phenomenological and microscopic levels, including change in the energy spectrum of atoms in these materials with the advent of the 'superconducting' gap at temperatures below the critical transition, as well as the above-critical temperature 'pseudo-gap' have been analyzed. Although the origin of the pseudo-gap is not completely understood, it can be considered as an independent phase transition in the substance prior to the transition to the zero resistance state and insusceptibility (or insensitivity) to external magnetic field in high-temperature superconductors. Features of multi-gap and gapless superconducting materials as well as their ability to further increase the temperature of supercritical transition are discussed. Large resources to create the necessary electron and phonon spectra in the process of high-temperature superconductivity formation are associated with the use of nanoscale structures and nanoparticles of conductors and dielectrics. Electrical conductive contacts between nanoparticles and tunnel chains of nanoclusters, where delocalized electron spectra form similar energy shells to the atomic or nuclear shells, play a significant part here. It is required to further investigate the occurrence of high-temperature superconductivity at the level of interphase layers (non-autonomous phases) in nanostructures containing a large fraction of the substance in this condition. It is essential to develop adequate methods for synthesis of nanoparticles of variable size, structure and morphology, as well as techniques for their consolidation that would ensure the preservation of superconductivity of individual nanoparticles, their chemical, thermal, magnetic and current stability in the dissipative processes with functional and fluctuation effects.

Keywords: high-temperature superconductivity, energy spectrum, 'superconducting' and 'pseudo-' gaps, layered and nanoscopic structures, non-autonomous phases, chemical, thermal, current, and magnetic resistance.

Received: 20 August 2016

Revised: 27 October 2016

Contents

1. Introduction

The phenomenon of superconductivity occurs in certain substances and materials at temperatures below a critical value, Tc, which is specific for each material. Phenomenologically, it is considered as the combined effect of the complete absence of electrical DC resistance and negligible susceptibility to an external magnetic field [1].

The electric effect of superconductivity was discovered by H. Kamerlingh-Onnes in 1911 by means of mercury experiments at very low temperatures. He found that the electrical resistance of mercury gradually decreases with reducing temperature to ~ 4.2 K and then almost abruptly becomes zero [2]. Thereafter, a similar phenomenon was observed for a number of other metals (lead, tin, thallium, uranium, etc.) when cooled to temperatures close to absolute zero. It was also accompanied by changes in their thermal properties in contrast to behavior of metals that cannot be superconductive, such as silver, copper, gold, platinum, etc. In the latter case, the electrical resistance gradually decreased with temperature, approaching a residual (zero if a metal is hypothetically pure) value at 0 K.

Magnetic effect of superconductivity was discovered by W. Meissner and R. Ochsenfeld in 1933. They demonstrated that in parallel, the superconductors are technically perfect diamagnetic materials if they are in a magnetic field of a magnitude less than a critical value Hc, i.e. they push magnetic lines completely out of the sample volume [3, 4]. The description of this effect in terms of electrodynamics, proposed in 1935 by brothers F. London and H. London [5] in addition to J. C. Maxwell's [6] equations, allowed us to estimate the depth of magnetic field penetration into the superconductor. In the case of metals, this area covers hundreds of atomic layers and has the skin layer of superconducting current of thickness $\sim 10 - 100$ nm. The proposed approach also allowed us to associate the superconductivity with the transition of current carriers to the state with the least possible momentum.

The phenomenological theory of superconductivity [7] created by V. L. Ginzburg and L. D. Landau in 1950 describes the transition to the superconducting state as the formation of phase coherence in the substance electronic system but does not determine the charge of the superconducting current carriers and does not explain the causes of superconductivity. The Ginsburg–Landau equations derived on this basis involving a L. P. Gorkov's microscopic approach [8] in 1958, match well with the superconductor behavior at critical temperatures and are still used for the experimental data interpretation and in technical applications [9]. The detailed microscopic theory of superconductivity [10] was developed in 1957 by J. Bardeen, L. N. Cooper and J. R. Schrieffer. It named as the BCS-theory – using the first letters of their surnames. According to this theory, electrons experience attraction at temperatures below Tc due to the interaction with the thermal vibrations of positively charged crystal lattice. Their excitations, in the form of acoustic frequency elastic waves and corresponding quasi-particles (phonons), are distributed over the entire space of the material. In the context of quantum mechanics, it is described as the electron-phonon interaction that does not stop, even at absolute zero, according to Heisenberg's uncertainty principle. Due to the fact that it is stronger than the Coulomb repulsion between the electrons, some electrons (with energies close to the Fermi level) are merged into so-called Cooper pairs. According to the Pauli exclusion principle, in contrast to individual initial states of electrons as fermion particles with half-integer spin which comply with Fermi–Dirac statistics, the paired electrons behave coherently as a single quantum-mechanical system of identical boson particles with integer spin which comply with the Bose–Einstein statistics [11]. Due to this fact, they cannot exchange energy portions with the crystal lattice that are lower than the energy resulting from their coupling. Since, according to the principle of wave-particle duality, any particle can be viewed as a wave of certain amplitude, frequency and phase according to de Broglie relations [12], Cooper pairs as coherent quasi-particles constitute a single wave together. It is described with the general wave function where the amplitude square determines the density of Cooper pairs on the spatial scale (length) of coherence. Herewith, there is no scattering of electron waves on thermal vibrations of the substance lattice and the paired conduction electrons can flow through it without energy loss and therefore without resistance, which also does not allow the external magnetic field to penetrate inside the material. To meet these requirements for conventional materials, according to the classical Bardeen-Cooper-Schrieffer theory, the critical temperature may not exceed the limit of about 40 K (-233 °C).

It should be noted that it was G. Fröhlich who first identified the connection of the superconductivity phenomenon with the lattice vibrations in 1950. He proposed a hypothesis of the influence of the ion mass on the critical transition temperature, with the latter being inversely proportional to the square root of the ionic mass in the isotope collection of the given superconductor [13]. Experiments with isotopic substitutions conducted by E. Maxwell and other researchers [14, 15], confirmed the isotopic effect predicted by G. FrÖhlich and showed that there is a direct effect of ion mass on inter-ion distances in the lattice and the value of the Fermi energy. Consequently, the existence of the isotopic effect cannot be a reliable proof of the phonon mechanism as being solely responsible for the pairing of electrons and the appearance of superconductivity. The BCS theory is also found insufficient in terms of its inability to explain why particular superconductors have a certain critical temperature and therefore in terms of impossibility to predict the ways to increase it. This has led to the creation of other high-temperature superconductivity models (currently, there are more than 100 proposed) where various mechanisms of electrons pairing are considered [16]. They use ideas about spin and charge fluctuations, polarons, plasmons, excitons, magnetons, magnons, solitons and other quasi-particles acting as energy quanta of excitation waves in the system, as well as about the super-exchange between them and the electrons which complements electron-phonon or direct interaction between the electrons. Other ideas are expressed as well, even those concerning the opposition of superconductivity to 'super-magnetism' [17]. However, these developments have neither resulted in noticeable progress in order to understand the superconductivity phenomenon nor made it possible to predict the composition and structure of new superconductors. An indicative opinion in this respect is the one of B. T. Matthias who managed to synthesize, apparently, the largest number of new superconductors [18]. He argued that, despite the existence of numerous theories of superconductivity, the only concept that helped him in the discovery of new superconductors was D. I. Mendeleev's periodic table of elements. This situation has been persisting in the theory of superconductivity so far. The developed theories do not explain the possibility of creating high-temperature superconducting materials (HTSC) which are studied mostly empirically, by complication of their composition and structure and identifying correlations between the obtained properties, occurring physical and chemical processes and external thermal, electrical, magnetic and other influences. Fundamental and practical physical and chemical problems and results of these studies are published in numerous original articles as well as in various summary reviews and monographs [19–36] where other details and additional references can be found.

This review deals with the poorly represented but promising and intensively developing directions of modern research in the field of high-temperature superconductivity nanostructures. In addition, major statements of the above papers which are important for the analysis of the subject are also addressed as appropriate in the review.

2. Superconductivity thermodynamics and electrodynamics

Thermodynamically, the transition to the superconducting state is associated with the substance phase changes (phase transitions) [37] occurring when the temperature changes and accompanied by the changes in some of its thermodynamic and electromagnetic properties. According to the general thermodynamic theory, the transition to superconductivity and vice versa can be first and second order, which is confirmed experimentally (Fig. 1).

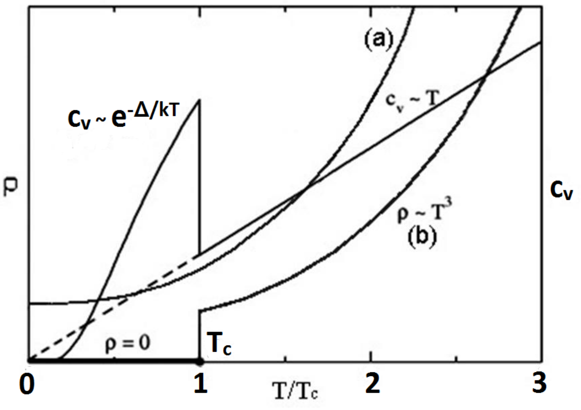

FIG. 1. The pattern of electrical resistance decrease (ρ) and heat capacity variations (CV) for substances that do not become (a) and become (b) superconductive when cooled (taken from [70])

The first order transition is characterized by an abrupt change of extensive parameters at the Tc transition point, above all, of thermal energy, entropy and volume which are the first derivatives of the thermodynamic potential of the system on its intensive parameters, temperature and pressure. The second order transition is characterized by an abrupt change in the second derivatives of the thermodynamic potential (thermal capacity, thermal expansion factor, different ways of responsiveness) while the internal energy, density and other first order derivatives, according to the parameter set of the general system condition, are maintained at the transition point. Thermodynamic fluctuations arising at the superconducting phase emerge at the spatial scale, corresponding to the coherence length. Phase symmetry can change simultaneously as well; however, phase transitions in superconductors are not caused by changing the crystalline state of the body and the lattice symmetry and are only connected with change of its qualitative electromagnetic properties [38].

The idea of two existing superconductor orders which differ in response to the external magnetic field was first proposed in 1952 by A. A. Abrikosov and N. I. Zavaritsky [39, 40] based on experimental results obtained by L. B. Schubnikov for magnetization curves of superconducting alloys [41, 42], and data obtained by N. I. Zavaritsky for the critical magnetic fields of thin superconducting films [43]. The soft superconductor transition from a normal to a superconducting state, depending on external magnetic conditions, can be both first and second order phase transition, whereas the hard superconductor transition from a normal to a superconducting state shall be a second order phase transition only under all conditions. Herewith, soft superconductors have the only Hc value of the critical magnetic field intensity; they are not superconductive if it increases. However, the possible distortions of the field due to the heterogeneous interaction with the differently-shaped conductor segments can result in the simultaneous existence of large alternating areas of superconducting and normal phases separated by a substance in the 'intermediate' phase in this sample. The hard superconductors have two critical magnetic field $Hc1$ and $Hc2$

values, between which it partially penetrates into the superconductor in the form of so-called Abrikosov vortex lattice [40] whose cores are non-superconducting (normal), and the superconducting currents screening the normal vortex area circulate around them. As a result, *Hc1* field transforms the conductor into the 'mixed' (metastable in nature) state and preserves its superconducting properties, and the field above $Hc2$ destroys them. Experimental observation of the structures of soft and hard superconductors being in the intermediate and mixed states was carried out in 1967 by H. Tauble and U. Essman [44], and N. V. Sarma [45, 46] using the electron microscope of 10 nm resolution. The schematic figure of magnetic field distribution in the conductors of different types is represented in Fig. 2 according to [31, 38].

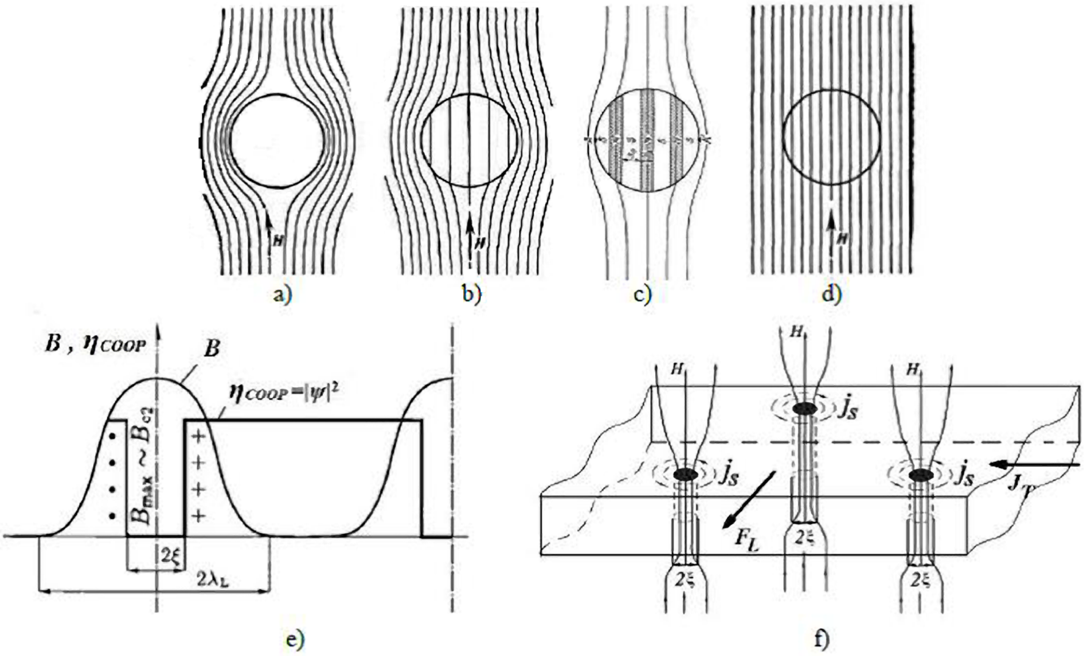

FIG. 2. Magnetic field distribution around the superconducting body (Figures taken from [31, 38]): a) – superconducting state; b) and c) – intermediate state where the alternating superconducting and normal areas emerge; d) – normal state; e) – hypothetical structure of the superconducting vortex (quantum filaments of magnetic flux, where crosses and dots show schematically the direction of a superconducting vortex current); f) – the Schubnikov phase (diagram); ψ-amplitude of the common wave function of the coherent Cooper pairs, where the amplitude square determines the η-density of Cooper pairs; e) spatial pattern of the mixed state (the specific section is shown, where $H = B/\mu_0$ is for the magnetic field tension and induction, j_S stands for screening supercurrent, 2ξ stands for the vortex core diameter, J_T stands for the transport current, F_L stands for the Lorentz force)

Along with the 'diamagnetic' scenario of superconductivity destruction, the alternative, 'paramagnetic', is possible where the strong magnetic field can change the spin orientation of one of the electrons in a Cooper pair and simultaneously change its energy similar to the known P. Zeeman splitting effect [47]. As a result, the pair changes into an unstable triplet and superconductivity is destroyed. In conventional superconductors, the 'diamagnetic' mechanism is actuated prior to the 'paramagnetic' one. However, in iron-based superconductors where the 'paramagnetic' mechanism is more effective, the preservation of superconductivity is possible even when it is not supposed to exist with respect to this mechanism. Theoretically, such an effect was predicted almost simultaneously by R. Ferrell, P. Fulde [48] and A. I. Larkin, Yu. N. Ovchinnikov [49]. According to this, when the spin orientation of one of the electrons in a Cooper pair is changed by the magnetic field along with a simultaneous change of its energy, the Fermi energy of this pair will also change, resulting in a difference from the Fermi energy of unchanged pairs, and as a consequence, the superconductivity will be preserved. The new phase of the superconducting electron liquid, predicted by them, was called the FFLO phase using the first letter of their surnames [50].

As confirmed by numerous experiments, superconductors can change from one type to another. Impurities in the materials play a fundamental role in such transitions [38]. The theory of such 'impure' superconductors was suggested by P. W. Anderson in 1959 [51]. There is also a theoretical background for discussion and some experimental evidence for the existence of type 1.5 superconductors which comprise the combined properties of type 1 and 2 [52, 53]. According to theoretical considerations [52] when a magnetic field increases, type 1.5 superconductors are characterized by a coherent transition from Meissner 'vortex-free' condition with the complete expulsion of magnetic field lines from the sample volume in weak fields to a certain intermediate state. Here, vortices penetrate into the superconductor not forming a regular triangular lattice of Abrikosov vortices repelling one other as in type 2 superconductors but some unstable irregular clusters of vortices which attract to each other as during the transition to the normal area of type 1superconductors. Upon further magnetic field amplification, they change to a mixed or vortex state of type 2 superconductor where the Abrikosov homogeneous triangular lattice is formed. This is reminiscent of the behavior of molecular forces repulsing vortices from each other at short distances and attracting at long distances whereby vortex combinations resulting in the latter case were called by authors of the theory as vortex 'molecules'. Experiments with single crystals of magnesium diboride, MgB_2, [53] revealed that the magnetic field really penetrates into them as it was theoretically predicted, that is, when a magnetic field $H < Hc1$ is weak, the superconductor is in Meissner condition and if the field amplifies, the vortices penetrate into the superconductor and form a web-shaped lattice instead of a triangular one (Fig. 3a). Further gradual magnetic field amplification leads to transformation of the web-shaped vortex lattice into alternating stripes and the formation of vortex clusters of differing density (Fig. 3b) approximately $\sim$ 100 nm in size and containing about 30 – 50 vortices, and then the regular triangular lattice of Abrikosov vortices as in type 2 superconductors will appear (Fig. 3c).

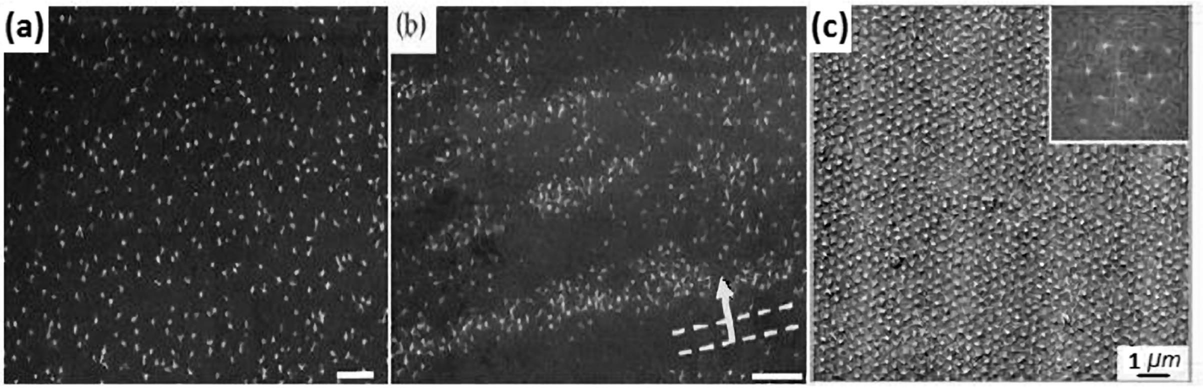

FIG. 3. Web-shaped (a, b) and regular (c) vortex structures in MgB_2 films: a) at 4.2 K in an external magnetic field with induction of 0.0001 T and b) at the same temperature, but in the field of 0.0005 T (Figure taken from the article [53]), c) at a temperature of $T \sim 6$ K and in a weak magnetic field (Figure taken from the article [54])

However, those with differing opinions will point out that the formation of irregular vortex lattice and its flow in weak fields corresponds to the well-known phenomenon of pinning – the magnetic field $H > Hc1$ penetration into a type 2 superconductor in the form of separate ('quantized') vortex filaments, i.e. flux lines, (see Fig. 2) and their consolidation on the defects present there [55, 56]. Such filaments may also remain in the superconductor at fields less than $Hc1$, and even at zero field if it is achieved by lowering from the area of larger fields, $H > Hc2$. This is associated with the arising induction ('Meissner') currents flowing around the superconductor surface. They seek not only to escape the penetration of external magnetic fields into the superconductor but also prevent the magnetic field vortex filaments (field lines) from releasing of its thickness, those ones that penetrated the sample at temperatures $T > Tc$ when it was not superconducting yet. This also determines, in contrast to type 1 superconductors, the irreversible (hysteretic) magnetization curve for type 2 superconductors being in Abrikosov condition, predicted theoretically by K. P. Bin and J. D. Livingston, which is practically very diverse (Fig. 4, [38]). At temperatures close to the critical temperature of superconductivity Tc, the hysteresis phenomenon almost disappears.

Along with the critical external magnetic field there is also the critical current which limits the superconductivity due to creation of the self-magnetic field of critical value with induction $Bc = \mu_0 Hc$. Its energy

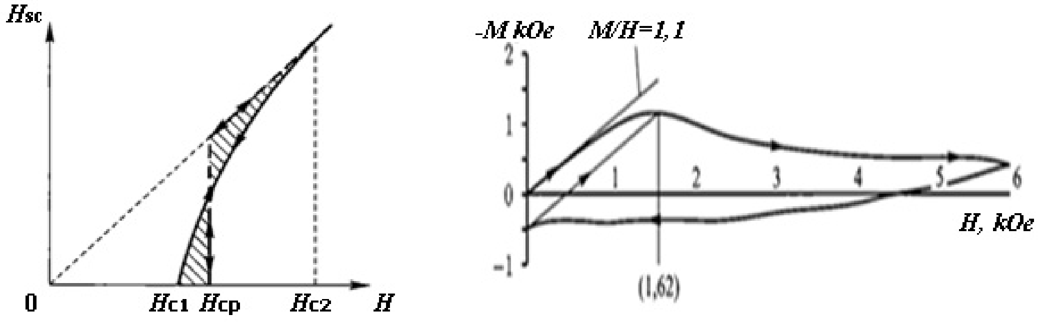

FIG. 4. External magnetic-field dependence of the magnetic H intensity in ideal hard and soft superconductors with the same thermodynamic H_{ave} – critical field (a), and the actual magnetization curve conforming to the sample (b). Herein, $M = pmV$ is for the magnetization vector; pm is for the magnetic moment vector; V is for the volume [38]

$W = mu_0 H^2 c/2 = B^2 c/2\mu_0 = Gn(T) - Gc(T)$ is thermodynamically related to the difference of free Gibbs energies of the normal $Gn(T)$ and the superconducting $Gc(T)$ states, regardless of whether the critical current only escapes the external magnetic field or it is a transport current that does not depend on the field. The excess of energy in magnetic line bonds to the centers of their spinning consolidation during the current flow, when the Lorentzian force influencing the vortices reaches a critical value, leading to an immediate change of their position (the magnetic flux jump) accompanied by a simultaneous temperature rise which may be sufficient to create the normal state of the superconductor [57].

The disturbance of this equilibrium but naturally metastable state of the superconductor vortex lattice with a trapped magnetic flux can probably occur during the flow of weak currents of subcritical value under the triggering action of external perturbations, including thermal and magnetic fluctuations of small intensities. However, unlike the previous case, the process of magnetic flux redistribution (so-called magnetic flux creep) in massive superconductors is long enough at a typical speed of thermal fluctuations. It manifests itself in a slow creep (in the perpendicular direction to the current density vector and the magnetic field induction vector) of pinned mutually repelling vortices to their general ‘Abrikosov’ state, with an equally slow magnetization relaxation to the equilibrium logarithmical value in time [58]. J. Giaever [59] carried out a direct observation of such movement of the niobium particles sawed on a lead foil. In all cases, the irreversible processes accompanied by heat release due to the energy dissipation of superconducting current, take place in the superconductor. Phase diagrams for superconductors of various kinds during tension H change of an external magnetic field and temperature T are schematically represented in Fig. 5 (based on [60, 61]).

Experimental studies on the magnetization structure and dynamics for different kinds of superconductors with different composition stoichiometry, of different shape and size have been carried out in many scientific centers [62] by means of magnetic neutron diffraction and magnetic decoration (under the electron microscope by coating the superconductor surface with tiny magnetic iron or nickel particles). They have allowed ‘visual’ illustration of these processes, including the emergence of intermediate-mixed (‘semi-Meissner’) state and assessing their energy performance.

Another coherent effect of superconductivity should be noted. It lies in the specific tunnel junction of superconducting pairs from one superconductor to another through a very thin dielectric layer separating them, when a current passed is less than the critical value, as well as in the voltage drop in their contact with the simultaneous emission of electromagnetic waves when a current passed is greater than the critical value [63, 64]. The effect was predicted in 1962 by B. D. Josephson [65] based on the BCS theory. It was confirmed experimentally for the stationary case in 1963 by P. Anderson and J. Rollo [66], although the same phenomenon of resistance disappearance in the small contact between the two metals during transition to the superconducting state was observed in 1932 by W. Meissner and R. Holm [4]. According to modern concepts [67], the microscopic mechanism for Cooper pair tunneling is associated with the so-called ‘Andrey’s’ reflection [68, 69] of quasiparticles localized in the potential well in the contact area. Thus, there is a change of signs of the effective mass and the charge carriers along with the transformation of an electron into a hole or vice versa and Josephson current value can achieve the value of a normal tunneling current through contact at the gap range stress in the superconductor energy spectrum [67].

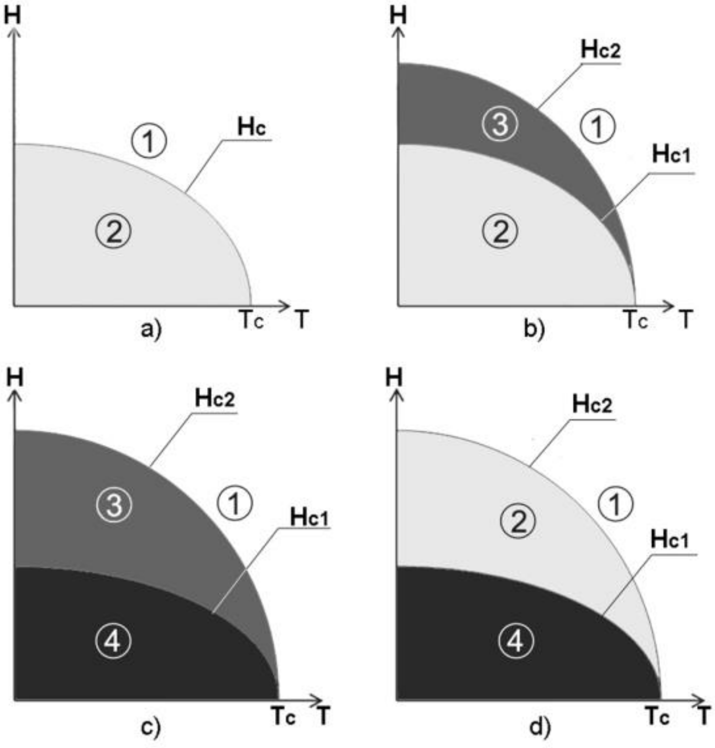

FIG. 5. Schematic state phase diagrams for various superconductors (based on [60,61]): a) type 1 superconductors; b) type 2 superconductors; c) and d) – probable phase diagram for type 1.5 superconductors in case of different two-gap state parameters. Diagram section 1 shows the normal state, section 2 shows the Meissner state (the Meissner phase), section 3 shows mixed, or vortex state (the Schubnikov phase), section 4 shows the state characterized by a non-uniform vortex lattice

3. Energy spectrum of superconducting materials, energy 'gap' and 'pseudo-gap' in HTSC

Along with the above mentioned macroscopic effects in superconducting materials, there are also transformations at the microscopic level in the form of changes in the atom energy spectrum. The usual set of discrete electron energy levels in each atom that are allowed by quantum laws, fissionable to very large number of sublevels due to the huge number of atoms interacting with each other in a solid, almost merges into a continuous spectrum. Its feature for metals at temperatures above the critical lies in blocking the area of free 'conduction' electrons (those having more energy) and the area of bound 'valence' electrons (having lower energy values), whereas in case of semiconductors and insulators, these areas are separated by an energy gap (a band gap where there are no electrons). The coupling of electrons into Cooper pairs in metals at temperatures below the critical Tc leads to the emergence in their energy spectrum of the 'superconducting' energy gap, symmetric with respect to the Fermi level, of about $\Delta(T) \sim 10^3 E_F$ width. It separates the equilibrium 'paired' electrons contained therein from other 'non-superconducting' particles which may be above or below the gap. This fact makes it different from the energy gaps in semiconductors or insulators where there are no electrons (Fig. 6).

Since the combined energy of a Cooper pair in the superconducting gap at the Fermi level is less than the total energy of two free electrons, in order to separate them back it is necessary to expend energy equal to the doubled gap energy $2\Delta(T) = 3.5kTc$, the value of which is determined by the critical temperature Tc. Therefore, the higher Tc is, the more energy is needed to break this pair. In this case, to break the rigidly connected system of all Cooper pairs an energy of $2\Delta(T)\eta_{coop}$ will be required. But at temperatures above the critical value, the superconducting energy gap vanishes, $\Delta(T) = 0$ and the Cooper pair density also becomes zero $\eta_{coop} = 0$. The type of dependence of the superconducting energy gap width on temperature is shown in Fig. 7 for Al ($Tc \sim$ 1.18 K) [38] and for YbB$_2$ ($Tc \sim$ 115 K) according to [72].

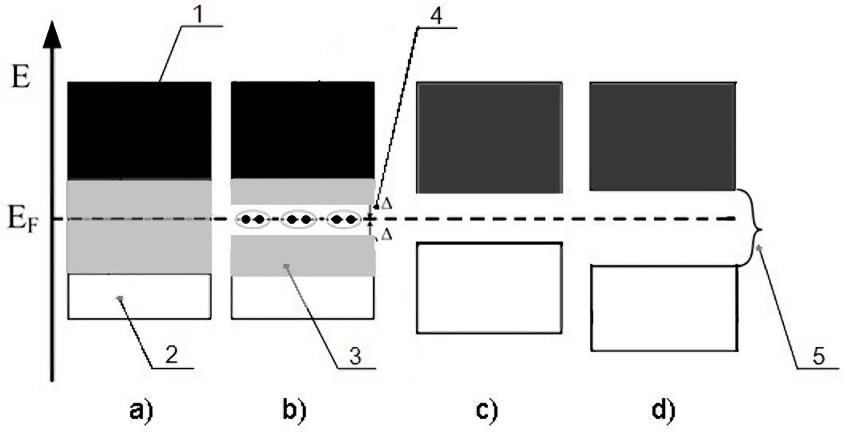

FIG. 6. Schematic image of the substance energy spectrum being in various states (based on Figures from [70, 71]): a) – low-temperature superconductor at temperatures above Tc (normal state) and a normal metal; b) – low-temperature superconductor at temperatures below Tc (superconducting state); c) – semiconductor; d) – insulator; 1 – conduction band, 2 – valence band; 3 – mutual intersection (overlap) of both bands; 4 – symmetric superconducting 'Δ and Δ' gap of the Cooper pairs (marked with ovals); 5 – band gap. E_F is for the Fermi level energy

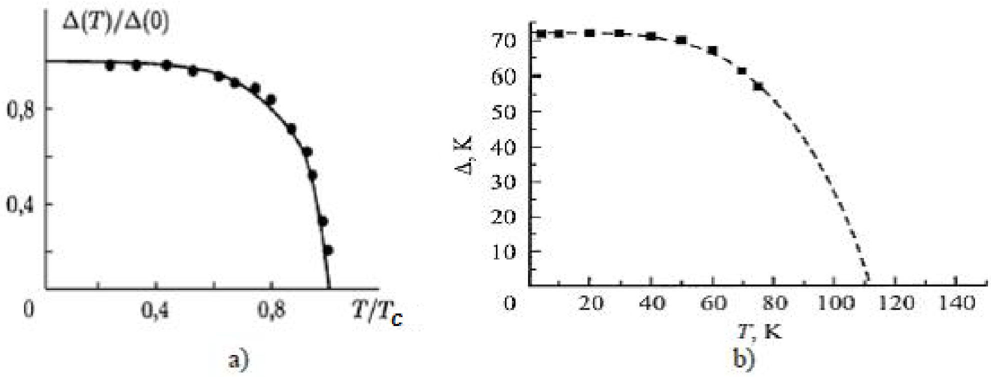

FIG. 7. The energy gap width dependence on the temperature: a) – for Al in relative units according to [38]; b) – for YbB_2 in absolute units according to [72]

The superconducting Cooper pairing has its own characteristics in samples placed in a magnetic field. This will happen in the case when the energy advantage of the transition from normal to superconducting state will exceed the energy cost caused by the displacement magnetic field. For type 1 conductors in fields which are larger than the critical value $Hc1$, the superconducting state is unprofitable and should be destroyed. However, as mentioned above, the possible distortion of the critical field due to the heterogeneous interaction with differently shaped conductor areas can lead to the simultaneous existence in the sample of sufficiently large areas of superconducting and normal phases separated by a substance in the 'intermediate' phase with the 'positive' surface separation energy obtained externally due to the supply of the magnetic field energy. At the same time, as noted above, when the field in the form of beams or individual vortex filaments penetrates into the type 2 superconductor, some of them may remain in such a superconductor in fields between $Hc1$ and $Hc2$, as well as in fields less than $Hc1$ and even in case of zero field if it is achieved by lowering from the area of larger fields, $H > Hc2$. Meanwhile, the conductor goes into the 'mixed' (metastable by nature) state along with preserving the superconducting properties and 'negative' surface separation energy into the largest possible number of normal and superconducting phases as a state that is energetically most favorable and does not require an external energy supply.

However, the presence of impurity of magnetic atoms in the conductor significantly reduces the critical temperature of transition to superconducting state until it is completely liquidated, whereas non-magnetic impurities have only a small effect on the transition temperature [26]. We also determined that in the case of superconductors with magnetic impurities, the energy gap magnitude becomes zero somewhat earlier than the superconductivity disappears, since their energy spectrum has pairs with different binding energy including that arbitrarily close to zero. Such gapless superconductors [73] are characterized by several unusual properties, in particular, a linear heat capacity dependence on the temperature, as in case of normal metals. Superconductors with magnetic impurities possess other interesting properties, for example, the theoretical possibility for the existence of a phase that is simultaneously superconducting and ferromagnetic, which can also enhance the superconducting transition temperature [74].

It should be noted that in spite of the significant theoretical results, there have not been notable achievements in the practical search of materials with high transition temperature for the superconducting state for a long time. The 'warmest' superconductors from a large number of metals and hundreds of alloys identified, up to 1986, were considered to be the intermetallic films of niobium germanide Nb_3Ge where $Tc = 23$ K. This value was the maximum one which had been managed to achieve for the critical transition temperature over 75-year research period, meanwhile the BCS theory did not predict the substances of a higher critical temperature. In the late 1960's to the early 1970's, great hopes were pinned on the organic complex synthesis with superconducting charge transfer, for example, complexes of TCNQ-TTF (tetracyanoquinodimethane-tetrathiafulvalene) [75–77]. However, despite the synthesis of a number of promising compounds, it was found that superconductivity in these complexes is unstable even at low current densities. Progress has become more significant only with introduction of the scientific paper by J. G. Bednorz and K. A. Muller who established in 1986, that ceramics of the La–Ba–Cu–O compound based on oxides of copper, lanthanum and barium (compound $La_{2-x}Ba_xCu_{04}$) becomes superconducting at a temperature of 30 K [78]. Yu. D. Tretyakov specified this issue in his article 'Chemical superconductors before the Third Millennium' [79] '...The most striking fact was that it was not any particular organic or polymeric structure, on which theoretical physicists had pinned their hopes, that exhibited superconductivity, but oxide ceramics which is typically characterized as dielectric or superconducting. However, the most amazing fact for experts was that the oxide compounds exhibiting superconductivity had been synthesized long ago. In 1978, this was made by the IONKh RAN (Kurnakov Institute of General and Inorganic Chemistry of Russian Academy of Sciences) staff, namely V. Lazarev, B. Kahan and I. Chaplygin who published their results a year later in the "Journal of inorganic chemistry (1979, v. 24. No. 6)".... They tried to investigate the synthesized samples but liquid helium was not available to them, likewise to the French researchers K.Michel and B.Pavo who synthesized similar and many other cuprates independently of their Russian colleagues. ...However, it goes without saying that Bednorz and Muller were not plagiarists, they discovered what they were purposefully and persistently looking for despite any predictions and theories'.

This discovery and the other one followed soon thereafter in 1987, concerning 93 K superconductivity in the Y–Ba–Cu–O system ($YBa_2Cu_3O_{7-x}$ compound [80]) stimulated the search for copper-containing superconductors with a higher temperature all around the world. In 1988, the superconducting transition temperature of cuprate series with alkaline earth metals without rare earth elements in the $Bi_2Sr_2Ca_{x-1}Cu_xO_{2x+4}$ compound synthesized by the Maeda group, reached 108 K [81, 82], and in case of cuprate materials in the Tl–Ba–Ca–Cu–O system ($Tl_2Ba_2Ca_2Cu_3O_{10}$ compound discovered by Sheng Z. Z. and Hermann A. M. in 1988) it was 125 K [83, 84]. The discovery of superconducting mercury cuprates in 1993 by S. N. Putilin and E. V. Antipov increased the transition temperature to 138 K ($HgBa_2Ca_2Cu_3O_{8+x}$ compound doped by Tl), and under external pressure of 350 thousand atmospheres, the transition temperature increases to 164 K (-109 °C) [85, 86]. It is only 19 K less than the minimum temperature registered on earth. To date, there are more than 50 known original layered HTSC-cuprates [79].

Although the use of metal superconductors instead of ceramic ones solved the problem of increasing Tc, it simultaneously created a problem of reduction of the critical Jc currents that destroy superconductivity. As noted by Tretyakov Yu. D. [79], the latter was the result of fundamental differences of metallic and ceramic superconductors. If the first ones are isotropic and have a coherence length of up to 20 nm, the second ones are highly anisotropic and their coherence length does not exceed 2 nm. As a result, in the polycrystalline condition, the crystallites' boundary in the ceramic superconductors is comparable with the coherence length and creates an effective barrier to the movement of magnetic vortices and increases the critical current, which is very important in technical applications, for example, to obtain strong magnetic fields. In particular, in the systems that generate, accumulate, and transport electric current, in magnetic cushion transport or in NMR-scanners, superconductivity must be maintained at currents of about 10^5 A/cm^2 in a magnetic field of 2 to 10 T, while the first samples of superconducting cuprates obtained using the traditional ceramic processes, had rather small critical current value of about $Ic \sim 1$ A/cm^2 [87]. Due to the high responsiveness of this parameter to the structural characteristics of superconducting ceramics, in order to prepare and treat it with heat, at the P. Makdgin's [79] suggestion they began to apply melt technologies used traditionally in the manufacture of metal but not ceramic materials. This became possible due to exceptional high fusibility of superconducting cuprates compared to the conventional oxide ceramics based on MgO, Al_2O_3 or ZrO_2. However, due to incongruent nature of melting (melting with decomposition where the solid phase is converted into a melt and solid phase of another compound), the melt product is not single-phased as a rule. However, the presence of inclusions of non-superconducting phases responsible for the emergence of additional pinning centers, i.e., braking of the magnetic vortices, contributes to a significant increase of superconductive stability in a magnetic field. In this case, the peak effect revealed in rare earth ceramic system Ln–Ba–Cu–O (Ln = La, Nd, Sm, Gd, Eu) [79], occurs at the same time. The nature of pinning associated with the peak effect, is fundamentally different from the pinning due to the introduction of hetero-phase non-superconducting inclusions. Based on the study of microstructural phase changes related the peak effect in the system, it is presumably associated with the formation of nanoscale areas of solid solutions at the original substance spinodal decomposition during formation and cooling of the melt enriched with barium and copper oxides [78]. The discovery of this effect gave rise to hopes for a radical improvement in technology and process parameters of superconducting cuprate materials which have recently been given considerable attention (see, for example, papers [88–91]).

Along with this, research was conducted on superconductivity of non-cuprate compounds, in particular, of Mg–B, Ba–Na–Ge, Na–WO_3 systems [31, 92–96], as well as iron compounds, ferronickel and iron selenides [97–110]. To date, there is a wide class of such materials which give new opportunities to further increase the transition temperature of the superconductivity with the simultaneous increase in the critical current value. These data give reason to believe that in case of both copper and non-cuprate superconductors, layered materials including nanostructured ones are the most promising.

The anisotropy of physical properties along and across the layers, which determines the peculiarity of the superconducting Cooper pairing, has been shown to play a special role in increasing temperature of the superconducting transition for all layered compounds [111]. In particular, discovered in 2001, superconducting MgB_2 compound of the alkaline earth metal Mg and wide bandgap semiconductor B with alternating magnesium and boron layers and a transition temperature of $Tc \approx 40$ K, a record for borides, has two superconducting gaps were predicted theoretically and confirmed experimentally [112, 113]. In quasi-two-dimensional Bor hole bands (σ-bands) the superconductivity transition forms a $\Delta E\sigma$ gap in the quasiparticle spectrum, which is a band of forbidden energies for single electrons and of holes with values of about 10 – 11 MeV at the maximum Tc. The superconducting gap $\Delta E\pi$, forbidden band of approximately 1.5 – 3 MeV width, is also formed in three-dimensional magnesium bands (π-bands). The interaction of these two 'varieties' of Cooper pairs in two-band MgB2 material with the double-gap superconductivity ensures a high Tc. As noted above, the doping leads to a decrease in the critical transition temperature Tc while increasing the critical current [92]. High-temperature superconducting state was also experimentally observed on surfaces of alkali metals, in particular, localized spots of the surface superconducting phase were found on the superficially doped crystal of Na–WO_3 at a critical temperature of 91.5 K [94, 95].

An alternating layered structure is also characteristic for a new class of high temperature superconductors discovered in 2008 by a H. Hosono's group [97, 98], i.e. layered iron compounds and pnictides (group V elements in the periodic table: nitrogen, phosphorus, arsenic, antimony, bismuth, etc.), or chalcogenides (group VI, main subgroup elements: oxygen, sulfur, selenium, tellurium, polonium). Compounds $LnFeAsO_{1-x}F_x$ (Ln= La – Gd), in particular, $La[O_{1-x}F_x]FeAs$ where $Tc = 26$ K [97, 98], $Sm[O_{1-x}F_x]FeAs$ where $Tc = 55$ K [99], $Nd[O_{1-x}F_x]FeAs$ [100], $Gd_{1-x}Th_xFeAsO$ where $Tc = 56$ K [101] were synthesized on this basis, demonstrating for the first time the superconductivity of materials containing magnetic components of Fe atoms in alternating layers, despite screening by a tetrahedron of As or Se atoms. Subsequently, superconducting Fe compounds were synthesized with Ce, As, F, As, K, Se, Te, Rb, K, Na and other elements [102–108].

The energy spectrum of each band in substances with such multi-band structure has its own gap, which leads to at least two superconducting bosonic condensates and multi-gap superconductivity similar to the case of magnesium diboride [109–112]. The presence at the Fermi level of two conduction electron types (π- and σ-electrons) of different dynamical (effective) mass which is manifested in the particle motion in the electric field of the crystal lattice of each structural area of such material, leads to different width of each of the superconducting energy gaps $\Delta\pi$ and $\Delta\sigma$, to different superconductivity types (type 1 for paired π-electrons and type 2 for σ-electrons), and to the divergence of other coherence characteristics. Now there are several collections of iron-based superconductors, including new compounds created in FIAN (P. N. Lebedev Physical Institute of the Russian Academy of Sciences) from barium, iron and 122-type arsenic. The materials of this group are being studied very actively now, their production is simpler than the synthesis of their analogues in other collections, for example those consisting of gadolinium, arsenic, iron, and oxygen, such as GdOFeAs doped with fluorine which replaces the oxygen [113].

In accordance with the early theoretical two-gap superconductor models proposed by V. A. Moskalenko and H. Suhl [114, 115] independently, without interband interaction, both gaps behave accordingly with BCS theory and become zero at their own critical temperatures Tc^L and Tc^S. And by having this interaction as shown by experiments [116, 117], both gaps go to zero when a $T = Tc$ is the same and when $T < Tc$, one of the gaps is more than the BCS-value and the other is less (Fig. 8).

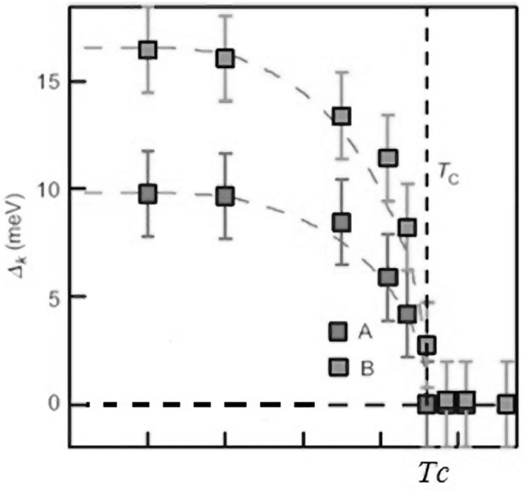

FIG. 8. The superconducting gap dependence on temperature in the two-gap HTSC $Bi_2Sr_2CaCu_2O_{8+x}$ [117]

During further development of the theory (I. I. Mazin, [118]) they proposed an alternative mechanism of Cooper pair formation, based on the magnetic resonance of dynamic magnetic susceptibility and then they suggested the interband interaction model for spin and even orbital fluctuations [120].

Type 1 and 2 phase transitions occurring in the two-gap superconductors with increasing temperature, change state with a non-uniform vortex lattice to a state with a regular (triangular) vortex lattice depending on the external magnetic conditions, then the condition of unevenly spaced vortices with a non-uniform vortex lattice can be observed again and, finally, they change to the Meissner state [121]. These phenomena, discussed above in connection with the superconductor transitions from one type to another when the magnetic field is changed, cause a very unusual kind of hysteretic magnetization curve (Fig. 9).

The specificity of ‘iron’ superconductors lies in the fact that in superconductivity, they exhibit another, antiferromagnetic, phase transition which transforms the magnetic moments of the substance’s atoms (in this case neighboring Gd atoms) into the state of oppositely directed and equal in magnitude, which reduces the total material magnetization to zero. This magnetic condition is opposite in a way to a condition of the ferromagnetic materials where, if the temperature is below a certain critical value (the Curie point), magnetic moments of all atoms are directed in one way resulting in the ability to become magnetized in the absence of an external magnetic field. The substance becomes antiferromagnetic at the temperature being below a certain T_N value (called the Néel point) and remains antiferromagnetic up to Tc. It should be noted that the anti-ferromagnetism emerges in these and many other compounds at high temperatures as a phase that precedes superconductivity at a higher temperature, or in the ‘ancestor’ non-doped compounds. As a number of theorists believe, this means that the ‘glue’ that connects the electrons into superconducting pairs, is their interaction with magnetic fluctuations [122].

In 2009 – 2014 anoxic iso-structured layered selenides $A_xFe_{2-Y}Se_2$ (A= K, Rb, Cs, Te, Tl etc.) were obtained, among which there are superconducting compounds [104–108,123]. Superconducting properties are found in the β-phase of iron monoselenide $FeSe_{1-\delta}$, with a significant non-stoichiometry of the chalcogen $\delta \sim 0.18$. From the phase diagrams of the system Fe–Se–Te, it follows that tetragonal modification of the β-phase is stable at temperatures ranging from room temperature to $\sim$ 844 °C, while that in the system Fe–Se is stable to $\sim$ 457 °C (Fig. 10, [124]). To obtain SC-samples in the Fe–Se and Fe–Se–Te(S) systems, both standard material science methods and less time consuming ways of obtaining poly- and monocrystals [125]. FeSe has a much simpler crystal structure, but it has many of the same magnetic and electronic properties (including superconductivity) as the iron-based pnictide superconductors (Fig. 11, according to [126]).

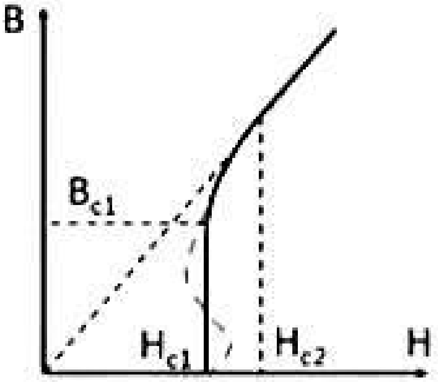

FIG. 9. The magnetic induction dependence on the magnetic field applied and the magnetization hysteresis for two-gap superconductors (schematically, according to numerical simulation of systems such as MgB_2 and layered Fe-containing compounds [121])

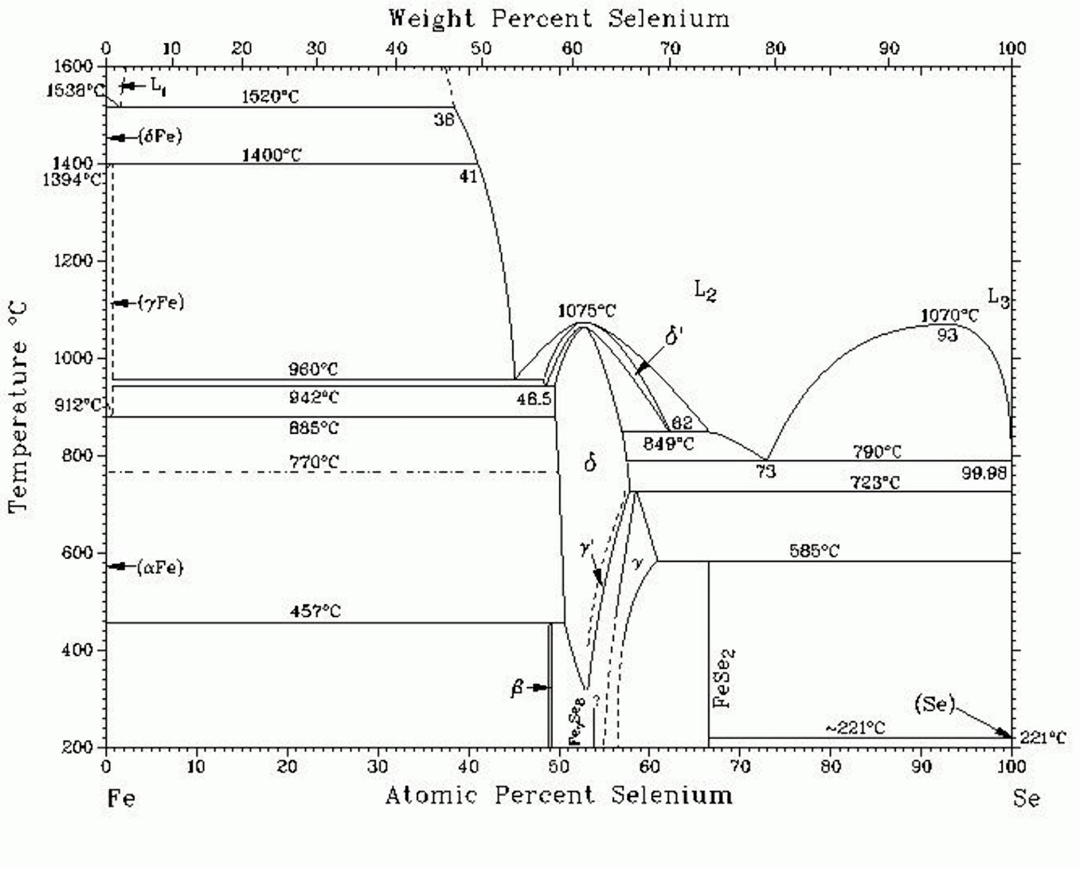

FIG. 10. The phase diagram of the system Fe–Se according to [124]. Superconducting properties are found in the β-phase of iron monoselenide $FeSe_{1-\delta}$

The critical magnetic field which such compounds are able to withstand while remaining a superconductor, according to experts from FIAN (P. N. Lebedev Physical Institute of the Russian Academy of Sciences) is a great value about 130 T [38]. This parameter, in addition to the other two (Tc and Jc), is very important for technical applications. As for the new compounds, it almost matches the achieved value of $Hc2 = 100$ T for the most studied

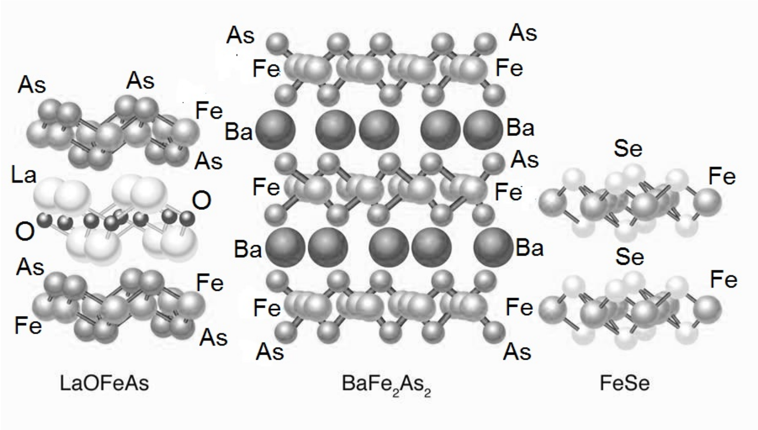

FIG. 11. Comparison of the crystal structures of the iron-based pnictide superconductors on the example of LaOFeAs (left) and $BaFe_2As_2$ (center) and FeSe (right), based on [126]

TABLE 1. Electrical and technical specifications of some commercially available superconductors (according to [38])

Compounds	Tc, K	Jc, A/cm^2 at 4.2 K	Hc, T at 4.2 K
NbTi	9.5÷10.5	(3÷8) 10^4	12.5÷16.5
Nb3Sn	18.1÷18.5	(1÷8) 10^5	12÷13
NbN	14.5÷17.8	(2÷9) 10^7	8÷13 (25 at 1.2 K)

TABLE 2. Parameters of some HTSC materials (based on [128, 129])

Compounds	Tc, K	Number of CuO_2 layers
$La_{1.85}Sr_{0.15}CuO_4$	40	1
$YBa_2Cu_3O_7$	92	2
$Bi_2Sr_2CaCu_2O_8$	95	2
$Bi_2Sr_2Ca_2Cu_3O_{10}$	115	3
$Tl_2Ba_2Ca_2Cu_3O_{10}$	122	3
$HgBa_2Ca_2Cu_3O_8$	134	3

cuprate superconductor Y–Ba–Cu–O having almost twofold critical temperature of 92 K ($YBa_2Cu_3O_7$ compound) and $Bi_2(Sr_2Ca_2)Cu_3O_{10}$ having $Tc = 110$ K but considerably lower critical current. Meanwhile the maximum magnetic field obtained by the 'traditional' commercially available superconductors (NbTi, Nb_3Sn and NbN) is now fivefold smaller and only reaches 25 – 28 T (Table 1 [38]).

The theoretical assumptions concerning the definite role of increasing the number of layers for enhancing the critical Tc temperature, made on the basis of the effect of Josephson tunneling of Cooper pairs between the layers of HTSC materials [127], initially received an experimental confirmation in experiments with the homologous cuprate series (Table 2, based on [128, 129]).

Along with this, without using any behavior patterns for electrons in a normal or superconducting state, in his study, A. J. Leggett [129] derived a simple formula for estimating the critical temperature change depending on the n-number of CuO_2 layers in HTSC families of the same structural type in comparison with a single-layer specimen from the same homologous series as the inequality $Tc^{(n)} - Tc^{(1)} = To(1 - 1/n)$, where To is an individual constant for each family. In particular, this formula results in $[Tc^{(3)} - Tc^{(2)}]/[Tc^{(2)} - Tc^{(1)}] = 1/3$, which was consistent with the available experimental data 0.25 – 0.34 for homologous series of cuprate HTSC having a number of layers $n = 2$ and $n = 3$ (see, for example, Table 2).

However, the subsequent experiments with a multi-layered metal oxide HTSC [130, 131] by methods of scanning quantum-interference microscopy (SQUID) and nuclear magnetic resonance (NMR) showed that the

Josephson's interlayer tunneling is not a basic mechanism for high-temperature superconductivity. The bell-shaped curve $Tc(n)$ with the cascading branch when increasing the layers number greater than $n > 3$ and the redistribution of charge carriers from 'internal' to 'external' layers within one unit cell was also identified. The proposed theoretical model, that takes into account the last factor on the phenomenological level [132], describes the behavior of $Tc(n)$ with a maximum at $n = 3$ quite well (Fig. 12).

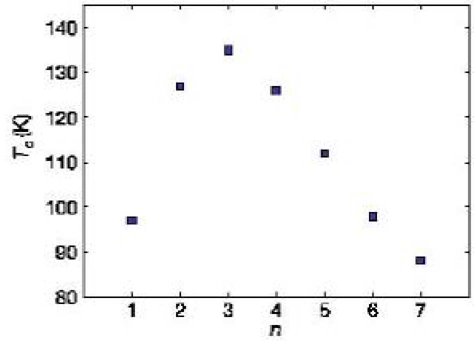

FIG. 12. The temperature dependence of the superconducting transitions on the number of CuO_2 planes in the unit cell (schematically, according to [129] for homologous series of $HgBa_2Ca_{n-1}Cu_nO_{2n+2+\delta}$)

It should be noted that the nature of superconductivity in high-temperature materials produced is still not fully clear. They are not 'conventional' superconductors in terms of the Bardeen–Cooper–Schrieffer theory, for which the predicted critical temperature should not exceed the above limit of about 40 K (−233 °C), and the prospects in this area for achieving even a higher transition temperature are not clear. However, according to this theory, all that is required to achieve a high Tc is a favorable combination of high frequency phonons, strong electron-phonon bonding, and high density of states [133]. As recently shown by A.P. Drozdov, M.I. Eremets, I.A. Troyan, V. Ksenofontov and S.I. Shylin [134], these conditions can be theoretically fulfilled for metallic hydrogen and covalent hydrogen-dominated compounds. This idea was confirmed by computational studies predicting the transition temperature in the range of 50 – 235 K for many hydrides, in particular for hydrogen sulfide (H_2S), which is transformed to a metallic state at a pressure of 90 GPa, and the critical temperature for transition into the superconducting state depends on the temperature at which the sample becomes compressed. The results of experimental studies concerning the influence of these factors on the hydrogen sulfide's resistivity and the transition temperature obtained by the authors in 2015 are shown in Fig. 13.

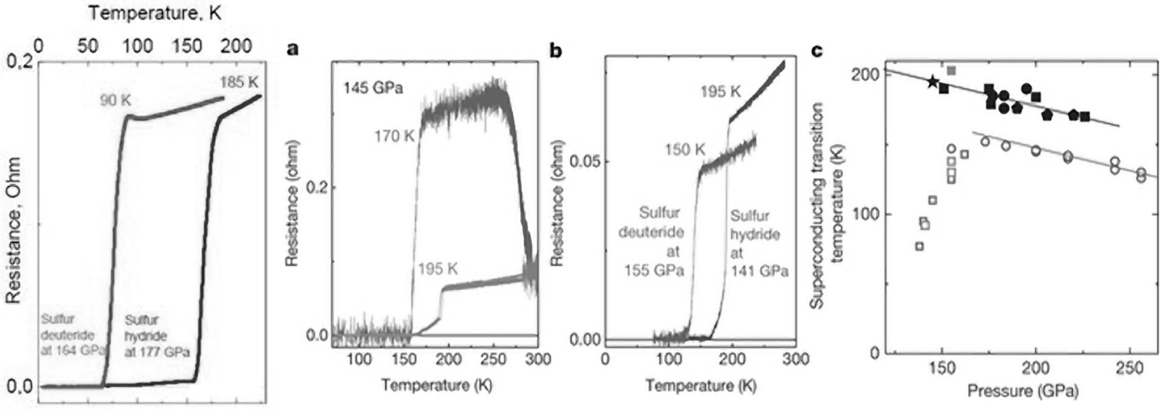

FIG. 13. The effect of sample pressure and temperature before compression on the electrical resistance and critical temperature of sulfur hydride and deuteride transition into the superconducting state (Figures taken from [134])

In their experiments, they recorded a new supercritical transition Tc temperature of about 203 K (or −70 °C) exceeding the previously noted record Tc level of 164 K (−109 °C) of 'unusual' (in the above sense) mercury-containing superconducting cuprates for the compound $HgBa_2Ca_2Cu_3O_{8+x}$, which was achieved at an external pressure of 35 MP. The ‘normal’ hydrogen sulfide (H_2S) was compressed at high pressures of about 153 GPa and a temperature of more than 220 K, and, according to the authors, the superconducting transition was due to the formation of H_3S from H_2S by decomposition under pressure and strong isotopic shift of normal hydrogen to deuterium with the formation of D_2S. The hydrogen sulfide transition into the superconducting state is confirmed by direct measurements through the presence of the Meissner effect using the method of nuclear resonant scattering of synchrotron radiation by the independent international research team [135]. There are predictions on the possibility to further increase Tc in the hydrogen sulfide based materials, for example, by replacing some sulfur atoms with phosphorus, platinum, potassium, selenium and tellurium; these predictions stimulate new directions of research on the hydrides superconductivity [135–139].

The above data on critical temperatures at which range of materials become superconductive, are compared to some characteristic temperatures in natural conditions in Fig. 14.

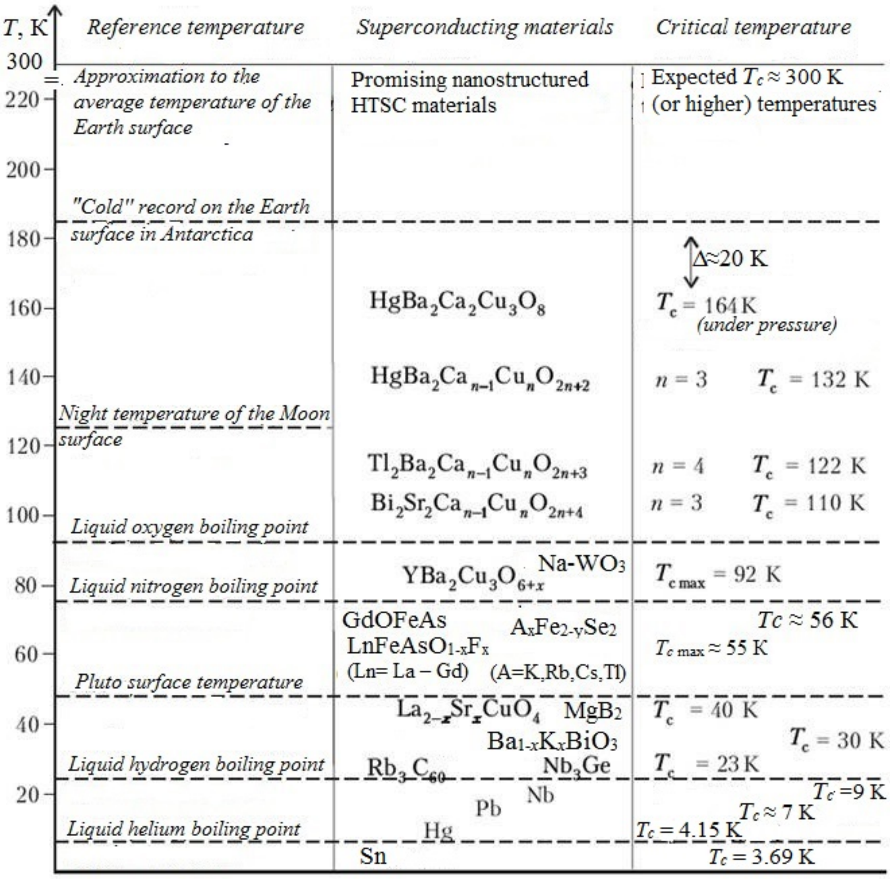

FIG. 14. Comparison of critical superconducting transition temperatures of some materials with representative temperatures existing in natural conditions (based on [29])

There are still no generally accepted results for the synthesis of more high-temperature superconductors, although there was some information about superconductivity in the materials based on diamond and other systems at a critical temperature close to room temperature [136–138]. At the same time, using different experimental techniques [139, 140] it was recorded that there is another energy gap emerging at a temperature above the critical, which was called as a ‘phony’ gap or a ‘pseudo-gap’ because of its inexplicable origin [30, 137–143]. A number of researchers explain its appearance with the phase transition to a special ‘pseudo-gap’ state, and various hypotheses of the phenomena occurring during this process are considered in the proposed models. For example, it is argued that at temperatures above Tc, Cooper pairs are not destroyed but only lose their coherence, i.e. lose the connection between them [144], or that a pseudo-gap at above the superconducting transition temperature appears due to the influence of clusters of superparamagnetic or antiferromagnetic ordering as a kind of ‘magnetic glue’ which occurs when a high-temperature superconductor is not doped or poorly doped with charge carriers [145]. It is also thought that such a mechanism lies in the formation of spin- or charge-density standing waves involving magnetically ordered structures of indirect exchange via the conduction electrons in their organization, leading to the formation of virtual quasi-localized states, but other ideas exist as well [143–148].

It is worth mentioning the opposing view of the same large number of researchers that see no relation between transition into the pseudo-gap state and any phase transition and explain it by suppression of the electronic states density of one-particle excitations near the Fermi level. This is indicated, in particular, by typical dependence of the superconducting gap characteristics on the external magnetic field, whereas the pseudo-gap practically does not depend on it [149, 150]. This is evidenced by, for example, the data in the papers [117] and [151] which together show that at $T = T^* > Tc$, a large spatially inhomogeneous gap (pseudo-gap), irrelevant to superconductivity, is formed in HTSC, while at $T = Tc$, the superconducting gap is formed, which is uniform and much smaller in size.

These contradictions show that the authentic origin of the pseudo-gap is still unclear.

4. Energy 'pseudo-gap' as an independent phase transition in high-temperature superconductors

It is possible to distinguish the relationship of the energy pseudo-gap occurrence accompanied by formation of local incoherent Cooper pairs from other, competing with this, conditions by availability (in case of superconductive pseudo-gap) or absence (in another case) electron-hole symmetry of its energy spectrum relative to the Fermi level. However, it is clear that regardless of the specific mechanism, the emergence of the energy pseudo-gap can be considered as an independent phase transition in the substance prior to the transition to superconductivity in HTSC. Experimental evidence for this fact was presented by a large group of specialists from several research organizations in Japan, USA and Thailand [140]. Using a scanning tunneling microscope, they found that a significant role for the occurrence of this state is played by a critical level of doping of the superconductor $Ca_2CuO_2Cl_2$ with sodium atoms, beyond which the material becomes superconducting at a rather high temperature. It was also revealed that when doping the original superconductor with sodium at very low levels, the atoms were observed to form in nanometer clusters which always appear during the pseudo-gap formation [152]. At the same time as the sodium atom concentration was increasing, their individual clusters began to merge gradually and when they were completely coupled, the material demonstrated the properties of superconductor.

The spontaneous appearance of thermodynamically non-equilibrium Cooper pairs (superconducting fluctuations) at temperatures above Tc results in, compared to conventional one-electron mechanism, the additional charge transfer known as 'Aslamazov–Larkin contribution' [153, 154], as well as excess conductivity, or paraconduction [155]. Herewith, its conductivity and heat capacity, sound absorption factor, thermal EMF, Hall coefficient, anomalies of tunneling transition current-voltage characteristic, diamagnetic susceptibility and other phenomena can be significantly increased even in the normal phase of the superconductor material in the immediate vicinity above Tc. However, when the superconducting transition temperature is reached, the expected superconducting fluctuations, a consequence whereof is the effect of superconductivity, are not only suppressed but may be missing at all.

The common feature of all cuprate HTSC families with different types of doping is a bell-shaped critical Tc temperature dependence on the x-concentration of charge carriers (with a maximum at $x_{opt} \sim 0.2$ for p-doping and at $x_{opt} \sim 0.15$ for n-doping), as presented on the generalized phase diagram (Fig. 15) using papers [111, 156].

Considered in [157], the original explanation of this dependency within the theory of Josephson tunneling of Cooper pairs between CuO_2 layers which, as already noted, also predicted an increase in Tc with increasing number of CuO_2 layers in the unit cell [127], is not consistent with the above bell-shaped Tc dependence on the number of layers with a maximum at $n = 3$ (see Fig. 12). The latter assumption about the relation of the possible mechanism of both effects with the 'Andreev' reflection is indirectly confirmed by the aforementioned NMR data in cuprate HTSC [131] which showed that in case of a large number ($n > 3$) of CuO_2 layers, charge carriers are distributed non-uniformly, their concentration within a single unit cell in the 'internal' layers is smaller than in external ones. The results of the numerical modeling of these phenomena [158] based on phenomenological representation of the free energy of the system as a function of two interacting order parameters, superconducting and non-superconducting, indicate their possible connection with a certain ordering (probably, that of charge density waves) that competes with superconductivity. According to this widely discussed hypothesis in the literature (see, e.g., reviews [143, 144, 157]), the latter also determines the appearance of the pseudo-gap. In the above phase diagram (Fig. 15) it is located in the area of the current carrier concentration which is less than optimal and corresponds to the maximum Tc temperature, and reveals itself with a number of anomalies in their electronic properties in both normal and superconducting state. Due to the reduced carrier concentration in 'internal' layers of a multilayer unit cell, the pseudo-gap size is large in these layers, and the actual superconducting order is suppressed, which leads to decrease of Tc when $n > 3$. This conclusion from modeling results confirms the competing contribution of the phenomena considered to the formation of superconducting correlations; however, it does not clarify the underlying mechanism of high-temperature superconductivity, by which, in particular, only

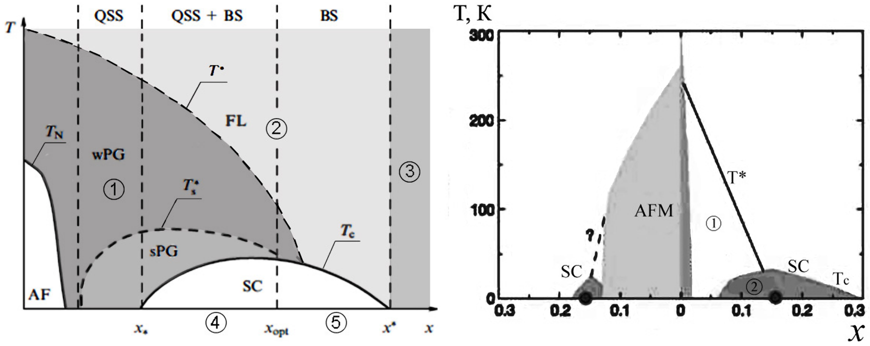

FIG. 15. Typical phase diagrams for cuprates of different hole and electron doping x-levels (according to [111, 156]): a) – only hole doped (p-type); b) – both n-doped (on the left, for the (La,Pr,Nd)$_{2-x}$Ce$_x$CuO$_{4-y}$ compound) and p-doped (on the right, for the La$_{2-x}$Sr$_x$CuO$_{4-y}$ compound). The figures indicate the following: 1 – a zone of incomplete doping, 2 – a zone of optimal doping, 3 – a zone of excessive doping, 4 and 5 – zones of poor and heavy doping, respectively. The letters indicate the following: FL – the normal Fermi-liquid area (normal phase); SC – the superconductivity area (the superconductivity phase); PG – the pseudo-gap phase area; sPG and wPG – strong and weak pseudo-gap areas, respectively; BS and QSS – areas of bound and quasi-stationary states of Cooper pairs, respectively, QSS+BS – area of their coexistence; AF and AFM – anti-ferromagnetism areas (antiferromagnetic phase); QCP – quantum critical point. Specific temperatures: Tc – the superconducting transition temperature; $T*$ – the pseudo-gap transition temperature; $Ts*$ – the temperature of strong and weak pseudo-gaps crossover; T_N – the antiferromagnetic transition temperature (the Néel temperature), x – the doping level

a single CuO$_2$ layer is superconducting. The question also remains open in terms of how to achieve a relatively uniform distribution of carriers in the layers so that the pseudo-gap deterring the critical temperature growth in superconducting macro-structures would not appear because of their unbalance.

5. Peculiar properties of nanostructure superconductivity

The possibility of superconductivity in metallic and non-metallic systems, and even in organic compounds at high temperatures was substantiated by V. L. Ginzburg [22, 28] and W. A. Little [75–77]. They believed that the creation of room-temperature superconductors (RTSC) is one of the most important problems in the field of nanotechnology.

Fundamentally, this technology can be implemented by depositing atomic layers, for example, by atomic layer deposition (ALD), first proposed by V. B. Aleskovski in the mid-twentieth century [159, 160] and usually called as the method of molecular layering (ML) in the Russian scientific literature [161]. The specificity of this method lies in the possibility of forming a molecular or atomic monolayer on complex-shape substrates without forming three-dimensional nuclei by cyclic alternate supply of gaseous (MOCVD – Metal Organic Chemical Vapor Deposition) or liquid (with subsequent pyrolysis – MOD – Metal Organic Deposition) precursor reagents of the buffer layer and the base material to the substrate in a way that the chemical reactions leading to the film growth occur only in chemisorbing layers, that is, with the exception of reactions in the gas phase. Meanwhile a given increase in the thickness of the formed film is easily and accurately controlled by the number of deposition cycles using the ability for self-organization (self-restraint) of surface reactions culminating automatically with the exhaustion of all reactive sites on the surface.

Another technological approach to produce the HTS conductors is the layer deposition in vacuum using the laser method (PLD – Pulsed Laser Deposition), electron or ion beam (Electron beam Deposition or Sputtering) and magnetron sputtering. Here, a high-temperature superconducting layer is deposited by ablation. When this technology is used, superconducting compound molecules or clusters, instead of individual atoms, should be transported from the target to the substrate and deposited on it [162, 163].

The mixed technology can be applied, for example, the buffer layers are applied by sputtering, and the HTSC layer is applied by chemical means.

In general, this enables the construction of both *2D*-layered and *3D*-dimensional superconducting nanostructures which are unique in terms of reproducibility and high conformity of the formed layers, thickness and density uniformity, number of defects, stoichiometric composition. A large variety of conductors and dielectrics can be used to generate the required electron-phonon spectra and obtain the superconductivity effect at a high temperature.

However, the existence of the superconductivity at high critical temperature in amorphous metal nanofilms [164] and in a number of nano-carbon substances synthesized based on insertion of the potassium atoms into fullerenes and nanotubes and the doping of a fullerene crystal with tribromomethane molecules [165, 166] shows that to obtain the superconductivity, the availability of an ordered structure similar to the layered cuprates or ferrous compounds is not required [167]. High-temperature superconductivity is typical of many other nanostructures. For example, it is typical of ultrathin NbC films and films from the aforementioned magnesium diboride, $\mathrm{MgB_2}$ [168], ultra-narrow silicon (Si) quantum p-wells bounded by δ-barriers and heavily doped with boron [169], copper-containing fullerene quantum-well samples of endohedral nanostructures with the included element atom location inside the carbonic structure [170] and also of other nanostructures limiting the charge carrier movement in one, two, or three dimensions.

Discrete quantization levels of the charge carrier energy resulting from these limitations give rise to a great diversity of the superconductivity characteristics in the nanostructures compared to bulk samples of the same materials and open up opportunities for creating new materials as well. Thus, research on dependence of a critical value of the parallel $Hc_{\|}$ magnetic field for thin nanofilms superconductors NbC and $\mathrm{MgB_2}$ on their thickness and the mean free path of the electrons showed that at low temperatures the critical $Hc_{\|}$ field can significantly exceed the critical Hc_2 field [168]. In case of NbC films, near the Tc critical temperature, the parallel critical $Hc_{\|}$ field varied depending on the film d thickness in proportion of $\sim\ (1/d)^{3/2}$, which is also the case for pure superconductors [171] and the observed temperature dependence of $Hc_{\|}(T)\ \sim\ (1-T/Tc)^{1/2}$ satisfy the superconductor vortex-free condition in the whole temperature range below Tc. In a perpendicular magnetic $Hc^{\perp}$ field, in case of both type 1 and 2 thin and ultra-thin superconductor plates being of thickness that is much less than the London penetration depth, the Meissner and the transport currents are almost constant by thickness. This leads to the transformation of the Abrikosov vortex into the so-called Pearl vortex [172] where the motion's speed can reach 103 cm/s [173], as well as to the effect of local variations in the magnetic field direction (the 'vapor trail' in a magnetic field and even the 'contrail precursor' accompanying this vortex [174–176]). This effect reveals under the action of Lorentz force while passing both direct and alternating transport currents which make the vortices move uniformly or oscillate, and therefore, either keep fixed the shape of distribution of the vortex magnetic field in time or change it during the oscillation period while maintaining the general character of distribution (Fig. 16). Since the inversion of the longitudinal magnetic field component makes the vortices pull towards each other [177, 178], the moving Pearl vortices in thin films of superconductors are arranged in chains which can be observed in magneto-optical experiments.

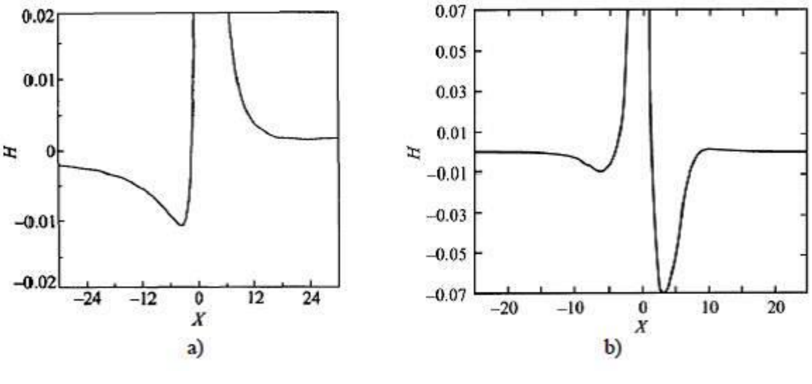

a) b)

FIG. 16. The distribution of stationary (a) and flash (b) magnetic field $H = 2\pi\lambda^2 Hc \perp /\Phi_0$ with respect to $X = x/\lambda$ in the direction of motion, respectively, for a uniformly moving Pearl vortex [174, 175]; the minima correspond to the 'inversion precursor' in front of and to 'vapor trail' behind the vortex center. Herein, x is for the distance from the vortex center, λ – the London penetration depth, Φ_0 – the magnetic flux quantum

Similar effects are also seen in the above-mentioned strongly anisotropic layered high-temperature superconductors, where the vortex structure is presented by vortices of two types, the properties of which differ markedly. The internal magnetic flux perpendicular to the superconducting layers is formed of point vortices merging into chains perpendicular to the layers, similar to Pearl vortices in thin films. Parallel to the layers, the magnetic flux is formed from vortices which are similar to vortices in tunnel transitions being parallel to the transition plates. The interaction between these vortices and the formation of composite vortices, which contain vortex segments of both types, leads to a complex dynamics of magnetic flux in strongly anisotropic layered superconductors [179].

Great opportunities to produce different types of self-ordering nanostructures such as quantum wires and crystallography-oriented quantum dot systems are provided by means of a method of molecular beam epitaxy [180], as well as ion implantation and non-equilibrium impurity diffusion methods [181]. As the method of atomic layer deposition (ALD) [182], they are widely applied in modern technology of semiconductors and nanoelectronics in the synthesis of other functional materials in planar technology [183–185]. In particular, created on this basis, the silicon sandwich nanostructures on the Si(100) n-type surface which are ultra-narrow silicon quantum p-wells with high current carrier mobility, bounded by heavily boron-dope δ-barriers, show high-temperature superconductivity with $Tc = 145$ K and the superconducting gap value of 0.044 eV [186]. As the authors suggest, superconductivity arises as a result of the transfer of hole (p-type) bi-polarons of small radius through the dipole boron centers with negative correlation energy at the 'silicon quantum well – δ-barrier' boundary. To create them, the fractal self-organization of the initial micro-defect distribution on the surface of oxidized single-crystal silicon [187] is applied; this process recurs during the quantum wells self-organization and, apparently, is a 'Sierpinski wipes'-type fractal modification [188] with an incorporated longitudinal silicon self-ordered quantum well (Fig. 17).

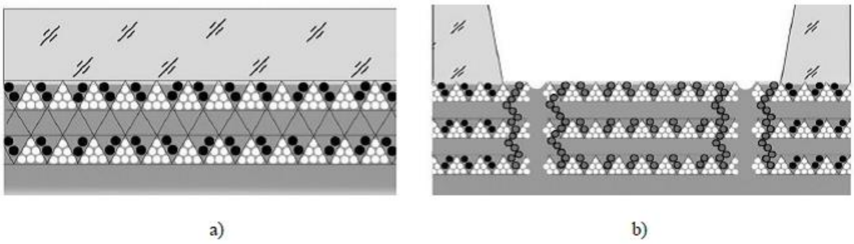

FIG. 17. The diagram of self-ordered silicon wells produced on Si (100) surface under conditions of injection of the proper silicon interstitial atoms (white circles) and vacancies (black circles) during pre-oxidation (a) and subsequent micro-defect passivation under short-time boron diffusion by the vacancy mechanism (dark areas) (b) according to [187]

The superconductivity in *3D*-fragments of carbon deposits with a high content of multivariable spatial nanotubular structures were discovered by V. I. Tsebro, O. E. Omel'yanovskii, and A. P. Moravskii from the Physical Institute of RAN (FIAN) (P. N. Lebedev Physical Institute of the Russian Academy of Sciences). They discovered almost undamped currents and magnetic flux capture at liquid helium temperatures, just as it occurs in a multivariable superconducting structure, moreover, the captured magnetic flux was damped very slowly even at room temperature [189].

Predicted theoretically, the phenomenon of oscillations in the critical temperature of the superconducting transition in the form of reentrant superconductivity in layered 'superconductor - ferrimagnet' nano-hetero-structures based on niobium and copper-nickel alloy is experimentally confirmed [190]. It may be considered as a direct proof that the inhomogeneous Larkin–Ovchinnikov–Fulde–Ferrell superconductivity (the above mentioned FFLO phase) occurs in the context of anomalous manifestation of the mechanism of 'paramagnetic' superconductivity destruction. In these experiments, samples of atomically-smooth thin film structures, produced using the known method of vacuum magnetron sputtering, were used.

The anomalous temperature-dependent diamagnetism existing within the range of room temperature to 750 K is discovered in aerosol-generated nickel oxide nanoparticles which were studied at the Institute of Structural Macrokinetics and Materials Science of the Russian Academy of Sciences during the crucibleless synthesis in the levitation-jet generator [191–193]. This effect is associated with the emergence of superconductivity on the surface of nanoparticles of averagely 10 to 30 nm in size and with different content of metallic nickel clusters. It was found that the thickness of the superconducting surface layer is independent of the particles size and is about 6 nm (approximately 30 atomic layers); however, in case of smaller particles, the anomalous diamagnetism disappears completely at room temperature. Evaluation of the second critical field for the superconductivity vanishing indicates the expected value of at least 15 T at 300 K. Further consolidation of powder of these particles with the above-mentioned magnetic behavior peculiarities was also studied applying the method of laser sintering under conditions ensuring the preservation of the superconductivity in the individual nanoparticles [194].

A promising way to create such layers with nanometer and sub-nanometer thicknesses and precisely-controlled chemical composition on the nanoparticle surface is the synthesis of composite ‘core-shell’-structured nanoparticles. Both the above mentioned ML-ALD method of chemical layer deposition [195] and the method based on self-organization of nanoparticles of variable composition can be used for this purpose, for example, during the formation thereof in hydrothermal conditions due to displacement of the excessive components in composition from the resulting solid ‘core’ solution to a ‘shell’ that surrounds it [196–198].

The following progress of such technologies to achieve compact nanostructured superconducting materials is interconnected with both the development of new methods for the synthesis of ‘core-shell’ nanoparticles and new sintering methods in parallel with the study of individual nanoparticle interactions in the consolidated system. To solve the said problems and the problem of formation of nanomaterial structure and properties in general, the non-autonomous phases and corresponding non-autonomous substance condition play a particularly important role [199]. They are formed at the joints between macro-volumes of a substance as an intermediate transition surface or internal structures where a composition, a structure and properties are determined by space or mass limits, and which cannot exist as a separate thermodynamic phase. Apparently, the definition of a non-autonomous substance condition was given for the first time by Defaye and Prigozhin in their papers [200, 201] in order to thermodynamically describe a substance which is localized in the boundary areas of volume phases and differs from them by its unique state equation (phase equation, according to J. W. Gibbs’s terminology). The concept of ‘non-autonomous phase’ was used most successfully to describe the solid-phase processes (see for example [202–205]), although this approach also shows promise in the description of processes in the area of solid, liquid and gaseous phase contact [206–208]. Herewith, nanometer-scale environments with spatial limitations in one or several primary directions, where the walls neither exchange substance nor interact chemically with the substance localized in their limited space, can be considered as nano-reactors. The dimensional change of reaction zone affects the chemical or phase transformations occurring there (a known effect of reactor process scaling [209, 210]. It is characterized by highly quick mass transfers in nano-reactors compared to their macro-sized counterparts. This, combined with the limited proportion of a substance contained there, provides a set of fundamentally new properties, in particular, the ability to save individual characteristics of nanoscale objects in the consolidated system with a great proportion of substance in the non-autonomous phases.

To study the emerging high-temperature superconductivity in ensembles of interacting nanoparticles [206], nanoscale approaches developed in earlier models of V. L. Ginzburg and W. A. Little [22, 75–77] are involved, which are discussed in detail by L. V. Keldysh [211]. In particular, they proved the existence of the effect of superconductivity amplification during formation of various current contacts between nanoparticles of metals and alloys (tin, indium, lead, vanadium, zinc, lanthanum and their oxides) [208] where the delocalized electron spectra form energy shells similar to the atomic or nuclear energy shells [212, 214–216].

The study of the superconductivity phenomenon at the level of interphase layers also indicates the possibility to create tunneling chains of metal nanoclusters with a total charge transfer [217]. This creates the chance to ‘vastly’ intensify the superconducting pairing and significantly increase the critical superconducting transition temperature up to the room temperature value [218]. This is caused by such a distinctive feature of nanoparticles as a discrete structure of their electron spectra due to the relatively small number of atoms compared to the massive volumes of regular solids. As a result, the superconducting energy gap value may exceed the difference between the energy levels that arise due to the finite particle size (a finite number of atoms in it) or come up with it [219]. In addition, as the energy levels are not equidistant, they can be highly degenerate and fairly close to each other in the vicinity of the Fermi level, which leads to the density peak of states at the Fermi level. According to estimates [220] detailed in [218], such a ‘dimensional’ quantization leads to the effect of Tc increase by value of $\delta Tc/Tc \approx (2-3)$, which was discovered in thin films and granular materials [220–224]. A similar situation in the clusters considerably stimulates the electron pairing; moreover, one can expect a tremendous intensify thereof compared to volume pairing, which emphasizes the importance of the nanoparticle shell structure for pairing as specified by W. Knight and several other researchers [225]. Most assuredly, this type of pairing also affects the optical, magnetic, thermodynamic and other properties of the clusters.

One of the important issues is still a resistance of high-temperature superconducting materials, especially nanostructured ones, to various functional and fluctuation effects which primarily affect chemical, thermal, current and magnetic stability and cause energy dissipation in superconductors.

6. Dissipative phenomena, chemical, thermal, current and magnetic stability of nanostructured high-temperature superconductors

The problem of functional stability for the composition, structure and properties of superconducting nanostructures under the thermal, current and magnetic influences reflects the problem of the overall nanomaterial sustainability in many ways [29]. It depends greatly on the production method: either by nanocluster aggregation, in particular, under conditions close to thermodynamic equilibrium [226, 227], or by dispersion from the consolidated substance during non-equilibrium thermodynamic processes while applying outside powerful energy fluxes. The latter method increases greatly the energy saturation of nanoparticles, which may lead to their specific behavior and cause the threshold phenomena (see, for example: [228–234]). In all cases, a significant role in forming the nano-structure stability is played self-organization phenomena [235] including those happening at the formation level of the above-mentioned non-autonomous phases with particular physical chemistry.

Even being outside the functional impacts (while storing or preparing for use), most superconducting compounds are only thermodynamically stable within a limited range of temperatures and oxygen partial pressures, beyond which they are in a state of metastable equilibrium. To stabilize these compounds, dopants are applied that chemically 'deform' the crystal structure and can lead to a significant change in functional parameters of the HTSC material under usage conditions because of geometry changes in superconducting and dielectric areas, as well as the charge redistribution between them. One of the simplest ways to evaluate stability of the synthesized oxide superconductors is based on the known Goldschmidt's geometric tolerance criterion [236, 237], according to which the perovskite-like A–Cu–O structure (where A is for atoms of K, Rb, Cs, Tl, etc.) will be sustainable in the above sense, if the $(R_A + R_O)/\sqrt{2}\,(R_{Cu} + R_O)$ ratio lies in the range of 0.8 – 1, where R stands for ionic radii of constituent elements. The additional influence of other geometrical factors in the structures of specific chemical compounds is considered, e.g., in [29, 238, 239]. As for the superconducting complex oxides of the last generations representing, as a rule, solid solutions of different non-homogeneity that depends on the production technology and subsequent heat treatment, there is an urgent problem of chemical phase metastability in conditions of low-temperature decomposition of the solid solution supersaturated by one or more components, as well as its instability in relation to small spinodal fluctuations which lead to delamination and formation of coherent areas of significantly different chemical composition [240]. When thermally influenced, nanomaterials may show other processes that affect their stability, particularly those related to the relaxation of internal micro-stresses and the subsequent grain growth, the change in the numerous boundary surfaces and the appropriate proportion of non-autonomous phases in the total material volume, diffusion and effects of border segregation of the individual components [241, 242].

These phenomena can become significantly intensified under the influence of various physical fields (magnetic, electric, power, radiation, etc.), primarily functionally conditioned, especially those leading to the above considered thermodynamic phase transitions of a substance or those corresponding to extreme working conditions of type 2 superconducting materials wherein the current density can reach a value of $j = 10^5 - 10^7$ A/cm^2, and the superconductivity maintained in magnetic fields is up to $H = 10^5 - 10^6$ G (10 – 100 T) (Fig. 18, [243]).

Since the superconductors are used due to their ability to resist the damaging effects of high currents and magnetic fields arising at working conditions in most practical applications, much attention is paid to studies of dissipative processes accompanying and contributing to the emergence and evolution of current and magnetic instabilities in superconducting materials. In the development of such instabilities, a special role is played by thermal fluctuations that can lead to overall instability of the critical state itself under certain conditions, which is evidenced by the so-called 'giant' creep phenomenon [244]. As a result, the spontaneous temperature rise taking place in some volume of the superconductor material reduces the pinning forces that bind the individual vortex filaments of the occupied magnetic field to the existing defects, which leads to the vortex lattice disequilibrium and the magnetic flux movement accompanied by heat release due to energy dissipation of the superconducting currents. In turn, this causes a further increase in the sample temperature and, in case of large values of the external magnetic field and transport current in high-temperature superconductors, can turn into a snowballing process of interrelated temperature and electromagnetic field perturbations as a flux jump. In contrast to the usual slow creep of magnetic flux and its logarithmical relaxation through time at small currents, a 'giant creep' can result in the loss of current, magnetic and thermodynamic stability, which ultimately can cause complete destruction of superconductivity [245, 246].

A very unusual example of development of these 'thermal' instabilities in superconductors can be the experimentally observed self-similar tree-like or branching formation of normal (non-superconducting) fractal structures which emerge incrementally at temperatures ranging slightly below Tc and which are never observed when reaching Tc. The latter circumstance is still not theory-based despite the large amount of experimental data on such formations which emerge especially well as the macroscopic ones in thin films during the magnetic field penetration (Fig. 19) [247].

A possible explanation of this phenomenon as 'deterministic chaos' [248] can lie in percolation vortex depinning mechanism proposed in [249] to describe the resistive state of thin film of superconductors near the critical current. This approach relates the transition of a superconductor end portion into the resistive state to the viscous

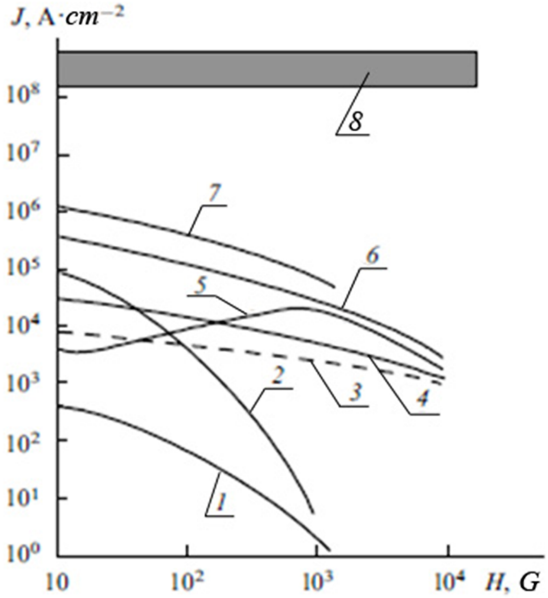

FIG. 18. The stability of the critical-current density for various HTSC materials, depending on the external magnetic field magnitude at 77 K according to [243]: 1 – sintered ceramics, 2 – Bi2212 tapes, 3 – coarse grain ceramics and single crystals, 4 – Y123, 5 – pure Nd123, 6 - Nd123 with ^{235}U embedded and irradiated with slow (thermal) neutrons, 7 – thin films, 8 – the theoretical limit

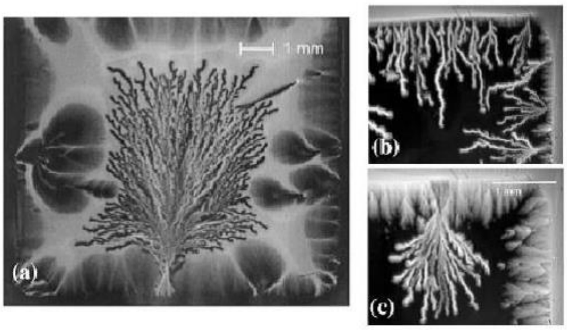

FIG. 19. Magneto-optical images of the treelike branching structures in thin films of YBaCuO at temperatures of 4.2 K (a), in MgB_2 at a temperature of 3.8 K (b) and 10 K (c). Figures taken from the review [247]

flow of vortices and the formation of randomly distributed vortex cores (joined chains of normal state – ‘flow clusters’), the probability of formation thereof determines the achievement of the percolation threshold to be below the critical value the total de-pinning (Fig. 20).

This model also results in a universal power law dependence of volt-ampere characteristics of the resistive state of the film superconductors near the critical current and allows us to express the exponent in this dependence through the universal *2D* flow theory critical indices of $\gamma \approx 1.3 - 1.6$ [250]. It agrees satisfactorily with the experimental data for high-temperature superconductors and weakly depends on the HTSC type and sample quality [251] in contrast to conventional type 2 low-temperature superconductors where an exponential dependence of the resistive volt-ampere characteristic is typical.

As noted above, induction (‘Meissner’) currents that occur near the superconductor surface tend not only to escape the penetration of external magnetic fields in the superconductor but also not to let the vortex filaments of the magnetic field out of its thickness, which penetrated into the sample at temperatures $T > Tc$ when it had not been superconductive yet. Therefore, the HTSC stability assessment and the consideration of dissipative

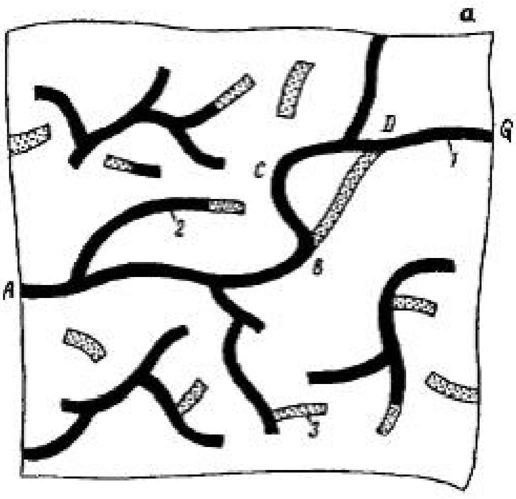

FIG. 20. Percolation *2D*-structure in the system of vortex pinning centers in a thin film [249]. Black color denotes the areas where vortices may flow steadily; grey color denotes extra areas appearing when the Lorentz force increases due to the transport current step-up

processes thereof under different perturbations and functional regime regulation should be carried out based on the general non-equilibrium thermodynamics methods [252], taking into account the high-tension electromagnetic field emerging in such materials long before the superconductivity is destructed. With this in mind, we should search the mechanisms to maintain the HTSC superconductivity at the AC current input in overloaded regimes of non-intensively cooled HTS magnets, when the input current peak values can significantly exceed the so-called quench current which defines the boundary of steady states during the DC current flow in the superconductor [38,253].

7. Conclusion

The analysis of achievements, challenges and prospects for materials with high transition temperature of the superconducting state indicates a large variety of existing approaches to solve this problem which is relevant in scientific and practical terms.

The obtained experimental results and the proposed theoretical models describing the physical mechanisms of the superconductivity's occurrence at a phenomenological and microscopic level, including those on atom energy spectrum modification, relate the further progress in the understanding of the 'superconducting' gap origin at a temperature below the critical transition, as well as the 'pseudo-gap' above the critical temperature. Although the pseudo-gap origin is not completely understood, it can be considered as an independent phase transition in the substance prior to the transition to a zero-resistance state and insusceptibility to external magnetic field in high temperature superconductors. In this respect, studies of the characteristics of multi-gap and gapless superconducting materials, their abilities to further increase the supercritical transition temperature and the critical current magnitude are also of considerable interest.

Large reserves to create the necessary electron and phonon spectra during the high-temperature superconductivity formation are associated with nanoscale structures and nanoparticle systems of conductors and dielectrics. Herein, a significant role is played by features of their electronic spectrum with a noticeable discrete structure due to the relatively small number of atoms compared to the massive volumes of regular solids, and the formation of the different current contacts between the nanoparticles and the creation of the tunnel circuits. The study of the superconductivity phenomenon at the level of interphase layers (non-autonomous phases) and in the nanoparticles also indicates the possibility to create tunnel chains of metal nanoclusters of certain parameters along with the total charge transfer, where the delocalized electron spectra form energy shells similar to the atomic or nuclear shells. This makes possible the 'vast' intensifying of superconducting pairing and a strong increase in the critical temperature of the superconducting transition.

Implementing of these possibilities requires further study of the superconductivity at the level of the non-autonomous phases in these structures, developing adequate methods of synthesis of nanoparticles of variable size, structure and phase composition, as well as consolidation technologies thereof ensuring the preservation of individual nanoparticle superconductivity along with its chemical, thermal, current, and magnetic resistance.

A special role in the instability development, when there are functionally-related effects, is played by thermal fluctuations that are able to lead to the overall supercritical state instability akin to the 'giant' creep phenomenon under certain conditions. It is also necessary to search for the mechanisms to preserve the HTSC superconductivity at AC current input therein in the overloaded modes when the peak values of input currents can significantly exceed the quench current which sets the boundary of steady states during the DC current flow in the superconductor.

In general, the research lines considered reveal resources to find suitable nanoscale structures and materials with high superconductivity transition temperature.

8. Post Scriptum

Before the submission of the present review to the Journal it became known that Nobel prize in Physics 2016 was awarded to David J. Thouless, F. Duncan, M. Haldane and J. Michael Kosterlitz [254] 'for theoretical discoveries of topological phase transitions and topological phases of matter'. The use of the topological concept for studying of space properties which remain unchanged at its remaining invariable at its continuous deformations allows one to describe the order disturbance in the condensed systems, in particular, transition to a superfluid or superconducting state. On this basis the mechanism of phase superconducting transition is explained at low temperatures even in thin (two-dimensional) layers with a stepwise change of conductivity with the increase of induction of the imposed magnetic field as well as the mechanism of disappearance of superconductivity at high temperatures. The latter transition was received the name of Berezinskii–Kosterlitz–Thouless (BKT) transition [255–257], but the Soviet physicist-theorist Vadim Berezinskii participated in theory development in the 1970's has not lived up to getting the Nobel Prize. Approximately at the same time F. D. Haldane discovered that topological representations could be used for properties description of the one-dimensional magnetic chains appearing in some materials [258–260]. It is expected that such theoretically grounded search for unusual topological phases (or states) of matter could help researchers in quantum physical phenomena in the field of materials science, electronics, in quantum computer creation.

In this regard it should be also mentioned the work of Yu. F. Antonov and J. B. Danilevich [38] where the topological approach for new type of superconductor topologial electrical machines of high power (the electric engines and electric generators, electromagnetic couplings and DC transformers) has been considered. Here, the local changes of superconductors phase state are considered as topological transformations taking into account that for superconducting structures of any geometrical form and connectivity the fundamental value of quantization of the magnetic flux as the direct consequence of rigid phase coherence remains unchanged as a topological property of those structures.

Technical operation of such machines is provided by electromagnetic effects caused by phase transitions accompanied by the formation of intermediate and mixed states of superconductors and movements of quantum filaments due to the change of connectivity of superconducting circuits using a specially developed resistive-superconducting switch.

Acknowledgments

The author would like to thank Prof. V. V. Gusarov for useful discussions. This work was financially supported by the Russian Foundation for Basic Research, project No. 15-08-03238 A.

References

[1] *Physical encyclopedia*. Chief editor A.M. Prokhorov. Great Russian encyclopedia, 1998, Moscow, (in Russian).
[2] Kamerlingh-Onnes H. Further experiments with liquid helium. On the electrical resistance of pure metals, etc. VI. On the sudden change in the rate at which the resistance of mercury disappears. Comm. Phys. Lab. Univ. Leiden, 1911, **124**.
[3] Meissner W., Ochsenfeld R. Ein neuer Effekt bei Eintritt der supraleitfhigkeit. *Naturwiss*, 1933, **33** (44), P. 787–788.
[4] Meissner W. New work on superconductivity. *Uspekhi Fizicheskikh Nauk*, 1935, **15** (2), P. 208–220 (in Russian).
[5] London F., London H. The Electromagnetic Equations of the Supraconductor. *Proc. Roy. Soc. London*, 1935, **71**, P. 71–88.
[6] *The Scientific Letters and Papers of James Clerk Maxwell (1846–1862)*. Ed. P.M. Harman. Cambridge: University Press, 1990–2002, **1–3**.
[7] Ginzburg V.L., Landau, L.D. On the theory of superconductivity. *JETP*, 1959, **20**, P. 1064 (in Russian).
[8] Abrikosov A.A., Gorkov L.P., Dzyaloshinskii I.E. *Methods of quantum field theory in statistical physics*. Fizmatgiz, Moscow, 1962 (in Russian).
[9] Belyavskii V.I., Kopaev Yu.V. Ginzburg-Landau equations for high-temperature superconductors. *Phys. Usp.*, 2007, **50**, P. 540–545.
[10] Bardeen J., Cooper L.N., Schrieffer J.R. Theory of Superconductivity. *Phys. Rev.*, 1957, **108**, P. 1175.
[11] Landau L.D., Lifshitz E.M. *Curse of Theoretical physics*, 9: Statistical physics, Part 2. Nauka, Moscow, 1985 (in Russian).

[12] Feynman R., Leighton R., Sands M. *The Feynman lectures on Physics*. Addison-Wesley Publishing Company, Ing, Reading, Massachusetts, Palo Alto. London. 1964, **2**.

[13] Fröhlich H. Theory of the superconducting state. *Phys. Rev.*, 1950, **79** (5), P. 845.

[14] Maxwell E. Isotope Effect in the Superconductivity of Mercury. *Phys. Rev.*, 1950, **78**, P. 477.

[15] Reynolds C.A., Serin B., Wright W.H., Nesbitt L.B. Superconductivity of isotopes of mercury. *Phys. Rev.*, 1950, **78**, P. 487.

[16] Belyavskii V.I., Kopaev Yu.V. First International Conference 'Fundamental Problems of High-Temperature Superconductivity'. *Phys. Usp.*, 2005, **48**, P. 177–182.

[17] Fedyukin V.K. *The fundamentals of alternative 'theory of superconductivity'*. SpbGIEU, St. Petersburg, 2009 (in Russian).

[18] Geballe T.H., Hulm J.K. *Bernd Theodor Matthias*. National Academies Press: Biographical Memoirs, 1996, **70**.

[19] Schrieffer J.R. *Theory of Superconductivity*. Perseus Books, New York, 1964.

[20] de Genes P.G. *Superconductivity of metals and alloys*. W.A. Benjamin, New York, 1966.

[21] Lynton E.A. *Superconductivity*. Methuen & Co. Ltd, London, 1969.

[22] Ginzburg V.L. The problem of high-temperature superconductivity. II. *Sov. Phys. Usp.*, 1970, **13**, P. 335–352.

[23] Tinkham M. *Introduction to superconductivity*. McGraw Hil, New York, 1975.

[24] Vonsovskii S.V., Izyumov Yu.A., Kurmaev E.Z. *Superconductivity of transition metals, their alloys and compounds*. Nauka, Moscow, 1977 (in Russian).

[25] Schmidt V. *Itroduction to the physics of superconductors*. Nauka, Moscow, 1982 (in Russian).

[26] Abrikosov A.A. *The fundamentals of the theory of metals*. Nauka, Moscow, 1987 (in Russian).

[27] Ginzburg V.L. On heat transfer (heat conduction) and the thermoelectric effect in the superconducting state. *Phys. Usp.*, 1998, **41**, P. 307–311.

[28] Ginzburg V.L. Superconductivity: the day before yesterday – yesterday – today – tomorrow. *Phys. Usp.*, 2000, **170** (43), P. 573–583.

[29] Tretyakov Yu.D., Gudilin E.A. Chemical principles of preparation of metal-oxide superconductors. *Russian Chemical Reviews*, 2000, **69** (1), P. 3–40 (in Russian).

[30] Sadovskii M.V. Pseudogap in high-temperature superconductors. *Phys. Usp.*, 2001, **44**, P. 515–539.

[31] Ginzburg V.L., Andryushin E.A. *Superconductivity*. Alpha-M, Moscow, 2006 (in Russian).

[32] Maksimov E.G. High-temperature superconductivity: the current state. *Phys. Usp.*, 2000, **43**, P. 965–990.

[33] Kopaev Yu.V. High-temperature superconductivity models. *Phys. Usp.*, 2002, **45**, P. 655–659.

[34] Chernoplekov N.A. State of the art in applied high-current superconductivity. *Phys. Usp.*, 2002, **45**, P. 659–665.

[35] Belyavskii V.I, Kopaev Yu.V. Generalizing considerations about the nature of high-temperature superconductivity (based on the proceedings of M2S-HTSC-VII). *Phys. Usp.*, 2004, **47**, P. 409–416.

[36] Mourachkine A. *Room-Temperature Superconductivity*. Cambridge International Science Publishing, Cambridge, 2004.

[37] Rumer Y.B., Ryvkin M.S. *Thermodynamics, Statistical Physics and Kinetics*. Nauka, Moscow, 1977 (in Russian).

[38] Antonov Yu.F., Danilevich J.B. *The Topological Superconducting Electrical Machines*. Fizmatlit, Moscow, 2009 (in Russian).

[39] Abrikosov A.A. About the magnetic properties of superconductors of the second group. *JETP*, 1957, **32**, P. 1442 (in Russian).

[40] Abrikosov A.A. The type-II superconductors and the vortex lattice (Materials Nobel Lecture, Stockholm 2003 and Science Division, Argonne National Laboratory, Argonne, USA). *Uspekhi Fizicheskikh Nauk*, 2004, **174** (11), P. 1235–1239 (in Russian).

[41] Schubnikov L.B., Chotkewitsch B.I., Schepelev J.D., Rjabinin J.N. Magnetische Eigenschaften supraleitender Metalle und Legierungen. *Phys. Z. Sowiet*, 1936, **10** (2), P. 165–192.

[42] Shubnikov L.V., Khotkevich V.I., Shepelev Yu.D., Ryabinin Yu.N. Magnetic properties of superconducting metals and alloys . *JETP*, 1937, **7** (2), P. 221–237 (in Russian).

[43] Slezov V.V, Papirov I.I., Shepelev A.G. *Discovery of the Shubnikov phase (type ii superconductors)*. National Science Center, Kharkov Institute of Physics and Technology, 2008, **823** (in Russian).

[44] Tauble H, Essman U. Die Beobachtung magnetischer Strukturen von Supraleitern zweiter Art. *Physica Status Solidi*, 1967, **20**, P. 95–111.

[45] Sarma N.V. Direct evidence for the laminar add flux models of mixed state in type II superconductors. *Physics Letters A*, 1967, **25** (4), P. 315–316.

[46] San-Zham D., Sarma G., Tomas E. *Type II superconductivity*. Pergamon press, Oxford-London-Edinburgh-New York Toronto – Sydney – Paris – Braunschweig, 1969.

[47] Zeeman P. Doubles and triplets in the spectrum produced by external magnetic forces. *Phil. Mag.*, 1897, **44**, P. 55.

[48] Fulde P., Ferrell R.A. Superconductivity in a Strong Spin-Exchange Field. *Phys. Rev. A*, 1964, **135**, P. 550.

[49] Larkin A.I., Ovchinnikov Yu.N. Inhomogeneous state of superconductors. *JETP*, 1964, **47** (3), P. 1136–1146.

[50] Proshin Yu.N., Khusainov M.G. On the manifestations of the state of the Larkin-Ovchinnikov-Fulda-Ferrell in bimetallic structures ferromagnet-superconductor. *JETP Letters*, 1997, **66** (8), P. 527–532.

[51] Anderson P.W. Theory of dirty superconductors. *Journal of Physics and Chemistry of Solids*, 1959, **11** (1–2), P. 26–30.

[52] Babaev E., Speight M. Semi-Meissner state and neither type-I nor type-II superconductivity in multicomponent superconductors. *Phys. Rev. B*, 2005, **72**, P. 180502.

[53] Moshchalkov V., Menghini M., et al. Type-1.5 Superconductivity. *Phys. Rev. Lett.*, 2009, **102**, P. 114501.

[54] Vinnikov L.Ya., Karpinski J.,. et al. Vortex structure in MgB_2 single crystals observed by the Bitter decoration technique. *Phys. Rev. B*, 2003, **67**, P. 1–3.

[55] Gor'kov L.P., Kopnin N.B. Movement vortexes and resistance of superconductors of the second kind in the magnetic field. *Uspekhi Fizicheskikh nauk*, 1975, **116** (3), P. 413.

[56] Mints R.G.,. Rakhmanov A.L. Magnetic instabilities in hard orproviding. *Uspekhi Fizicheskikh nauk*, 1977, **121** (3), P. 499–524 (in Russian).

[57] Malkov M.P., Danilov I.B., Zeldovich A.G. *Handbook of physical-technical fundamentals of cryogenics*. Energoatomizdat, Moscow, 1985 (in Russian).

[58] Yeshurun Y., Malozemoff A.P. Giant Flux Creep and Irreversibility in an Y-Ba-Cu-O Crystal: An Alternative to the Superconducting-Glass Model. *Phys. Rev.*, 1988, **60**, P. 2202–2205.

[59] Buckel W. *Superconductivity: Fundamentals and Applications (Physics)*. Mir, Moscow, 1975 (in Russian).

[60] Postnikov V.S. *Physics and chemistry of solid state*. Metallurgy, Moscow, 1978 (in Russian).

[61] URL: `http://elementy.ru/novosti_nauki/431450/Sverkhprovodimost`.

[62] Aksenov V.L. Neutron diffraction cuprate high-temperature superconductors. *Uspekhi Fizicheskikh Nauk*, 2002, **172** (6), P. 701–705 (in Russian).

[63] Langenberg D.N., Scalapino D.J., Taylor B.N. The Josephson Effects. *Scientific American*, 1966, **214** (5), P. 30.

[64] Langenberg, D.N., Scalapino D.J., Taylor B.N. The Josephson effects. *Uspekhi Fizicheskikh Nauk*, 1967, **91** (2), P. 317–320 (in Russian).

[65] Josephson B.D. Possible new effects in superconductive tunnelling. *Phys. Lett.*, 1962, **1** (7), P. 251–253.

[66] Anderson P.W., Rowell J.M. Probable observation of the Josephson superconducting tunnelling effect. *Phys. Rev. Lett.*, 1963, **10**, P. 230–232.

[67] Ponomarev Y.G. Tunnel and St. Andrew spectroscopy of high-temperature superconductors. *Uspekhi Fizicheskikh Nauk*, 2002, **72** (6), P. 705–711 (in Russian).

[68] Andreev A.F. Thermal conductivity of the intermediate state of superconductors. *Journal of Experimental and Theoretical Physics*, 1964, **46**, P. 18–23 (in Russian).

[69] Andreev A.F. Electrodynamics of the intermediate state of superconductors. *Journal of Experimental and Theoretical Physics*, 1966, **51**, P. 1510 (in Russian).

[70] URL: `http://www.nkj.ru/news/24322/`.

[71] URL: `http://elementy.ru/novosti_nauki/431568/...Yuriy_Erin`.

[72] Altshuler T.C, Bresler M.S. On the nature of the energy gap of dodecaborate YbB_{12}. *Physics of the solid state*, 2002, **44** (8), P. 1465 (in Russian).

[73] Tsidil'kovskii I.M. *Gapless semiconductors – a new class of substances*. Academy of Sciences of the USSR. Series: Academic reading, Nauka, Moscow, 1986 (in Russian).

[74] Elesin V.F., Kapaev V.V., Kopaev Yu.V. Coexistence of ferromagnetism and nonuniform superconductivity. *Phys. Usp.*, 2004, **47**, P. 949–953.

[75] Little W.A. Possibility of Synthesizing an Organic Superconductor. *Phys. Rev.*, 1964, **134**, P. 416.

[76] Little W.A. Superconductivity at Room Temperature. *Scient. Amer.*, 1965, **212** (2), P. 21.

[77] Little W. Superconductivity at room temperature. *Uspekhi Fizicheskikh Nauk*, 1965, **86** (2), P. 315–326 (in Russian).

[78] Bednorz J.G, Muller K.A. Possible highT superconductivity in the Ba–La–Cu–O system. *Z. Phys. B: Cond. Mat.*, 1986, **64** (2), P. 189–193.

[79] Tretyakov Yu.D. Chemical superconductors before the Third Millennium. URL: `www.chem.msu.su/rus/journals/xr/tretyak.html`.

[80] Wu M.K., Ashburn J.R., et al. Superconductivity at 93 K in a new mixed-phase Y-Ba-Cu-O compound system at ambient pressure. *Phys. Rev. Lett.*, 1987, **58**, P. 908.

[81] Maeda H., Tanaka Y., et al. New high-Tc superconductors without rare earth element. *Physica C*, 1988, **153** (602), P. 7.

[82] Matsui Y. Maeda H., Tanaka Y., Horiuchi S. High-resolution electron microscopy of modulated structure in the new high-Tc superconductors of the Bi-Sr-Ca-Cu-O system. *Jpn. J. Appl. Phys.*, 1988, **2** (27), P. 36l.

[83] Sheng Z.Z., Hermann A.M. Bulk superconductivity at 120 K in the Tl–Ca/Ba–Cu–O system. *Nature*, 1988, **332**, P. 138–139.

[84] Torardi C.C., Subramanian M. A., et al. Crystal Structure of $Tl_2Ba_2Ca_2Cu_3O_{10}$, a 125 K Superconductor. *Science*, 1988, **240** (4852), P. 631–634.

[85] Putilin S.N., Antipov E.V., Chmaissem O., Marezig M. Superconductivity at 94 K in $HgBa_2Cu0_{4+\delta}$. *Nature*, 1993, **362**, P. 226–228.

[86] Abakumov A.M., Antipov E.V., et al. Complex oxides with coherent intergrowth structures. *Russian Chemical Reviews*, 1995, **64** (8), P. 719.

[87] Campbell A.M., Evetts J.E. *Critical currents in superconductors*. Taylor and Francis Ltd, London, 1972.

[88] Tretyakov Y.D., Gudilin E.A. Chemical design of metal-oxide superconductors. *Physica B: Condensed Matter*, 2002, **321** (1–4), P. 249–256.

[89] Tretyakov Y.D., Gudilin E.A., Reddy E.S., Schmitz G.J. Modern preparation metods of oriented thick films of superconducting cuprates. *Crystallography Reports*, 2004, **49** (2), P. 233–239.

[90] Reddy E.S., Tarka M., Gudilin E.A., Schmitz G.J. A novel process for textured thick film $YBa_2Cu_3O_y$ coated conductors based on constitutional gradients principle. *Superconductor Science and Technology*, 2005, **16** (6), P. 859–873.

[91] Martynova I., Tsymbarenko D., et al. Solution deposition of ultrasmooth alumina on long-length metallic substrate for 2G superconducting tapes. *Materials Research Bulletin*, 2016, **78**, P. 64–71.

[92] Liu Zi-Kui, Zhong Yu, Schlom D.G. Computational Thermodynamic Modeling of the Mg-B System. *Calpha*, 2001, **25** (2), P. 299–303.

[93] Grosche F.M., Yuan H.Q., et al. Superconductivity in the Filled Cage Compounds Ba_6Ge_{25} and $Ba_4Na_2Ge_{25}$. *Phys. Rev. Lett.*, 2001, **87**, P. 107.

[94] Reich S., Tsabba Y. Possible nucleation of a 2D superconducting phase on WO_3 single crystals surface doped with Na+. *Eur. Phys. J. B*, 1999, **9** (1), P. 1–4.

[95] Levi Y., Millo O., et al. Evidence for localized high-Tc superconducting regions on the surface of Na-doped WO_3. *Europhys. Lett.*, 2000, **51** (5), P. 564–570.

[96] Aliev A.E. High-Tc superconductivity in nanostructured $NaxW0_{3-y}$: sol-gel route. *Supercond. Sci. Technol.*, 2008, **21**, P. 1–9.

[97] Kamihara Y., Watanabe T., Hirano M., Hosono H. Iron-Based Layered Superconductor La [$O_{1-x}F_x$] FeAs ($x = 0.05 - 0.12$) with $Tc = 26$ K. *Journal of the American Chemical Society*, 2008, **130** (11), P. 3296–3297.

[98] Takahashi H., Igawa K., et al. Superconductivity at 43 K in an iron-based layered compound $LaO_{1-x}F_xFeAs$. *Nature*, 2008, **453** (7193), P. 376–378.

[99] Ren Z.A., Lu W., et al. Superconductivity at 55 K in iron-based F-doped layered quaternary compound $Sm[O_{1-x}F_x]FeAs$. *Chin. Phys.Lett.*, 2008, **25**, P. 2215.

[100] Ren Z.A., Yang J., et al. Superconductivity in the iron-based F-doped layered quaternary compound $Nd[O_{1-x}F_x]FeAs$. *Europhys. Lett.*, 2008, **82** (5), P. 57002.

[101] Wang C., Li L.J., et al. Thorium-doping-induced superconductivity up to 56 K in $Gd_{1-x}Th_xFeAsO$. *Europhys. Lett.*, 2008, **83** (6), P. 67006.

[102] Zhao J., Huang Q., Clarina de la Cruz, et al. Structural and magnetic phase diagram of $CeFeAsO_{1-x}F_x$ and its relation to high-temperature superconductivity. *Nature Materials*, 2008, **7**, P. 953–959.

[103] Mazin I.I., Singh D.J., Johannes M.D., Du M.H. Unconventional Superconductivity with a Sign Reversal in the Order Parameter of $LaFeAsO_{1-x}F_x$. *Phys. Rev. Lett.*, 2008, **101**, P. 057003.

[104] Wu M.K., Hsu F.C., et al. The development of the superconducting PbO-type β-FeSe and related compounds. *Physica C*, 2009, **469** (9–12), P. 340–349.

[105] Guo J., Jin S., et al. Superconductivity in the iron selenide $K_xFe_2Se_2$ ($0 < x < 1.0$). *Phys. Rev. B*, 2010, **82**, P. 180520(1–4).

[106] Martinelli A., Palenzona M., et al. From antiferromagnetism to superconductivity in $Fe_{1+y}Te_{1-x}Se_x$ ($0 \leq x \leq 0.20$): Neutron powder diffraction analysis A. Martinelli. *Phys. Rev. B*, 2010, **81**, P. 094115(1–10).

[107] Roslova M.V., Lebedev O.I., et al. Diversity of microstructural phenomena in superconducting and nonsuperconducting $Rb_xFe_{2-y}Se_2$: a transmission electron microscopy study at the atomic scale. *Inorg. Chem.*, 2013, **52**, P. 14419–14427.

[108] Grinenko V.V., Efremov D.V., et al. Superconducting specific heat jump $\Delta C(Tc)$ for $K_{1-x}Na_xFe_2As_2$. *Physical Review B*, 2014, **89**, P. 060504(R).

[109] Blinkin A.A., Derevyanko V.V., et al. Evolution of structure and properties of MgB_2 superconductor during isothermal annealing. *Physics of the solid state*, 2005, **47** (9), P. 1546–1551 (in Russian).

[110] Ivanovskii A.L. New superconductors based on five-component transition metal oxypnictides . *Uspekhi Khimii*, 2010, **79** (1), P. 3–14 (in Russian).

[111] Kopaev Yu.V., Belyavskii V.I., Kapaev V.V. With cuprate luggage to room-temperature superconductivity. *Phys. Usp.*, 2008, **51**, P. 191–198.

[112] Chen X.K., Konstantinović M.J., et al. Evidence for Two Superconducting Gaps. *Phys. Rev. Lett.*, 2001, **87**, P. 157002.

[113] Korotkov N.Y., Frolov K.V., et al. Mössbauer Study of a New Superconductor GdOFeAs. *Journal of Superconductivity and Novel Magnetism*, 2013, **26** (9), P. 2877-?2879.

[114] Moskalenko V.A. Superconductivity of metals taking into account the overlap of the energy bands. *Fizika Metals*, 1959, **8** (4), P. 503 (in Russian).

[115] Suhl H., Matthias B.T., Walker L.R. Bardeen – Cooper – Schrieffer theory of superconductivity in the case of overlapping bands. *Phys. Rev. Lett.*, 1959, **3**, P. 552.

[116] Kuzmicheva T.E., Kuzmichev S.A., et al. Experimental study of intrinsic multiple Andreev reflections effect in GdO(F)FeAs superconductor array junctions. *European Physics Letters*, 2013, **102**, P. 67006.

[117] Lee W.S., Vishik I.M., et al. Abrupt onset of a second energy gap at the superconducting transition of underdoped Bi2212. *Nature*, 2007, **450** (7166), P. 81.

[118] Mazin I.I., Schmalian J. Pairing Symmetry and Pairing State in Ferropnictides: Theoretical Overview. *Physica C*, 2009, **469**, P. 614–627.

[119] Kuroki K., Onari S., et al. Unconventional Pairing Originating from the Disconnected Fermi Surfaces of Superconducting $LaFeAsO_{1-x}F_x$. *Phys. Rev. Lett.*, 2008, **101**, P. 087004.

[120] Kontani H., Onari S. Orbital-Fluctuation-Mediated Superconductivity in Iron Pnictides: Analysis of the Five-Orbital Hubbard-Holstein Model. *Phys. Rev. Lett.*, 2010, **104**, P. 157001.

[121] Shi-Zeng Lin, Xiao Hu. Vortex States and Phase Diagram of Multi-component Superconductors with Competing Repulsive and Attractive Vortex Interactions. *Phys. Rev. B*, 2011, **84**, P. 214505.

[122] Izyumov Yu.A., Proshin Yu.N., Khusainov M.G. Competition between superconductivity and magnetism in heterostructures of the ferromagnet-superconductor. *Successes of physical barriers. Sciences*, 2001, **172** (2), P. 113–154.

[123] Wurmeh S., Lebedev O., et al. New Layered Intermetallic Iron-based Superconductors and Related Compounds: Controlling Physical Properties by Using Iso- and Heterovalent Substitutions . *Journal RFBR*, 2014, 81 (1), P. 64–76 (in Russian).

[124] Kubaschewski O. *Iron – Binary Phase Diagrams*. Springer-Verlag, Berlin, 1982, 185 p.

[125] Volkov M.P., Melekh B.A.-T., Bakharev V.I., Kartenko N.F. Obtaining poly- and single crystals of superconducting iron monochalcogenides for short times of synthesis. *Technical physics Letters*, 2010, **36** (6), P. 8–14 (in Russian).

[126] Viewpoint: The iron age of superconductivity. URL: `http://physics.aps.org/articles/v1/28`.

[127] Chakravarty S., Sudbo A., Anderson P.W., Strong S. Interlayer Tunneling and Gap Anisotropy in High-Temperature Superconductors. *Science*, 1993, **261**, P. 337

[128] Sadovskii M.V. High-temperature superconductivity in layered iron compounds. *Uspekhi Fizicheskikh Nauk*, 2008, **178** (12), P. 1243–1271.

[129] Leggett A.J. Cuprate Superconductivity: Dependence of Tc on the c-Axis Layering Structure. *Physical Review Letters*, 1999, **83** (2), P. 392 (in Russian).

[130] Moler K.A., Kirtley J.R., et al. Images of interlayer Josephson vortices in $Tl_2Ba_2Co_{6+d}$. *Science*, 1998, **279**, P. 1193–1196.

[131] Kotegawa H., Tokunaga Y., et al. Unusual magnetic and superconducting characteristics in multilayered high-Tc cuprates: ^{63}Cu NMR study. *Phys. Rev. B*, 2001, **64**, P. 064515.

[132] Kuzemska I.G., Kuzemsky A.L., Cheglokov A.A. Superconducting Properties of the Family of Mercurocuprates and Role of Layered Structure. *Journal of Low Temperature Physics*, 2000, **118** (3–4), P. 147–152.

[133] Ginzburg V.L. Once again about high-temperature superconductivity. *Contemporary Physics*, 1992, **33**, P. 15–23.

[134] Drozdov A.P., Eremets M.I., et al. Conventional superconductivity at 203 Kelvin at high pressures in the sulfur hydride system. *Nature*, 2015, **525**, P. 73–76.

[135] Troyan I., Gavriliuk A., et al. Observation of superconductivity in hydrogen sulfide from nuclear resonant scattering. *Science*, 2016, **351** (6279), P. 1303–1306.

[136] Prins J.F. Ion implantation of diamond for electronic applications. *Semiconductor Science and Technology*, 2003, **8** (3), P. 131.

[137] Scheike T., Böhlmann W., Esquinazi P. et al. Can Doping Graphite Trigger Room Temperature Superconductivity? Evidence for Granular High-Temperature Superconductivity in Water-Treated Graphite Powder. *Advanced Materials*, 2012, **24** (43), P. 5826–5831.

[138] Kawashima Y. Possible room temperature superconductivity in conductors. *AIP Advanced*, 2013, **3** (5), P. 052132.

[139] Tripodi P., Gioacchino D. Di, Borelli R., Vinko J.D. Possibility of high temperature superconducting phases in PdH. *Physica C*, 2003, **388–389**, P. 571–591.

[140] He R.H., Karapetyan H., et al. From a Single-Band Metal to a High-Temperature Superconductor via Two Thermal Phase Transitions. *Science*, 2011, **331** (6024), P. 1579–1583.

[141] Damascelli A. Probing the Electronic Structure of Complex Systems by ARPES. *Physica Scripta*, 2004, **109**, P. 61–74.

[142] Stolow A., Bragg A.E., Neumark D.M. Femtosecond time-resolved photoelectron spectroscopy. *Chem. Rev.*, 2004, **104**, P. 1719.

[143] Boyarsky L.A. Pseudogap effects in strongly correlated electron systems. *Low temperature Physics*, 2006, **32** (8–9), P. 1078–1084.

[144] Boyarsky L.A. Pseudogap phenomena in superconductors. The gap and the pseudogap in systems with waves of spin/charge-density. The General approach and the applicability of the two-fluid model. *Physics of the solid state, semiconductors, nanostructures. Vestnik NSU. Series Physics*, 2007, **2**, P. 145–151.

[145] Batlogg B., Varma C. The underdoped phase of cuprate superconductors. *Phys. World*, 2000, **13** (2), P. 33.

[146] Loktev V.M., Quick R.M., Sharapov S.G. Phase actuations and pseudogap phenomena. Not coherent and 'unbalanced' Cooper pairs in HTSC. *Phys. Rep.*, 2001, **349** (1), P. 1–123.

[147] Mathur N.D., Grosche F.M., Julian S.R., et al. Magnetically mediated superconductivity in heavy fermion compounds. *Nature*, 1998, **394**, P. 39.

[148] Izyumov Yu.A. Spin-fluctuation mechanism of high-Tc superconductivity and order-parameter symmetry. *Phys. Usp.*, 1999, **42**, P. 215–243.

[149] Kaul S.N., Kumar S., Rodriges Fernandez J. et al. Unconventional superconductivity in LaAg1–xMn$_x$: Relevance of spin-fluctuation-mediated pairing. *Europhys. Lett.*, 2006, **74** (1), P. 138.

[150] Krasnov V.M., Kovalev A.E., Yurgens A., Winkler D. Magnetic field dependence of the superconducting gap and the pseudogap in Bi2212 and HgBr2-Bi2212, studied by intrinsic tunnelling spectroscopy. *Phys. Rev. Lett.*, 2001, **86**, P. 2657–2660.

[151] Boyer M.C., Wise W.D., et al. Imaging the two gaps of the high-temperature superconductor $Bi_2Sr_2CuO_{6+x}$. *Nature Physics*, 2007, **3** (11), P. 802–806.

[152] Belyavskii V.I., Kopaev Yu.V. Superconductivity of repulsive particles. *Phys. Usp.*, 2006, **49**, P. 441–467.

[153] Aslamazov L.G., Larkin A.I. The Influence of fluctuations on the properties of overproud-nick at temperatures above the critical. *Physics of the solid*, 1968, **10** (4), P. 1104–1111 (in Russian).

[154] Aslamasov L.G., Larkin A.I. The influence of fluctuation pairing of electrons on the conductivity of normal metal. *Phys. Lett. A*, 1968, **26**, P. 238–239.

[155] Maki K. The Critical Fluctuation of the Order Parameter in Type-II Superconductors. *Prog. Theor. Phys.*, 1968, **39** (4), P. 897–906.

[156] Da Silva Neto E.H., Comin R., et al. Charge ordering in the electron-doped superconductor $Nd_{2-x}Ce_xCuO_4$. *Science*, 2015, **347** (6219), P. 282–285.

[157] Mizen K.V., Ivanenko O.M. Phase diagram of $La_{2-x}M_xCuO_4$ as a key to understanding the nature of high temperature superconductors. *Uspekhi Fizicheskikh Nauk*, 2004, **174** (5), P. 545–563 (in Russian).

[158] Chakravarty S., Kee H.-Y., Vlker K. An explanation for a universality of transition temperatures in families of copper oxide superconductors. *Nature*, 2004, **428** (6978), P. 53–55.

[159] Aleskovskij V.B. Chemistry and technology of solid substances. *J. Appl. Chem. USSR*, 1974, **47**, P. 2145 (in Russian).

[160] Aleskovski V.B. Chemical Assembly materials. *Vestnik Akad. Of Sciences of the USSR*, 1975, P. 48–51 (in Russian).

[161] Malygin A.A., Drozd V.E., Malkov A.A., Smirnov V.M. From V.B. Aleskovskii's 'Framework' Hypothesis to the Method of Molecular Layering/ Atomic Layer Deposition. *Chemical Vapor Deposition*, 2015, **21**, P. 216–240.

[162] *Second-Generation HTS Conductors*. Ed. by Goyal A. New York: Inc. Springer-Verlag, 2004.

[163] Tolstoy V.P. Synthesis of thin-layer structures by the ionic layer deposition method. *Uspekhi Khimii*, 1993, **62** (3), P. 237–242 (In Russian).

[164] Kuz'menko V.M., Lazarev G.G., Mel'nikov V.I., Sudovcov A.I. Critical parameters of the amorphous metal film (a Review). *Ukrainian physical journal*, 1976, **21** (6), P. 883–903.

[165] Eletskii A.V., Smirnov B.M. Fullerenes and carbon structures. *Phys. Usp.*, 1995, **38**, P. 935–964 (in Russian).

[166] Galikeev A.R. *New forms of polymeric hydrocarbon*. Ufa: Ufa. State oil. Tech. Univ., 2001.

[167] Yang H.B., Rameau J.D., Johnson P.D., at al. Emergence of preformed Cooper pairs from the doped Mott insulating state in $Bi_2Sr_2CaCu_2O_{8+delta}$. *Nature*, 2008, **456**, P. 77–80.

[168] Shabanova N.P., Krasnoslobodtsev S.I., Varlashkin A.V., Golovashkin A.I. Parallel critical magnetic field of thin films NbC and MgB_2. *Scientific session Moscow engineering physics Institute*, 2006, **4**.

[169] Bagraev N.T., Klyachkin L.E., et al. Superconducting properties for silicon nanostructures. *Semiconductor physics and technology*, 2009, **43** (11), P. 1481–1495 (in Russian).

[170] Prikhod'ko A.V., Kozyrev S.V. Superconductivity in quantum-well nanostructures. *Scientific and technical sheets SPbSPU*, 2007, **4**, P. 221–226 (in Russian).

[171] Shapoval E.A. Critical Fields of Thin Superconducting Films. *JETP*, 1966, **22** (3), P. 647–653 (in Russian).

[172] Pearl J. Current distribution in superconducting films carrying quantized fluxoids. *Appl. Phys. Lett.*, 1964, **5**, P. 65.

[173] Samus A.N., Popkov A.F., et al. Resistive State and dynamics of vortices in superconducting films. *Superconductivity: physics, chemistry, technology*, 1991, **4** (7), P. 1324 (in Russian).

[174] Lomtev A.I. Contrails live an isolated vortex pearl in a thin film magnetic superconductor. *JETP Letters*, 2000, **71** (10), P. 618 (in Russian).

[175] Lomtev A.I. Inversion satellites" secluded oscillating vortex pearl in a thin film magnetic superconductor. *Physics of the solid state*, 2001, **43** (11), P. 1945–1951 (in Russian).

[176] Umezawa H., Matsumoto H., Tachiki M. *Thermo Field Dynamics and Condensed States*. Amsterdam (Netherlands): North-Holland Publishing Company, 1982.

[177] Grishin A.M., Martynovich A.Y., Yampolsky S.V. Inversion of the magnetic field and the chain of vortices in anisotropic superconductors. *JETP*, 1990, **97** (6), P. 1930–1946 (in Russian).

[178] Buzdin A.I., Simonov A.Yu. Magnetic flux Penetration in layered superconductors. *JETP*, 1990, **98** (6), P. 2074–2085 (in Russian).

[179] Kaul S.N., Kumar S., Rodriges Fernandez J. et al. Unconventional superconductivity in $LaAg_{1-x}Mn_x$: Relevance of spin-fluctuation-mediated pairing. *Europhys. Lett.*, 2006, **74** (1), P. 138.

[180] Ipatova I.P., Shchukin V.A., et al. Formation of strained superlattices with a macroscopic period via spinodal decomposition of III–V semiconductor alloys. *Sol. St. Commun.*, 1991, **78** (19), P. 19–24.

[181] Bagraev N.T., Gehlhoff W., et al. Quantum-Well Boron and Phosphorus Diffusion Profiles in Silicon. *Def. Dif. Forum*, 1997, **143–147**, P. 1003.

[182] Malygin A.A. Nanotechnology molecular layering: principles and applications (a review). *Nanotechnologies in Russia*, 2007, **2** (3–4), P. 87 (in Russian).

[183] Mazel E.Z., Press F.P. *Planar silicon technology devices*. Moscow, Energy, 1974 (in Russian).

[184] *VLSI Technology: Fundamentals and Applications Editors*. Ed. by Yasuo Tarui. Springer Series in Electronics and Photonics, **12**, Springer-Verlag, 1986.

[185] Jaeger R.C. *Film Deposition – Introduction to Microelectronic Fabrication* (2nd). UpPer Saddle River: Prentice Hall, 2002

[186] Poindexter E.H., Caplan P.H., Deal B.E., Gerardy G.J. *The Physics and Chemistry of* SiO_2 *and* $Si–SiO_2$ *Interfaces*. Plenum Press, New York, 1988.

[187] Bagraev N., Bouravleuv A., et al. Self-assembled impurity superlattices and microcavities in silicon. *Def. Dif. Forum*, 2001, **194**, P. 673.

[188] Feder J. *Fractals*. Plenum Press, New York, 1988.

[189] Tsebro V.I., Omeljnovskij O.E., Moravian A.P. Undamped currents and capture the magnetic flux in the fragments of the carbon deposits containing multilayer nanotubes. *JETP Letters*, 1999, **70** (7), P. 457–462 (in Russian).

[190] Khusainov M.G. Nonuform superconducting states and umklapp processes in ferromagnet-superconductor nanostructuctures. *E. J. Magnetic Resonance in Solid*, 2004, **6** (1), P. 104–118.

[191] Morozov Y.G., Belousova O.V., et al. Electric field-assisted levitation-jet aerosol synthesis of Ni/NiO nanoparticles. *Journal of Materials Chemistry*, 2012, **22** (22), P. 11214–11223.

[192] Kuznetsov M.V., Morozov Y.G., Belousova O.V. Levitation jet synthesis of nickel ferrite nanoparticles. *Inorganic Materials*, 2012, **48** (10), P. 1044–1051.

[193] Morozov Y.G., Ortega D., et al. Some peculiarities in the magnetic behavior of aerosol generated NiO nanoparticles. *Journal of Alloys and Compounds*, 2013, **572**, P. 150–157.

[194] Shishkovsky I., Morozov Y. Electrical and magnetic properties of multilayer polymer structures with nano inclusions as prepared by selective laser sintering. *Journal of Nanoscience and Nanotechnology*, 2013, **13** (2), P. 1440–1443.

[195] Gusarov V.V., Malkov A.A., Ishutina Zh., Malygin A.A. Phase formation in a nanosize silicon oxide film on surface of aluminum oxide. *Tech. Phys. Lett.*, 1998, **24** (1), P. 3–8 (in Russian).

[196] Smirnov A.V., Fedorov B.A., et al. Core-shell nanoparticles forming in the $ZrO_2–Gd_2O_3–H_2O$ system under hydrothermal condition. *Doklady Physical Chemistry*, 2014, **456** (1), P. 171–173 (in Russian).

[197] Almjasheva O.V., Smirnov A.V., et al. Structural features of $ZrO_2–Y_2O_3$ and Gd_2O_3 nanoparticles forming under hydrothermal condition. *Russian Journal of General Chemistry*, 2014, **84** (5), P. 710–716 (in Russian).

[198] Tomkovich M.V., Andrievskaya E.R., Gusarov V.V. Formation under hydrothermal condition of nanoparticles based on system $ZrO_2–Gd_2O_3$. *Nanosystems: Physics, Chemistry, Mathematics*, 2011, **2** (2), P. 6–14 (in Russian).

[199] Gusarov V.V., Almjasheva O.V. The role or status of substances in the formation of structure and properties of materials. Chapter 13 in the book *Nanomaterials: properties and applications*. Ed. by Yaroslavtsev A.B. Scientific world, Moscow, 2014 (in Russian).

[200] Defay R. *Etude Thermodynamique de la Tension Superficielle*. Paris, Gauthier-Villars and Cie, 1934, 372 p.

[201] Defay R., Prigogine I. *Tension superficielle et adsorption*. Liege, Ed. Desoer, 1951, 295 p.

[202] Gusarov V.V., Suvorov A.S. Self-accelerating processes of development of solid-phase systems (synthesis and function). In book *Future directions of chemistry and chemical technology*. Ed. S. Dudyrev. Chemistry, Leningrad, 1991, P. 153–158 (in Russian).

[203] Gusarov V.V., Ishutin J.N., Malkov A.A., Malygin A.A. Peculiarities of solid-phase chemical reaction of mullite formation in nanoscale film composition,. *Dokl. Academy of Sciences*, 1997, **357** (2), P. 203–205 (in Russian).

[204] Tauson, V.L., Loginov B.A., Akimov V.V., Lipko V.S. Sticky Nonautonomous phases as potential sources of incoherent elements. *Dokl. Academy of Sciences*, 2006, **406** (6), P. 806 (in Russian).

[205] Neiman A.Ya., Uvarov N.F., Pestereva N.N.. Solid state surface and interface spreading: An experimental study. *Solid State Ionics*, 2007, **177** (39–40), P. 3361.

[206] Rusanov A.I. *Phase equilibria and surface phenomena*. Chemistry, Leningrad, 1967, 388 p. (in Russian).

[207] Pervov V.S., Mikheikin I.D., Makhonina E.V., Buckiy V.D. Supramolecular assemblies in eutectic alloys. *Uspekhi Khimii (Progress in chemistry)*, 2003, **72** (9), P. 852 (in Russian).

[208] Neumann A.J., Tsipis E.V., et al. *Surface. X-ray, synchrotron and neutron studies*, 2001, **10**, P. 68 (in Russian).

[209] Kafarov V.V., Meshalkin V.P. *Analysis and synthesis of chemical-technological systems*. Chemistry, Moscow, 1991, 432 p. (in Russian).

[210] Cohen M.H., Douglass D.H. Superconductive Pairing Across Electron Barriers. *Phys. Rev. Lett.*, 1967, **19**, P. 118.

[211] Keldysh L.V. Superconductivity in nonmetallic systems. *Sov. Phys. Usp.*, 1965, P. 496–500 (in Russian).

[212] Morozov Y.G., Petinov V.I. Superconductivity in the ensembles of small metallic particles. *Solid State Communs.*, 1981, **40**, P. 991.

[213] Geppert-Mayer M., Jensen J.H.D. *Elementary Theory of Nuclear Shell Structure*. John Wiley u. Sons, Inc., New York; Chapman and Hall, Ltd., London, 1955.

[214] Goeppert Mayer M. *Nuclear Shell Structure*. Modern Physics for the Engineer, McGraw Hill, 1961.

[215] Goeppert Mayer M. Nuclear Shell Structure. *Uspekhi Fizicheskikh Nauk*, 1964, **82** (4), P. 749–768 (in Russian).

[216] Trunev A.P. The structure of atomic nuclei and binding energy in the shell model. *J. Chaos and Correlation*, 2012, **1**, P. 1–19.

[217] Friedel J. BCS superconductivity for weakly coupled clusters. *Journal de Physique II, EDP Sciences*, 1992, **2** (4), P. 959–970.

[218] Kresin V.Z., Ovchinnikov Yu.N. 'Giant' strengthening of superconducting pairing in metallic nanoclusters: strong increase in the transition temperature and the possibility of superconductivity at room temperature. *Uspekhi Fizicheskikh Nauk*, 2008, **78** (5), P. 449 (in Russian).

[219] Perenboom J., Wyder P., Meier F. Electronic-properties of small metallic particles. *Phys. Rep.*, 1981, **78**, P. 173–292.

[220] Anderson P.W. Theory of dirty superconductors. *Journal of Physics and Chemistry of Solids*, 1959, **11** (26), P. 26–30.

[221] Abeles B. Applied Solid State Science. In *Advances in Material and Device Research*, ed. by R. Wolfe. Academic Press, New York, 1976, **6**, P. 1.

[222] Dynes R.C., Garno J.P., Rowell J.M. Electrical Conductivity in Quench-Condensed Metal Films. *Phys. Rev. Lett.*, 1978, **40**, P. 479.

[223] Deutscher G. *New Superconductors: From Granular to High Tc*. World Scientific, Singapore, 2006, 244 p.

[224] Parmenter, R. Size Effect in a Granular Superconductor. *Phys. Rev.*, 1968, **166**, P. 392.

[225] Knight W. In *Novel Superconductivity*, Ed. by S.A. Wolf, V.Z. Kresin. New York: Plenum Press, 1987.

[226] Pozhidaeva O.V., Korytkova E.N., Drozdova I.A., Gusarov V.V. Phase state and particle size of ultradispersed zirconium dioxide as influenced by conditions of hydrothermal synthesis. *Russian Journal of General Chemistry*, 1999, **69** (8), P. 1219–1222.

[227] Almyasheva O.V., Gusarov V.V. Features of the phase formation in the nanocomposites. *Russian Journal of General Chemistry*, 2010, **80** (3), P. 385–390.

[228] Uvarov N.f., Boldyrev V.V. Dimensional effects in chemistry of heterogeneous systems. *Progress of chemistry*, 2001, **70** (4), P. 307–329.

[229] Mastai Y., Gedanken A. In *The Chemistry of Nanomaterials: Synthesis, Properties and Applications*, Ed. by Rao C.N.R., Muller A., Cheetham A.K. Weinheim: Wiley-VCH, 2004, **1**, P. 113.

[230] Gusarov V.V. The thermal effect of melting in polycrystalline systems. *Thermochim. Acta*, 1995, **256** (2), P. 467–472.

[231] Kovalenko A.N., Kalinin N.V. Thermodynamic instability of Compound and for-mation of nanosized parti-cles nearby the critical point of phase generating media. *Nanosystems: physics, chemistry, mathematics*, 2014, **5** (2), P. 258–293.

[232] Bulgakov A.V., Bulgakova N.M. Burakov I.M., etc. *The Synthesis of nanoscale materials under the influence of powerful streams of energy on matter*. Institute of Thermophysics SB RAS, Novosibirsk, 2009.

[233] Kotov Yu.A., Bagazeev A.V., Beketov I.V. etc. Characteristics of nickel oxide nanopowder obtained an electric explosion delay. *Technical physics letters*, 2005, **75** (10), P. 39–43 (in Russian).

[234] Sedoy V.S., Valevich V.V., Gerasimova N.N. Synthesis of highly dispersed powders method of electric explosion in Gaza with a pressure. *Physics and chemistry of materials processing FHOM*, 1999, **4**, P. 92–95 (in Russian).

[235] Tretyakov Yu.D. Self-organisation processes in the material chemistry. *Uspekhi Khimii (Russian Chemical Reviews)*, 2003, **72** (8), P. 731–763.

[236] Goldschmidt V.M. Die Gesetze der Krystallochemie. *Die Naturwissenschaften*, 1926, **21**, P. 477–485.

[237] Urusov V.S., Eremin N.N. *Crystal chemistry*. Publishing house of Moscow University, Moscow, 2005 (in Russian).

[238] Tugova E.A. A comparative analysis of the formation processes of Ruddlesden-Popper phases in the La_2O_3–SrO–M_2O_3 (M = Al, Fe) systems. *Glass Physics and Chemistry*, 2009, **35** (4), P. 416–422.

[239] Tugova E.A., Gusarov V.V. Influence of structural mismatch of the layers forming the phase Ruddlesden-Popper $Ln_nMFe_nO_{3n+1}$ on their resistance. *Proceedings of VIII International conference 'Amorphous and microcrystalline semiconductors'*. St. Petersburg, 2012, p. 329–330.

[240] Goodilin E.A., Oleynikov N.N., et al. On the stability region and structure of the $Nd_{1+x}Ba_{2-x}Cu_3O_z$ solid solution. *Physica C*, 1996, **272** (182), P. 65–78.

[241] Andrievskii R.A. Thermal stability of nanomaterials. *Uspekhi khimii (Russian Chemical Reviews)*, 2002, **10** (71), P. 853–866.

[242] Andrievskii R.A. Thermal stability of consolidate metallic nanomaterials. *Uspekhi khimii (Russian Chemical Reviews)*, 2014, **4**, P. 365–375.

[243] Mints R.G., Rakhmanov L.L. Magnetic instabilities in hard superconductors. *Uspekhi Fizicheskikh Nauk*, 1977, **121** (3), P. 499–524 (in Russian).

[244] Romanovskii V.R. Macroscopic flux-creep electrodynamics of high temperature superconductor. In book *Studies of high temperature superconductors. Advances in research and applications*. Nova Science Publishers, New York, 2005.

[245] Romanovskii V.R. Thermal mechanisms of the formation, destruction, and degradation of critical current states of high-temperature superconductors. *Doklady Physics*, 2009, **54** (4), P. 196.

[246] Romanovskii V.R. Magnetic, overcurrent and thermal instabilities in superconductors (review results of existing stability theory). *Vestnik Bauman Moscow State Technical University, Ser. 'Engineering'*, 2012, P. 17–32 (in Russian).

[247] Altshuler E., Johansen T.H. Colloquium: Experiments in vortex avalanches. *Rev. Mod. Phys.*, 2004, **76**, P. 471.

[248] Schuster H.G. *Deterministic Chaos – An Introduction Physik*. Verlag, Weinheim, 1984.

[249] Snarsky A.A., Palicky E.A., Palti A.M., Morozovskii A.E. Percolation mechanism of depinning vortices in the resistive state of thin films of superconductors of the second kind. *JETP Letters*, 1995, **61** (2), P. 112–116 (in Russian).

[250] Shklovsky B.I., Efros A.L. Percolation Theory and conductivity of strongly inhomogeneous media. *Uspekhi Fizicheskikh Nauk*, 1975, **117** (3), P. 401–433 (in Russian).

[251] Solovjev V.A., Pan V.M., Freyhard H.C. Anisotropic flux dynamics in single-crystalline and melt-textured $YBa_2Cu_3O_{7?\delta}$. *Phys. Rev. B*, 1994, **50** (18), P. 13724-?13734.

[252] Kovalenko A.N. Regulation and thermodynamic stability of nonequilibrium processes of rapid transformation of energy. *Proceedings of CKTI (I.I.Polzunov Joint Stock Company CKTI)*, 1996, **281** (2), P. 53–62 (in Russian).

[253] Arkharov A.M., Lavrov N.A., Romanovskii V.R. Features conditions electrodynamic stabilization of composites based on high-temperature superconductors with different types of nonlinearity in their current-voltage characteristics. *Journal of technical physics*, 2014, **84** (6), P. 77–85 (in Russian).

[254] URL: `https://www.nobelprize.org/nobel_prizes/physics/laureates/2016/press.html`.

[255] Hadzibabic Z., Krüger P., et al. Berezinskii–Kosterlitz–Thouless crossover in a trapped atomic gas. *Nature*, 2006, **441**, P. 1118.

[256] Berezinskii V.L. Destruction of long-range order in one-dimensional and two-dimensional systems having a continuous symmetry group I. Classical systems. *Sov. Phys. JETP*, 1971, **32** (3), P. 493–500.

[257] Kosterlitz J.M., Thouless D.J. Ordering, metastability and phase transitions in two-dimensional systems. *Journal of Physics C: Solid State Physics*, 1973, **6**, P. 1181–11203.

[258] Gibney E., Castelvecchi D. Physics of 2D exotic matter wins Nobel: British-born theorists recognized for work on topological phases. *Nature. London: Springer Nature*, 2016, **538** (7623), P. 18.

[259] Haldane F.D.M. Quantum Hall effect without Landau levels: a condensed-matter realization of the parity anomaly. *Phys. Rev. Lett.*, 1988, **61**, P. 2015.

[260] Haldane F.D.M. Geometrical Description of the Fractional Quantum Hall Effect. URL: `https://arxiv.org/abs/1106.3375`, 2011.

NANOSYSTEMS: PHYSICS, CHEMISTRY, MATHEMATICS, 2016, 7 (6), P. 971–982

Phonon transmission across an interface between two crystals

A. P. Meilakhs
Ioffe Physical Technical Institute, St. Petersburg, Russia
mejlaxs@mail.ioffe.ru

DOI 10.17586/2220-8054-2016-7-6-971-982

A new model of phonon transmission across interface between two crystals is proposed which takes into account the mismatch of crystal lattices. It has been found that the mismatch of lattices results in phonon scattering at the interface even in the absence of defects. As it has been shown, at the normal incidence, longitudinally polarized phonons have much larger transmission coefficient than that of transversely polarized phonons, excluding special resonance cases. Allowance for this factor results in a calculated Kapitza resistance value that is approximately three times greater. For the quasi one-dimensional case, an exact solution has been obtained.

Keywords: Interface, Kapitza resistance, Lattice dynamics.

Received: 6 March 2016. Revised: 4 August 2016.

1. Introduction

When heat flows through the boundary between two crystals, the temperature at the interface experiences a sharp jump. The proportionality coefficient between the heat flux and the temperature jump is known as the thermal boundary resistance or the Kapitza resistance. The Kapitza resistance is a crucial parameter for calculating the heat conductivity of nanocomposite materials. These materials are needed for the development of compact, inexpensive, easily-fabricated heat sinks for electronic devices, primarily for computer processors [1, 2]. The study of thermal transmission across the crystal interface, on in its own, attracts the attention to the problem of phonon transmission across the crystal interface since, in the majority of cases, the phonons are responsible for the energy transfer across the interface. Additionally, several thermal devices, such as thermal transistors [3], thermal rectifiers [4] and thermal logical gates [5] have been recently suggested. An accurate description of crystal lattice dynamics is important for these purposes.

Various approximations are used in the theory of thermal boundary resistance. Two basic approaches are the so called Acoustic Mismatch Model (AMM) and Diffusive Mismatch Model (DMM). In the first approach [6, 7], it is suggested that the interfacial coefficients of the phonon transmission and reflection could be calculated using the elasticity theory. However, firstly, this approximation is suitable only for calculation of the Kapitza resistance at low temperatures. Secondly, this approximation doesnt take into account the phonon scattering at the crystal interface. The values of the Kapitza resistance calculated within AMM occurred significantly higher than the experimentally determined values [8].

The second approach [9] suggests, vice versa, that the interfacial scattering is very strong, and phonons incident at the interface ‘forget’ their initial direction and uniformly scatter in all directions. The Kapitza resistance calculated within this approach is higher than the value calculated within the AMM, but still doesn’t give the good agreement with the experimental data [8].

Thus, it is necessary to develop more accurate model of the phonon transmission across the interface, which takes into account the atomic structure of actual crystals. The simplest model of this kind is the one-dimensional chain with the interface. Such a model has been detailed in papers [10, 11]. Paper [12] describes the three-dimensional model of lattice dynamics near the interface. However, this model does not take into consideration the lattice mismatch of the two crystals.

More complicated models are studied by computer simulation. Thus, in paper [13] it was found that longitudinal phonons have the significantly higher interfacial transmittance coefficient than the transverse phonons. Phonon transmission across the interface is studied with a Green’s function method in [14]. It is also suggested that atoms located at the interface are randomly displaced from the position that they would occupy if they were in volume of the crystal.

The role of anharmonicity of oscillations in the phonon transmission across the interface is considered in the paper [15]. In the most recent study [16], it has been found that atoms at the interface oscillate with a frequency exceeding the maximum possible frequency in a given crystal.

The presented paper proposes an analytical description of dynamics of the crystal lattice near the interface which takes into account the mutual mismatch of the lattices. The main assumption is that displacements of atoms at the interface are not random, but determined by forces affecting them from the side of atoms of the adjacent crystal. Generally the exact solution in such a model is not possible. At the same time, the essential qualitative effects related to the lattice mismatch can be found. In particular, it is possible to explain why the transverse phonons have much lower transmission coefficients compared to longitudinal ones. It turns out that the lattice mismatch, even in the absence of defects, results in phonon scattering at the interface. This scattering is not random, but has a certain structure.

2. The model

We consider the interface between two crystals having the structure of a simple cubic lattice and contacted by both crystal surfaces $(1,0,0)$ (Fig.1). The axis x is normal to the interface. In each of the crystals we take into account the interaction with the atoms of the first and second coordination groups. Such a model of a three-dimensional crystal lattice is the most simple and well-studied [17].

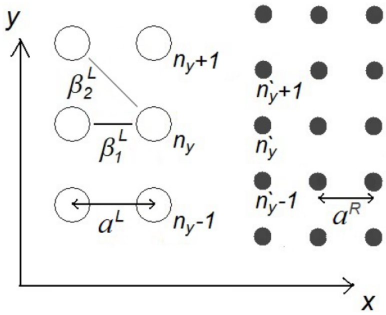

FIG. 1. Shown are the interface between two crystals (viewed from the side) and the atomic bonds considered in the model. The lattice constants are denoted as a^L, a^R; the interfacial atoms are numbered.

The lattice constants for the crystals on the left and on the right are a^L, a^R, respectively. The constants of the quasi elastic coupling with the atoms of the first and second coordination groups for the atoms of the left crystal and for the atoms of the right crystal are β_1^L, β_2^L, β_1^R, β_2^R, accordingly. We neglect the changes of the quasi elastic coupling constants and lattice constants near the interface. It is assumed that interactions between the atoms are due to short-range forces, and that with the atoms of the opposite crystal, only the atoms lying at the interface interact.

We introduce the following numbering: n_x is the numbering of atoms along the axis x. For the left crystal the numbering goes from minus infinity to zero. Atoms in the interface plane are numbered as zeroes. For the right crystal the numbering goes from zero to plus infinity. n_y, n_z is the numbering of atoms in the interface plane, it goes from the minus to plus infinity. The bold marking denotes a set of indexes $\mathbf{n} = (n_x, n_y, n_z)$.

Atoms located near the interface are influenced by an external potential produced by atoms from the opposite side of the interface. Due to this influence, the crystal is deformed, and the equilibrium position of an atom changes relative to its position in an ideal crystal. We perform the expansion of energy in the Taylor series in displacements of atoms from the positions which the nearest-to-interface atoms would occupy if they would not interact with atoms of an adjacent crystal. Derivatives of higher than third order, i.e. anharmonic terms, are not taken into consideration. The following expressions are valid for atoms on both sides therefore the index denoted the side is omitted.

Thus, we obtain:

$$U(..,\vec{r}_{\mathbf{n}},...) = \sum_{\mathbf{n},\alpha} \frac{\partial U}{\partial r_{\mathbf{n},\alpha}} r_{\mathbf{n},\alpha} + \frac{1}{2} \sum_{\mathbf{n},\alpha} \sum_{\mathbf{l},\beta} \frac{\partial^2 U}{\partial r_{\mathbf{n},\alpha} \partial r_{\mathbf{l},\beta}} r_{\mathbf{n},\alpha} r_{\mathbf{l},\beta}, \tag{1}$$

where $r_{\mathbf{n},\alpha}$ – is the displacement of $\mathbf{n}$-th atom along the axis α, $\alpha = x, y, z$; $U(..,\vec{r}_{\mathbf{n}},...)$ is the potential energy as a function of the displacement.

In the equilibrium position, the condition $\forall \mathbf{n}, \dfrac{\partial U}{\partial r_{\mathbf{n},\alpha}} = 0$ is fulfilled. We substitute the introduced expression for the potential energy into Eq. (1), and obtain:

$$\frac{\partial U}{\partial r_{\mathbf{n},\alpha}} + \sum_{\mathbf{l},\beta} \frac{\partial^2 U}{\partial r_{\mathbf{n},\alpha} \partial r_{\mathbf{l},\beta}} r^0_{\mathbf{l},\beta} = 0. \tag{2}$$

This system of $3N$ equations (N, number of atoms) determines the displacements $r^0_{\mathbf{l},\beta}$ at zero temperature in the absence of atomic oscillations, or 0-displacements, that are displacements of atoms from the position about which the potential energy is expanded into the Taylor series, to the equilibrium position.

Now, we set temperature to not equal to zero and atoms oscillate about the equilibrium position. Then the total displacement of an atom consists of the 0-displacement and its displacement due to thermal oscillations: $r_{\mathbf{n},\alpha} = r^0_{\mathbf{n},\alpha} + u_{\mathbf{n},\alpha}$. The expression for the potential energy can be rewritten as:

$$U(..,\vec{r}_{\mathbf{n}},...) = \sum_{\mathbf{n},\alpha} \frac{\partial U}{\partial r_{\mathbf{n},\alpha}} (r^0_{\mathbf{n},\alpha} + u_{\mathbf{n},\alpha}) + \frac{1}{2} \sum_{\mathbf{n},\alpha} \sum_{\mathbf{l},\beta} \frac{\partial^2 U}{\partial r_{\mathbf{n},\alpha} \partial r_{\mathbf{l},\beta}} (r^0_{\mathbf{n},\alpha} + u_{\mathbf{n},\alpha})(r^0_{\mathbf{l},\beta} + u_{\mathbf{l},\beta}). \tag{3}$$

According to the Newtons second law:

$$m\ddot{u}_{\mathbf{n},\alpha} = -\frac{\partial U}{\partial u_{\mathbf{n},\alpha}} = -\frac{\partial U}{\partial r_{\mathbf{n},\alpha}} - \sum_{\mathbf{l},\beta} \frac{\partial^2 U}{\partial r_{\mathbf{n},\alpha} \partial r_{\mathbf{l},\beta}} (r^0_{\mathbf{l},\beta} + u_{\mathbf{l},\beta}). \tag{4}$$

By using the definition of the 0-displacement (2), we have:

$$m\ddot{u}_{\mathbf{n},\alpha} = -\sum_{\mathbf{l},\beta} \frac{\partial^2 U}{\partial r_{\mathbf{n},\alpha} \partial r_{\mathbf{l},\beta}} u_{\mathbf{l},\beta}. \tag{5}$$

Thus, by taking into account only the terms of the Taylor series containing derivatives of not higher than the second order, the 0-displacements are completely excluded from the equations of lattice vibrations.

Let us define the interface, at which the average 0-displacements are much less than the lattice constant, as ideal. Interaction of 0-displacements with lattice vibrations is revealed only if the terms of Taylor series with third and higher derivatives are taken into account. Obviously, if the model of an ideal interface could be described properly, the real interface, the latter should be sufficiently smooth, and the interaction between atoms on opposite sides of the interface essentially weaker than interaction between atoms of the same crystal.

3. Equation for the quasi one-dimensional case

Let's consider first the simple case where the phonon falls normally at the interface, that is, the wave vector components are parallel to the interface q_y, $q_z = 0$.

We define $u^L_{\mathbf{n},\alpha}$ to be the displacement of the $\mathbf{n}$-th atom lying on the left side of the interface along the axis α, and $u^R_{\mathbf{n}',\beta}$ the displacement of the $\mathbf{n}'$-th atom on the right side of the interface along the axis β. Newtons second law for the $\mathbf{l}$-th atom of the left crystal lying at the interface is then given by:

$$m\ddot{u}^L_{\mathbf{l},\alpha} = -\sum_{\mathbf{n}\neq\mathbf{l},\beta} \frac{\partial^2 U}{\partial u^L_{\mathbf{l},\alpha} \partial u^L_{\mathbf{n},\beta}} u^L_{\mathbf{l},\beta} - \sum_{\beta} \frac{\partial^2 U}{\partial u^L_{\mathbf{l},\alpha} \partial u^L_{\mathbf{l},\beta}} u^L_{\mathbf{l},\beta} - \sum_{\mathbf{n}',\beta} \frac{\partial^2 U}{\partial u^L_{\mathbf{l},\alpha} \partial u^R_{\mathbf{n}',\beta}} u^R_{\mathbf{n}',\beta}. \tag{6}$$

We take into account that:

$$\frac{\partial^2 U}{\partial u^L_{\mathbf{l},\alpha} \partial u^L_{\mathbf{l},\beta}} = -\sum_{\mathbf{n}\neq\mathbf{l}} \frac{\partial^2 U}{\partial u^L_{\mathbf{l},\alpha} \partial u^L_{\mathbf{n},\beta}} - \sum_{\mathbf{n}'} \frac{\partial^2 U}{\partial u^L_{\mathbf{l},\alpha} \partial u^R_{\mathbf{n}',\beta}}, \tag{7}$$

as follows from the fact that the energy does not change if the atoms of both crystals are displaced by an equal distance in the same direction. Substitution of Eq. (7) in Eq. (6) gives:

$$m\ddot{u}^L_{\mathbf{l},\alpha} = -\sum_{\mathbf{n}\neq\mathbf{l},\beta} \frac{\partial^2 U}{\partial u^L_{\mathbf{l},\alpha} \partial u^L_{\mathbf{n},\beta}} (u^L_{\mathbf{n},\beta} - u^L_{\mathbf{l},\beta}) - \sum_{\mathbf{n}',\beta} \frac{\partial^2 U}{\partial u^L_{\mathbf{l},\alpha} \partial u^R_{\mathbf{n}',\beta}} (u^R_{\mathbf{n}',\beta} - u^L_{\mathbf{l},\beta}). \tag{8}$$

The first term in the right part of Eq. (8) describes the interaction of an atom with atoms of the same crystal, the second one relates to the interaction with atoms lying on the other side of the interface.

We seek a solution in the form of superposition of the incident, reflected and transmitted waves. We do not take into consideration the wave scattering at the interface, so that the wave vector components of the reflected and transmitted waves, parallel to the interface, equal zero. In this case, there are three reflected and three transmitted waves with different polarizations. Let us assume that from the left, at the interface falls the wave of unit amplitude and polarization 1. Then, for an atom on the left side (not necessary at the interface itself) we obtain:

$$u^L_{\mathbf{n},\alpha} = \exp{(i\omega t)} \Big(\exp{(-iq^L_1 a^L n_x)} e^L_{1\alpha} + A_1 \exp{(iq^L_1 a^L n_x)} e^L_{1\alpha} + A_2 \exp{(iq^L_2 a^L n_x)} e^L_{2\alpha} + A_3 \exp{(iq^L_3 a^L n_x)} e^L_{3\alpha} \Big). \tag{9}$$

Here, indexes $1, 2, 3$ denote polarization, $A_{1,2,3}$ amplitudes of the reflected waves with different polarization, $q_{1,2,3}$ are x-components of the wave vectors. $\vec{e}^{\,L}_{1,2,3}$ stand for the polarization vectors, e_α for the component of the polarization vector in direction of the axis α. At the interface $n_x = 0$, so for interfacial atoms each exponent in Eq. (9) becomes unity.

The wave vector values $q_{1,2,3}$ are assumed to be known for the given frequency ω, because the disperse relation for the waves in a simple cubic lattice is known [17]. Near the interface, it also may be that the values $q^L_{2,3}$ are imaginary, that is, the oscillation is gradually damping inward into the crystal (see the paper [11] and discussion in section **7**). Subsequently, we assume that the phonon falls at the interface from the left, and so the crystal from the side of which the phonon falls, will be called as 'left' for brevity.

Similarly, for crystal atoms to the right of the interface we have:

$$u^R_{\mathbf{n}',\alpha} = \exp{(i\omega t)}\Big(B_1 \exp{(-iq^R_1 a^R n'_x)}\, e^R_{1\alpha} + B_2 \exp{(-iq^R_2 a^R n'_x)}\, e^R_{2\alpha} + B_3 \exp{(-iq^R_3 a^R n'_x)}\, e^R_{3\alpha}\Big), \tag{10}$$

where $B_{1,2,3}$ are the amplitudes of the transmitted waves.

Equations (9) and (10) are the solutions to Newtons equations for the atoms lying off the interface, since $q_{1,2,3}$ and ω satisfy the dispersion relations for lattice vibrations. The problem thus reduces to finding the $A_{1,2,3}$, $B_{1,2,3}$ which would satisfy Newtons equations for the interfacial atoms. For this purpose we substitute Eqs. (9) and (10) in Eq. (8) and try to simplify the expression obtained. For the term describing the interaction of an atom with atoms of the same crystal, we can proceed in a way similar to that in [12]. We divide both parts of Eq. (8) by $\exp{(i\omega t)}$, and then for the first term in the right part, we have:

$$\begin{gathered}\sum_{\mathbf{n}\neq\mathbf{l},\beta} \frac{\partial^2 U}{\partial u^L_{\mathbf{l},\alpha} \partial u^L_{\mathbf{n},\beta}} (u^L_{\mathbf{n},\beta} - u^L_{\mathbf{l},\beta}) = \sum_{\mathbf{n}\neq\mathbf{l},\beta} \frac{\partial^2 U}{\partial u^L_{\mathbf{l},\alpha} \partial u^L_{\mathbf{n},\beta}} \Big((1 - \exp{(-iq^L_1 a^L n_x)}) e^L_{1\beta} + \sum_j A_j (1 - \exp{(iq^L_j a^L n_x)}) e^L_{j\beta} \Big) = \\ \sum_{\mathbf{n}\neq l,\beta} \frac{\partial^2 U}{\partial u^L_{\mathbf{l},\alpha} \partial u^L_{\mathbf{n},\beta}} (1 - \exp{(-iq^L_1 a^L n_x)}) e^L_{1\beta} + + \sum_j A_j \sum_{\mathbf{n}\neq\mathbf{l},\beta} \frac{\partial^2 U}{\partial u^L_{\mathbf{l},\alpha} \partial u^L_{\mathbf{n},\beta}} (1 - \exp{(-iq^L_j a^L n_x)}) e^L_{j\beta}.\end{gathered} \tag{11}$$

We take into account that the frequency and the polarization vector can be expressed in terms of the dynamic matrix [17], for both crystals:

$$\omega^2 e_{j\alpha} = \frac{1}{m} \sum_{\mathbf{n}\neq\mathbf{l},\beta} \frac{\partial^2 U}{\partial u_{\mathbf{l},\alpha} \partial u_{\mathbf{n},\beta}} (1 - \exp{(-iq_j a(n_x - l_x))} e_{j\beta} = \sum_\beta D_{\alpha\beta}(q_j) e_{j\beta}(q_j). \tag{12}$$

In Eq. (11), the summation is over the atoms of the same crystal only. To the right of the interfacial atom of the left crystal (for interfacial atoms $n_x = 0$), there are no more atoms of that crystal ($n_x \leq 0$), that can be formally taken into consideration in the form of the condition $l_x \leq n_x$. We introduce the notation:

$$D^{L\times}_{\alpha\beta}(q_j) = \frac{1}{m^L} \sum_{\substack{\mathbf{l}\neq\mathbf{n},\beta \\ l_x \leq n_x}} \frac{\partial^2 U}{\partial u^L_{\mathbf{n},\alpha} \partial u^L_{\mathbf{l},\beta}} (1 - \exp{(iq^L_j a^L l_x)}), \tag{13}$$

which is for the dynamic matrix describing the atom lying at the interface. Here, we can ignore the fact that $n_x \leq 0$, since for an interfacial atom it was taken into account in the expression $l_x \leq n_x$. So we can operate with Eq. (13) formally.

Denote the difference of the two dynamic matrices (one for an atom in the depth of the crystal and the other for an atom at the interface) as:

$$^{\otimes}D^L_{\alpha\beta}(q^L_j) = D^L_{\alpha\beta}(q^L_j) - D^{L\times}_{\alpha\beta}(q_j) = \frac{1}{m^L} \sum_{\substack{\mathbf{l}\neq\mathbf{n},\beta \\ l_x > n_x}} \frac{\partial^2 U}{\partial u^L_{\mathbf{n},\alpha} \partial u^L_{\mathbf{l},\beta}} (1 - \exp{(iq^L_j a^L l_x)}). \tag{14}$$

We substitute Eqs. (12), (13) in Eq. (8) and transfer the first term of the right part of Eq. (8) to the left. The expression thus obtained can be written in new notations in the form:

$$\sum_j A_j \sum_\beta {}^{\otimes}D^L_{\alpha\beta}(q^L_j) e^L_{j\beta} + {}^{\otimes}D^L_{\alpha\beta}(-q^L_1) e^L_{1\beta} = -\sum_{\mathbf{n}',\beta} \frac{\partial^2 U}{\partial u^L_{\mathbf{n},\alpha} \partial u^R_{\mathbf{n}',\beta}} (u^R_{\mathbf{n}',\beta} - u^L_{\mathbf{n},\beta}). \tag{15}$$

Now, we rearrange the right part of Eq.(15) by using the relation:

$$K_{\mathbf{n},\alpha\beta} = \sum_{\mathbf{n}'} \frac{\partial^2 U}{\partial u^L_{\mathbf{n},\alpha} \partial u^R_{\mathbf{n}',\beta}}, \tag{16}$$

which is the matrix of the interfacial interaction, describing the interaction of an atom with atoms lying on the opposite side of the interface, where $n_x = 0$ is supposed. Unlike the conventional dynamic matrix, this type of matrix depends on the n, because each atom at the interface is differently located relative to atoms on the opposite side of the interface.

Substituting Eqs. (10), (16) into Eq. (15), we come to:

$$\sum_j A_j \overset{\otimes}{\sum_\beta} D^L_{\alpha\beta}(q^L_j)e^L_{j\beta} +^{\otimes} D^L_{\alpha\beta}(-q^L_1)e^L_{1\beta} = -\sum_\beta K_{\mathbf{n},\alpha\beta}\Big(-e^L_{1\beta} + \sum_j (B_j e^R_{j\beta} - A_j e^L_{j\beta})\Big). \tag{17}$$

Then, we sum over all values of n in Eq.(17) and divide the result by a total number of atoms N at the interface on the left. The left part of the expression is unchanged for it is independent of the number n of the atom. In the right part of the expression, we obtain:

$$K^L_{\alpha\beta} = \frac{1}{N}\sum_{\mathbf{n}} K_{\mathbf{n},\alpha\beta}. \tag{18}$$

This is the averaged matrix describing the interaction of atoms across the interface. By performing such an averaging, we do not take into account that the atoms nearest to the interface differ in their position relative to atoms on the opposite side of the interface, and, hence, interact differently with them. Taking account of this difference involves the appearance of scattering, which calls for mathematical technique presented below in Sec. **5**. In this section, we proceed ignoring the scattering. The problem in this case becomes quasi-one-dimensional.

Let the relation:

$$M^{L,\pm}_{\alpha j} = \sum_\beta \big({}^{\otimes}D^L_{\alpha\beta}(\pm q_j) - K^L_{\alpha\beta}\big)e^L_{j\beta}, \tag{19}$$

be the second dynamical matrix. It expresses the forces acting on atoms near the interface in terms of amplitudes of waves differing in polarization on the left side of the interface. To write the analogous expression for the forces acting on atoms on the other side of the interface, we introduce:

$$I^L_{\alpha j} = \sum_\beta K^L_{\alpha\beta} e^R_{j\beta}. \tag{20}$$

With new notations, Eq. (17) can be rewritten in the form:

$$M^{L,-}_{\alpha j} A_j + I^L_{\alpha j} B_j = -M^{L,+}_{\alpha 1}, \tag{21}$$

where the summation is supposed to be performed over the repetitive index j standing for the wave polarization.

By writing Newtons second law for atoms on the right of the interface, one can rearrange the obtained expression in a similar way. A distinction is in the fact that the averaged matrix of the interfacial interaction is defined as:

$$K^R_{\beta\alpha} = \frac{1}{N'}\sum_{\mathbf{n}'}\sum_{\mathbf{n}} \frac{\partial^2 U}{\partial u^L_{\mathbf{n},\alpha}\partial u^R_{\mathbf{n}',\beta}} = \frac{N}{N'}K^L_{\alpha\beta}, \tag{22}$$

where N' is a number of atoms nearest to the interface in the crystal on the right. The amounts of atoms near the interface are related as inverse squares of the lattice constants. Thus, we obtain:

$$K^R_{\beta\alpha} = \left(\frac{a^L}{a^R}\right)^2 K^L_{\alpha\beta}, \tag{23}$$

which represents the fact that the force acting on the right crystal from the side of the left one is equal, in magnitude, to the force acting on the left crystal from the side of the right one. Finally, we have:

$$M^{L,-}_{\alpha j} A_j + I^L_{\alpha j} B_j = -M^{L,+}_{\alpha 1}, \quad M^{R,+}_{\alpha j} B_j + I^R_{\alpha j} A_j = -I^R_{\alpha 1}. \tag{24}$$

This is the sought-for system of equations.

4. Theorem on the interfacial interaction and the exact solution in the quasi-one-dimensional case

Let us study the matrix of interfacial interaction, $K_{\alpha\beta}$, using the fact that the interaction energy of two crystals is invariant with respect to the displacements by any linear combination of the lattice vectors. We consider first the general case when the lattice parameters are incommensurate, that is, their ratio is irrational, $a^L/a^R \notin \mathbb{Q}$. In this case, linear combinations of the lattice vectors and, hence, a set of rearrangements converting the system into itself, is dense on the plane. It is reasonable to require that the energy be continuous as the function of the relative displacement of the crystals. Since the energy is constant on the dense set and, besides, is continuous, it is constant.

To be specific, we will demonstrate that $K_{yy} = 0$. We displace the first crystal by a small distance Y along the axis y. The energy in a new state will, on the one hand, be equal to the initial one, and on the other, be a different amount of work done by the force of interaction between crystals:

$$E = E + \int\limits_{0}^{Y} K_{yy} y dy \Rightarrow K_{yy} Y^2/2 = 0 \quad \Rightarrow \quad K_{yy} = 0. \tag{25}$$

For the other seven components of the matrix $K_{\alpha\beta}$ (except for K_{xx}), the proof can be performed in a similar way. Thus, we conclude that, with initial assumptions, the only nonzero component of the matrix of interfacial interaction is K_{xx}.

We now consider a case of resonance where $a^L/a^R \in \mathbb{Q}$. It is obvious that the above reasoning is inapplicable. Let $a^L/a^R = p/q$ and $p/q < 1$. The interaction energy U of two crystals will be described by a periodical function of their relative displacement with a period qa^L. We expand it and $K_{\alpha\beta}$ into the Fourier series and substitute the result in Eq. (16). The first, largest term of the series turns out to be:

$$K^R_{\alpha\beta 1} = \frac{1}{q^2 (a^L)^2} U_1. \tag{26}$$

We drop the other terms and obtain the following assessment for the case of equal potentials of the interatomic interaction:

$$K_{\alpha\beta} \sim 1/q^2, \quad a^L/a^R = p/q, \quad K_{\alpha\beta} = 0, \quad a^L/a^R \notin \mathbb{Q}. \tag{27}$$

Such a function experiences a discontinuity in all rational points, which is impossible from the physical point of view. This paradox can be resolved from the consideration that this function was obtained ignoring the interaction with 0-displacements which are large near the resonance. Accounting for the anharmonic coupling with 0-displacements leads to smearing of spikes at rational points. As a result, the actual matrix of the interfacial interaction will be given by a smooth envelope for the function (27).

Hence, we come to the following qualitative result: the atomic oscillations perpendicular to the plane of the interface interact intensively with the atomic oscillations on the opposite side of the interface only in the case when the ratio of the lattice constants is close to a rational number with a small denominator. Otherwise, this interaction is weak.

This result can be illustrated by an interesting analogy in nebular mechanics, where the close commensurability of revolution periods of planets, i.e., the proximity of a ratio of periods to a rational number with a small denominator, leads to the strong long-period perturbation [18].

Using the predetermined theorem on the matrix of the interfacial interaction, one can obtain an exact solution in the quasi-one-dimensional nonresonance case. We write explicitly the expressions for the elements of the matrix ${}^{\otimes}D_{\alpha\beta}(q_j)$, recalling that in considered model we take into account the interaction with the atoms of the first and second coordination groups only (see Fig. 1), indexes L, R are ommited:

$$\begin{gathered} {}^{\otimes}D_{xx}(q_j) = \frac{\beta_1 + 2\beta_2}{m}(1 - e^{iq_x a}), \\ {}^{\otimes}D_{yy}(q_j) = {}^{\otimes}D_{zz}(q_j) = \frac{\beta_2}{m}(1 - e^{iq_x a}), \\ {}^{\otimes}D_{xy}(q_j) = {}^{\otimes}D_{xz}(q_j) = {}^{\otimes}D_{yz}(q_j) = 0. \end{gathered} \tag{28}$$

The remaining three components are also equal zero since the matrix is symmetrical.

We denote $K^L_{xx} = \beta^L$, $K^R_{xx} = \beta^R$.

Let a longitudinally polarized wave is incident at the interface. Substituting Eqs. (27), (28) in Eq. (18), we get:

$$M^{L,\pm}_{x,1} = \frac{\beta^L_1 + 2\beta^L_2}{m^L}\left(1 - \exp\left(\pm i q^L_x a^L\right)\right) - \frac{\beta^L}{m^L}. \tag{29}$$

In addition, one can easily see that according to the theorem on the matrix of interfacial interaction all nondiagonal components of the matrix M equal zero. Hence, when the incident wave is longitudinally polarized, the reflected and transmitted waves also have longitudinal polarization. The system of six linear equations (23) transforms into the simple system of two linear equations:

$$M^{L,-}_{x,1} A_1 + \beta^L B_1 = -M^{L,+}_{x,1}, \quad M^{R,+}_{x,1} B_1 + \beta^R A_1 = -\beta^R, \tag{30}$$

From whence, it follows:

$$A_1 = \frac{\beta^L \beta^R - M^{L,+}_{x,1} M^{R,+}_{x,1}}{M^{L,-}_{x,1} M^{R,+}_{x,1} - \beta^L \beta^R}, \quad B_1 = \frac{\beta^R \left(M^{L,+}_{x,1} - M^{L,-}_{x,1}\right)}{M^{R,+}_{x,1} M^{L,-}_{x,1} - \beta^L \beta^R}. \tag{31}$$

This solution coincides with the result obtained in the paper [10] for a one-dimensional chain if one rewrite it in the above notations.

Later, we consider the case where the wave with transverse polarization is incident at the interface. For the sake of specificity, we assume that the oscillations occur along the axis y. Since, according to the theorem on the matrix of interfacial interaction we have $K_{yy} = 0$, the corresponding equations for the transmission coefficient have the form:

$$M_{y,2}^{L,-} A_2 = -M_{y,1}^{L,+}, \quad M_{y,2}^{R,+} B_2 = 0, \tag{32}$$

whence $B_2 = 0$, $|A_2| = 1$.

Actually, however, K_{yy} is small but does not equal zero, because the 0-displacements, although small, are nonzero. It was shown in the paper [10] that for small incident wave frequencies, the transmission coefficient is independent of the interaction force of atoms at the interface, but determined by acoustic impedances of media on opposite sides of the interface. However, when the interaction force of interfacial atoms is weak, the transmission coefficient of phonons decreases fast with increased frequency. Since the heat transport is carried out by phonons of all frequencies, we can neglect the contribution to the energy transport across the interface from atomic oscillations parallel to the interface.

5. Fourier transform of the matrix of interfacial interaction

In order to study the phonon transmission across the interface between two crystals in more general case when a phonon is incident at arbitrary angle, and take into consideration the scattering, a special mathematical apparatus is required which is presented below. For simplicity, we consider the one-dimensional case, because subsequent generalization to more dimensions is trivial.

Let us have an infinite one-dimensional chain of atoms spaced a^L apart. The atoms of the chain are numbered from minus infinity to plus infinity, and the axis x is located so that the zero-th atom has the coordinate $x = 0$. We place the chain into the external potential $\Phi(x)$ with a period a^R, $\Phi(x + a^R) = \Phi(x)$.

Let's expand the $\Phi(x)$ into the Fourier series:

$$\Phi_k = \frac{1}{2\pi a^R} \int_0^{a^R} \Phi(x) \exp\left(-2\pi i k x / a^R\right) dx,$$

$$\Phi(x) = \sum_{k=-\infty}^{+\infty} \Phi_k \exp\left(2\pi i k x / a^R\right). \tag{33}$$

Then, the potential energy of n-th atom, Φ_n, will equal $\Phi(na^L)$, or

$$\Phi_n = \sum_{k=-\infty}^{+\infty} \Phi_k \exp\left(2\pi i k n (a^L/a^R)\right). \tag{34}$$

One can demonstrate that the inverse rearrangement is also valid:

$$\Phi_k = \lim_{N\to\infty} \frac{1}{2N} \sum_{n=-N}^{N} \Phi_n \exp\left(-2\pi i k n (a^L/a^R)\right). \tag{35}$$

Actually,

$$\lim_{N\to\infty} \frac{1}{2N} \sum_{n=-N}^{N} \Phi_n \exp\left(-2\pi i k n (a^L/a^R)\right)$$

$$= \lim_{N\to\infty} \frac{1}{2N} \sum_{n=-N}^{N} \Big(\sum_{k'=-\infty}^{+\infty} \Phi_{k'} \exp\left(2\pi i k' n (a^L/a^R)\right)\Big) \exp\left(-2\pi i k n (a^L/a^R)\right)$$

$$= \sum_{k'=-\infty}^{+\infty} \Phi_{k'} \lim_{N\to\infty} \frac{1}{2N} \sum_{n=-N}^{N} \exp\left(2\pi i (k'-k) n (a^L/a^R)\right) = \sum_{k'=-\infty}^{+\infty} \Phi_{k'} \delta_{k'k} = \Phi_k. \tag{36}$$

For what follows, Eq. (34) can be conveniently rewritten so that it would correspond to the expansion in exponents with the wave vectors q_k lying in the first Brillouin zone, i.e., $q_k \in (-\pi/a^L, \pi/a^L)$. To do so, we introduce:

$$q_k = \frac{2\pi}{a^L} \left(\left\{ k\frac{a^L}{a^R} + \frac{1}{2} \right\} - \frac{1}{2} \right), \tag{37}$$

and, finally, we obtain:

$$\Phi_n = \sum_{k=-\infty}^{+\infty} \Phi_k \exp\left(iq_k a^L n\right). \tag{38}$$

Equation (34) can be applied to the matrix $K_{\mathbf{n},\alpha\beta}$ and that to use it for description of the phonon transmission across the interface of two crystal we have to rearrange it. Really,

$$K_{\mathbf{n},\alpha\beta} = \frac{\partial}{\partial u^L_{\mathbf{n},\alpha}} \sum_{\mathbf{n}'} \frac{\partial U}{\partial u^R_{\mathbf{n}',\beta}}. \tag{39}$$

The function:

$$\Phi = \sum_{\mathbf{n}'} \frac{\partial U}{\partial u^R_{\mathbf{n}',\beta}} \tag{40}$$

is periodical (the period a^R), since the potential produced by atoms of the right crystal for atoms of the left crystal is periodical. Hence, we can introduce:

$$K_{\mathbf{k},\alpha\beta} = \lim_{N\to\infty} \frac{1}{N} \sum_{\mathbf{n}} K_{\mathbf{n},\alpha\beta} \exp\left(-2\pi i \mathbf{k}\mathbf{n}(a^L/a^R)\right),$$
$$K_{\mathbf{n},\alpha\beta} = \sum_{\mathbf{k}=-\infty}^{+\infty} K_{\mathbf{k},\alpha\beta} \exp\left(2\pi i \mathbf{k}\mathbf{n}(a^L/a^R)\right), \tag{41}$$

where $\mathbf{k} = (0, k_y, k_z)$.

6. Equation and the theorem on the interfacial interaction in the general case

Let the wave of the unit amplitude, polarization 1 and wave vector $\mathbf{q}_1$ fall at the interface. Notations: $\mathbf{q}_{||} = (0, q_y, q_z)$ are the wave vector components parallel to the interface, and $\mathbf{n}_{||} = (0, n_y, n_z)$ are the atom numbers along the axes y, z parallel to the plane of the interface. We seek the solution for the left side in the form of superposition of the incident and reflected waves:

$$u^L_{\mathbf{n},\alpha} = \exp(i\omega t)\Big(\exp(-iq^L_{1,x} n_x a^L + i\mathbf{q}^L_{||}\mathbf{n}_{||}a^L)e^L_{1\alpha}$$
$$+\sum_{j,\mathbf{k}} A_{\mathbf{k},j} \exp(iq^L_{j,x} n_x a^L + i(\mathbf{q}_{||} + 2\pi i\mathbf{k}/a^R)\mathbf{n}_{||}a^L)\, e^L_{\mathbf{k},j\alpha}\Big), \tag{42}$$

And for the right side, in the form of superposition of the transmitted waves:

$$u^R_{\mathbf{n}',\alpha} = \exp(i\omega t) \sum_{j,\mathbf{k}'} B_{\mathbf{k}',j} \exp(iq^L_{j,x} n'_x a^R + i(\mathbf{q}_{||} + 2\pi i\mathbf{k}'/a^L)\mathbf{n}'_{||}a^R)\, e^L_{\mathbf{k},j\alpha}. \tag{43}$$

We substitute Eqs. (42), (43) into Eq. (8). Then, we divide the obtained equation by $\exp i(\mathbf{q}_{||}\mathbf{n}_{||}a^L)$ and multiply by $\exp(2\pi i\mathbf{l}/a^R)\mathbf{n}_{||}a^L)$. Then, we sum over $\mathbf{n}$ so that the total number of additives would equal N, and divide by N.

We introduce:

$$K_{\mathbf{n},\alpha\beta}(\mathbf{q}_{||}) = \sum_{\mathbf{n}'_{||},\beta} \frac{\partial^2 U}{\partial u^L_{\mathbf{n},\alpha}\partial u^R_{\mathbf{n}',\beta}} \exp\left(i\mathbf{q}_{||}(\mathbf{n}'_{||}a^R - \mathbf{n}_{||}a^L)\right), \tag{44}$$

$$K^L_{\mathbf{k}\mathbf{k}',\alpha\beta}(\mathbf{q}_{||}) = \sum_{\mathbf{n}'_{||}\mathbf{n}_{||},\beta} \frac{\partial^2 U}{\partial u^L_{\mathbf{n},\alpha}\partial u^R_{\mathbf{n}',\beta}} \exp\left(i\mathbf{q}_{||}(\mathbf{n}'_{||}a^R - \mathbf{n}_{||}a^L)\right) \exp\left(2\pi i(\mathbf{k}_{||}\mathbf{n}_{||}a^L/a^R + \mathbf{k}'_{||}\mathbf{n}'_{||}a^R/a^L)\right). \tag{45}$$

Similarly, as was done in section **3**, we introduce the second dynamic matrices; the matrix describing the interaction of the waves with the same $\mathbf{q}_{||}$:

$$M^{L,\pm}_{\mathbf{k},\alpha j} = \sum_{\beta}\left({}^{\otimes}D_{\alpha\beta}(\pm\mathbf{q}^L_{j,x} + \mathbf{q}_{||} + 2\pi i\mathbf{k}/a^R) - K_{0,\alpha\beta}\right)e^L_{\mathbf{k},j\beta}, \tag{46}$$

the matrix describing the interaction with the oscillations on the opposite side of the interface:

$$I^L_{\mathbf{k},\alpha j}(\mathbf{q}_{||}) = \sum_{\beta} K^L_{\mathbf{k}\mathbf{k}',\alpha\beta}(\mathbf{q}_{||})e^R_{\mathbf{k}',j\beta}. \tag{47}$$

and the matrix describing the interaction with the oscillations of the same crystal, but with another $\mathbf{q}_{||}$:

$$S^{L,\pm}_{\mathbf{k},\alpha j} = \sum_{\beta} K_{\mathbf{k},\alpha\beta} e^{L}_{\mathbf{k},j\beta}. \tag{48}$$

In these notations, we can finally write:

$$M^{L,-}_{\mathbf{l},\alpha j} A_{\mathbf{l},j} + \sum_{\mathbf{k}} S^{L}_{\mathbf{k},\alpha j} A_{\mathbf{l}-\mathbf{k},j} + \sum_{\mathbf{k}'} I^{L}_{\mathbf{k}',\alpha j}(\mathbf{q}_{||}) B_{\mathbf{k}',j} = -M^{L,+}_{\mathbf{0},\alpha 1}\delta_{\mathbf{l0}}. \tag{49}$$

For the right crystal a similar approach gives:

$$M^{R,+}_{\mathbf{l}',\alpha j} B_{\mathbf{l},j} + \sum_{\mathbf{k}'} S^{R}_{\mathbf{k}',\alpha j} B_{\mathbf{l}'-\mathbf{k}',j} + \sum_{\mathbf{k}} I^{R}_{\mathbf{k},\alpha j} A_{\mathbf{k},j} = -I^{R}_{\mathbf{0},\alpha 1}\delta_{\mathbf{l0}}. \tag{50}$$

Equations (57) and (58) taken together form a complete system of equations describing the transmission, reflection and scattering of phonons at the interface between two crystals.

Thus, it is seen that, on the one hand, even in the model of an ideal interface without defects and roughness, scattering due to the mismatch of the crystal lattices appears. Alternatively, the assumption in DMM that a phonon incident on the interface 'forget' its initial direction is, generally speaking, incorrect. The scattering reveals a quite determined structure; the wave vector of the transmitted wave, parallel to the interface, differs from the wave vector of the incident wave by an integer number of the vectors of the reciprocal lattice of the left crystal, while the wave vector, parallel to the interface, of the reflected wave differs from the wave vector of the incident wave by an integer number of the vectors of the reciprocal lattice of the right crystal. For vectors of the scattered phonons lying in the first Brillouin zone, all that remains is to rearrange them using Eq. (37).

It is impossible to solve the infinite system of Eqs. (57) and (58) analytically. However, if the function Φ, in terms of which the matrix $K_{\mathbf{n},\alpha\beta}$ is determined in Eq. (39), is rather smooth, the coefficients of its expansion into the Fourier series decreases rapidly, as do the matrices $K_{\mathbf{k},\alpha\beta}$ describing the scattering. In this case, one can choose a finite number of the terms from the system (57, 58) and solve it numerically. In the case when the matrices $K_{\mathbf{k},\alpha\beta}$ are large, even at large values of $\mathbf{k}$, one can consider the assumption of the DMM as being valid.

To facilitate the numerical calculation of the problem, it is reasonable to invoke the theorem on the matrix of the interfacial interaction in the general. Lets expand the function Φ into the Fourier series:

$$\Phi(x) = \sum_{\mathbf{k}=-\infty}^{+\infty} \Phi_k \exp\left(2\pi i \mathbf{k} x / a^R\right). \tag{51}$$

On substitution into Eq. (39), we find that the matrix $K^{L}_{\mathbf{k},\alpha\beta}$ is expressed in terms of the components of Φ as:

$$K^{L}_{\mathbf{k},\alpha\beta} = k_\alpha \Phi_k. \tag{52}$$

Thus, $K_{(0,k_z),y\beta} = 0$ and $K_{(k_y,0),z\beta} = 0$. We use the fact that according to Eq. (23), $K^{R}_{\beta\alpha} = (a^L/a^R)^2 K^{L}_{\alpha\beta}$ and that for $K^{R}_{\beta\alpha}$ the expression analogous to Eq. (39) is valid. We obtain:

$$K^{L}_{0,\alpha\beta} = \beta\delta_{\alpha x}\delta_{\beta x}. \tag{53}$$

Thus, the atomic oscillations parallel to the interface do not contribute to the transmission of phonons without scattering at the interface.

7. The uniform crystal limited case

To test the system (49, 50), let us formaly apply it to the case of uniform crystal. We will formally name the plane $(1,0,0)$ in the crystal with simple cubic lattice as a boundary. Which means $a^L = a^R = a$; $\beta^L_1 = \beta^R_1 = \beta_1$, $\beta^L_2 = \beta^R_2 = \beta_2$. Obviously enough, in this case, the phonons will not reflect at the 'interface' because there can be no reflection in a uniform medium so $|B_1| = 1$, $A_i = B_2 = B_3 = 0$. Let us check that it follows from the system (49, 50).

In the considered case, the matrix of interfacial interaction does not depend on the number of atoms:

$$K_{\mathbf{n},\alpha\beta}(\mathbf{q}_{||}) = K_{\alpha\beta}(\mathbf{q}_{||}) = \sum_{\mathbf{n}'_{||},\beta} \frac{\partial^2 U}{\partial u^{L}_{\mathbf{n},\alpha}\partial u^{R}_{\mathbf{n}',\beta}} \exp\left(i\mathbf{q}_{||}(\mathbf{n}'_{||} - \mathbf{n}_{||})a\right), \tag{54}$$

and all different matrices $K^{L}_{\mathbf{kk}',\alpha\beta}$ degenerate into a single matrix

$$K^{L}_{\mathbf{kk}',\alpha\beta} = K^{R}_{\mathbf{kk}',\alpha\beta} = K_{\alpha\beta}(\mathbf{q}_{||}) = \sum_{\mathbf{n}'_{||}\mathbf{n}_{||},\beta} \frac{\partial^2 U}{\partial u^{L}_{\mathbf{n},\alpha}\partial u^{R}_{\mathbf{n}',\beta}} \exp\left(i\mathbf{q}_{||}(\mathbf{n}'_{||} - \mathbf{n}_{||})a\right). \tag{55}$$

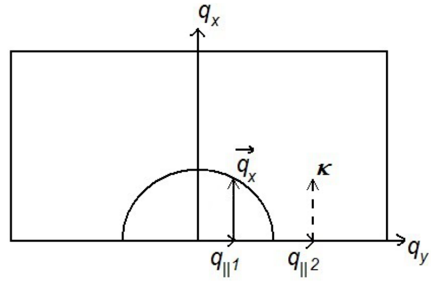

FIG. 2. A surface of constant frequency in the Brillouin zone. It is shown that a phonon with the component of the wave vector parallel to the interface, $q_{||1}$ passes through it. When an incident phonon has the component of the wave vector parallel to the interface $q_{||2}$, on the opposite side there appears an inward-damping oscillation with the damping coefficient κ (shown by dashed arrow)

The second dynamical matrices also degenerate into a single one:

$$M^{L,\pm}_{\alpha j} = \sum_{\beta} \big({}^{\otimes}D_{\alpha\beta}(\pm\mathbf{q}^{L}_{j,x} + \mathbf{q}_{||}) - K_{\alpha\beta} \big) e_{j\beta}, \tag{56}$$

the matrix describing the interaction with the oscillations on the opposite side of the interface:

$$I^{L}_{\alpha j}(\mathbf{q}_{||}) = \sum_{\beta} K_{\alpha\beta}(\mathbf{q}_{||}) e_{j\beta}, \tag{57}$$

and

$$S^{L,\pm}_{\mathbf{k},\alpha j} = 0. \tag{58}$$

After a similar transformation of the right crystal matrices, an infinite system of equations (49, 50) becomes a system of six equations:

$$\begin{aligned} M^{L,-}_{\alpha j} A_j + I^{L}_{\alpha j} B_j &= -M^{L,+}_{\alpha 1}, \\ M^{R,+}_{\alpha j} B_j + I^{R}_{\alpha j} A_j &= -I^{R}_{\alpha 1}. \end{aligned} \tag{59}$$

Let us verify that $B_1 = \exp(i\mathbf{q}_x a)$, $A_i = B_2 = B_3 = 0$ is a solution. Indeed, after the substitution, we obtain:

$$\begin{aligned} I^{L}_{\alpha 1} \exp(i\mathbf{q}_x a) &= -M^{L,+}_{\alpha 1}, \\ M^{R,+}_{\alpha 1} \exp(i\mathbf{q}_x a) &= -I^{R}_{\alpha 1}. \end{aligned} \tag{60}$$

We substitude equations (56, 57) into the first equation of the system (60) and obtain:

$$\sum_{\beta} K_{\alpha\beta}(\mathbf{q}_{||}) e_{1\beta} \exp(i\mathbf{q}_x a) = -\sum_{\beta} \big({}^{\otimes}D_{\alpha\beta}(\pm\mathbf{q}^{L}_{1,x} + \mathbf{q}_{||}) - K_{\alpha\beta} \big) e_{1\beta}. \tag{61}$$

By defenition (55) $K_{\alpha\beta}(\mathbf{q}_{||})\,(1 - \exp(i\mathbf{q}_x a)) =^{\otimes} D_{\alpha\beta}(\mathbf{q}^{L}_{j,x} + \mathbf{q}_{||})$, from which it follows that (61) holds identically. The second equation in the system is quite similarly checked (60).

8. Refraction of phonons at the crystal interface

Let's give a qualitative description of refraction of phonons at the crystal interface. To do so, we display the surface of the constant frequency ω in the Brillouin zone (Fig. 2) and make a projection of this surface onto the plane (q_y, q_z). If the component $\mathbf{q}_{||}$ of the incident phonon is lying in the limits of this projection, it is easy to see that for the transmitted phonon the wave vector component normal to the interface, q_x, is equal to the q_x of that point in the Brillouin zone which was projected into the point $\mathbf{q}_{||}$.

If the component $\mathbf{q}_{||}$ of the incident phonon lies beyond the projection, the transmitted phonon does not appear, because there is no the q_x such that the phonon with the wave vector $(q_x, q_{||y}, q_{||z})$ has the frequency ω. In this case, there occurs an oscillation directed into the depth from the interface, with the damping coefficient κ and wave vector parallel to the interface $\mathbf{q}_{||}$. The specific cases of such oscillations are well known Rayleigh waves [19]. Just as there are three branches of oscillations for the given $\omega, \mathbf{q}_{||}$, one should perform the above procedure for each of them.

If the frequency of the incident wave exceeds the maximum possible in the given branch, in the crystal, an inward-damping oscillation at any value of $\mathbf{q}_{||}$ occurs. Oscillations of this kind were predicted in the model of a one-dimensional chain in paper [11]. Probably, it is such oscillations that were found in numerical simulations in work [16].

The maximum frequency of the transverse oscillations for a simple cubic lattice lies inside and not on the boundary of the Brillouin zone [17]. At some frequencies, the surface of constant frequency for these oscillation branches is closed (Fig. 3). In this case to every $\mathbf{q}_{||}$, lying inside the projection of the isofrequency surface onto the plane (q_y, q_z), correspond two values of q_x. To these two values of q_x correspond different values of the derivative $\partial\omega/\partial q_x$, and, hence, different directions for energy propagation.

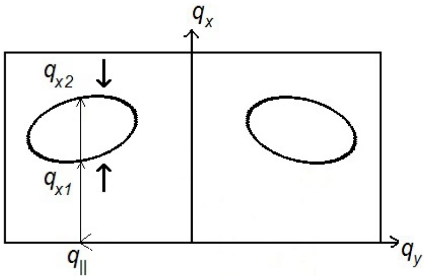

FIG. 3. It was shown that to each component $\mathbf{q}_{||}$, lying inside the projection of the isofrequency surface onto the (q_y, q_z), correspond two values of q_x. To these two values of q_x correspond different values of the derivative $\partial\omega/\partial q_x$, and, hence, different directions for energy propagation (shown by solid arrows)

The transmitted waves should have the same sign q_x as the incident (and the reflected the opposite) due to the principle of causality. In addition, because of the energy conservation law, the energy flux direction is the same for the incident and transmitted waves. If we assume that the incident wave is one in which the energy propagates towards the interface, then the value of q_x in such a wave can be both positive and negative. Correspondingly, one should take the sign of q_x in the transmitted and reflected waves. The uncertainty is thus eliminated.

An interesting effect occurs when the parallel-to-the interface component of the wave vector, $q_{||}$, of the incident phonon is beyond the Brillouin zone of the right crystal (Fig. 4). In this case, the phonon is refracted and undergoes the Bragg scattering simultaneously. Then it appears that the refracted phonons have the opposite direction of propagation, in the plane of the interface, relative to the incident phonons. Thus, inverse refraction takes place.

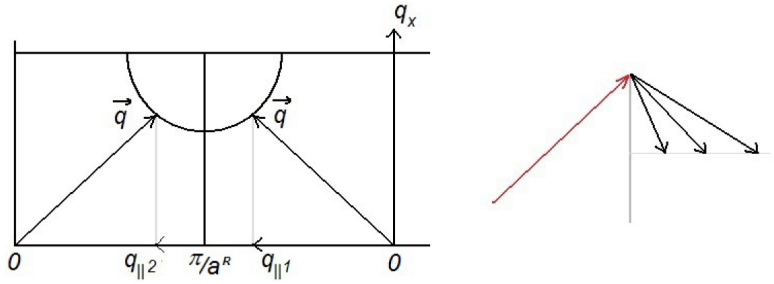

FIG. 4. Schematically displayed is the surface of the constant frequency in the Brillouin zone. It was shown that the incident phonon with the parallel-to-interface wave vector component $q_{||}$ lying outside the Brillouin zone of the right crystal, is refracted in the opposite direction

It is interesting to note, that the energy flux in the direction perpendicular to the interface should be conserved for each solution of the system of Eqs. (57), (58). However, for each solution, the energy flux in the plane of the interface can be different on the opposite sides from the interface. This means that at the interface not only the temperature may undergo a jump but the thermal flux parallel to the interface plane as well.

9. Conclusion

In this paper, we have studied the model of the interface between two crystals taking into consideration the mismatch of crystal lattices. The basic assumption of the model is that displacements of atoms near the interface are not random but determined by interaction with atoms of the other crystal. We have shown that in the harmonic approximation, such displacements have no effect on phonon transmission across the interface. The equation was set up, which determines the amplitudes of the transmitted and reflected waves of lattice oscillations. The exact solution has been derived for the quasi-one-dimensional case.

It was shown that the mismatch of lattices leads to the scattering of phonons at the crystal interface. In other words, the scattering appears even in the case of the ideal interface in the absence of defects and roughness. On the other hand, such scattering occurs non-uniformly in all directions but has a certain structure.

It has been established that the finiteness of the lattice parameter results, at certain angles of incidence, in the backward phonon refraction at the interface. A new family of lattice oscillations has been described, which includes only the atoms lying near the crystal interface. It was predicted that at the plane parallel to the interface, the heat flow experience a discontinuity at the interface.

The main result of our study is that we have shown that the oscillations of atoms in the plane of the interface interact weakly with the oscillations of atoms on the opposite side of the interface, except for specific resonance cases. In the case of normal incidence of phonons at the interface, the transmission coefficient of the transversely polarized phonons is much less as compared to that of the longitudinally polarized phonons. For an arbitrary angle of incidence, the transmission coefficients of phonons of any polarization are less than that calculated with the elasticity theory, even in the case of low frequencies. Allowance for this factor leads one to conclude that the calculated value of Kapitza resistance is approximately three times greater. Calculation of the interface thermal resistance, performed by means of the method proposed in the work [20], gives significantly lower values, as compared to those experimentally obtained. Accounting for the smallness of the transmission coefficient of transversely polarized phonons explains this discrepancy.

Acknowledgements

The author thanks E. D. Eidelman and G. V. Budkin for helpful critical comments, and A. Ya. Vul for attention to this study. The work was supported by the Russian Foundation for Basic Research (Project No. 16-03-01084 A).

References

[1] Kidalov S. V., Shakhov F. M. Thermal Conductivity of Diamond Composites. *Materials*, 2009, **2**, P. 2467–2495.

[2] Zhang C., Wang R., et al. Low-temperature densification of diamond/Cu composite prepared from dual-layer coated diamond particles. *J. Material Science*, 2015, **26**, P. 185-190.

[3] Li B., Wang L., Casati G. Negative differential thermal resistance and thermal transistor. *Appl. Phys. Lett.*, 2006, **88**, 143501.

[4] Terraneo M., Peyrard M., Casati G. Controlling the Energy Flow in Nonlinear Lattices: A Model for a Thermal Rectifier. *Phys. Rev. Lett.*, 2002, **88**, P. 094302.

[5] Wang L., Li B. Thermal Memory: A Storage of Phononic Information. *Phys. Rev. Lett.*, 2008, **101**, P. 267203.

[6] Khalatnikov I. M. Heat Transfer Between Solids and Liquid Helium II. *JETP*, 1952, **22**, P. 687

[7] Little W. A. The Transport Of Heat Between Dissimilar Solids At Low Temperatures. *Can. J. Phys.*, 1959, **37**, P. 334–349.

[8] Stoner R. J., Maris H. J. Kapitza conductance and heat flow between solids at temperatures from 50 to 300 K. *Phys. Rev. B*, 1993, **48**, P. 16373.

[9] Swartz T., Pohl R. O. Thermal resistance at interfaces. *Rev. Mod. Phys.*, 1989, **61**, P. 605–608.

[10] Zhang L., Keblinski P., Wang J.-S., Li B. Interfacial thermal transport in atomic junctions. *Phys. Rev. B*, 2011, **83**, P. 064303.

[11] Meilakhs A. P., Eidelman E. D. New Model of Heat Transport across the MetalInsulator Interface by the Example of Boundaries in a DiamondMetal Composite. *JETP Letters*, 2013, **97**, P. 38–40.

[12] Young D. A., Maris H. J. Lattice-dynamical calculation of the Kapitza resistance between fcc lattices. *Phys. Rev. B*, 1989, **40**, P. 3685–3693.

[13] Hu M., Keblinski P., Schelling P. K. Kapitza conductance of siliconamorphous polyethylene interfaces by molecular dynamics simulations. *Phys. Rev. B*, 2009, **79**, P. 104305.

[14] Tian Z., Esfarjani K., Chen G. Enhancing phonon transmission across a Si/Ge interface by atomic roughness: First-principles study with the Greens function method. *Phys. Rev. B*, 2012, **86**, P. 235304.

[15] Saaskilahti K., Oksanen J., Tulkki J., Volz S. Role of anharmonic phonon scattering in the spectrally decomposed thermal conductance at planar interfaces. *Phys. Rev. B*, 2014, **90**, P. 134312.

[16] Yang N., Luo T. et. al. Thermal Interface Conductance between Aluminum and Silicon by Molecular Dynamics Simulations. *J. Comp. and Theor. Nanoscience*, 2015, **12**, P. 168.

[17] Anselm A. I. *Introduction to Semiconductor Theory*. Englewood Cliffs.: Prentice-Hall, 1981.

[18] Arnold V. I. *Collected Works*, Vol. 1, Springer, 2009, 253 p.

[19] Landau L. D., Lifshitz E. M. *Course of Theoretical Physics, Vol. 7: Theory of Elasticity*. New York.: Pergamon, 1986.

[20] Meilakhs A. P. Nonequilibrium Distribution Function in the Presence of a Heat Flux at the Interface between Two Crystals. *Phys. Solid State*, 2015, **57**, P. 148–152.

NANOSYSTEMS: PHYSICS, CHEMISTRY, MATHEMATICS, 2016, 7 (6), P. 983–1001

Silicene is a phantom material

E. F. Sheka

Department of Theoretical Physics and Mechanics
Peoples' Friendship University of Russia,
Str. Miklukho-Maklay, 6, Moscow 117198, Russia

sheka@icp.ac.ru

DOI 10.17586/2220-8054-2016-7-6-983-1001

The paper presents a comparative consideration of sp^2 nanocarbons and their silicon and higher tetrels analogues from the viewpoint of the spin molecular theory taking into account the electron correlation in open-shell molecules. High radicalization of silicene and quantum instability of flat honeycomb 2D structures of germanene and stanene make all the species phantom materials leaving graphene the only one-atom thick 2D solid free of the crucial restrictions.

Keywords: silicene, siligraphene, boronitrosilicene, spin molecular theory, unrestricted Hartree-Fock formalism, open-shell molecules.

Received: 30 May 2016

1. Introduction

Silicene holds a special place in graphene science. This phantom material was called into being by an unprecedented activity of the graphene science development, while not of the science itself, but of its theoretical-computational part predominantly. Actually, the first appeal to silicene took place even before the 'graphene era' in 1994 [1] when looking for Si and Ge analogues of graphite. Since the sought-for materials did not exist (as well as they have not existed until now) the study was restricted to the theoretical consideration. Evidently, one-atom thick monolayer of the Si- (and Ge-) graphite of presumably sp^2 electron configuration was the mainly studied model. Because of hexagonal honeycomb structure of the layers, the prediction of Dirac cones attributed to π bands at K points of the Brillouin zone was quite expected. This was the point from which a close similarity between graphene and its virtual heavier-tetrel analogues started. The repeated reference to the subject took place 13 years later [2] when the term *silicene* was introduced to describe virtual free standing one-atom thick honeycomb monolayer consisting of silicon atoms. In the frame of tight-binding approximation, a description of silicene was suggested in terms of Dirac fermions similarly to the one described for graphene. The study was the beginning of a large stream of theoretical and computational studies, implementing and securing representation in the scientific community about a new highly promising material (see reviews [3–8] and references therein).

The era of real silicene started in 2008 when a possibility to obtain strips of adsorbed silicon atoms on Ag(110) surface was firstly announced [9]. A new and attractive word *silicene* was largely used across the publication, though no one-atom honeycomb free-standing structure was fixed. Just as a response to the publication, a quantum-chemically grounded skeptical view on silicene's existence was suggested [10]. As if supporting this conclusion and making sure that the free-standing silicene cannot be obtained, experimenters have focused their efforts on obtaining hexagon-packed structure of silicon atoms monolayers on different surfaces. By 2012 a few groups had succeeded in experimental observations of the sought silicon monolayers obtained in due course of epitaxial growth in ultra high vacuum on different surfaces of crystalline silver [11–14] and diboride [15]. Successful experiments on Ir [16] and other substrates (see a comprehensive review [17]) then followed. The produced monolayers are tightly connected with substrates and are rightly referred to as *epitaxial silicene* [1]. The monolayers behave as typical objects of surface science, subordinating to crystallography of substrates in the best way and undergoing phase transitions when the substrate crystallography favors them.

Epitaxial silicene demonstrates some properties, such as the availability of Dirac cones in the electronic bands at Fermi level [11, 14] and lays the foundation of the report on the silicene field-effect transistor due to growth–transfer–fabrication process that was devised via epitaxial silicene encapsulated delamination with native electrodes [18]. However, these features are mostly related to the physics of adlayers on different substrates, which is rich and highly variable but has no connections with that demonstrated by real free standing graphene sheets. Therefore, remaining in the field of graphene science, one should join for a common discussion theoretical consideration of graphene and virtual silicene only. And the first question which must be answered is: Why free standing silicene cannot exist? The current paper is aimed at answering the question on the basis of clarifying what we know about spin effects in *sp*^{2} nanosilicons and relativistic electrons of silicene and what the difference is between the latter ones and those of graphene.

2. Dirac Fermions in 2D Silicene Crystal

Theoretical investigations of silicene have been presented in hundreds of publications. However, paradoxically they cover a rather narrow range of topics. The first thing to note concerns a complete ignoring (except two papers [10, 19]) crystalline-molecular dualism that is so picturesque in graphene and forms two streams in the graphene theoretical investigations, dividing them into solid state and molecular ones. In the case of silicene, there is solely the first one, moreover, with a substantial predominance of Dirac's fermions concept. Evidently, it is due to a desire to see properties in silicene that may be useful when applied in electronics and spintronics. Addressing quantum chemical calculations, it is the reason for a particular preference of periodical boundary conditions (PBC) in constructing models for further computational studying within the DFT approach mainly, involving its tight-binding version.

Because the Si-Si interatomic distance is larger than that of C-C, π-π (better to say p_z-p_z) overlap weakens due to which two DFT PBC honeycomb configurations are usually considered, namely, planar and buckled shown in the top of Fig. 1. π Bands structures in the bottom of the figure are obtained by using *ab initio* calculations [21]. As in the case of graphene, π bands of silicene involve cones in the vicinity of the Fermi level at energy E_f which is a consequence of hexagon symmetry of the considered honeycomb structures. In the absence of spin-orbit coupling (SOC), the bands in this region are described by the Dirac-like Hamiltonian $\hbar v_F \boldsymbol{\sigma} \cdot \boldsymbol{\kappa}$. However, the SOC in silicene is quite considerable due to significant intrinsic SOC in silicon atoms. Accordingly, the quasirelativistic Hamiltonian is modified by including SOC and takes the form [20]:

$$\hat{H} \approx \begin{pmatrix} -\xi\sigma_z & v_F(k_x + ik_y) \\ v_F(k_x + ik_y) & \xi\sigma_z \end{pmatrix}, \tag{1}$$

where v_F is the Fermi velocity of π electrons near the Dirac points with nearly linear energy dispersion, σ_z is Pauli matrix and ξ presents the effective SOC. The above equation results in the spectrum:

$$E(\boldsymbol{\kappa}) = \pm\sqrt{(v_F k)^2 + \xi^2)}. \tag{2}$$

Therefore, one can estimate the energy gap, which is 2 ξ at the Dirac points and is of 0.07 *meV* and 1.55 *meV* for planar and buckled silicene, respectively. Such presentation of the low-energy band structure has been widely accepted in general, although repeated calculations disclose some quantitative variations.

Much effort has been invested to experimentally observe Dirac fermions (see rev. [7] and references therein). At the same time it was not about a confirmation of theoretical consideration, since it does not concern the difference between virtual and epitaxial silicene that was obvious. The insisting attempts were challenged by the fact that the Dirac cones are a consequence of hexagonal symmetry of one-atom thick layers which could be expected in the case of epitaxial silicene as well. Actually, a similar packing in monolayers of adsorbed atoms were not so rare in surface science when a proper substrate was selected. The expectations came true and the Dirac cones were observed for monolayers of silicon atoms at Ag (111)-(1x1) surface by angle-resolved photo-electron spectroscopy (ARPES) [11] and quasiparticle interference (QPI) [14]. The Ag(111) surface happens to be the most suitable for hosting regular structures of atomic silicon adsorbate. Apparently it is coherent with the regular hexagon-packed adlayers of silver on Si(111)-(1x1) surface that were the beloved objects of the surface science.

Fig. 2 exhibits the Dirac cone obtained by ARPES [11]. A clearly seen energy gap of 0.3 *eV* was observed. The value greatly exceeds that caused by the SOC and points to a strong substrate influence. The problem of the substrate still remains a contested point hindering the justification for applying the quasirelativistic Dirac fermion concept to the description of epitaxial silicene [17]. This is particularly the case due to the still unmet expectations of the spin Hall Effect the observation of which at suitable temperatures is favored by significant SOC.

3. Spin Effects of Silicon-Based Open-Shell Molecules

3.1. Peculiarities of the $N_D(R)$ Graphs of C=C, Si=C, and Si=Si Bonds

In order to better understand the spin effects of silicene molecules , we will address the cluster (molecular) approach to the silicene model structure instead of PCB duplication of primitive unit cells so that possible quantum instability of low-dimensional systems can be avoided [22]. Next, the standard closed-shell DFT formalism, which is mainly used and which is practically unable to disclose spin effects, will be substituted by the unrestricted Hartree-Fock (UHF), which has established itself as a very effective means of detecting delicate spin features of molecules [23, 24]. The effects determine the characteristics for the open-shell character of the latter and

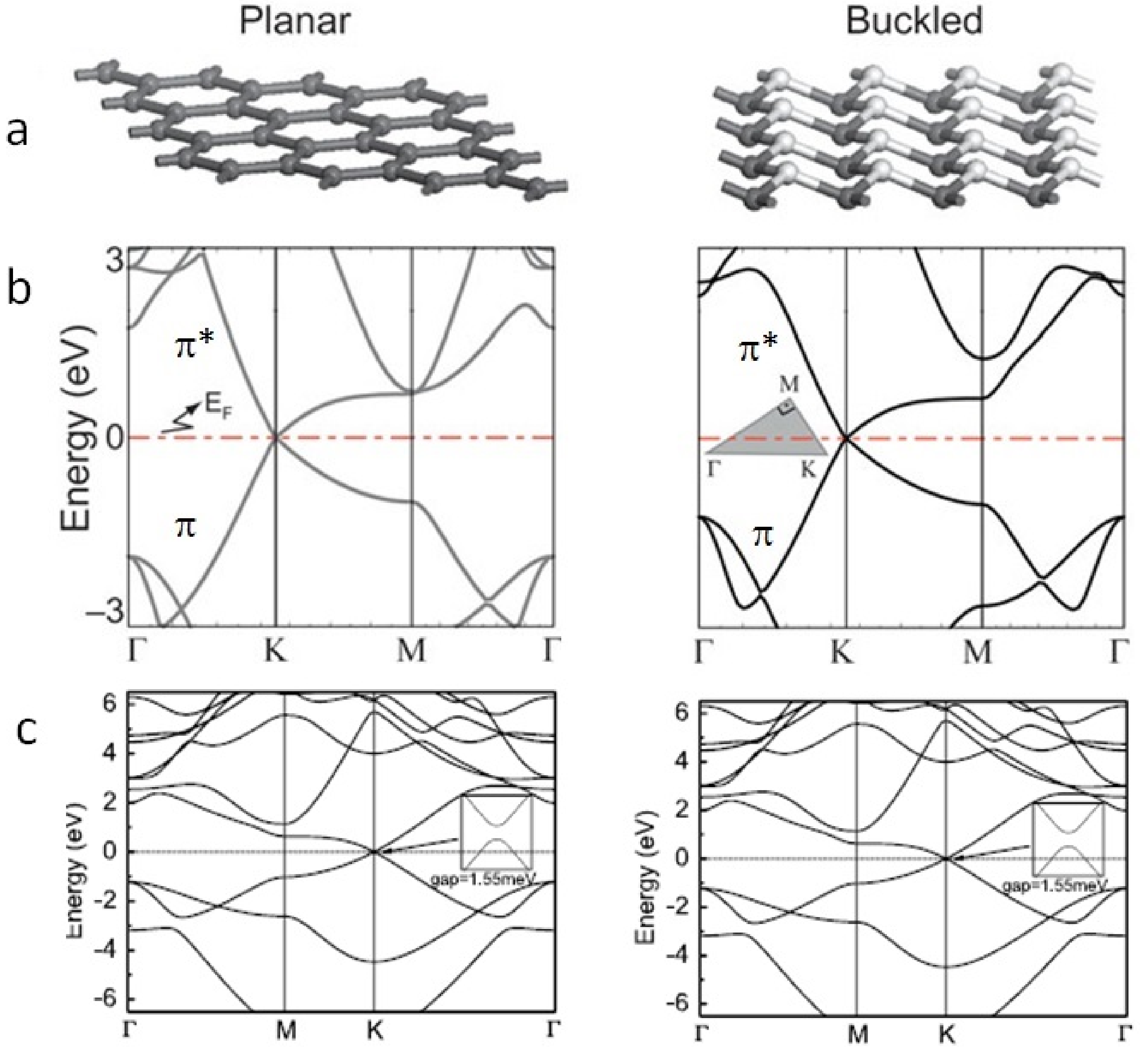

FIG. 1. (a),(b). Geometry and band structure of flat and buckled DFT PBC silicene (adapted from [21]). (c) Band structure involving SOC (adapted from [20])

are described by spin contamination of their electronic states that causes the availability of effectively unpaired electrons of N_D total number. Concerning *sp*^{2} siliceous molecules, we meet the spin effects first when looking for disilene molecules. Based on the data of a scrupulous study of the issue [25], Fig. 3 presents $N_D(R)$ graphs related to the dissociation of ethylene, silaethylene (or silaethene), disilene and disilane molecules. Comparing the graphs for C=C and Si=Si bonds, a drastic difference becomes evident. In the case of ethylene, one can distinctly see that π electrons govern the molecule's continuous dissociation when the interatomic distance changes from 1.4 Å to 1.9 Å and then comes the turn of σ electrons until the dissociation is completed at 2.8 Å. At equilibrium the molecule is a closed-shell one with the C=C bond of 1.326 Å in length. Oppositely, π electrons are practically unobservable under disilene dissociation since already in equilibrium they are almost fully transformed into a pair of effectively unpaired electrons ($N_D = 1.78e$). Therefore, disilene has no closed-shell phase at all and in the equilibrium state is open-shell one. Essentially similar but quantitatively different is the situation for the Si=C bond of silaethylene. As seen in the figure, at equilibrium, the molecule is open-shell one, the radicalization of which requires $0.153e$.It is well documented that both silaethylene and disilene molecules are highly reactive and their stabilization usually occurs at low temperatures in rare gas matrices [26].

Since the π electrons of silaethylene and disilene are highly dissociated, the valence electron hybridization is evidently not *sp*^{2} one. This is consistent with the previouh conclusion that because of the large size and the inner-shell electron's shielding in silicon atoms, the overlap between p_z-orbitals in the relevant molecules is negligibly small, and thus tends to not form π-bonds preferentially [27]. This feature greatly influences the valence

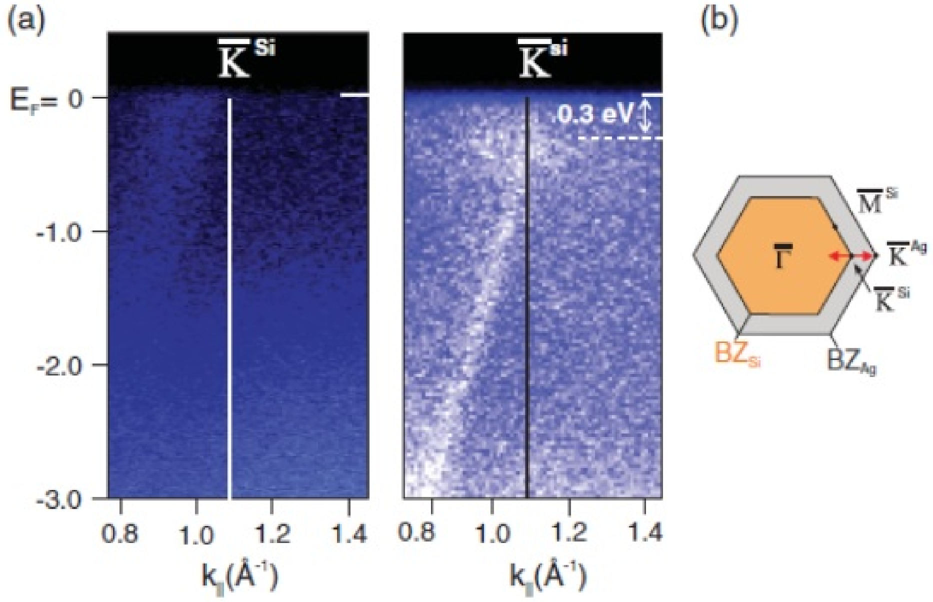

FIG. 2. (a) Angle-resolved photo-electron spectroscopy intensity map for the clean Ag surface (left) and after formation of the 2D Si adlayer (right), taken along the $\vec{\Gamma} \cdot \vec{K}^{Ag}$ direction through the silicene $\vec{K}^{Si}$ point ($h\nu$=126 eV). (b) Brillouin-zone scheme of the 2D Si layer with respect to the Ag(111)-(1×1) surface. The red arrow indicates the ARPES measurement direction (adapted from [11])

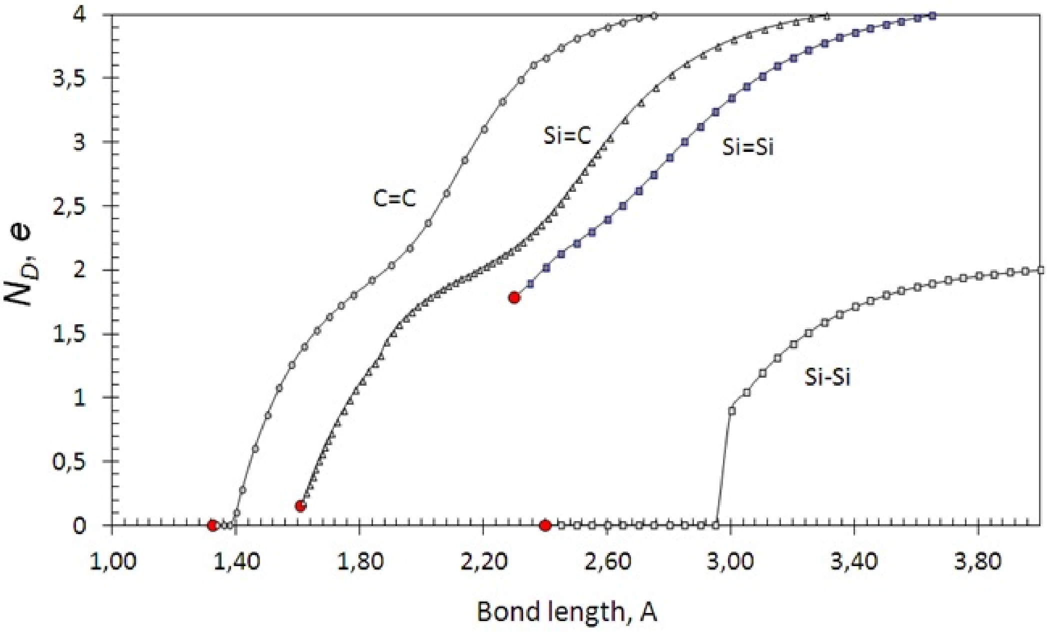

FIG. 3. $N_D(R)$ graphs related to the dissociation of double C=C, Si=C and Si=Si as well as single Si-Si bonds. Big balls mark the bonds in the equilibrium state of ethylene, silaethylene, disilene and disilane molecules, respectively. UHF AM1 calculations

electrons' hybridization, changing it from *sp*^{2} for carbon atoms to *sp*^{3}-like for silicon [28] when p_z electrons become effectively unpaired. Consequently, the number of effectively unpaired electrons presents a measure of the transition between the two hybridization modes. When the value per atom, namely, N_{DA}, is zero, the relevant atoms retain their *sp*^{2} mode. When N_{DA} is unity one should speak about a complete unpairing of p_z electrons and of *sp*^{3} hybridization with the only difference that the feature concerns not valence-terminated atoms (as in the case of disilane) but radicals. Within this range one can speak of *sp*^{3}-like hybridization that gradually strengthens while N_{DA} increases from zero to unity. In the case of ethylene the equilibrium-state N_{DA} is zero, which provides a clear vision of the *sp*^{2} hybridization of the molecule atoms. In disilene, $N_{DA} = 0.89e$, which is quite close to unity, which amply explains why the equilibrium Si-Si distance in this case (2.30 Å) is close to that of disilane (2.40 Å).

3.2. Silicon Analogues of sp^2 Carbonaceous Molecules

To make the picture more complete, the results obtained for siliceous molecules will be discussed alongside with those related to the core-equivalent carbon analogs. The data of a complete family of such-selected X-compounds (X=C, Si) is presented in Table 1. The number of odd electrons N counts all valence electrons that do not participate in the formation of σ bonds; $\Delta E^{RU} = E^{RHF} - E^{UHF}$ presents the difference of energies related to closed-shell (restricted) and open-shell (unrestricted) odd electron configurations. Eight different molecules were compared, among which there are X-benzene, fullerene X_{60}, fragments of (6,6) and (10,0) single-walled X-nanotubes, with both empty and hydrogen-terminated end atoms, and (3,7) X-hexagon flat fragments with two types of the edgeatom termination. The computations have revealed a high similarity in the shape of equilibrium structures of the molecules with the only difference concerning the length of the relevant C=C and Si=Si bonds. As for ΔE^{RU} and N_D parameters, the first one is a consequence of the spin-dependent splitting of the degenerate restricted Hartree-Fock (RHF) states and is given in the table in absolute and percentage values, the latter given in parentheses with respect to the E^R energy. The second parameters present the total number of effectively unpaired electrons N_D and the doubled spin contamination since due to the numbers of spins α and β and are equal, $N_D = 2\Delta\hat{S}^2$. In parentheses is given roughly averaged value, α obtained by just dividing N_D to the number of X-type atoms involved. The actual distribution of the value over the molecule's structure is quite irregular (see numerous examples in [23]) and should be calculated for each molecule individually.

The data listed in Table 1 exhibit a tremendous difference in the data for carbon and silicon molecules caused by the difference in the correlation of their p_z electrons. Thus, in the carbon family the electron correlations and transformations from closed-shell to open-shell molecules have exhibited themselves starting from fullerene C_{60}, while benzene molecule is well defined closed-shell species. In the series of condensed aromatics, the electron correlation becomes visible in naphthalene and strengthens when the molecule size increases [29]. Thus nature seems to let benzene play a particular role for establishing and proving the aromaticity concept as well as for introducing π electrons in organic chemistry. In contrast to benzene, fullerene C_{60}, as well as the studied fragments of carbon nanotubes and graphene belongs to the open-shell class of molecules and exhibit quite strong electron correlation. This very effect explains unique peculiarities of the species concerning their chemistry, magnetism, and biomedical behavior that have been discussed in detail previously [23]. At the same time, the p_z N_D values fill the interval (0.17 e – 0.39 e) due to which the species are not completely radicalized and the atom hybridization, though *sp*^{3}-like one, is close to *sp*^{2}. Both these features account for the production and existence of the carbon species under ambient conditions.

In contrast to the above case, all the quantities related to the silicon counterparts clearly highlight a very strong electron correlation and the atom hybridization close to the radical *sp*^{3} one in all the cases This results in practically complete radicalization of the species. Actually, as seen in the table, the N_D values are equal to or even slightly exceed the number of odd electrons N in all the cases making molecules N-fold radicals. A complete radicalization of the species evidently prevents from their production and existence at ambient conditions. A schematic view of the difference between carbon and silicon valence deficient compounds, presented in Fig. 4 on the background of the graph of ethylene, clearly shows the difference between the two families of species.

Therefore, the silicon-based open-shell molecules exhibit tremendous spin effects that are consequence of a strong correlation of their p_z electrons, on the one hand, and cause high radicalization of the molecules as whole, on the other [29]. The last feature is the main reason that prevents one from obtaining these species experimentally. As for computational description, the open-shell character of the molecules mandatorily requires their consideration in the framework of the CI theory. While the UHF formalism covers CI effects virtually [30] the DFT (including UDFT) is quite insensitive to the latter. At the same time, most published computational results have been obtained when using one of the available DFT closed-shell versions thus making the performed considerations unrealistic.

TABLE 1. Equilibrium structures of silicon-based molecules and ΔE^{RU} and N_D parameters of the equi-X-core (X=C, Si) molecules; number of odd electrons N and effectively unpaired N_D in e; energies in $kcal/mol$

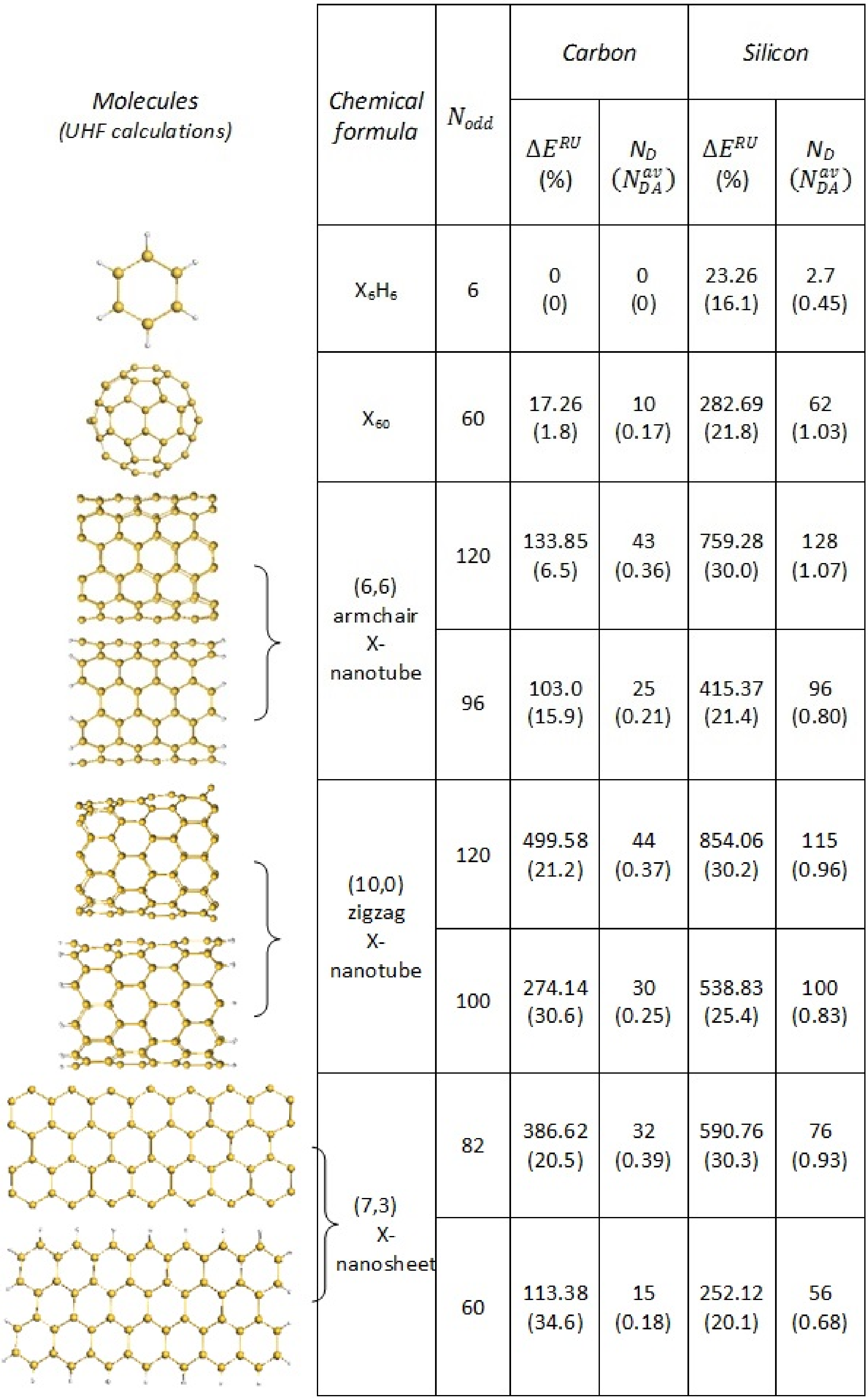

Molecules (UHF calculations)	Chemical formula	N_{odd}	Carbon		Silicon	
			ΔE^{RU} (%)	N_D (N_{DA}^{av})	ΔE^{RU} (%)	N_D (N_{DA}^{av})
	X_6H_6	6	0 (0)	0 (0)	23.26 (16.1)	2.7 (0.45)
	X_{60}	60	17.26 (1.8)	10 (0.17)	282.69 (21.8)	62 (1.03)
	(6,6) armchair X-nanotube	120	133.85 (6.5)	43 (0.36)	759.28 (30.0)	128 (1.07)
		96	103.0 (15.9)	25 (0.21)	415.37 (21.4)	96 (0.80)
	(10,0) zigzag X-nanotube	120	499.58 (21.2)	44 (0.37)	854.06 (30.2)	115 (0.96)
		100	274.14 (30.6)	30 (0.25)	538.83 (25.4)	100 (0.83)
	(7,3) X-nanosheet	82	386.62 (20.5)	32 (0.39)	590.76 (30.3)	76 (0.93)
		60	113.38 (34.6)	15 (0.18)	252.12 (20.1)	56 (0.68)

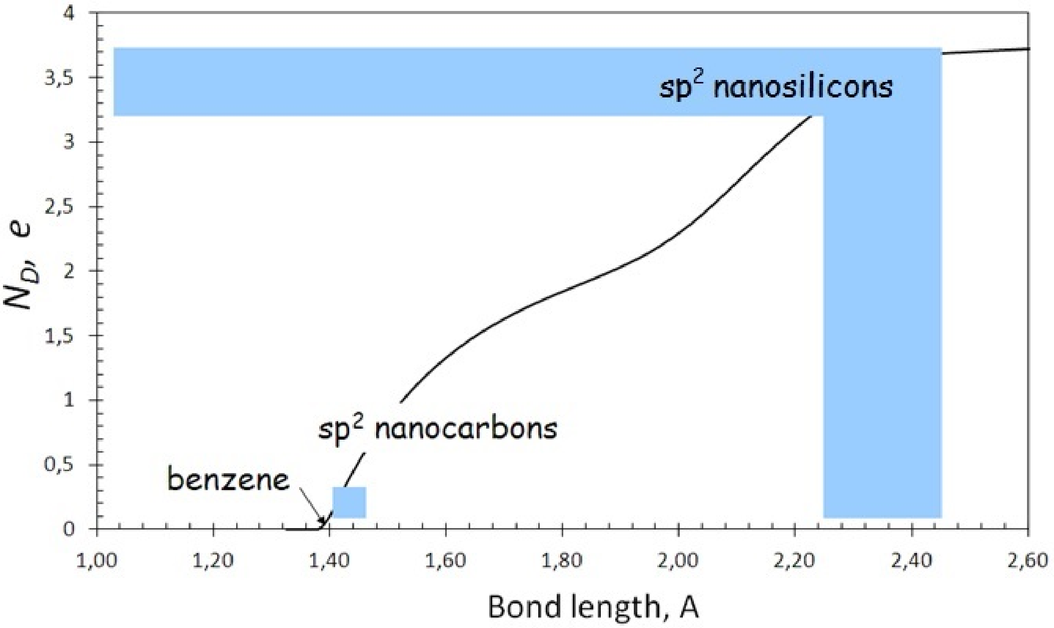

FIG. 4. A schematic presentation of the difference in the $N_D(R)$ graphs of *sp*^{2} nanocarbons and nanosilicons

4. Last News on New One-Atom Thick 2D Silicene-Based Material Si_2BN

The use of widely-accessible DFT PBC techniques has led to a virtually endless stream of publications claiming prediction of more and more ‘new 2D materials’ with a number of attractive properties (see [22] and references therewith, but a few) The latest, but certainly not to be the last one was discussed on Ray Kurzweil’s Accelerating Intelligence website on March 25, 2016. It concerned the prediction of a new one-atom thick 2D material Si_2BN made of light inexpensive earth-abundant elements boron, nitrogen, and silicon “that might push graphene into the background”. The news was accompanied with a PR movie that is still rare in practice, but certainly points to the emergence of a new trend in the presentation of scientific results directly from the authors. The material in question is based on silicon and exactly speaking presents a boronitrosilicene As in the majority of similar cases, it is predicted computationally and the authors appeal to a conventional, gentlemen’s set, including flat structure, inherent metallicity, easy flexibility high strength and presumably conductivity for heralding their discovery of “a new class of single-atom-thick graphenelike material formed from Si_2BN with unusual characteristics using *ab initio* simulations” [31]. The authors are absolutely convinced in their discovery and are not at all embarrassed by the fact that their pristine silicene is a virtual material. Apparently it should be assumed that in the framework of theoretical concepts shared by them that silicene is as real as graphene.

One could only rejoice in this power of faith in the omnipotence of quantum-chemical calculations, if only errors were not made by the authors in their calculations. Since similar errors occur frequently and tend to build on one another, it is worthwhile to consider them in detail, and in this case, Si_2BN is a good example to clearly illustrate this point. As mentioned earlier, the first trouble awaits computational experts when constructing the model structure of the species in question. Following the work of others, the authors [30] used PBC to duplicate a selected unit cell for getting an extended regular structure fully ignoring possible quantum instability of lowdimensional structures [21], which impugn the PBC application. In the case of covalent structures, involving different covalent bonds, in particular, one should be particularly careful. Thus, in the case of Si_2BN one deals with four types of covalent bonds, namely: Si=Si, Si=B, Si=N, and B-N. Not all the bonds are quite stable. Unfortunately, not much is known about the three double bonds. However, judging by the relevant single bonds, one might expect considerable instability for the Si=B bonds only. Actually, highly stable structures are characteristic for crystalline silicon and silicon nitrides while silicon boride’s crystal is metastable, primarily due to the instability of Si-B bonds [31]. The authors of the discussed paper [30] met this trouble when composing the unit cell for Si_2BN: only one of three compositions retained planar structure in the course of the further optimization. This fact should have warned the authors of the fullest confidence in the stability of the PBC-replicated structure. As will be shown below, this unease was confirmed.

The second issue concerns the calculation technique used, which as usual was one of standard versions of closed-shell DFT theory. To be confident in the correctness of the techniques application it is necessary to verify that the studied system is a closed-shell one. Graphene and silicene are open-shell systems, which is caused by length of the relevant C=C and Si=Si bonds [25]. Since the latter constitute the majority of the Si_2BN species another situation should be hardly expected in this case. The correlated open-shell systems require UHF or other CI technique for their consideration.

Following the computational study of silicene, which was discussed in detail in Section 3, let us consider Si_2BN from the viewpoint of the UHF calculations. Outlining that Si_2BN is based on the silicene honeycomb structure it would be useful for the future to mark it as s-$BNSi_2$ (as used for graphene-like materials, such as siligraphenes – see the next Section). Presented in Fig. 5a displays the (5, 5) s-$BNSi_2$ regular structure (the molecule presents a right-angled sheet with five benzenoid-like units along armchair and zigzag edges, respectively) that is coherent with the working model considered in [31]. The molecule is flat and the atom distribution is governed by chemical bonds Si=Si of 2.29 Å; Si=B of 1.62 Å; Si=N of 1.54 Å; and B-N of 1.44 Å. The first three bonds correspond to the UHF-equilibrated molecules $H_2Si{=}SiH_2$; $H_2Si{=}BH$; and $H_2Si{=}NH$, respectively. The edge silicon atoms are terminated by hydrogens. As seen in Fig. 5b, subjected to further optimization, the structure retains its flat geometry but losses honeycomb packing and becomes irregular thus becoming a perfect exhibition of quantum instability for the the PBC structure considered in [31]. The same relates to fragments of the pristine (5, 5) s-$BNSi_2$ involving quasi-benzene, quasi-naphthalene and quasi-pentacene. None of these fragments preserves the hexagonal quasibenzenoid structure involving simultaneously Si=Si, Si=N, and Si=B bonds.

To ascertain if this instability is caused by either the three-set bond group or silicon atoms entering each of the bonds, the analogous graphene (5, 5) g-BNC_2 molecule, composed in the same manner as s-$BNSi_2$, was analyzed. Fig. 5c presents the equilibrium structure of the molecule while Fig. 5d exhibits the state of its radicalization in view of the N_{DA} map that exhibits the distribution of N_D effectively unpaired electrons over the molecule's atoms. The main pattern of the map is provided by carbon atoms excluding two top and two bottom nitrogen atoms presented by their dangling bonds. The map gives evidence for both the availability of local spins at the carbon atoms and their differing values at different atom locations which reveals a peculiar distribution of C=C bond lengths over the molecule.

In view of the difference between equilibrium structures of the (5, 5) s-$BNSi_2$ and (5, 5) g-BNC_2 molecules it is possible to conclude that the breakdown of the former is caused by the chemical bonds silicon atoms being too long to be accommodated by shorter Si=B, Si=N, and B-N bonds to provide a regular honeycomb structure. Not considering these chemical features leads to erroneous heralding of 'new materials' that cannot exist even virtually. Unfortunately, such errant statements on the DFT-based PBC predictions of new materials in the current graphenics have become more commonplace In view of this it is worthwhile to remember bitter words of Roald Hoffmann in his notes on "Small but Strong Lessons of Chemistry in Nanoscience" [33]: "It is clear that quantum-mechanical modeling of molecules and extended structures has become easy to do. Much too easy, I would say... What worries me more (and just what you would expect from me ...) is that the calculations are done in a way blindly, with no calibration on related chemistry, no controlling checks with chemical intuition".

5. Silagraphenes

Another phantom material related to *sp*^{2} hybridized silicon atoms concerns the recently heralded 'new materials' called siligraphenes [34–36]. Adjusting the new nomenclature with that previously used in organosilicon chemistry, it would be better to call these compounds siligraphenes similar to silaethylene, silaalkane, and so forth. As in the case of boronitrosilicene, silagraphenes were created computationally by using a DFT PBC approach. The main idea was to place the silicon and carbon atoms constituting the cubic spatial structure of silicon carbide in one plane. Thus, by modulating Si=C bond lengths flat configurations of silagraphenes g-$Si_xC_{1-x}$with x as the governing parameter [35], g-SiC_1 and g-SiC_3 [34] and g-SiC_7 [36] were constructed. And again, the indispensable and failsafe DFT used in its standard versions related to closed-shell approximation supplemented by PBC readily issued a positive conclusion concerning the models: silagraphenes are stable graphene-like flat 2D materials of honeycomb-like structure, the latter being slightly irregular due to the difference between the C=C and Si=C bond lengths. Thus, the obtained new materials are characterized by typical spectra of the Dirac fermions. Meeting the next temptation of a possible tuning of the conical energy spectrum, the Si:C content ratio was suggested as a desired modulator. The full readiness of silagraphenes applicability to advanced electronics and spintronics was heralded.

The example discussed in the previous section compels us to treat these optimistic statements with caution. Fig. 6 presents a comparative view on isostructural silagraphenes and pristine graphene on the basis of (5, 5) nanographene (NGr) in the UHF formalism framework. The panels on the right of the figure show the equilibrium

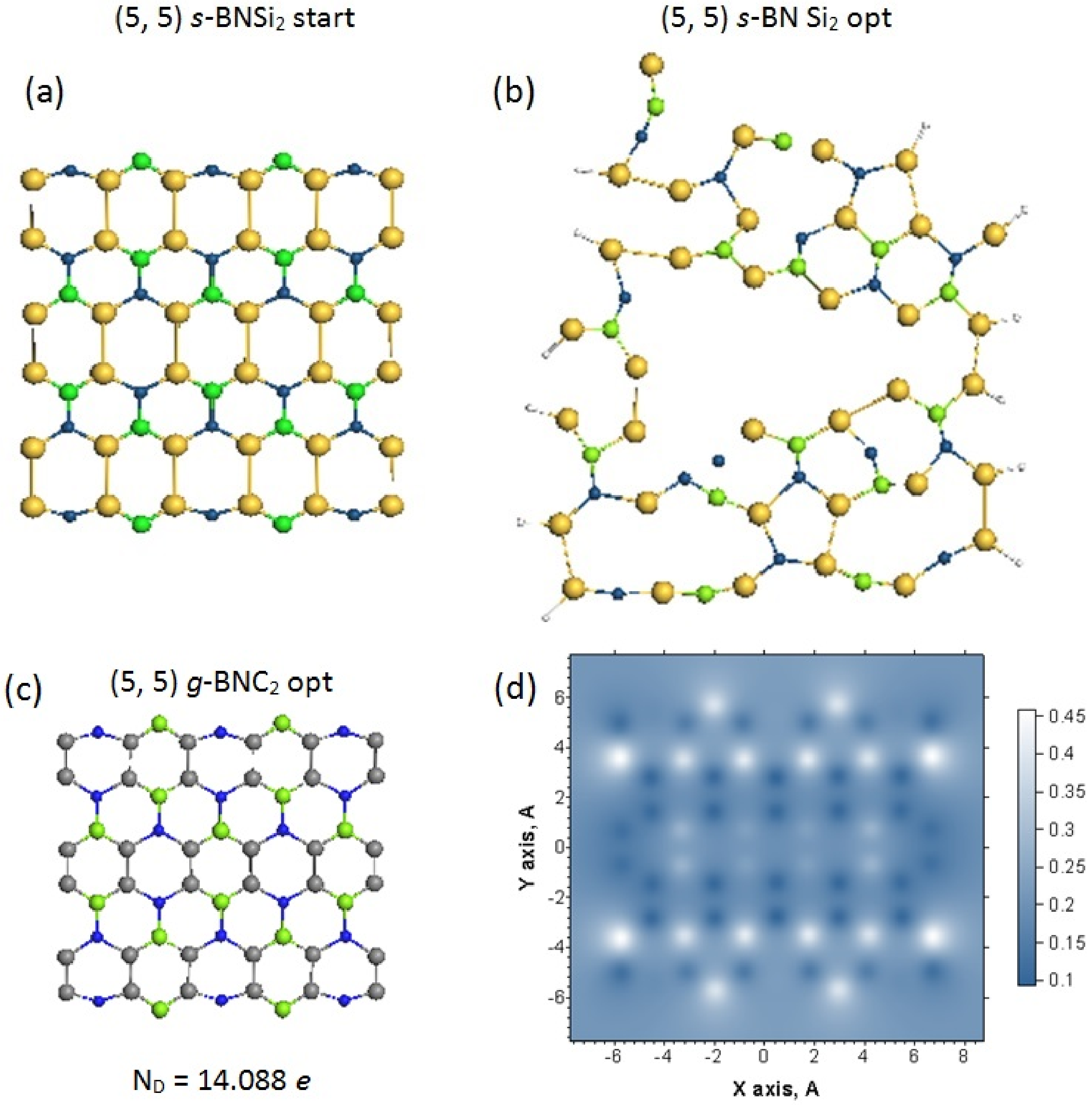

FIG. 5. Start (a) and optimized (b) structures of the s-BNSi$_2$ molecule; (c) optimized structure and (d) N_{DA} map of the effectively unpaired electrons (local spins) distribution of g-BNC$_2$ molecule. Hydrogen atoms terminating edge silicon (a) and carbon (c) atoms are not shown. AM1-UHF calculations. Big and small light-grey, dark gray and small dark balls mark silicon, nitrogen, carbon and boron atoms, respectively

structures for three molecules, namely: (5, 5) NGr, (5, 5) g-SiC$_3$ and (5, 5) g-SiC$_7$. Si=C and C=C bond lengths lay in the intervals of {1.76-1.66} Å and {1.44-1.23} Å in g-SiC$_3$ while of {1.73-1.66} Å and {1.48-1-27} Å in g-SiC$_7$. All Si=C bonds are longer than the equilibrium length in the silaethylene molecule which constitutes 1.60 Å and provides a considerable radicalization of the molecule as seen in Fig. 3. Therefore, the silicon components of both silagraphenes are obviously radicalized pointing to the open-shell character of the molecules electronic states. The carbon component retains its open-shell character as well since there are several C=C bonds longer than 1.395 Å. At the same time, some of the C=C bonds of the pristine graphene remarkably shorten, which is caused by the accommodation of the neighboring Si=C and C=C bonds to provide a continuous honeycomb core structure for the molecular. The C=C bond shortening is quite severe, which shows that the accommodation of the two types of bonds not to be a facile matter. The instability of g-SiC$_7$ can be understood in terms not only of the bond length changing but as a result of the alternating Si=C and C=C bonds governing the accommodation which causes a departure from the stable flatness, buckling the gSiC$_3$ core. A summary of the total numbers of effectively unpaired electrons is indicated at each panel. As is seen in the figure, the value is quite large in all the cases supporting open-shell nature of the studied molecules. The quantity is peculiarly distributed over the molecule atoms as seen in left panels of Fig. 6. Evidently, the edge atoms with two dangling bonds each dominate in the distribution. Both silicon and carbon atoms are among the dominants.

To reveal what is going in the inner part of the molecules the edge atoms are terminated by hydrogens, which considerably inhibits the radicalization. Fig. 7 repeats the picture presented in Fig. 6 while influenced by the termination. As is seen in Fig. 7, on first glance, the termination does not affect the core structure much while N_{DA} maps in the left panels disclose the influence by a considerable changing of their shape caused by the redistribution of C=C and Si=C lengths in due course of the termination. The Si=C and C=C bonds intervals become remarkably narrower, namely: $\{1.74\text{-}1.70\}$ Å and $\{1.42\text{-}1.37\}$ Å in $g\mathrm{SiC}_3$ while $\{1.69\text{-}1.67\}$ Å and $\{1.47\text{-}1.38\}$ Å in $g\mathrm{SiC}_7$. Nevertheless, the terminated $g\mathrm{SiC}_7$ remains buckled thus pointing to the consequence of Si=C and C=C bonds as main factor for comfortable flat accommodation. The difference in atom sizes and covalent bonds lays the foundation of the atom accommodation within a sheet, the flatness of which should be examined before DFT PBC modeling of new materials and not taken for granted as was done in [34–36]. Thus, g-SiC_7 is the same flake 'new material' as s-BNSi_2 discussed in the previous Section.

6. UHF-Based Determination of a^{SO} SOC Constant of Siliceous *sp*^{2} Molecule

In contrast with carbon counterparts, all silicon molecules, involving so called "Si=Si double bonds", do not exist and can be considered only virtually. Consequently, the evaluation of SOC parameters acquires a virtual character as well. To be in line with the procedure applied to carbonaceous species [25] we have selected fullerene Si_{60} and (5, 5) NSil molecule to look at the splitting of spin orbital energies when they are considered in the RHF and UHF approaches. Fig. 8 shows the result of the RHF and UHF application to a set of 28 spin orbitals in the vicinity of the HOMO-LUMO gaps of both molecules. When comparing it with the data for C_{60} and (5, 5) NGr [25], the outward effect in the cases of both carbon and silicon molecules is quite common. Thus, high degeneracy for the RHF states of both fullerenes, caused by their I_h symmetry, is evidently removed. In the case of (5, 5) molecules it is less evident due to not so vivid degeneracy of the RHF states. As for the a^{50} constant values, in the case of silicon molecules, they are obtained by following the Lande interval rule [25] and fill the interval of 9 *meV* – 194 *meV* and 4 *meV* – 210 *meV* for the considered spin orbitals of Si_{60} and (5, 5) NSil, respectively. As well as in the case of carbonaceous molecules, the values involve the energy splitting caused by lowered symmetry in the UHF states. To determine the magnitude of this contribution is not yet possible. If one takes into account the evaluation of splitting the energy band at K points of silicene crystal (0.07 *meV* – 1.55 *meV*) [37], the structure-induced contribution is quite considerable.

7. A Few Comments about Germanene and Stanene

Along with silicene, considerable attention has been paid lately to honeycomb structures, consisting of the next members of the tetrel family, namely, germanium and stannum [6, 37–43]. For a long time the studies have been limited to DFT computations, supplemented by PBCs, of pencil-drawn structures presenting virtual germanene and stanene. As was found similarly to silicene, the electronic band structure of two latter crystals can be described in a quasirelativistic approach with the main attention to Dirac fermions. A joint picture of the band structure of graphene, silicene, germanene and stanene is shown in Fig. 9. The model structures are presented in the figure by similar honeycomb configurations. However, to fit the energy minimum, the flat structure of graphene should be buckled, even more so in the cases of germanene and stanene.

Empirical implementation of the associated 2D structures was achieved as epitaxial growth of corresponding monolayers on crystallographically suitable surface, namely on Ag(111), Pt(111), Au(111), and finally on Al(111) [41] and Si(111) [42] in the case of germanene and on $\mathrm{Bi}_2\mathrm{Te}_3$(111) in the case of stanene [43]. In all the cases the choice of the relevant substrate has been done on the basis of knowledge accumulated in the field of surface science. All the chosen substrates were able to promote hexagonal atom packing in the corresponding adlayers that provided Dirac cone structure of the related electronic bands.

The successful realization of epitaxial germanene and stanene does not match the validity of structure and electronic properties of the relevant virtual crystals. If in the case of silicene one could speak about a likeness of atomic structure of virtual silicene molecule and epitaxial silicene, although even in this case the structure of the molecule (see insert in Fig. 9b) still significantly differs from both flat and curved crystal structures (Fig. 1a). It is not actually the case of germanene and stanene. The matter is not about a pencil-drawn virtual species, but about stability of a honeycomb configuration for germanene and stanene molecules that was already discussed for

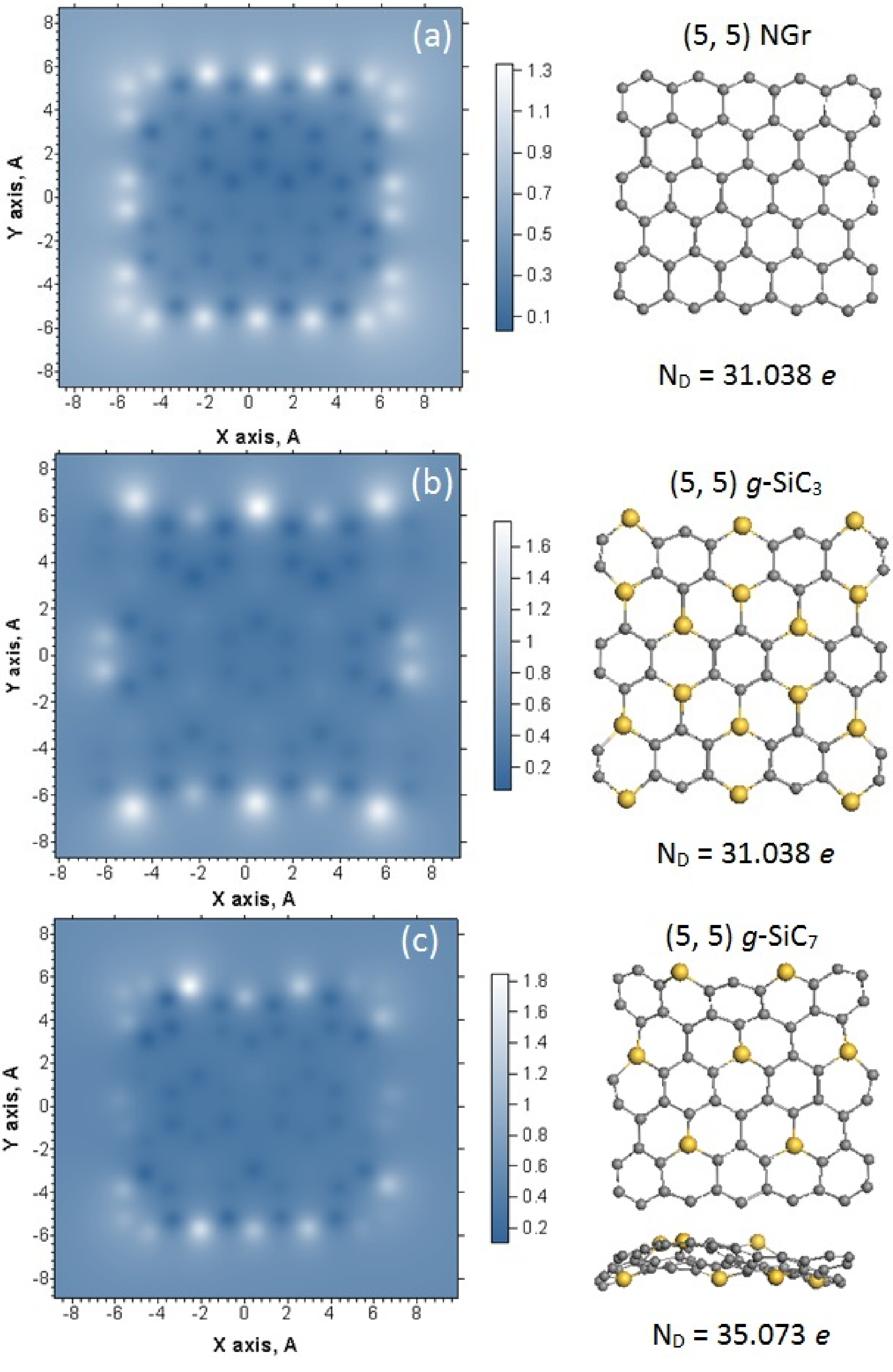

FIG. 6. Equilibrium structures (right panels) and N_{DA} maps (left panels) of bare (5, 5) Ngr (a), (5, 5) g-SiC_3 (b) and (5, 5) g-SiC_7 (top and side views) (c) molecules. Scales show the amplitude of the N_{DA} values changing. UHF AM1 calculations. Small gray and big-light gray balls mark carbon and silicon, atoms, respectively

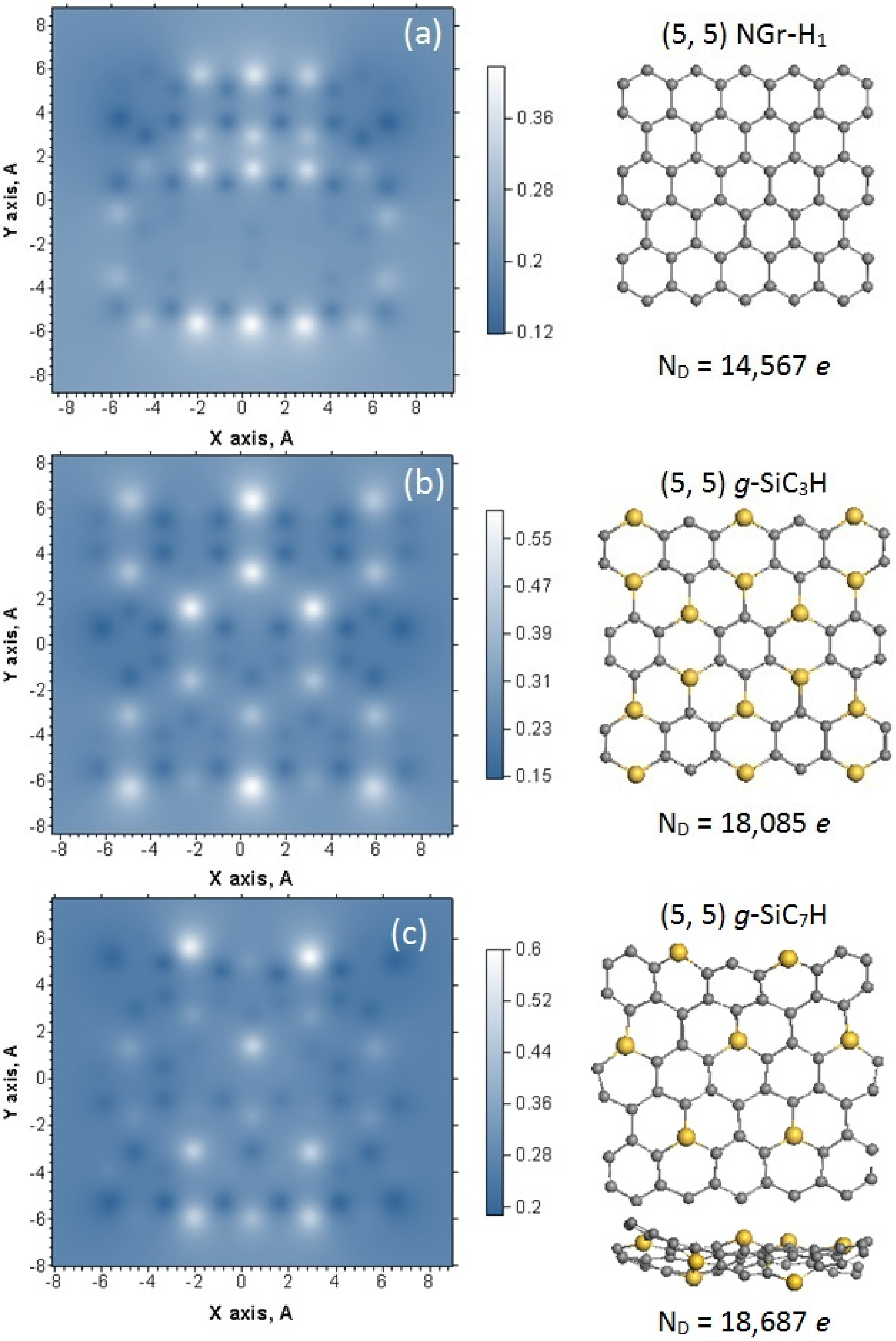

FIG. 7. Equilibrium structures (right panels) and N_{DA} maps (left panels) of hydrogen-terminated (5, 5) Ngr (a), (5, 5) g-SiC$_3$ (b) and (5, 5) g-SiC$_7$ (top and side views) (c) molecules. Scales show the amplitude of the N_{DA} values changing. Hydrogen atoms are not shown. UHF AM1 calculations. Atom marking see in the caption to Fig. 6

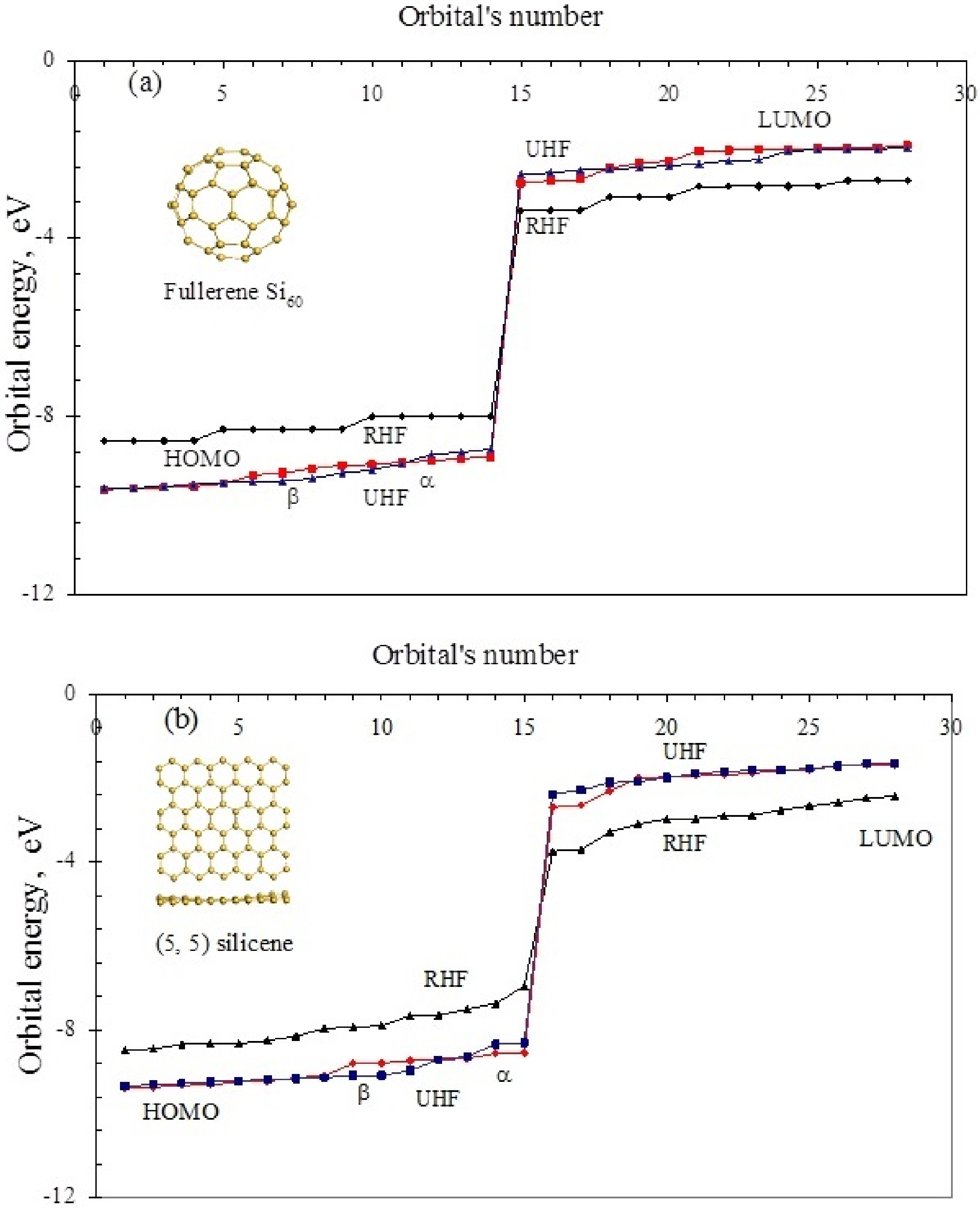

FIG. 8. Energies of 25 spin orbitals in the vicinity of HOMO-LUMO gaps of fullerene Si_{60} (a) and (5, 5) NSil molecule (b). UHF AM1 calculations

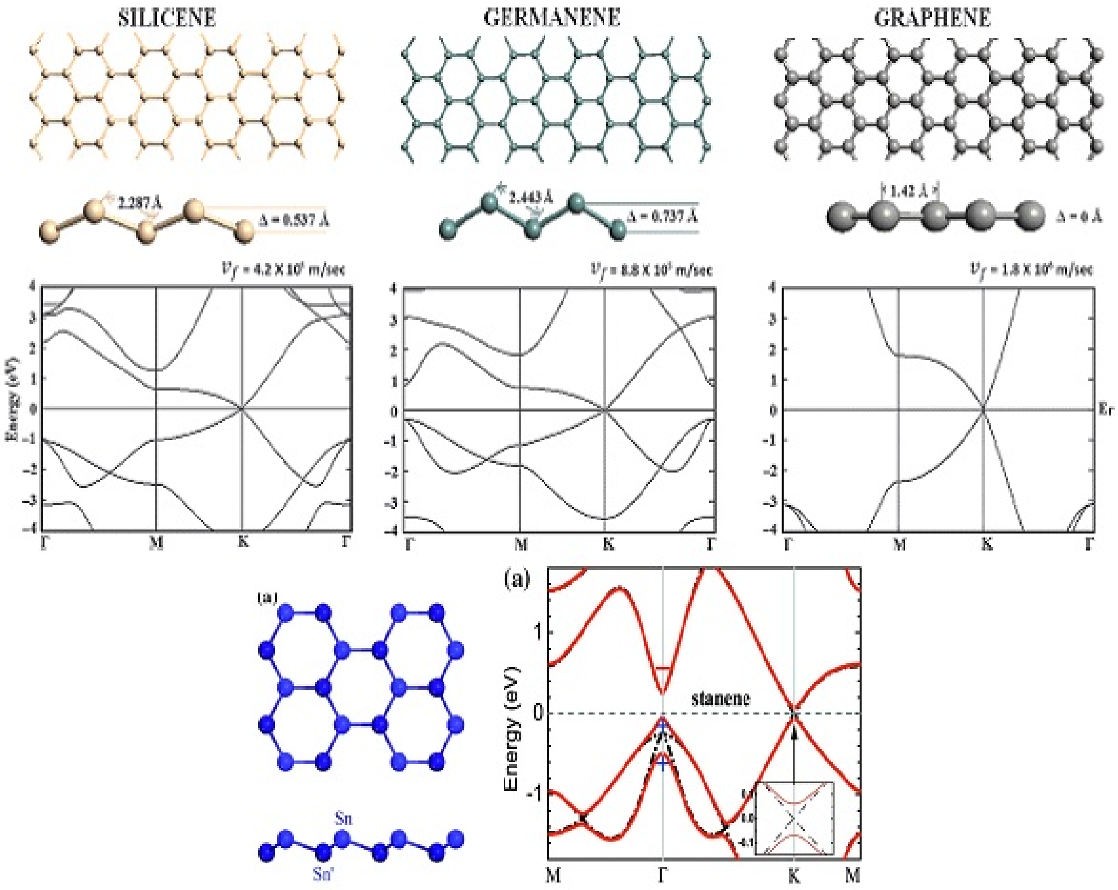

FIG. 9. Structure, band-structure with Fermi velocities of silicene, germanene and graphene (adapted from [39] and [41])

s-BNSi$_2$. To clarify this point, let us look at single-hexagon and multi-hexagon structures of the tetrel family atoms.

Figure 10 presents UHF equilibrium structures of benzene-like X_6H_6 (X=C, Si, Ge, and Sn) molecules while Table 2 accumulates their structural and radicalization parameters. The benzene-like pattern is characteristic for all the molecules, absolutely flat in case of C_6H_6 and Si_6H_6 while somewhat out of planarity for Ge_6H_6 and Sn_6H_6. In the latter case, the benzene-like configuration is energetically less favorable (by 25%) comparing with the boat-like configuration shown in Figs. 10e-f. All the benzene-like molecules are characterized by uniform bond length while there are two bond lengths in the boat-like Sn_6H_6 molecule. The transition from closed-shell to open-shell behavior is marked by the R^{db}_{cov} [25] values which are given in Table 2 as well. When $R^{db}_{eq} < R^{db}_{cov}$, the relevant molecule in the ground state is a closed-shell one. According to the table, this concerns Ge_6H_6 and one of Sn_6H_6 molecules, which explains why the molecules are not radicalized ($N_D = 0$) similarly to C_6H_6 for which $R^{db}_{eq} \cong R^{db}_{cov}$. Therefore, only in Si_6H_6 molecule all the bonds are radicalized due to $R^{db}_{eq} > R^{db}_{cov}$ as well as two longer bonds of the boat-like Sn_6H_6 molecule for the same reason.

Following this brief analysis of the structural and radical character of the X_6H_6 molecules, one finds both similarity and difference of the species at the basic level. Obviously, similarity inspires hope to obtain silicene, germanene and stannene as prospective new-material playground of the around-graphene science. The similarity excuses a voluntary choice of the majority of computationists to take the flat honeycomb structure of graphene as the basic tetrene DFT PBC models. At the same time, the difference between the molecules casts doubt on the soundness of the basic model choice. Let us see how these concerns are valid.

Figure 11 presents the results for the optimization of the preliminary equi-structural honeycomb compositions of X_{66} tetrenes. The configuration corresponds to a rectangular (5×5)nanoX fragment that involves five hexagons along armchair and zigzag directions, respectively. The equilibrium structures are presented in top and side projections. As seen in the figure, carbon and silicon compositions preserve the honeycomb structure, perfectly

TABLE 2. X=X bond lenght, Å, and molecular chemical susceptibility $(N_D), e$ in the benzene-like and (5 × 5) honeycomb (X_{66}) tetrenes

Molecule		C	Si	Ge	Sn
X_6H_6	R^{db}_{eq}	1.395	2.293	2.026	2.544(4), 2.593(2)*, 2.256**
	R^{db}_{cov}	1.395	1.80	2.10	2.55
	N_D	0.05	2.68	0	1.030**
X_{66}– (5×5)nanoX	R^{db}_{eq}	1.291-1.469***	2.214-2.330***	1.941-2.407***	2.023-2.709**
	N_D	16.63	42.51	5.56	10.96

*The shortest and longest bonds of the molecules in Fig. 10e and Fig. 10d.

**The data related to the molecule in Fig. 10g.

***The data are related to equilibrium structures in Fig. 11

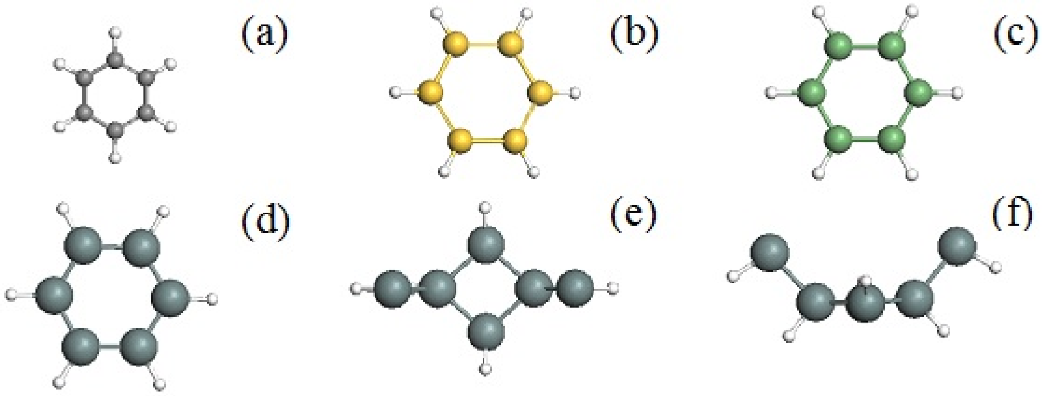

FIG. 10. Equilibrium structure of X_6H_6 molecules when X=C (a), Si (b), Ge (c), and Sn (d-f). In the latter case, benzene-like (d) and boat-like (top (e) and side (f) views) compositions are presented. Gray, light-gray, big gray, steel-gray, and white balls mark carbon, silicon, germanium, tin, and hydrogen atoms. The balls' sizes roughly correspond to the relevant van der Waals diameters. UHF AM1 for X=Si, Ge and UHF PM3 for X=Sn calculations (adapted from [25])

planar in the former case and of slightly violated planarity in the latter. In both cases, the X=X bond length values are quite dispersed and occupy interval, the limit values of which are given in Table 2. The presence of bonds, the lengths of which exceed R^{db}_{cov}, provides a considerable radicalization of the fragments (N_D) in both cases.

A detailed radicalization of the two honeycomb structures C_{66} ([5,5] NGr) and Si_{66} ([5, 5] NSil) are presented by N_{DA} maps in Fig. 12. As is seen in the figure, 22 edge atoms dominate in both distributions. Their positions do not coincide due to the different numeration of atoms in the model molecules. The radicalization of graphene does not prevent it from existing under ambient conditions because the latter is mainly concentrated on the circumference and thus is usually well inhibited by the termination of edge atoms. As for silicene, the termination of edge atoms is not enough to inhibit its high radicalization since the latter remains still high on the atoms in basal plane as well due to which free standing one-atom thick silicene sheet cannot exist under ambient conditions. Actually, as noted in numerous publications, epitaxial silicene is highly chemically active [7] and can survive in UHV only. Once designed for a practical application under ambient conditions, say, for field-effect transistors it should be laminated by thin Al or AlO_2 films [18]. It is worthwhile to remember a deep comment of Roald Hoffmann concerning the chemical peculiarity of silicene [38]: "... There is a growing literature out there of the Si analogue, silicene... And that literature talks about silicene as if it were graphene. In part this is an attempt to live off graphene's mystique, but part comes out of lack of knowledge of chemistry... I don't often say something categorical, but I will say that a pristine free standing single layer sheet of silicene (or a Si nanotube) will not be made. Silicene exists and will be made only on a support of some sort, metal or semiconductor. The reason for this is, of course, the well-known kinetic and energetic instability of Si–Si double bonds... They will latch on chemically to every piece of molecular dirt around."

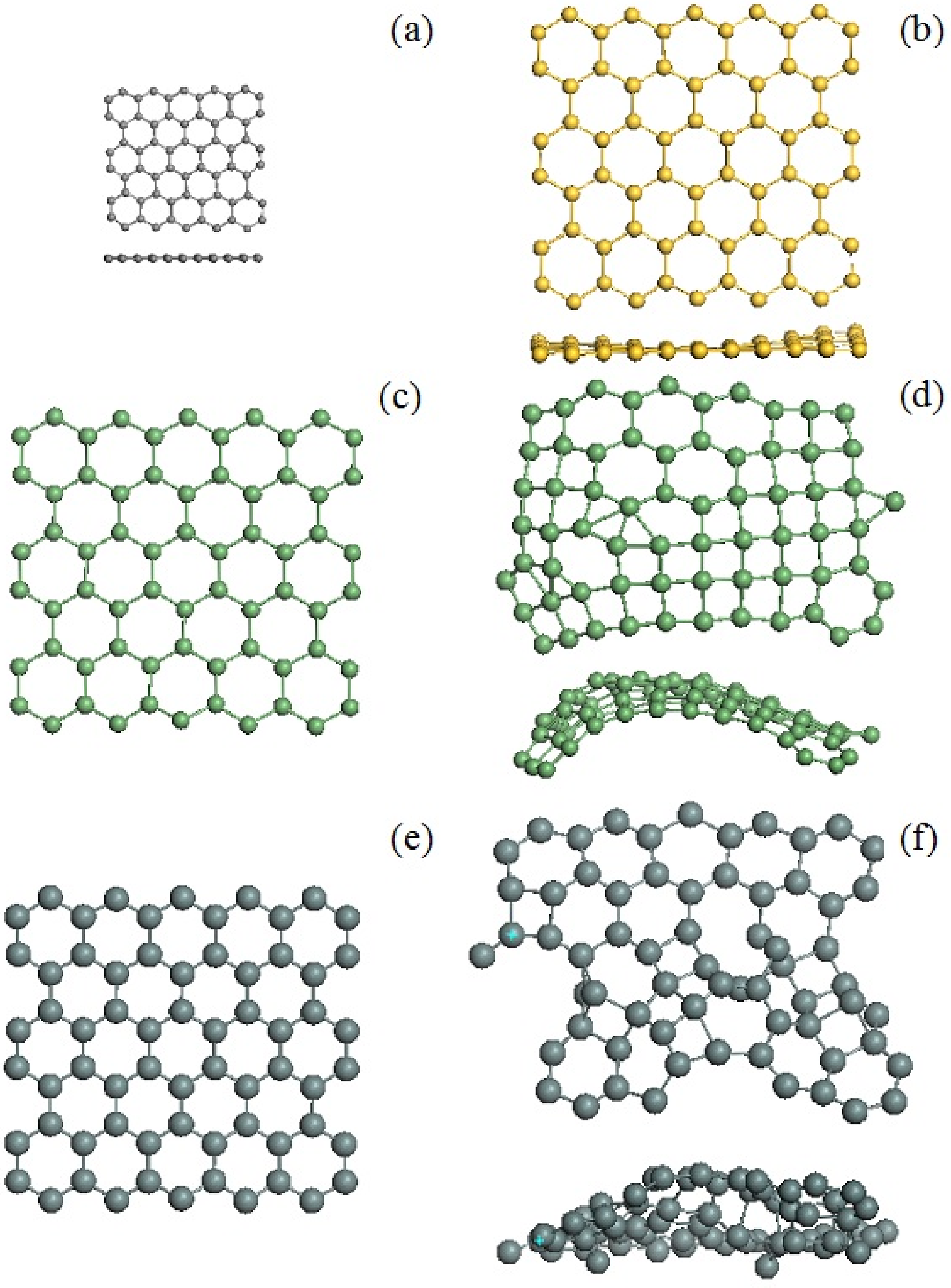

FIG. 11. Equilibrium structure of X_{66} (5x5) nanoX honeycomb fragments. (a) C_{66}; (b) top and side views of Si_{66}; (d) top and side views of Ge_{66}; (f) top and side views of Sn_{66}. (c) and (e) Ge_{66} and Sn_{66} start configurations, respectively. Atom marking see in the caption to Fig. 10. The balls' sizes roughly correspond to the relevant van der Waals diameters. UHF AM1 and UHF PM3 calculations for X=C, Si, Ge and X=Sn, respectively (adapted from [25])

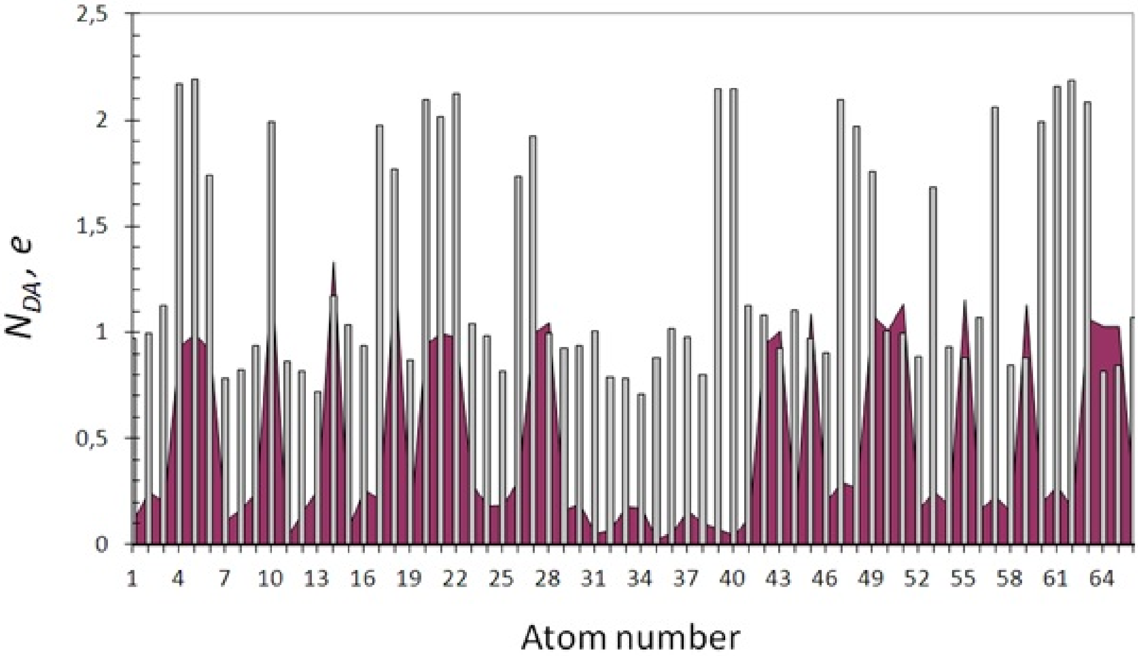

FIG. 12. N_{DA} distribution over atoms of bare (5, 5) NGr (filled area) and (5, 5) NSil (bars) molecules. UHF AM1 calculations

In contrast to the above species, X_{66} tetrenes of germanium and tin do not preserve the honeycomb structure in due course of the optimization. Their initial structures in Fig. 11c and Fig. 11e are just replicas of the equilibrium structure of Si_{66} in Fig. 11b. The followed optimization drastically disturbs the structures leaving only small clusters of condensed hexagon rings and making them considerably non planar thus showing an obvious quantum instability of the 2D species similar to that discussed for (5, 5) s-BNSi$_2$. The bond lengths cover much wider interval, abandoned with short bonds, for which $R_{eq}^{db} < R_{cov}^{db}$. The latter explains why the total radicalization of both fragments is less than in the case of C_{66} and Si_{66} (see Table 2). Possibly, such a large dispersion of the X=X bond length resulted from the extended isomerism of the species, which is characteristic for Ge- and Sn-tetrenes in contrast to C- and Si-ones, lays the foundation of the quantum instability.

According to the data presented in Fig. 11 and Table 2, the high radicalization and quantum instability of the honeycomb 2D structure are two main reasons that greatly complicate the existence of higher tetrene materials in practice. The former is mainly related to Si_{66} fragments while the latter concerns Ge_{66} and Sn_{66}. As for germanene and stanene, the data from Table 2 tell that the fragment radicalization is much lower than for graphene and cannot be considered as the main difficulty for the species existence. However, until now none of numerous attempts to obtain free standing either germanene or stanene in practice has been successful. The inability of the tetrene atoms to form a lengthy honeycomb structure is apparently the major deterrent due to which the formation of the desired free standing sheets is not achievable. As we see above, this obstacle was overcome by the choice of a suitable substrate surface on which the adsorbed tetrels can form hexagon-patterned structures.

8. Conclusion

Carbon is the first member of the tetrel family of group 14 atoms of Mendeleev's table and the outstanding importance of $C \leftrightarrow C$ bonds for organic chemistry is very stimulating for looking for a similar behavior of $X \leftrightarrow X$ chemical bonds formed by heavier tetrels. The similarity and dissimilarity of different members of the family have been the topic of heated discussions for more than a century. The current science regarding graphene represents a new milestone of activity in this direction and is full of suggestions for new prototypes of graphene the foremost of which are based on the equivalent-electron atoms such as silicon, germanium and stannum. However, for formally implemented in PBC honeycomb structures, these species suffer from high radicalization and quantum instability leaving graphene and partially graphene-based materials the only representative of one-atom-thick 2D crystals.

Acknowledgements

The author is grateful to P.V. Avramov for fruitful discussions. The work was performed under financial support of the Peoples' Friendship University of Russia, grant: 022203-0-000.

References

[1] Takeda K., Shiraishi K. Theoretical possibility of stage corrugation in Si and Ge analogs of graphite. *Phys. Rev. B*, 1994, **50**, P. 14916–14922.

[2] Guzman-Verri G., Lew Yan Voon L.C. Electronic structure of silicon-based nanostructures. *Phys. Rev. B*, 2007, **76**, P. 075131.

[3] Kara A., Enriquez H., Seitsonen A.P., Voon L.L.Y., Vizzini S., Aufray B., Oughaddou H. A review on silicene - new candidate for electronics. *Surf. Sci. Rep.*, 2012, **67**, P. 1–18.

[4] Yamada-Takamura Y., Friedlein R. Progress in the materials science of silicene. *Sci. Technol. Adv. Mater.*, 2014, **15**, P. 064404(12pp).

[5] Voon L.L.I., Guzmàn-Verri G.G. Is silicene the next graphene? *MRS Bull*, 2014, **39**, P. 366–373.

[6] Bhimanapati G.R., Lin Z., Meunier V., Jung Y., Cha J., Das S., Xiao D., Son Y., Strano M.S., Cooper V.R., Liang L., Louie S.G., Ringe E., Zhou W., Sumpter B.G., Terrones H., Xia F., Wang Y., Zhu J., Akinwande D., Alem N., Schuller J.A., Schaak R.E., Terrones M., Robinson J.A. Recent advances in two-dimensional materials beyond graphene. *ACS Nano*, 2015, **22**, P. 12168–12173.

[7] Oughaddou H., Enriquez H., Tchalala M., Yildirim H., Mayne A., Bendounan A., Dujardin G., Ali M., Kara A. Silicene, a promising new 2D material. *Prog. Surf. Sci.*, 2015, **90**, P. 46–83.

[8] Lew Yan Voon L.C. Zhu J. Schwingenschloechloel U. Silicene: Recent teoretical advances. *Appl. Phys. Rev.*,2016, **3**, P. 040802.

[9] Kara A., Léandri C., Dávila M.E., De Padova P., Ealet B., Oughaddou H., Aufray B., Le Lay G. Physics of silicene stripes. *J. Supercond Nov. Magn.*, 2008/2009, 22, P. 259–263.

[10] Sheka E.F. *May silicene exist?*, 2009. arXiv:0901.3663 [cond-mat.mtrl-sci].

[11] Vogt P., De Padova P., Quaresima C., Avila J., Frantzeskakis J., Asensio M.C., Resta A., Ealet B., Le Lay G. Silicene: Compelling experimental evidence for graphenelike two-dimensional silicon. *Phys. Rev. Lett.*, 2012, **108**, P. 155501.

[12] Lin C.-N., Arafune R., Kawahara R., Tsukahara N., Minamitani E., Kim Y., Takagi N., Kawai N. Structure of silicene grown on Ag(111). *Appl. Phys. Express*, 2012, **5**, P. 045802.

[13] Chiappe D., Grazianetti C., Tallarida G., Fanciulli M., Molle A. Local electronic properties of corrugated silicene phases. *Adv. Mater.*, 2012, **24**, P. 5088–5093.

[14] Chen L., Liu C.C., Feng B., He X., Cheng P., Ding Z., Meng S., Yao Y.G., Wu K.H. Evidence for Dirac fermions in a honeycomb lattice based on silicon. *Phys. Rev. Lett.*, 2012, **109**, P. 056804.

[15] Fleurence A., Friedlein R., Ozaki T., Kawai H., Wang Y., Yamada-Takamura Y. Experimental evidence for epitaxial silicene on diboride thin films. *Phys. Rev. Lett.*, 2012, **108**, P. 245501.

[16] Meng L., Wang Y., Zhang L., Du S., Wu R., Li L., Zhang Y., Li G., Zhou H., Hofer W.A., Gao H.J. Buckled silicene formation on Ir(111). *Nano Lett.*, 2013, **13**, P. 685–690.

[17] Zhong H.-X., Quhe R.-G., Wang Y.-Y., Shi J.-J., Lü J. Silicene on substrates: A theoretical perspective. *Chin. Phys. B*, 2015, **24**, P. 087308.

[18] Tao L., Cinquanta E., Chiappe D., Grazianetti C., Fanciulli M., Dubey M., Molle A., Akinwande D. Silicene field-effect transistors operating at room temperature. *Nat. Techn.*, 2015, **10**, P. 227–231.

[19] Sheka E.F. Why sp^2-like nanosilicons should not form: Insight from quantum chemistry. *Int J. Quant. Chem.*, 2013, **113**, P. 612–618.

[20] Liu C.-C., Feng W., Yao Y. Quantum spin Hall effect in silicene and two-dimensional germanium. *Phys. Rev. Lett.*, 2011, **107**, P. 076802.

[21] Cahangirov S., Topsakal M., Aktürk E., Şahin H., Ciraci S. Two- and one-dimensional honeycomb structures of silicon and germanium. *Phys. Rev. Lett.*, 2009, **102**, P. 236804.

[22] Avramov P., Demin V., Luo M., Choi C.H., Sorokin P.B., Yakobson B., Chernozatonskii L. Translation symmetry breakdown in low-dimensional lattices of pentagonal rings. *J. Phys. Chem. Lett.*, 2015, **6**, P. 4525–4531.

[23] Sheka E.F. *Fullerenes: Nanochemistry, Nanomagnetism, Nanomedicine, Nanophotonics*. CRC Press, Taylor and Francis Group: Boca Raton, 2011.

[24] Sheka E.F. Spin-orbit concept of open-shell systems, 2015. arXiv: 1511:05483 [physics.chem-ph].

[25] Sheka E.F. Stretching and breaking of chemical bonds, correlation of electrons, and radical properties of covalent species. *Adv. Quant. Chem.*, 2015, **70**, P. 111–161.

[26] Morkin T.L., Owens T.R., Leigh W.J. Kinetic studies of the reactions of Si=C and Si-Si bonds. in *The Chemistry of Organic Silicon Compounds*, ed. Z. Rappoport and Y. Apeloig, John Wiley & Sons, Chichester, 2001, Vol. 3, P. 949–1026.

[27] Karni M., Kapp J., Schleyer P.R., Apeloig Y. Theoretical aspects of compounds containing Si, Ge, Sn and Pb. in *The Chemistry of Organic Silicon Compounds*, ed. Z. Rappoport and Y. Apeloig, John Wiley & Sons, Chichester, 2001, Vol. 3, P. 1–164.

[28] Wang S. A comparative first-principles study of orbital hybridization in two-dimensional C, Si, and Ge. *Phys. Chem. Chem. Phys.*, 2011, **13**, P. 11929–11938.

[29] Sheka E.F., Chernozatonskii L.A. Bond length effect on odd electrons behavior in single-walled carbon nanotubes. *J. Phys. Chem. A*, 2007, **111**, P. 10771.

[30] Fucutome H. Unrestricted Hartree-Fock theory and its applications to molecules and chemical reactions. *Int. J. Quant. Chem.*, 1981, **20**, P. 955–1065.

[31] Andriotis A.N., Richter E., Menon M. Prediction of a new graphenelike Si2BN solid. *Phys. Rev. B*, 2016, **93**, P. 081413(R).

[32] Aselage T.L. The coexistence of silicon borides with boron-saturated silicon: Metastability of SiB_3. *J. Mat. Res.*, 1998, **13**, P. 1786–1794.

[33] Hoffmann R. Small but strong lessons from chemistry for nanoscience. *Angew Chem. Int. Ed.*, 2012, **51**, P. 2–13.

[34] Zhao M., Zhang R. Two-dimensional topological insulators with binary honeycomb lattices: SiC_3 siligraphene and its analogs. *Phys. Rev. B*, 2014, **89**, P. 195427.

[35] Shi Z., Zhang Z., Kutana A., Yakobson B.I. Predicting two dimensional silicon carbide monolayers. *ACS Nano*, 2015, **9**, P. 9802–9809.

[36] Dong H., Zhou L., Frauenheim T., Hou T., Lee S.-T., Li Y. SiC_7 siligraphene: Novel donor material with extraordinary sunlight absorption. *Nanoscale*, 2016, **8**, P. 6994–6999.

[37] Balendhran S., Walia S., Nili H., Sriram S., Bhaskaran M. Elemental analogues of graphene: silicene, germanene, stanene, and phosphorene. *Small*, 2015, **11**, P. 640–652.

[38] Trivedi S., Srivastava A., Kurchania R. Silicene and germanene: A first principle study of electronic structure and effect of hydrogenation-passivation. *J. Comp. Theor. Nanosci.*, 2014, **11**, P. 781–788.

[39] Xu Y., Yan B., Zhang H.-J., Wang J., Xu G., Tang P., Duan W., Zhang S.-C. Large-gap quantum spin Hall insulators in tin films. *Phys. Rev. Lett.*, 2013, **111**, P. 136804.

[40] Cai B., Zhang S., Hu Z., Hu Y., Zoua Y. Zeng H. Tinene: a two-dimensional Dirac material with a 72 meV band gap. *Phys. Chem. Chem. Phys.*, 2015, **17**, P. 12634–12638.

[41] Derivaz M., Dentel D., Stephan R., Hanf M.-C., Mehdaoui A., Sonnet P., Pirri C. Continuous germanene layer on Al(111). *Nano Lett.*, 2015, **15**, P. 2510–2516.

[42] Tsai H.-S., Chen Y.-Z., Medina H., Su T.-Y., Chou T.-S., Chen Y.-H., Chueh Y.-L., Liang J.-O. Direct formation of large-scale multi-layered germanene on Si substrate. *Phys. Chem. Chem. Phys.*, 2015, **17**, P. 21389–21393.

[43] Zhu F.-F., Chen W.-J., Xu Y., Gao C.-l., Guan D.-D., Liu C.-H., Qian D., Zhang S.-C., Jia J.-F. Epitaxial growth of two-dimensional stanene. *Nat. Mat.*, 2015, **14**, P. 1020–1025.

NANOSYSTEMS: PHYSICS, CHEMISTRY, MATHEMATICS, 2016, 7 (6), P. 1002–1009

Assessment for applicability of the “tangent technique” in X-ray small-angle scattering

A. V. Smirnov, V. Yu. Kalyakin, B. A. Fedorov

ITMO University, 49, Kronverkskiy, St. Petersburg, 197101, Russia

borfedorov1@gmail.com, smirnav_2@mail.ru, slav.yrich@gmail.com

PACS 61.05.cf **DOI 10.17586/2220-8054-2016-7-6-1002-1009**

A number of simple model systems are used to examine the applicability of the “tangent technique”, employed in the small-angle X-ray scattering for estimating the particle size distribution function, as well as to ascertain the relative contributions of the scattering intensity by differently sized particles to the total scattering intensity. The undertaken analysis has shown that, even in the most favorable case-an ensemble of two groups of different-size particles-the “tangent technique” cannot be used either to find the particle size proper, or to ascertain the relative contributions of individual groups to the total scattering intensity.

Keywords: small-angle X-ray scattering, size distribution of nanoparticles, Guinier plot.

Received: 27 July 2016

Revised: 4 August 2016

1. Introduction

The numerous methods used to process experimental curves of X-ray small-angle scattering with the view to derive information on the structure of scattering objects include the “tangent technique” [1,2]. This seemed simple and convenient enough for estimating the size distribution of globular nanoparticles as well as for ascertaining the relative contributions of particles of each size to the total scattering intensity. At the same time, the technique, as even its authors remarked, is rather limited in its scope. Though it was proposed as early as the 1950’s and has since been repeatedly used in the small-angle scattering [3,4], no one has tried to evaluate the errors arising from its application. Moreover, no one has raised the issue whether its use is altogether possible. Will errors drive the required parameters beyond the reasonable values even in the case of the simplest scattering systems and in the scattering angle region, which is most suitable for application of the technique?

The present work attempts to answer the questions by undertaking a detailed analysis of applicability of the “tangent technique” in the cases of both model systems and a globular protein mixture.

2. Description of the technique

As is known, the intensity $I(q)$ of the small-angle X-ray scattering by a particle, which comprises N different scattering centers (atoms) and is chaotically oriented relative to the primary X-ray beam, can be represented with Debye formula [5]:

$$I(q) = \sum_{i,j=1}^{N} f_i(q) f_j(q) \frac{\sin(q r_{ij})}{q r_{ij}}, \tag{1}$$

where r_{ij} is the distance between the i-th and j-th atoms, $q = (4\pi/\lambda)\sin(\theta/2)$ is the magnitude of the reciprocal space vector (λ is the X-ray wavelength, θ is the scattering angle), $f_i(q)$ is the scattering factor of the i-th atom. If q is small, $f_i(q)$ is weakly dependent on q and $f_i(q) = f_i(0) = f_i$, the number of electrons in the i-th atom.

Expansion of Eq. (1) into a series gives:

$$I(q) = \sum_{i,j=1}^{N} f_i f_j \left(1 - \frac{q^2 r_{ij}^2}{6} + ...\right) = A^2 \left(1 - \frac{q^2 R_g^2}{3} + ...\right), \tag{2}$$

where $R_g^2 = \dfrac{\sum\limits_{i,j=1}^{N} f_i f_j r_{ij}^2}{2\sum\limits_{i,j=1}^{N} f_i f_j}$ is the squared electron radius of gyration of a particle and $A^2 = \sum\limits_{i,j=1}^{N} f_i f_j$ is the squared number of electrons in a particle.

The series expansion of function $A^2 \exp\left(-\frac{1}{3}R_g^2 q^2\right)$ is easily seen to have first two terms coincident with Eq. (2). This property underlies the Guinier technique (e.g. [6–9]): plotting the scattering intensity as $\ln\ I(q)$ vs. q^2 in the region of small angles yields a straight line, its slope allowing one to find R_g^2, i. e., the particle size.

Consider a system, consisting of differently sized particles, and assume the scattering intensity for each particle to follow the exponential law. Then, the scattering intensity for the entire system – without interference between individual particles – is presentable in the form:

$$\tilde{I}(q) = \sum_{i=1}^{N} K_i A_i^2 \exp\left(-\tfrac{1}{3}R_{gi}^2 q^2\right), \tag{3}$$

where N is the number of groups of particles with radii of gyration R_{gi} and K_i is the particle count in each group. Let the summation be from the largest ($i = 1$) to the smallest particle ($i = N$).

If the number of groups is rather small and radii of gyration R_{gi} vary from group to group appreciably, the "tangent technique" was believed to be fully justified, with inclusion of the following stages:

1) Plotting $\ln \tilde{I}(q)$ vs. q^2.

2) Drawing a tangent to the curve at the largest values of q, but in the scattering angle region, where exponential approximation Eq. (3) is valid for all groups of scattering particles.

3) Finding squared radius of gyration $\tilde{R}_{gN}^2$ for the smallest particles by the tangent slope according to Eq. (2) and value $\tilde{K}_N A_N^2$ by the intercept of the tangent on axis $\ln \tilde{I}(q)$. If A_N is known (roughly, the value A_N is one-half of the molecular mass of the particle), one also finds $\tilde{K}_N$, the particle count in group N.

4) Subtracting function $\tilde{K}_N A_N^2 \exp\left(-\frac{1}{3}\tilde{R}_{gN}^2 q^2\right)$ with already known values of $\tilde{K}_N$ and $\tilde{R}_{gN}^2$ from the experimental intensity Eq. (3). One finds scattering intensity $\tilde{I}(q)$ by the remaining particles and passes on to Operation 1) with substituting group N with group $N-1$.

Upon completion of the said cycle, the following sought parameters are calculated: radii of gyration $\tilde{R}_{gi}$ (sizes) of all particles included in the scattering system and the relative particle count in each group. One can also plot $\tilde{K}_i$ vs. $\tilde{R}_{gi}$ (which is sometimes done [4]) to evaluate the particle size distribution, which is dedicated to other methods in the small-angle scattering [10, 11].

Despite the deceptive simplicity of the technique and the value of the derived information, the application of the technique gives rise to several somewhat complex questions:

a) How is the angle region to be chosen for the condition of Eq. (2) to hold?

b) What are the grounds to believe that the scattering intensity in the vicinity of drawing each tangent is governed by *but one* group of particles, while other groups make no contributions whatsoever to the scattering curve in this angular region?

c) How is, when drawing tangents, the straight-line segment of the scattering curve to be distinguished from the curvilinear one, and in the presence of the unavoidable experimental error at that?

d) How is the number of groups with different values of R_g to be found under the conditions of an actual experiment?

There is, apparently, no general answer to the questions, so the present work examines a number of specific different-size systems to assess the applicability of the technique.

3. Analysis of the technique applicability

Simplify the problem statement as much as possible. To begin with, assume only two groups of differently sized particles ($N = 2$). This is evidently the most favorable model. If the technique proves inapplicable even for this model, there is no sense to increase the number of groups. Next, an interval of scattering angles is to be selected for drawing the tangents and, accordingly, to specify the particle sizes in each. The basic condition is that the intensity, plotted in Guinier coordinates for particles of both groups, had the shape of a straight line in the selected scattering angle interval. Of importance is also for the angular interval to be available experimentally. In terms of the magnitude of reciprocal space vector, the interval is defined from $q_{min} = 0.01$ nm^{-1} to $q_{max} = 0.14$ nm^{-1} (hereinafter, a bounded interval), which corresponds (at X-ray wavelength $\lambda_{CuK\alpha} = 0.154$ nm) to scattering angles from $\theta_{min} = 2.5 \cdot 10^{-4}$ rad to $\theta_{max} = 3.4 \cdot 10^{-3}$ rad and, respectively, to Bragg spacings from $d_{max} = 300$ nm to $d_{min} = 23$ nm. Particle sizes (radii of gyration R_g) were chosen as $R_{g1} = 15.56$ nm, $R_{g2} = 9.21$ nm. It has been shown for particles of such sizes that the required condition of straightness of Guinier plots in the said scattering angle interval holds reasonably well. Let K_1 and K_2 be the initial particle counts in each group, and $\tilde{K}_1$ and $\tilde{K}_2$ be those found by the "tangent technique".

For all particle groups considered under the said conditions, we calculated scattering intensities, constructed Guinier plots, evaluated the quantities $\tilde{R}_{g1}$, $\tilde{R}_{g2}$, $\tilde{K}_1$, $\tilde{K}_2$ by the "tangent technique" in a wide variation range of K_2/K_1, and estimated the errors of the quantities as compared to their true values. The results are presented in Tables 1-4. In each table, column 1 is the selected value of K_2/K_1; columns 2 and 3 are the calculated relative errors of quantities $\tilde{R}_{g1}$ and $\tilde{R}_{g2}$ $\left(\delta R_{gi} = \left(\tilde{R}_{gi} - R_{gi}\right)\Big/R_{gi}\right)$; columns 4 and 5 are the calculated relative errors of quantities $\tilde{K}_1$ and $\tilde{K}_2$ $\left(\delta K_i = \left(\tilde{K}_i - K_i\right)\Big/K_i\right)$.

Hypothetical particles with scattering intensity defined by Eq. (3) at N = 2. The scattering curve for each particle is shaped in Guinier coordinates as a straight line, yet the dependence of $\ln[K_1A_1^2\exp\left(-\frac{1}{3}R_{g1}^2q^2\right) + K_2A_2^2\exp\left(-\frac{1}{3}R_{g2}^2q^2\right)]$ on q^2 is no longer a straight line. In a wide scattering angle interval ($q_{min} = 0.01$ nm^{-1} to $q_{max} = 0.4$ nm^{-1}), of course, the effects related to the influence of different groups on the total scattering curve are separable (Fig. 1), and the "tangent technique" yields reasonable values for radii of gyration and particle counts in each group (Table 1). However, the effects cannot be separated in the said bounded scattering angle interval.

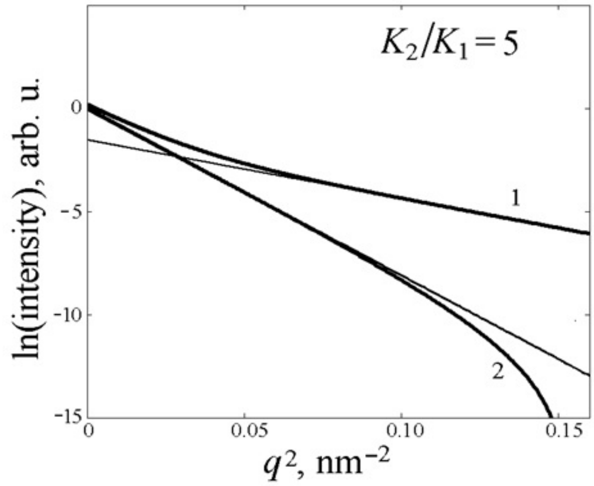

FIG. 1. Hypothetical particles. Curve 1 is the scattering intensity found according to Eq. (3) at $N = 2$; curve 2 is the difference scattering curve between intensity of Eq. (3) and the intensity of $\tilde{K}_2A_2^2\exp\left(-\frac{1}{3}\tilde{R}_{g2}^2q^2\right)$. All curves are plotted in Guinier coordinates. Straight lines are tangents to Curves 1 and 2. Wide scattering angle interval. See details in the text

TABLE 1. Hypothetical particles. Wide scattering angle interval ($q_{min} = 0.01$ nm^{-1} to $q_{max} = 0.4$ nm^{-1}). Relative errors of radii of gyration $\tilde{R}_{g1}$, $\tilde{R}_{g2}$ and weighting factors $\tilde{K}_1$, $\tilde{K}_2$ at different ratios K_2/K_1. See details in the text

K_2/K_1	$\delta R_{g1}, \%$	$\delta R_{g2}, \%$	$\delta K_1, \%$	$\delta K_2, \%$
5	0.08	0.13	–0.3	1.3
10	0.08	0.06	–0.3	0.6
20	0.08	0.03	–0.3	0.3
50	0.08	0.013	–0.3	0.13
100	0.08	$6{\cdot}10^{-3}$	–0.3	$6{\cdot}10^{-2}$
150	0.08	$4{\cdot}10^{-3}$	–0.3	$4{\cdot}10^{-2}$

Table 2 presents the results of applying the technique in a bounded interval at different ratios K_2/K_1. As seen, in the case of the number of small particles much greater than that of larger ones ($K_2/K_1 = 150$ and more), the contribution of the latter tells little on the scattering curve. Hence, quantities $\tilde{R}_{g2}$ and $\tilde{K}_2$ are evaluated comparatively well, but the calculation of quantities $\tilde{R}_{g1}$ and $\tilde{K}_1$ yields unacceptable errors. At a smaller K_2/K_1

TABLE 2. Hypothetical particles. Bounded scattering angle interval ($q_{min} = 0.01$ nm^{-1} to $q_{max} = 0.14$ nm^{-1}). Relative errors of radii of gyration $\tilde{R}_{g1}$, $\tilde{R}_{g2}$ and weighting factors $\tilde{K}_1$, $\tilde{K}_2$ at different ratios K_2/K_1. See details in the text

K_2/K_1	$\delta R_{g1}, \%$	$\delta R_{g2}, \%$	$\delta K_1, \%$	$\delta K_2, \%$
5	47	48	-90	419
10	46	38	-86	200
20	44	26	-82	96
50	43	14	-79	37
100	43	8	-78	18
150	43	5	-78	12

ratio, likely unacceptable errors emerge in evaluation of all four quantities in question. This can now be explained by the effect of the scattering intensity of larger particles on the total curve in the entire bounded interval. As a consequence, quantities $\tilde{R}_{g2}$ and $\tilde{K}_2$ are evaluated with great errors, while the errors in the evaluation of quantities $\tilde{R}_{g1}$ and $\tilde{K}_1$, naturally, grow significantly.

Homogeneous ellipsoids of revolution and spheres. As previously shown [12], the scattering intensity by the i-th homogeneous ellipsoid of revolution with electron density ρ is defined by expression $A_i^2 I_i^{el}(q)$, where $A_i = \rho V_i$, $V = \frac{4}{3}\pi a^2 b$ is the volume of the ellipsoid (b is the semi-major axis, a is the semi-minor axis),

$$I_i^{el}(q) = \int_0^1 \Phi^2 \left(q\sqrt{5R_{gi}^2 \left(1 + x^2 \left(\nu^2 - 1\right)\right) / \left(2 + \nu^2\right)} \right) dx \tag{4}$$

is its formfactor ($I_i^{el}(0) = 1$), $\Phi(t) = 3\dfrac{\sin t - t\cos t}{t^3}$, and $\nu = b/a$. Radius of gyration R_g is related to semi-axes a and b by $R_g = \sqrt{(2a^2 + b^2)/5}$.

The total scattering intensity for two groups of ellipsoids is representable as:

$$I^{el}(q) = K_1 A_1^2 I_1^{el}(q) + K_2 A_2^2 I_2^{el}(q), \tag{5}$$

where, as before, K_1 and K_2 are the particle counts in the first and second groups, respectively. We chose anisotropy ν = 2 the same for ellipsoids of both groups, since the calculations show the straight-line segment in Guinier plotting to prove to be the most extended at this anisotropy.

Table 3 presents the calculation results. They are close to those obtained for hypothetical particles in a bounded interval of scattering angles. And while the relative errors for quantities $\tilde{R}_{g2}$ and $\tilde{K}_2$ are comparatively small in the most favorable case ($K_2/K_1 = 150$), those for $\tilde{R}_{g1}$ and $\tilde{K}_1$ are as high as tens of percent.

TABLE 3. Ellipsoids of revolution. Relative errors of radii of gyration $\tilde{R}_{g1}$, $\tilde{R}_{g2}$ and weighting factors $\tilde{K}_1$, $\tilde{K}_2$ at different ratios K_2/K_1. Bounded scattering angle interval ($q_{min} = 0.01$ nm^{-1} to $q_{max} = 0.14$ nm^{-1}). See details in the text

K_2/K_1	$\delta R_{g1}, \%$	$\delta R_{g2}, \%$	$\delta K_1, \%$	$\delta K_2, \%$
5	47	44	-87	404
10	46	34	-83	194
20	45	24	-80	93
50	43	12	-77	36
100	43	6.3	-75	17
150	42	4.1	-73	11

The model of a scattering system is very often taken to be spheres. As follows from Eq. (4), the form-factor of the scattering intensity for spheres ($\nu = 1$) is:

$$I_i^{sph}(q) = \Phi^2\left(\sqrt{\tfrac{5}{3}}qR_{gi}\right), \tag{6}$$

and the total intensity for two groups of spheres is:

$$I^{sph}(q) = K_1A_1^2I_1^{sph}(q) + K_2A_2^2I_2^{sph}(q). \tag{7}$$

The results of the corresponding calculation are given in Table 4. They demonstrate that the errors in evaluating all four quantities prove to be unacceptable. In the most favorable case (as before, at $K_2/K_1 = 150$), the errors in evaluating quantities $\tilde{R}_{g1}$ and $\tilde{K}_1$ are as high as tens of percent, whereas quantity $\tilde{R}_{g1}$ at $K_2/K_1 = 5$ cannot be calculated at all, for the slope of the corresponding tangent happens to be positive.

TABLE 4. Spheres. Relative errors of radii of gyration $\tilde{R}_{g1}$, $\tilde{R}_{g2}$ and weighting factors $\tilde{K}_1$, $\tilde{K}_2$ K_2/K_1. Bounded scattering angle interval ($q_{min} = 0.01$ nm^{-1} to $q_{max} = 0.14$ nm^{-1}). See details in the text

K_2/K_1	$\delta R_{g1}, \%$	$\delta R_{g2}, \%$	$\delta K_1, \%$	$\delta K_2, \%$
5	unevaluable	64	unevaluable	482
10	26	49	-96	223
20	37	35	-91	105
50	40	20	-88	41
100	42	13	-91	21
150	49	10	-94	15

Globular proteins. The procedure for calculating the intensity of X-ray scattering by globular proteins in a solution, which was developed by one of the authors jointly with others [13–15], is applicable in the case when the coordinates of all atoms of the protein under study are known. Were we concerned with the scattering intensity of such protein in vacuum, the problem would not be difficult: it would suffice to use Debye formula Eq. (1). However, as was shown experimentally as early as in works [16,17], the presence of the solvent has an effect upon the entire scattering curve of a protein.

Briefly, the method of allowing for the solvent effect can be described as follows. If a protein contains N non-hydrogen atoms with coordinates r_i and scattering factor $f_i(q)$, its scattering intensity can be found in accordance with the expression:

$$I(q) = \langle I(\mathbf{q})\rangle = \left\langle \left| \sum_{j=1}^{N} f_j(q)\exp(i\mathbf{qr}) - \rho_s\Psi(\mathbf{q}) \right|^2 \right\rangle, \tag{8}$$

the averaging is done over all possible orientations of the protein relative to the primary beam, ρ_s is the solvent electron density, and function:

$$\Psi(\mathbf{q}) = \int_V \exp(i\mathbf{qr})\,dr \tag{9}$$

is the amplitude of scattering by that homogeneous volume of a protein particle, which is inaccessible to the solvent molecules. The calculation of the amplitude is a major difficulty. We developed a “cube method” [18], which bases on filling the entire particle volume, inaccessible to the solvent, with small cubes (with edges 0.0279 nm long); their dense packing ensures the homogeneity of density inside the molecule. Thus, the calculation of the amplitude of scattering in Eq. (9) reduces to finding the amplitude of scattering by a system of cubes (parallelepipeds). Next, scattering intensity $I(\mathbf{q})$ is evaluated at point $\mathbf{q}$ of the reciprocal space, and intensity $I(q)$ is found by averaging $I(\mathbf{q})$ over a sphere of radius $q = |\mathbf{q}|$ of the space. The procedure of the said averaging is described in [19].

Consider a mixture of two globular proteins with atom coordinates given in the PDB: human hemoglobin (http://files.rcsb.org/view/4ESA.pdb) and hen egg-white lysozyme (http://files.rcsb.org/view/6LYZ.pdb). Their radii of gyration are specified as $R_{g1} = 15.56$ nm and $R_{g2} = 9.21$ nm, respectively. For aqueous solution of the two proteins, scattering intensities were calculated and total curves were derived at different ratios K_2/K_1. Table 5 gives the values of all four estimated parameters in a wide variation range of K_2/K_1.

TABLE 5. Globular proteins in solution: human hemoglobin and hen egg-white lysozyme. Relative errors of radii of gyration $\tilde{R}_{g1}$, $\tilde{R}_{g2}$ and weighting factors $\tilde{K}_1$, $\tilde{K}_2$ at different ratios K_2/K_1. Bounded scattering angle interval ($q_{min} = 0.01$ nm^{-1} to $q_{max} = 0.14$ nm^{-1}). See details in the text

K_2/K_1	$\delta R_{g1}, \%$	$\delta R_{g2}, \%$	$\delta K_1, \%$	$\delta K_2, \%$
5	18	24	-77	56
10	19	15	-75	27
20	16	8.8	-75	14
50	3.5	4.8	-79	5.8
100	-61	3.3	-87	3.2
150	unevaluable	2.8	unevaluable	2.3

As is readily seen, when the number of lysozyme molecules is predominant in the solution, the lysozyme radius of gyration and the relative number of molecules are evaluated within 10% accuracy down to $K_2/K_1 = 50$. However, the hemoglobin scattering intensity in the region of very small angles is distorted by the scattering intensity of all lysozyme molecules, and, as a consequence, the errors in evaluation of quantities $\tilde{R}_{g1}$ and $\tilde{K}_1$ prove to be too great or the quantities are unevaluable altogether. At smaller ratios K_2/K_1, the evaluation errors of all four quantities are unacceptable. This result, likewise to the earlier-treated case of hypothetical particles, is explained by the effect of the scattering intensity of large particles upon the total curve now in the entire bounded interval, in particular, upon its right-hand part, which is used to calculate $\tilde{R}_{g2}$ and $\tilde{K}_2$.

4. Discussion of results

The main conclusion, following from the above examination, is that the "tangent technique" is, from the practical viewpoint, inapplicable to any of the analyzed scattering systems. This is demonstrated by the data given in all five tables.

To exemplify the conclusion graphically, consider the scattering intensity for two groups of ellipsoids of revolution in Guinier coordinates at a great value of ratio $K_2/K_1 = 150$ (Fig. 2a) and a small value of $K_2/K_1 = 5$ (Fig. 2b). Both figures show four scattering curves: 1 and 2 are those for the first and second groups of particles; 3 is the total scattering intensity, corresponding to Eq. (5); 4 is the difference scattering curve between intensities of Eq. (5) and $\tilde{K}_2 A_2^2 \exp\left(-\frac{1}{3}\tilde{R}_{g2}^2 q^2\right)$, where $\tilde{R}_{g2}$ is the radius of gyration of smaller particle, which was found by the slope of the tangent to the curve in the right-hand part of the bounded scattering angle interval.

For larger K_2/K_1 ratio values, the prevailing contribution to the total scattering intensity is seen from Fig. 2a to come from the scattering by small particles; still, the tangents to curves 2 and 3 in the right-hand part of the bounded interval differ a little both in the slope and the intercept on the axis of ordinates. The differences suffice to distort sought quantities $\tilde{R}_{g1}$ and $\tilde{K}_1$ substantially: the slopes of the tangents to curves 1 and 4 in the left-hand part of the bounded interval differ markedly, and the intercepts on the axis of ordinates differ, too. At the same time, quantities $\tilde{R}_{g2}$ and $\tilde{K}_2$ proper are evaluated well enough.

At relatively small values of ratio K_2/K_1 (Fig. 2b), the principal contribution to the total scattering intensity in the entire bounded interval comes from the large particle, so the tangents to curves 2 and 3 differ markedly even in the right-hand part of the interval. The intercepts of the tangents on the axis of ordinates differ markedly, too. In other words, a large error arises in the evaluation of quantities $\tilde{R}_{g2}$ and $\tilde{K}_2$, and, hence, even larger error in the evaluation of quantities $\tilde{R}_{g1}$ and $\tilde{K}_1$.

If the bounded scattering angle interval is extended, the technique is seen from Fig. 1 to be completely applicable, but solely for hypothetical particles, which are non-existent in nature. Indeed, there is no realistic particle, for which the scattering intensity would follow the exponential law *in a wide angular region*. Under any other dependence, even at the first stage of applying the technique (that is, in evaluation of $\tilde{R}_{g2}$ by the tangent slope), an appreciable error arises, which grows sharply in calculation of other quantities at hand.

It may seem that if the particle sizes (R_{g1} and R_{g2}) differ markedly, say, by an order of magnitude, the "tangent technique" is completely applicable. However, as follows from Eq. (3), the contributions to the total scattering intensity by large and small particles (at their equal shares in terms of numbers) differ $(R_{g1}/R_{g2})^6$ times. In this case, for their contributions to the scattering intensity to be comparable, one should take at least

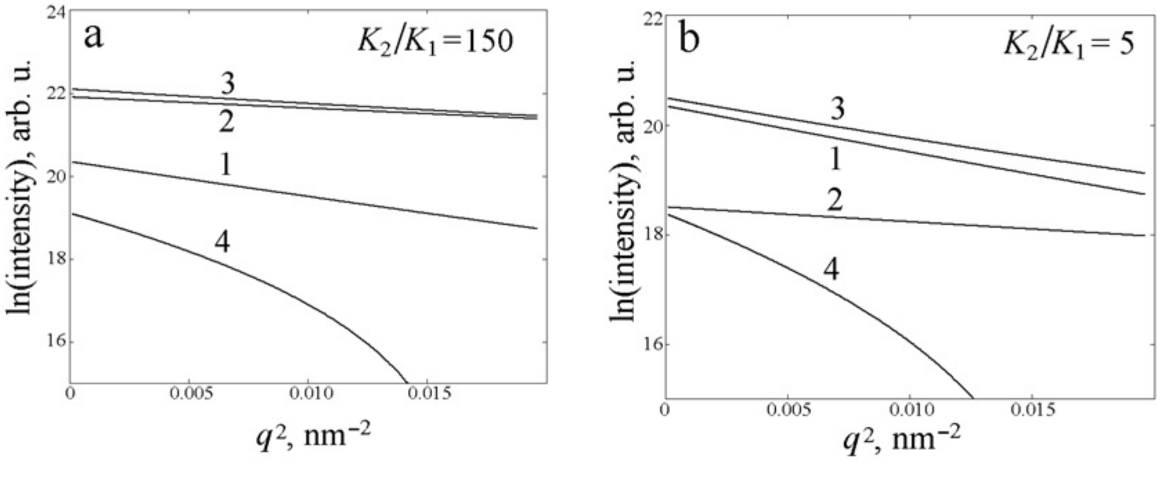

FIG. 2. Scattering intensities for two groups of ellipsoids of revolution. 1 and 2 are scattering curves for the first ($R_{g1} = 15.56$ nm) and second ($R_{g2} = 9.21$ nm) groups of ellipsoids, respectively; (3) is the total scattering intensity, found according to Eq. (5); 4 is the difference scattering curve between intensities of Eq. (5) and $\tilde{K}_2 A_2^2 \exp\left(-\frac{1}{3}\tilde{R}_{g2}^2 q^2\right)$. All curves are plotted in Guinier coordinates. See details in the text

million more small particles, which renders the technique absolutely impractical and the calculation of quantities $\tilde{R}_{g1}$ and $\tilde{K}_1$ fraught with even greater errors.

5. Conclusion

The results of the present work can be deemed negative. The grand total is that the “tangent technique” cannot be used for any different-size scattering particle groups either to find the particle size proper, or to ascertain the relative contributions of individual groups to the total scattering intensity. The statement is true for two groups of particles and even more so for a greater number of groups. The ratio of particle sizes in different groups does not affect the general negative result.

Acknowledgements

The authors are grateful to ITMO university student N. S. Bondarev for his assistance in calculations.

References

[1] Porai-Koshits E.A. Small Angle X-Ray Diffuse Scattering. *Uspekhi fizicheskikh nauk*, 1949, **39**(4), P. 573–611.

[2] Kitaigorodskii A.I. *X-ray Analysis of Fine-Grained Crystalline and Amorphous Bodies*, Gostekhizdat, Moscow-Leningrad, 1952, 588 p.

[3] Jellinek M.H., Soloman Ernest, Fankuchen I. Measurement and Analysis of Small-Angle X-Ray Scattering. *Ind. Eng. Chem. Anal. Ed.*, 1946, **18**(3), P. 172–175.

[4] Kyutt R.N., Smorgonskaya É.A., Danishevskii A.M., Gordeev S.K., Grechinskaya A.V. Structural studies of nanoporous carbon produced from silicon carbide. *Physics of the Solid State*, 1999, **41**(5), P. 808–810.

[5] Debye P. Zerstreuung von Röntgenstrahlen. *Annalen der Physik*, 1915, **351**(6), P. 809–823.

[6] Guinier A., Fournet G. *Small-Angle Scattering of X-Rays*, New-York, John Wiley, 1955, 268 p.

[7] Porod G. *General Theory* in *Small-Angle X-Ray Scattering*, edited by O. Glatter & O. Kratky. London, Academic Press, 1982, P. 17–52.

[8] Almjasheva O.V., Fedorov B.A., Smirnov A.V., Gusarov V.V. Size, morphology and structure of the particles of zirconia nanopowder obtained under hydrothermal conditions. *Nanosystems: Physics, Chemistry, Mathematics*, 2010, **1**(1), P. 26–36.

[9] Smirnov A.V., Deryabin I.N., Fedorov B.A. Small-angle scattering: the Guinier technique underestimates the size of hard globular particles due to the structure-factor effect. *J. Appl. Cryst.*, 2015, **48**, P. 1089–1093.

[10] Letcher J.H., Schmidt P.W. Small Angle X Ray Scattering Determination of Particle Diameter Distributions in Polydisperse Suspensions of Spherical Particles. *J. Appl. Cryst.*, 1966, **37**, P. 649–655.

[11] Kuchko A.V., Smirnov A.V. The computation of the nanoparticles volume distribution function and the specific surface area based on the small-angle X-ray scattering indicatrix by the method of the statistical regularization. *Nanosystems: Physics, Chemistry, Mathematics*, 2012, **3**(3), P. 76–91.

[12] Porod G. Abhängigkeit der Röntgen—Kleinwinkelstreuung von Form und Grösse der kolloiden Teilchen in verdünnten Systemen. IV. *Acta Physica Austriaca*, 1948, **2**, P. 255–292.

[13] Fedorov B.A., Ptitsyn O.B. and Voronin L.A. X-Ray Diffuse Scattering by Proteins in Solution. Consideration of Solvent Influence. *J. Appl. Cryst.*, 1974, **7**, P. 181.

[14] Denesyuk A.I. Large-Angle Diffuse Scattering, a New Method for Investigating Changes in the Conformation of Globular Proteins in Solutions, *J. Appl. Cryst.*, 1978, **11**, P. 473–477.

[15] Pavlov M.Yu., Fedorov B.A. The method of calculating the surface and the volume of the protein in a solvent. *Biofizika*, 1982, **27**(4), P. 609–613.

[16] Stuhrmann H.B. Ein neues Verfahren zur Bestimmung der Oberflächenform und der inneren Struktur von gelösten globularen Proteinen aus Röntgenkleinwinkelmessungen. *Zeitschr. Physik. Chem. Neue Folge*, 1970, **72**, P. 185–198.

[17] Ibel K., Stuhrmann H.B. Comparison of neutron and X-ray scattering of dilute myoglobin solutions. *J. Mol. Biol.*, 1975, **93**, P. 255–265.

[18] Pavlov M.Yu., Fedorov B.A. Improved technique for calculating X-ray scattering intensity of biopolymers in solution: Evaluation of the form, volume, and surface of a particle. *Biopolymers*, 1983, **22**, P. 1507–1522.

[19] Knyazev S.N., Kalyakin V.Yu., Deryabin I.N., Fedorov B.A., Smirnov A.V., Stepanov E.O., Porozov Yu.B. Prediction of Protein Conformational Mobility with Validation Using Small Angle X-Ray Scattering. *Biophysics*, 2015, **60**(6), P. 886–892.

NANOSYSTEMS: PHYSICS, CHEMISTRY, MATHEMATICS, 2016, 7 (6), P. 1010–1016

Development of the orbital-free approach for hetero-atomic systems

V. G. Zavodinsky[1], O. A. Gorkusha[2]

[1]Institute for Material Science, Khabarovsk, 680042, 153 Tikhookeanskaya str., Russia
[2]Institute of Applied Mathematics, Khabarovsk, 680000, 54 Dzerzhinskogo str., Russia
vzavod@mail.ru, o_garok@rambler.ru

PACS 03.65.-w **DOI 10.17586/2220-8054-2016-7-6-1010-1016**

The key problem of the orbital-free approach is calculation of kinetic energy, especially for hetero-atomic systems. In this work, we used the mono-atomic functionals of kinetic energy to construct the kinetic functionals of complicated systems. We constructed some atomic weights associated with densities of single atoms and then calculated kinetic functions for some atomic complexes. For the examples of SiC, SiAl, AlC, SiO and CO dimers we have demonstrated possibility of our approach to find equilibrium interatomic distances and dissociation energies for hetero-atomic systems.

Keywords: orbital-free, density functional, hetero-atomic systems, interatomic distances, dissociation energies.

Received: 4 April 2016

Revised: 10 May 2016

1. Introduction

Nanotechnology requires simulation methods, which could operate with huge numbers of atoms – up to millions. The most effective quantum methods (for example the Kohn-Sham (KS) method [1]) can work with only hundreds. Therefore, researchers are obliged to use for large nanosystems some less accurate methods with empiric potentials (for example [2, 3]).

The Kohn-Sham method is based on density functional theory (DFT) [4]. The orbital-free (OF) approach also follows this theory, however, it operates with the electron density only (without wave functions or orbitals) and if properly developed, can be applied for the simulation of very large systems: up to millions atoms [5]. Several groups [5–13] are working in this area with different success, and the calculation of the kinetic energy is noted as a main problem. In our previous papers [14–16], we suggested that there is no universal way to describe the kinetic energy of different atoms and compounds. We proposed some simple formulas for systems containing atoms of identical types and simulated the dimers and trimers with metallic and covalent bonds. For examples of Al, Si, and C, we obtained equilibrium interatomic distances, binding energies and interbonding angles in good accordance with published data. Now we try to describe how it is possible to extend our approach to systems with different types of atoms.

2. A general description of the OF approach

As it is known, DFT claims that the energy E of the ground state of any quantum system can be found by minimization of the some functional depending only on the electronic density of this system $\rho(\boldsymbol{r})$:

$$E[\rho] = \int \varepsilon(\rho) d\mathbf{r} = \int V(\mathbf{r})\rho(\mathbf{r}) d\mathbf{r} + \frac{1}{2}\int \varphi(\mathbf{r})\rho(\mathbf{r}) d\mathbf{r} + \int \varepsilon_{ex-c}(\rho) d\mathbf{r} + \int \varepsilon_{kin}(\rho) d\mathbf{r}, \tag{1}$$

where $V(\boldsymbol{r})$ is an external potential, $\varphi(\mathbf{r}) = \int \frac{\rho(\mathbf{r}')}{|\mathbf{r}-\mathbf{r}'|} d\mathbf{r}'$ is the electrostatic electron potential Hartree, ε_{ex-c} and ε_{kin} are exchange-correlation and kinetic energies (per electron).

Minimization of (1) means solution the following equation:

$$F[p] \equiv \frac{\delta\varepsilon[\rho]}{\delta\rho} = V(\mathbf{r}) + \varphi(\mathbf{r}) + \mu_{ex-c}(\rho) + \mu_{kin}(\rho) = 0, \tag{2}$$

where ρ have to satisfy the condition $\int \rho(\mathbf{r}) d\mathbf{r} = N$, N is the number of electrons in the system, $\mu_{ex-c}(\rho) = \frac{\delta\varepsilon_{ex-c}(\rho)}{\delta\rho}$, $\mu_{kin}(\rho) = \frac{\delta\varepsilon_{kin}(\rho)}{\delta\rho}$.

There are some realistic approximations for exchange-correlation potential $\mu_{ex-c}(\rho)$ there; the potential Hartree $\varphi(\mathbf{r})$ may be calculated using Fourier transformations or Poisson equations; the external potential $V(\mathbf{r})$ usually consists of atomic potentials or pseudopotentials. The only real problem is the kinetic potential μ_{kin}.

3. Pseudopotential approach

In practice, the DFT calculations are simpler if one uses pseudopotentials instead of full electron potentials. Therefore, let us rewrite the above equations in the pseudopotential approach, and, for simplicity, let us limit ourselves by s- and p-components of pseudopotentials and a diatomic system. Their distribution on more complicated cases is possible without any trouble. Thus, we will present the total density ρ_{12} as a sum of partial densities: $\rho_{12} = \rho_{12-s} + \rho_{12-p} + \ldots$

The electron energy of this system $E_{12} = \int \varepsilon_{12}(\rho_{12-s}, \rho_{12-p}) d\mathbf{r}$ must be minimal with the condition $\int \Big(\rho_{12-s} + \rho_{12-p}\Big) d\mathbf{r} = N_{12}$, where ε_{12} is the electron energy per electron for the two-atomic system with the total number of electrons N_{12}. In the other words, we have to find the density ρ_{12} that satisfies the system of two equations:

$$F_{12-s} = 0, \quad F_{12-p} = 0.$$

Here

$$F_{12-s} \equiv \frac{\delta\varepsilon_{12}}{\delta\rho_{12-s}} = V_{1-s}(r) + V_{2-s}(\mathbf{r}) + \varphi_{12}(\mathbf{r}) + \mu_{12}^{ex-c}(\rho_{12}) + \mu_{12-s}^{kin}(\rho_{12-s}), \tag{3a}$$

$$F_{12-p} \equiv \frac{\delta\varepsilon_{12}}{\delta\rho_{12-p}} = V_{1-p}(\mathbf{r}) + V_{2-p}(\mathbf{r}) + \varphi_{12}(r) + \mu_{12}^{ex-c}(\rho_{12}) + \mu_{12-p}^{kin}(\rho_{12-p}), \tag{3b}$$

where $V_{1-s}(\mathbf{r})$, $V_{2-s}(\mathbf{r})$, $V_{1-p}(\mathbf{r})$ and $V_{2-p}(\mathbf{r})$ are s and p components of pseudopotentials of the first and second atoms, $\varphi_{12}(\mathbf{r})$ and $\mu_{12}^{ex-c}(\rho_{12})$ are the electrostatic and exchange-correlation potentials calculated for the total electron density ρ_{12} of a dimer, $\mu_{12-s}^{kin}(\rho_{12-s})$ and $\mu_{12-p}^{kin}(\rho_{12-p})$ are partial kinetic potentials depending on corresponding partial densities ρ_{12-s} and ρ_{12-p}.

Thus we can write equations for finding ρ_{12-s} and ρ_{12-p}:

$$V_{1-s}(\mathbf{r}) + V_{2-s}(\mathbf{r}) + \varphi_{12}(\mathbf{r}) + \mu_{12}^{ex-c}(\rho_{12}) + \mu_{12-s}^{kin}(\rho_s) = 0, \tag{4a}$$

$$V_{1-p}(\mathbf{r}) + V_{2-p}(\mathbf{r}) + \varphi_{12}(\mathbf{r}) + \mu_{12}^{ex-c}(\rho_{12}) + \mu_{12-p}^{kin}(\rho_p) = 0, \tag{4b}$$

Obviously, for two isolated atoms we can write equations similar to (4a) and (4b):

$$V_{1-s}(\mathbf{r}) + \varphi_1^0(\mathbf{r}) + \mu_1^{ex-c}(\rho_1^0) + \mu_{1-s}^{kin}(\rho_{1-s}^0) = 0, \quad V_{1-p}(\mathbf{r}) + \varphi_1^0(\mathbf{r}) + \mu_1^{ex-c}(\rho_1^0) + \mu_{1-p}^{kin}(\rho_{1-p}^0) = 0 \tag{5a}$$

$$V_{2-s}(\mathbf{r}) + \varphi_2^0(\mathbf{r}) + \mu_2^{ex-c}(\rho_2^0) + \mu_{2-s}^{kin}(\rho_{2-s}^0) = 0, \quad V_{2-p}(\mathbf{r}) + \varphi_2^0(\mathbf{r}) + \mu_2^{ex-c}(\rho_2^0) + \mu_{2-p}^{kin}(\rho_{2-p}^0) = 0 \tag{5b}$$

As ρ_{1-s}^0, ρ_{1-P}^0, ρ_{2-s}^0, and ρ_{2-P}^0 are equilibrium atomic densities taken from DFT calculations, we can write for $V_{1-s}(\mathbf{r})$, $V_{1-p}(\mathbf{r})$, $V_{2-s}(\mathbf{r})$ and $V_{2-p}(\mathbf{r})$:

$$V_{1-s}(\mathbf{r}) = -\varphi_1^0(\mathbf{r}) - \mu_1^{ex-c}(\rho_1^0) - \mu_{1-s}^{kin}(\rho_{1-s}^0), \quad V_{1-p}(\mathbf{r}) = -\varphi_1^0(\mathbf{r}) - \mu_1^{ex-c}(\rho_1^0) - \mu_{1-p}^{kin}(\rho_{1-p}^0), \tag{6a}$$

$$V_{2-s}(\mathbf{r}) = -\varphi_2^0(\mathbf{r}) - \mu_2^{ex-c}(\rho_2^0) - \mu_{2-s}^{kin}(\rho_{2-s}^0), \quad V_{2-p}(\mathbf{r}) = -\varphi_2^0(\mathbf{r}) - \mu_2^{ex-c}(\rho_2^0) - \mu_{2-p}^{kin}(\rho_{2-p}^0). \tag{6b}$$

Putting (6a) and (6b) in (4) we obtain:

$$\varphi_{12}(\mathbf{r}) - \varphi_1^a(\mathbf{r}) - \varphi_2^a(\mathbf{r}) + \mu_{12}^{ex-c}(\rho_{12}) - \mu_1^{ex-c}(\rho_1^0) - \mu_2^{ex-c}(\rho_2^0) + \mu_{12-s}^{kin}(\rho_{12-s}) - \mu_{1-s}^{kin}(\rho_{1-s}^0) - \mu_{2-s}^{kin}(\rho_{2-s}^0) = 0, \tag{7a}$$

$$\varphi_{12}(\mathbf{r}) - \varphi_1^a(\mathbf{r}) - \varphi_2^a(\mathbf{r}) + \mu_{12}^{ex-c}(\rho_{12}) - \mu_1^{ex-c}(\rho_1^0) - \mu_2^{ex-c}(\rho_2^0) + \mu_{12-p}^{kin}(\rho_{12-p}) - \mu_{1-p}^{kin}(\rho_{1-p}^0) - \mu_{2-p}^{kin}(\rho_{2-p}^0) = 0. \tag{7b}$$

The kinetic dimer functionals $\mu_{12-s}^{kin}(\rho_{12-s})$ and $\mu_{12-p}^{kin}(\rho_{12-p})$ may be presented as follows:

$$\mu_{12-s}^{kin}(\rho_{12-s}) = \mu_{1-s}^{kin}(\rho_{1-s}^0) + \mu_{2-s}^{kin}(\rho_{2-s}^0) + \Delta\mu_{12-s}^{kin}(\rho_{12-s}), \tag{8a}$$

$$\mu_{12-p}^{kin}(\rho_{12-p}) = \mu_{1-p}^{kin}(\rho_{1-p}^0) + \mu_{2-p}^{kin}(\rho_{2-p}^0) + \Delta\mu_{12-p}^{kin}(\rho_{12-p}), \tag{8b}$$

where $\Delta\mu_{12-s}^{kin}(\rho_{12-s})$ and $\Delta\mu_{12-p}^{kin}(\rho_{12-p})$ are unknown functions of partial densities of the two-atomic system. These functions must approach zero if the interatomic distance approaches to infinity. Thus we can take the following simple approximation for them:

$$\Delta\mu_{12-s}^{kin}(\rho^{)}_{12-s} \approx \nu_{A-s}^{kin}(\rho^{)}_{12-s} - \nu_{A-s}^{kin}(\rho_{1-s}^0) - \nu_{A-s}^{kin}(\rho_{2-s}^0), \tag{9a}$$

$$\Delta\mu_{12-p}^{kin}(\rho^{)}_{12-p} \approx \nu_{A-p}^{kin}(\rho^{)}_{12-p} - \nu_{A-p}^{kin}(\rho_{1-p}^0) - \nu_{A-p}^{kin}(\rho_{2-p}^0), \tag{9b}$$

where $\nu_{A-s}^{kin}(\rho_s)$ and $\nu_{A-p}^{kin}(\rho_p)$ are some functions having the same kind for single atoms and for dimers formed from atoms of the same type A.

We can solve these equations with some fitting functions ν_{A-s}^{kin} and ν_{A-p}^{kin} and then calculate the total energy. We find the test functions from the simple request: they must lead to the equilibrium interatomic distances and binding energy for dimers. We hope that these functions will be suitable for more complicated systems in future.

The electron energy of a dimer $E_{\rm dim}^{el}$ contains the electrostatic energy:

$$E_{12}^{e-stat} = \int \left[V_{1-s}(\mathbf{r}) + V_{2-s}(\mathbf{r})\right] \rho_{12-s} d\mathbf{r} + \int \left[V_{1-p}(\mathbf{r}) + V_{2-p}(\mathbf{r})\right] \rho_{12-p} d\mathbf{r} + \frac{1}{2} \int \varphi_{12}(\mathbf{r}) \rho_{12} d\mathbf{r}, \tag{10}$$

the exchange-correlation energy $E_{12}^{ex-c} = \int \varepsilon_{12}^{ex-c}(\rho_{12}) d\mathbf{r}$ and the kinetic energy:

$$E_{12}^{kin} = E_1^{kin} + E_2^{kin} + \iint \left[\nu_{12-s}^{kin}(\rho_{12-s}) d\rho_{12-s} + \nu_{12-s}^{kin}(\rho_{12-p}) d\rho_{12-s}\right] d\mathbf{r}. \tag{11}$$

To find the equilibrium distance and the total energy $E_{\rm dim}^{tot}$, we need to add the repelling energy $E_{12}^{rep} = \dfrac{Z_1 Z_2}{|\mathbf{R}_1 - \mathbf{R}_2|}$, where Z_1 and Z_2 are positive charges of atomic ions with coordinates $\boldsymbol{R}_1$ and $\boldsymbol{R}_2$. Thus $E_{\rm dim}^{tot} = E_{12}^{e-stat} + E_{12}^{ex-c} + E_{12}^{kin} + E_{12}^{rep}$. The binding energy for a dimer (per one atom) would be calculated as follows: $E_b = \frac{1}{2}\left(E_{\rm dim}^{tot} - 2E_a\right)$, where E_a is the atomic energy.

4. Dimers with identical atoms

We took Al, Si, and C as test elements. We used the FHI98pp [17] package as a generator of pseudo-potentials and equilibrium partial electron densities. We calculated exchange and correlation potentials in the local density approach [18, 19]. Studied atoms were located in a cubic cell of the L size (L=30 a.u.; 1 a.u. = 0.529 Å). The cell was divided on $150 \times 150 \times 150$ elementary sub-cells for the integration with the step ΔL of 0.2 a.u. The results of these calculations were compared with published data.

We used the same types of kinetic functions μ_s^{kin} and μ_p^{kin} for isolated atoms and dimers and trimers, however they were found different for different types of atoms. Namely, we used

for Al: $\nu_s^{kin} = 1.0\rho_s^{1/4.5}$; $\nu_p^{kin} = 22.0\rho_p^{1/1.5}$;

for Si: $\nu_s^{kin} = 8.0\rho_s^{1/1.5}$; $\nu_p^{kin} = 1.6\rho_p^{1/3}$;

for C: $\nu_s^{kin} = 1.75\rho_s^{1/3}$; $\nu_p^{kin} = 1.8\rho_p^{1/3}$.

Calculated values of interatomic distances and binding energies for the Al_2, Si_2, and C_2 dimers are collected in Table 1 in comparison with other data. Agreement is rather satisfactory, when one considers that other calculated data are often differing from experimental results and each other.

TABLE 1. Equilibrium distances d and binding energies E_b (absolute values, per atom) for Si_2, Al_2 and C_2 in comparison with known data

Dimer	Source	d, Å	E_b,eV
Si_2	Our OF method	2.2	1.8
	Other calculations	2.21^a 2.23^b	1.599^a 1.97^b
	Experiment	2.24^c	3.0^c
Al_2	Our OF method	2.8	1.4
	Other calculations	2.95^d 2.51^e	1.23^d 1.55^e
	Experiment	2.56^f	1.56^f
C_2	Our OF method	1.4	3.0
	Other calculations	1.24^g 1.36^h	2.6^g 2.7^h
	Experiment	1.24^i	3.1^i

Notations: [a][20], [b][21], [c][22], [d][23],[e][24], [f][25], [g][26], [h][27], [i][28].

5. Dimers with different atoms

Let us rewrite equations (8a) and (8b) for a dimer contained atoms of types A and B:

$$\mu^{kin}_{AB-s}(\rho_{AB-s}) = \mu^{kin}_{A-s}(\rho^0_{A-s}) + \mu^{kin}_{B-s}(\rho^0_{B-s}) + \Delta\mu^{kin}_{AB-s}(\rho_{AB-s}), \tag{12a}$$

$$\mu^{kin}_{AB-p}(\rho_{AB-p}) = \mu^{kin}_{A-p}(\rho^0_{A-p}) + \mu^{kin}_{B-p}(\rho^0_{B-p}) + \Delta\mu^{kin}_{AB-p}(\rho_{AB-p}). \tag{12b}$$

The functions $\Delta\mu^{kin}_{AB-s}(\rho_{AB-s})$ and $\Delta\mu^{kin}_{AB-p}(\rho_{AB-p})$ have to be approximately equal to atomic functions $\Delta\mu^{kin}_{A-s(p)}$ or $\Delta\mu^{kin}_{B-s(p)}$ near atoms A or B, but they have to be mixtures of the atomic functions in the whole space. It seems to us that the simplest way to construct the functions $\Delta\mu^{kin}_{AB-s(p)}$ and $\mu^{kin}_{AB-s(p)}$ is to summarize the atomic functions with some weights:

$$\Delta\mu^{kin}_{AB-s}(\rho_{AB-s}) = W_{A-s}\Delta\mu^{kin}_{A-s}(\rho_{AB-s}) + W_{B-s}\Delta\mu^{kin}_{B-s}(\rho_{AB-s}); \tag{13a}$$

$$\Delta\mu^{kin}_{AB-p}(\rho_{AB-p}) = W_{A-p}\Delta\mu^{kin}_{A-p}(\rho_{AB-p}) + W_{B-p}\Delta\mu^{kin}_{B-p}(\rho_{AB-p}). \tag{13b}$$

For $\Delta\mu^{kin}_{A-s(p)}$ and $\Delta\mu^{kin}_{B-s(p)}$ we propose the following approximations:

$$\Delta\mu^{kin}_{A-s}(\rho_{AB-s}) \approx \nu^{kin}_{A-s}(\rho_{AB-s}) - \nu^{kin}_{A-s}(\rho^0_{A-s}) - \nu^{kin}_{A-s}(\rho^0_{B-s}), \tag{14a}$$

$$\Delta\mu^{kin}_{B-s}(\rho_{AB-s}) \approx \nu^{kin}_{B-s}(\rho_{AB-s}) - \nu^{kin}_{B-s}(\rho^0_{A-s}) - \nu^{kin}_{B-s}(\rho^0_{B-s}), \tag{14b}$$

$$\Delta\mu^{kin}_{A-p}(\rho_{AB-p}) \approx \nu^{kin}_{A-p}(\rho_{AB-p}) - \nu^{kin}_{A-p}(\rho^0_{A-p}) - \nu^{kin}_{A-p}(\rho^0_{B-p}), \tag{14c}$$

$$\Delta\mu^{kin}_{B-p}(\rho_{AB-p}) \approx \nu^{kin}_{B-p}(\rho_{AB-p}) - \nu^{kin}_{B-p}(\rho^0_{A-p}) - \nu^{kin}_{B-p}(\rho^0_{B-p}), \tag{14d}$$

where ν^{kin}_{A-s}, ν^{kin}_{A-p}, ν^{kin}_{B-s} and ν^{kin}_{B-p} are functions related to atoms A and B. For Al, Si and C they are found in the previous Section.

The weights W_{A-s}, W_{A-p}, W_{B-s} and W_{B-P} may be determined through Gauss functions fitted to atomic densities:

$$W_{A-s} = \frac{\alpha_{A-s}\exp\left(-\frac{(\mathbf{r}-\mathbf{R}_A)^2}{\beta_{A-s}}\right)}{\alpha_{A-s}\exp\left(-\frac{(\mathbf{r}-\mathbf{R}_A)^2}{\beta_{A-s}}\right) + \alpha_{B-s}\exp\left(-\frac{(\mathbf{r}-\mathbf{R}_B)^2}{\beta_{B-s}}\right)}; \tag{15a}$$

$$W_{B-s} = \frac{\alpha_{B-s}\exp\left(-\frac{(\mathbf{r}-\mathbf{R}_B)^2}{\beta_{B-s}}\right)}{\alpha_{A-s}\exp\left(-\frac{(\mathbf{r}-\mathbf{R}_A)^2}{\beta_{A-s}}\right) + \alpha_{B-s}\exp\left(-\frac{(\mathbf{r}-\mathbf{R}_B)^2}{\beta_{B-s}}\right)}; \tag{15b}$$

$$W_{A-p} = \frac{\alpha_{A-p}\exp\left(-\frac{(\mathbf{r}-\mathbf{R}_A)^2}{\beta_{A-p}}\right)}{\alpha_{A-p}\exp\left(-\frac{(\mathbf{r}-\mathbf{R}_A)^2}{\beta_{A-p}}\right) + \alpha_{B-p}\exp\left(-\frac{(\mathbf{r}-\mathbf{R}_B)^2}{\beta_{B-p}}\right)}; \tag{15c}$$

$$W_{B-p} = \frac{\alpha_{B-p}\exp\left(-\frac{(\mathbf{r}-\mathbf{R}_B)^2}{\beta_{B-p}}\right)}{\alpha_{A-p}\exp\left(-\frac{(\mathbf{r}-\mathbf{R}_A)^2}{\beta_{A-p}}\right) + \alpha_{B-p}\exp\left(-\frac{(\mathbf{r}-\mathbf{R}_B)^2}{\beta_{B-p}}\right)}. \tag{15d}$$

An example of fitting of the densities and weights is demonstrated in Figure 1. Values for α and β for Si, Al, C and O are presented in Table 2.

TABLE 2. Parameters of weight functions (α and β) for Si, Al, C and O atoms

Type of atom	α_s	α_p	β_s	β_p
Si	0.065	0.040	3.5	4.5
Al	0.065	0.005	3.5	4.5
C	0.200	0.160	1.5	1.8
O	0.300	0.450	1.0	1.5

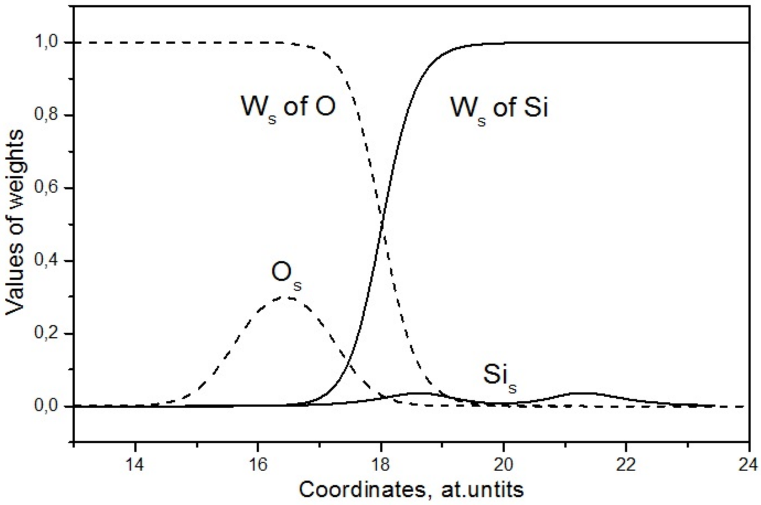

FIG. 1. The s-densities and the weights W_s for oxygen (dashed) and silicon atoms (solid)

We fulfilled calculations for the SiC, SiAl, AlC, SiO, CO, and AlO dimers with parameters shown in Table 2. The kinetic functions for oxygen $\nu_s^{kin} = 1.7\rho_s^{1/3} - 1.0\rho_s$ and $\nu_p^{kin} = 1.5\rho_p^{1/3.5} - 1.0\rho_p$ have been found through simulation of the SiO dimer and then they were used for other oxygen contained dimers. Results of calculations are presented in Table 3. Unfortunately, we did not find published data for the all studied heteroatomic dimers. Therefore, we compared our OF results also with results calculated by us in the framework of the KS DFT approach using the well-known package FHI96md [17].

TABLE 3. Equilibrium distances d and energies of dissociation E_d (absolute values) for SiC, SiAl, AlC, SiO, CO, and AlO

Dimer	Source	d, Å	E_d,eV
SiC	Our OF calculations	1.9	6.9
	Published calculations	1.8^a	7.7^a
	Our KS FHI96md calculations	1.69	6.66
SiAl	Our OF calculations	2.5	3.8
	Our KS FHI96md calculations	2.30	3.10
AlC	Our OF calculations	2.0	6.1
	Our KS FHI96md calculations	1.83	4.32
SiO	Our OF calculations	1.6	7.0
	Our KS FHI96md calculations	1.51	12.06
	Experiment	1.52^b	7.2^b
CO	Our OF calculations	1.0	9.5
	Our KS FHI96md calculations	1.11	15.96
	Experiment	1.13^c	9.6^c
AlO	Our OF calculations	1.8	3.0
	Our KS FHI96md calculations	1.55	9.0
	Experiment	1.62^c	5.27^c

Notations: ^{a}[30], ^{b}[31], ^{c}[32].

One can see from Table 3 that our OF equilibrium distances slightly exceed the experimental ones as well as the KS calculation results, except the CO dimer. As for the dissociation energy, the OF results for the SiO and CO dimers are closer to experimental data than the KS ones. The OF result for SiC correlates with our KS and known calculated values (there is no experimental data). OF calculated energies for the Al contained dimers are rather far from experimental values and from results of KS calculations. The reason for this discrepancy requires future investigation; however, it is remarkable that the KS results are also far from experimental energies in many cases. As a whole, we can conclude that the OF method is able to give us a rather satisfactory information on interatomic distances and energies of systems containing different atoms.

6. Conclusion

We showed the possibility for simulating the interactions of atoms of non-identical types in the framework of the orbital-free version of the density functional theory. For this purpose, we used a rather simple technique, namely: first, the atomic kinetic functions were found for homo-atomic dimers Si_2, Al_2, C_2 and for the SiO dimer; second, some atomic weights were proposed using Gaussians associated with atomic densities; third, kinetic functions for hetero-atomic dimers were constructed. Equilibrium interatomic distances and dissociation energies for the SiC, SiAl, AlC, SiO and CO dimers were found to be in satisfactory agreement with the Kohn-Shem calculations and experimental data.

As the calculation of the kinetic energy is a key point in the modeling of polyatomic systems in the orbital-free approach, it is possible to consider that our work opens a direct way to design an effective modeling method for complicated nanosystems and macromolecules with a large number of atoms.

References

[1] Kohn W., Sham J.L. Self-Consistent Equations including Exchange and Correlation Effects. *Phys. Rev.*, 1965, **140**, P. A1133–A1138.

[2] Konovalenko I.S., Zolnikov K.P., Psakhie S.G. Molecular dynamics investigation of deformation response of thin-film metallic nanostructures under heating. *Nanosystems: Physics, Chemistry, Mathematics*, 2011, **2**(2), P. 76–83.

[3] Smolin A.Yu., Roman N.V., Zolnikov K.P., Psakhie S.G., Kedrinskii V.K. Simulation of structural transformations in copper nanoparticles under collision. *Nanosystems: Physics, Chemistry, Mathematics*, 2011, **2**(2), P. 98–101.

[4] Hohenberg H., Kohn W. Inhomogeneous Electron Gas. *Physical Review*, 1964, **136**, P. B864–B871.

[5] Hung L., Carter E.A. Accurate Simulations of Metals at the Mesoscale: Explicit Treatment of 1 Million Atoms with Quantum Mechanics. *Chemical Physics Letters*, 2009, **475**, P. 163–170.

[6] Wang Y.A., Carter E.A. Orbital-free kinetic-energy density functional theory. *Progress in Theoretical Chemistry and Physics*, Kluwer, Dordrecht, 2000, 117 p.

[7] Huajie Chen, Aihui Zhou. Orbital-Free Density Functional Theory for Molecular Structure Calculations. *Numerical Mathematics: Theory, Methods and Applications*, 2008, **1**, P. 1–28.

[8] Baojing Zhou, Ligneres V.L., Carter E.A. Improving the orbital-free density functional theory description of covalent materials. *Journal Chemical Physics*, 2005, **122**, P. 044103–044113.

[9] Karasiev V.V., Trickey S.B. Issues and challenges in orbital-free density functional calculations. *Computational Physics Communications*, 2012, **183**, P. 2519–2527.

[10] Karasiev V.V., Chakraborty D., Shukruto O.A., Trickey S.B. Nonempirical generalized gradient approximation free-energy functional for orbital-free simulations. *Physical Review B*, **88**, P. 161108–161113(R).

[11] Wesolowski T.A. Approximating the kinetic energy functional $T_s[\rho]$: lessons from four-electron systems. *Molecular Physics*, 2005, **103**, P. 1165–1167.

[12] Junchao Xia, Chen Huang, Ilgyou Shin, Carter E.A. Can orbital-free density functional theory simulate molecules? *The Journal of Chemical Physics*, 2012, **136**, P. 084102(13).

[13] Lehtomäki J., Makkonen I., Caro M.A., Harju A. and Lopez-Acevedo O. Orbital-free density functional theory implementation with the projector augmented wave method. *Journal Chemical Physics*, 2014, **141**, P. 234102(7).

[14] Zavodinsky V.G., Gorkusha O.A. A practical way to develop the orbital-free density functional calculations. *Physical Science International Journal*, 2014, **4**(6), P. 880–891.

[15] Zavodinsky V.G., Gorkusha O.A. Quantum-Mechanical Modeling without Wave Functions. *Physics of the Solid States*, 2014, **56**(11), P. 2329–2335.

[16] Zavodinsky V.G., Gorkusha O.A. New Orbital-Free Approach for Density Functional Modeling of Large Molecules and Nanoparticles. *Modeling and Numerical Simulation of Material Science*, 2015, **5**, P. 39–46.

[17] Fuchs M., Scheffler M. Ab initio pseudopotentials for electronic structure calculations of poly-atomic systems using density-functional theory. *Computational Physics Communications*, 1999,**119**, P. 67–98.

[18] Perdew J.P., Zunger A. Self-interaction correction to density functional approximation for many-electron systems. *Physical Review B*, 1981, **23**, P. 5048–5079.

[19] Ceperley D.M., Alder B.J. Ground state of the electron gas by a stochastic method. *Physical Review Letters*, 1980, **45**, P. 566–569.

[20] Mukhtarov A.P., Normurodov A.B., Sulaymonov N.T. Umarova F.T. Charge States of Bare Silicon Clusters up to Si8 by Non-Conventional Tight-Binding Method. *Journal of nano- and electronic physics*, 2015, **7**, P. 01012(7).

[21] Raghavachari K., Logovinsky V. Structure and bonding in small silicon clusters. *Phys. Rev. Lett.*, 1985, **55**, P. 2853–2856.

[22] Tomanek D., Schluter M.A. Structure and bonding of small semiconductor clusters. *Phys Rev B*, 1987, **36**, P. 1208–1217.

[23] Martínez A., Vela A. Stability of charged aluminum clusters. *Physical Review B*, 1994, **49**, P. 17464(4).

[24] Kumar V., Sundararajan V. Ab initio molecular-dynamics studies of doped magic clusters and their interaction with atoms, *Physical Review B*, 1998, **57**, P. 4939–4942.

[25] Herzberg G. *Spectra of Diatomic Molecules*. Van Nostrand, New York, 1950.

[26] Chelikowsky J.R., Chou M.Y. Ab initio pseudopotential-local density description of the structural properties of small carbon clusters. *Physical Review B*, **37**, P. 6504–6507.

[27] Fougere P.F., Nesbet R.K. Electronic Structure of C_2. *J. Chem. Phys.*, 1966, **44**, P. 285–297.

[28] Huber K.P., Herzberg G. Molecular Spectra and Molecular Structure. IV. *Constants of Diatomic Molecules*. Reinhold, New York, 1979.

[29] Beckstedte M., Kley A., Neugebauer J., Scheffler M. Density functional theory calculations for poly-atomic systems: electronic structure, static and elastic properties and ab initio molecular dynamics. *Computational Physics Communications*, 1997, **107**, P. 187–205.

[30] Patrick A.D., Xiao Dong, Allison T.C., Blaisten-Barojas E. Silicon carbide nanostructures: A tight binding approach. *Journal of Chemical Physics*, 2009, **130**, P. 244704. http://dx.doi.org/10.1063/1.3157282

[31] *Deskbook of the Chemist*. Moscow, Chemistry, 1982, P. 336–341. http://www.chemway.ru/bd_chem/tbl_mol/w_tbl_r_m_08.php.

[32] Andersen T., Haugen H.K., Hotop H. Binding energies in atomic negative ions: III. *J. Phys. Chem. Ref.*, 1999, **28**, P. 1511–1534.

NANOSYSTEMS: PHYSICS, CHEMISTRY, MATHEMATICS, 2016, 7 (6), P. 1017–1023

The dependence of the critical energy density and hot-spot temperature on the radius of metal nanoparticles in PETN

A. A. Zvekov[2], A. P. Nikitin[2], E. V. Galkina[1], A. V. Kalenskii[1]
[1]Kemerovo state University, Kemerovo, 650000, Russia
[2]Federal Research Center of coal and coal chemistry SB RAS
(Institute of Coal Chemistry and Material Science SB RAS), Kemerovo, 650000, Russia
kriger@kemsu.ru

PACS 61.46.+w, 82.33.Vx **DOI 10.17586/2220-8054-2016-7-6-1017-1023**

The dependencies of critical energy density and corresponding hot-spot temperature were calculated in terms of thermal model of energetic materials laser initiation for 12 metal nanoparticles in pentaerythritol tetranitrate (PETN) at pulse duration 12 ns. We showed that the critical hot-spot temperature depends mostly on the nanoparticle's radius while its dependence on the specific heat of the metal is much weaker. The equations for the critical parameters of initiation on radius and specific heat of the nanoparticles were derived. The results are essential for the explosive compounds for optical detonator cup optimization.

Keywords: pentaerythritol tetranitrate, metal nanoparticles, laser radiation, hot-spot model.

Received: 4 August 2016

1. Introduction

The use of pulsed laser methods for the initiation of the explosive processes is under consideration now as a promising replacement for electrical methods of initiation. The main reason is the crucial increasing of safety in explosives utilization and the reduction and minimization of environmental risks and technological disasters. The use of explosives drastically lowers the costs for tunneling works, which determines the increasing scale of their utilization [1]. The most intensively developed way to improve the safety of storage, transportation and use of explosives is the development of energetic materials selectively sensitive to the needed impact [1, 2]. Optical detonators based on silver azide [3, 4] have minimum thresholds value when initiated with laser pulse, but they are also sensitive to other types of impact (heat, electric spark, etc.). To create selectively sensitive materials to laser radiation, one introduces light-absorbing nanoparticles [5] or the synthesis of new compound with absorption bands matching the wavelength of the radiation sources to the existing transparent explosives [6–8]. The minimum initiation energy density of explosive decomposition of the regular blasting explosives (PETN and RDX) with additives of aluminum [2, 9, 10], nickel [10, 11] and other metals nanoparticles is of the order of 1 J/cm^2, which is more than hundred times less than for pure pressed tablets of this explosives. This is an energy saving method to initiate due to the concentration of thermal energy in "hot-spots" and the implementation of thermal explosion in a microcenter variant. The initiation mechanism based on the energy absorption by small inclusions in the explosives volume was formulated in [12] for heavy metal azides. In [13–15], the model was modernized with optical properties and melting processes of nanoparticles and the matrix. The relevance of modernization and study of the hot-spot model is defined by its fundamental value for the development of the mechanisms of thermal explosion model representations, as well as by the applied one based on the selectively sensitive optical detonator creation.

The purpose of this work is the determination of the critical parameters for the initiation of explosive decomposition reaction calculation in the framework of the hot-spot model of thermal explosion, defining the role of the thermophysical parameters of the nanoparticles' material at the stage of formation and development of the reaction hot-spot and analysis of the results in dimensionless coordinates for the process. The compounds based on regular secondary explosives PETN and the nanoparticles of 12 metals were selected as model systems.

The process of initiating self-accelerating decomposition in transparent explosives and metal nanoparticles of different natures can be divided into several stages: the transfer of energy from the output window of the source of monochromatic radiation to nanoparticles, the absorption of the pulse energy of nanoparticles, heating the nanoparticles and labile matrix with the formation of the explosive decomposition hot-spot. The influence of phase transitions in the nanoparticle and the matrix were considered in [15], where it was shown that the melting has little effect on threshold values for initiation of PETN – aluminum nanoparticle systems. Depending on the material and radius of nanoparticles, the absorption efficiency varies considerably [14, 15]. The consideration of multiple scattering in the sample leads to a substantial increase of illumination in the sample's volume [17–19]. The values of the reflection coefficient from the front surface of the sample, experimentally defined in [20], also change significantly depending on sample parameters and radiation wavelength. The optical effect consideration greatly complicates the mechanism for explosive decomposition, but it is possible to allocate a relatively slow subsystem: heating of the nanoparticles where the ratio of the absorption efficiency coefficients of the nanoparticles is 1 [12], conductive heat transfer and thermal chemical decomposition of explosives. It is rational to take into account the peculiar features of nearly instantaneous propagation and absorption of laser light by metal nanoparticles by later correcting the calculated dependence of the nanoparticles' radii critical parameters on previously defined coefficients (as in [15,21,22]).

Additional assumptions implicitly used by the authors of the hot-spot model [12,17] are: metal nanoparticles do not have an oxide film; they are in tight contact with the matrix explosives; and do not interact with it chemically. The spherical symmetry originally used by the authors of the model, is due to three circumstances. First, in the case of pressed pellets of explosives, the light falling onto the sample undergoes multiple reflection on the grain boundaries and metal nanoparticles [17–19]. Because of the randomness of the reflection acts and the significantly negative values of the mean cosine of the scattering angle by metal nanoparticles in PETN [23], the light intensity averages over every direction. Second, the absorbed pulse energy, turning into heat, quickly spreads over the nanoparticles' volume, especially when they are not very big (less than 120 nm). The values of the thermal diffusivity of metals are much higher than that of PETN, which lead to almost uniform heating of the nanoparticles during the pulse duration ($\sim$ 10 ns) [24]. Third, with one-dimensional approach it is possible to produce the necessary mathematical calculations with much greater accuracy for a reasonable time. Thus, the use of spherical symmetry is justified. The system of differential equations describing the processes of conductive heat transfer, and heat generation due to chemical decomposition of energetic material, has the form [12]:

$$\begin{aligned}
&\frac{\partial T}{\partial t} = \alpha\left(\frac{\partial^2 T}{\partial x^2} + \frac{2}{x}\frac{\partial T}{\partial x}\right) + \frac{Q}{C}k_0 n \cdot \exp\left(-\frac{E}{k_B T}\right), && x > R,\\
&\frac{\partial n}{\partial t} = -k_0 n \cdot \exp\left(-\frac{E}{k_B T}\right), && x > R,\\
&\frac{\partial T}{\partial t} = \alpha_m\left(\frac{\partial^2 T}{\partial x^2} + \frac{2}{x}\frac{\partial T}{\partial x}\right), && x < R,
\end{aligned} \tag{1}$$

where T is temperature, n is relative concentration of explosives decreases in the course of the decomposition reaction from 1 to 0, $\alpha = 1.1{\cdot}10^{-3}$ cm^{2}s^1 and α_m are thermal diffusivities of the matrix and nanoparticle, k_B is Boltzmann constant, $E = 165$ kJ/(mol·K) is energy of activation, $Q = 9.64$ kJ/cm^3 is heat efficiency of the decomposition, $k_0 = 1.2{\cdot}10^{16}$ s^{-1} is pre-exponential factor [14], $= 2.22$ J/(cm^{3}K) is volumetric heat capacity of the explosives with boundary condition for $x = R$ is:

$$J - C_m\alpha_m \cdot \left.\frac{\partial T}{\partial x}\right|_{x \to R-0} + C\alpha \cdot \left.\frac{\partial T}{\partial x}\right|_{x \to R+0} = 0, \tag{2}$$

where C_m is volumetric heat capacity of the nanoparticle, $J(t)$ is is the absorbed density of the laser pulse radiation power. Tn terms of the model we neglecting the possible non-ideal thermal contact of the nanoparticle and the explosive [25] and possible diffusion of the explosive material [26].

The facilities based on a neodymium laser typically used for initiation of explosive decomposition have the dependence of the radiation power of the pulse close to the normal distribution function [27]. Taking the maximum intensity of the pulse as the reference time position, we obtain for the quantity $J(t)$ the expression:

$$J(t) = k_i H_0 \cdot \exp\left(-k_i^2 t^2\right)\big/\sqrt{\pi}, \tag{3}$$

where $k_i = \dfrac{2\sqrt{\ln(2)}}{t_i}$ is a parameter that determines the pulse duration; H_0 – the pulse energy density. Multipliers of equation (3) normalized the integral of $J(t)$ with respect to time on H_0. Model of explosive decomposition under initiation by a laser pulse is rational initially to explore in dimensional variables, with a further choice of dimensionless. To determine the critical parameters of explosive decomposition, the system of equations for the model (1-3) was numerically solved on the grid with a variable coordinate step by the method described in [24,28].

The calculations were performed for 12 metals to elucidate the role of thermophysical properties for the material nanoparticles. The values of heat capacities and thermal conductivities of the metals used were taken from [21]. The variation of the nanoparticles radius was carried out over the 10–120 nm range. This interval covers the radii used in the experimental studies of aluminum [2,19] and nickel [10,11] nanoparticles, a typical area radii of noble metal nanoparticles, 10–20 nm, by effectively absorbing electromagnetic radiation at the frequencies of plasmon resonance [22, 29] and relatively large radii of transition metals at which the radiation of the first harmonic of a neodymium laser is absorbed the most efficiently [23] though the plasmon band is observed in the UV region for aluminum nanoparticles [30].

2. The method of calculation and results

The calculation of the critical energy density was carried out using bisection method with the interval reduction achieving up to a relative accuracy of 10^{-8}. The determination of the system bifurcation point (1)–(3) with such precision requires the minimization of errors associated with the calculation of critical parameters for explosive decomposition initiation and definition of the explosive decomposition parameters close to the bifurcation point [31]. For further analysis, the maximum energy density at which the explosion was not observed H was retained. To consider the contribution of the chemical reaction in the threshold of initiation, the maximum temperature on the surface of the nanoparticles with the energy density $H(T_{max})$ and the time of its occurrence $t(T_{max})$ were calculated. The calculation of the maximum temperature T_{max0} for each system at the energy density of H without taking into account the heat flux due to chemical decomposition (installed $k_0 = 0$) and the time of appearance of maximum temperature $t(T_{max})$ was subsequently performed.

For 12 selected metals in PETN, we calculated selected characteristics of the process near the bifurcation point. Table 1 presents the results of calculations of H, T_{max}, $t(T_{max})$, T_{max0} and $t(T_{max0})$ with the radii of nanoparticles of cobalt ranging from 10–120 nm. The critical energy density values significantly depend upon the nanoparticles' radii, but an even more amazing result is the significant dependence of the temperature characteristic of the process on the radius of the nanoparticles. From Table 1, it follows that T_{max} is significantly higher than T_{max0}. The temperature difference increases with decreasing nanoparticle radius. For cobalt nanoparticles with a 10 nm radius and a pulse duration of 12 ns, the difference is around 346 K and in the limit of large radius is less than 40 K. The dependence $T_{max0}(R)$ is well described by the equation:

$$T_c\left(R\right) = T_\infty + \frac{r_T}{R}, \tag{4}$$

where the variable parameters T_∞ and r_T (4) are determined with approximation of the corresponding dependencies. The values of the variable parameters for the 12 considered metals in the matrix PETN are given in Table 2.

As one can see, the values of T_∞ for the 12 metals differ by only 19 K. The parameter r_T deviates maximally from the middle value by 2% only. Consequently, the critical temperature of the reaction hot-spot of explosive decomposition is almost independent on the nature of the metal nanoparticles.

Let us consider the dependence of the critical energy density of the radius and the nature of the nanoparticles. Consider a simplified model for thermophysical processes with heating of nanoparticles in inert matrices. The maximum change by primary hot-spot temperature without considering contribution of chemical decomposition of the matrix could be estimated with the expression [11, 12]:

$$\Delta T = \frac{3}{4\pi} \cdot \frac{\pi R^2 H}{C_m R^3 + C\left(\left(R+h\right)^3 - R^3\right)}. \tag{5}$$

In the numerator of formula (1), the energy absorbed by the nanoparticle as a result of the pulse action remains, and the denominator estimates the overall heat capacity of the system, involving heating of the matrix layer of thickness h and nanoparticles to the same temperature. The value h is the effective thickness of the heated layer of the matrix, determined by the pulse duration, heat capacity and thermal diffusivity of the matrix, but not the thermophysical properties of the nanoparticles (as the ration $\alpha << \alpha_m$ is fulfilled for all the metals). Using the formula (4), approximating the dependence of the critical temperature of the hot-spot on the nanoparticles' radii without a chemical reaction as T_{max0}, and dropping off the term proportional to h^3, we get:

$$H = \frac{4}{3R} \cdot \left(T_\infty + \frac{r_T}{R} - T_0\right) \cdot \left[C_m R^2 + 3Ch \cdot (R+h)\right]. \tag{6}$$

Approximation of the calculated dependences $H(R)$ by formula (6) was performed for all 12 selected metals in PETN applying the previously defined fitting parameters T_∞ and r_T that are given in columns 2 and 3 of Table 2. The array h is shown in column 4 of Table 2. From the estimated values of h, it follows that they are independent of the nature of the metal nanoparticles: the average value of $h = 34.87$ nm and a maximum deviation is only 0.5 %. This result is consistent with its physical meaning as the typical thickness of the heated layer.

Using formula (6) we could demonstrate the effect of the metals' specific heat on the dependence of $H(R)$. The coordinates of the minima for the dependences $H(R)$ for 12 metals in PETN (H_{min} and R_{min}) are presented

TABLE 1. Calculated with the radii of the cobalt nanoparticles R values H, T_{max}, $t(T_{max})$, T_{max0}, $t(T_{max0})$

R, nm	H, mJ/cm^2	T_{max},K	$t(T_{max})$,ns	T_{max0},K	$t(T_{max0})$, ns
10	136.170749	1497.06	4.0496	1150.90	1.3178
15	97.928431	1360.16	6.080	1107.83	1.9417
20	81.485410	1289.6	7.5321	1088.68	2.5232
25	72.908448	1245.46	8.6159	1077.56	3.0538
30	68.110572	1214.96	9.4775	1070.86	3.4867
35	65.3497462	1192.23	10.200	1066.07	3.8931
40	63.8247203	1174.39	10.722	1062.41	4.2578
45	63.1029816	1159.97	11.203	1059.51	4.6208
50	62.931098	1148.01	11.495	1057.11	4.9111
55	63.1510649	1137.91	11.601	1055.09	5.2318
60	63.6594571	1129.31	11.725	1053.32	5.4625
65	64.3858326	1121.89	11.692	1051.77	5.7452
70	65.2806344	1115.45	11.606	1050.37	5.9199
75	66.3080204	1109.81	11.596	1049.10	6.138
80	67.4414514	1104.82	11.558	1047.95	6.3609
85	68.6608745	1100.38	11.488	1046.87	6.5691
90	69.9508670	1096.38	11.465	1045.86	6.6802
95	71.2993787	1092.77	11.388	1044.92	6.8438
100	72.6968651	1089.47	11.400	1044.04	7.0616
105	74.1356704	1086.45	11.316	1043.19	7.2034
110	75.6095868	1083.66	11.349	1042.39	7.3449
115	77.1135275	1081.08	11.330	1041.62	7.4714
120	78.6438735	1078.68	11.316	1040.86	7.6307

in the last columns of Table 2. Assuming that the dependence $T_{max0}(R)$ at relatively large radii R_{min} corresponding to the minimum H, is weak, in this limit, the dependence $H(R)$ will match the radius of most heated nanoparticles [14]:

$$R_{\min} = \sqrt{\frac{6\alpha k_i C}{C_m}}. \tag{7}$$

Equation (7) leads to a linear dependence of the R_{min} square on the reverse value of the metal heat capacity (C_m). Fig. 1 shows the dependence of the abscissa of the minimum R_{min} as a dependence on the metal volume specific heat capacity in the rectifying coordinates. Points in the figure show the data for the metals lead, tin, aluminum, silver, gold, palladium, vanadium, chromium, copper, iron, cobalt, nickel, and their good linear approximation.

TABLE 2. Calculated critical parameters of explosive decomposition for PETN with various metal nanoparticles

Metal	T_∞, K	r_T, K·nm	h, nm	H_{min}, mJ/cm^2	R_{min}, nm
Pb	1070.45	1638.38	35.03	47.712	79.20
Sn	1071.39	1644.82	34.98	49.430	74
Al	1074.31	1688.38	34.85	54.987	61.3
Ag	1074.35	1689.10	34.85	55.206	60.90
Au	1074.43	1690.08	34.85	55.352	60.60
Pd	1075.68	1703.11	34.81	58.068	56
V	1076.33	1709.01	34.79	58.559	55.20
Cr	1076.03	1704.22	34.81	59.930	53.30
Cu	1075.99	1700.82	34.83	61.145	51.60
Fe	1076.73	1702.26	34.82	61.802	50.80
Co	1076.41	1698.39	34.84	62.928	49.40
Ni	1076.51	1693.51	34.85	64.097	48.10

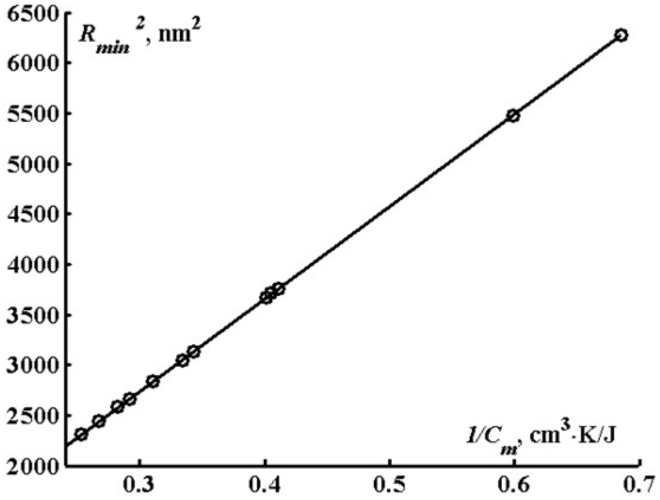

FIG. 1. The dependence of the square R_{min}, from the reverse value of the metal heat capacity (C_m) with pulse width was 12 ns. The dots are the data for the metals: lead, tin, aluminum, silver, gold, palladium, vanadium, chromium, copper, iron, cobalt, nickel. Line-approximation of the line passing through the origin

3. Conclusion

Using the characteristics of 12 metals in the present work allowed us to investigate the effect of nanoparticles' specific heat in the range from 1.46 (lead) to 3.96 J/(cm^3·K) (nickel) on the main characteristics of the process of laser initiation. The obtained analytical equations quantitatively describing the results of the calculations allow us to predict the influence of specific heat over a wide range that it is necessary to expand the range of materials considered as promising additives for the selective sensitivity of explosives by laser radiation.

Currently, the refinement of the hot-spot model for the laser initiation of thermal explosion of energetic materials containing metal nanoparticles occurs in a number of directions that span the optical and thermophysical processes. For this reason, the comparison with experiment of the results of this study is difficult. Previously it was shown [9] that taking into account the optical properties of individual metal nanoparticles allows us to reduce considerably the differences of the absolute theoretical and experimental values for the critical energy density. The last quantity can be reliably predicted if we know the kinetic parameters for the decomposition reaction in the temperature region in which a hot-spot is formed. Direct measurement of the rate constant over this temperature range is difficult, therefore, reasonable extrapolations from the low temperature region generally used may not always be applicable. Alternatively, the obtained expressions allow one to predict correctly the effect of the thermophysical parameters of nanoscale additives, which is essential in the development of new energetic materials.

Acknowledgements

This work was supported by Ministry of Education and Science of the Russian Federation (governmental project No. 2014/64) and Russian Foundation for Basic Research for the financial support (grant 14-03-31648).

References

[1] Chernai A.V., Sobolev V.V., Chernai V.A., Ilyushin M.A., Dlugashek A. Laser Ignition of Explosive Compositions Based on di-(3-hydrazino-4-amino-1,2,3-triazole)-Copper(II) Perchlorate. *Combustion, Explosion and Shock Waves*, 2003, **39**(3), P. 335–339.

[2] Aduev B.P., Nurmukhametov D.R., Furega R.I., Zvekov A.A., Kalenskii A.V. Explosive decomposition of PETN with nanoaluminum additives under the influence of pulsed laser radiation at different wavelengths. *Russian Journal of Physical Chemistry B*, 2013, **7**(4), P. 453–456.

[3] Kriger V.G., Kalenskii A.V., Zakharov Yu.A., Tsipilev V.P. Mehanizm tverdofaznoj cepnoj reakcii. *Materialovedenie*, 2006, **9**, P. 14–21.

[4] Kriger V.G., Kalenskii A.V., Zvekov A.A. Relaxation of electronically excited products of solid-state reactions in the crystal lattice. *Russian Journal of Physical Chemistry B*, 2012, **6**(1), P. 15–18.

[5] Aduev B.P., Belokurov G.M., Nurmukhametov D.R., Nelyubina N.V. Photosensitive material based on PETN mixtures with aluminum nanoparticles. *Combustion, Explosion, and Shock Waves*, 2012, **48**(3), P. 361–366.

[6] Greenfield M.T., McGrane S.D., Bolme C.A., Bjorgaard J.A., Nelson T.R., Tretiak S., Scharff R.J. Photoactive high explosives: linear and nonlinear photochemistry of petrin tetrazine chloride. *Journal of Physical Chemistry A*, 2015, **119**(20), P. 4846–4855.

[7] Evers J., Gospodinov I., Joas M., Klapötke T.M., Stierstorfer J. Cocrystallization of photosensitive energetic copper(II) perchlorate complexes with the nitrogen-rich ligand 1,2-di(1H-tetrazol-5-yl)ethane. *Inorganic Chemistry*, 2014, **53**(21), P. 11749–11756.

[8] Gerasimov S.I., Ilyushin M.A., Kuz'min V.A. A laser diode beam initiates a high-energy mercury perchlorate-polymer complex. *Technical Physics Letters*, 2015, **41**(4), P. 338–340.

[9] Kalenskii A.V., Zvekov A.A., Anan'eva M.V., Zykov I.Yu., Kriger V.G., Aduev B.P. Influence of laser wavelength on the critical energy density for initiation of energetic materials. *Combustion, Explosion, and Shock Waves*, 2014, **50**(3), P. 333–338.

[10] Aduev B.P., Nurmukhametov D.R., Furega R.I., Zvekov A.A. Controlling pentaerythrite tetranitrate sensitivity to the laser effect through the addition of nickel and aluminum nanoparticles. *Russian Journal of Physical Chemistry B*, 2014, **8**(3), P. 352–355.

[11] Zvekov A.A., Ananyeva M.V., Kalenskii A.V., Nikitin A.P. Regularities of light diffusion in the composite material pentaerythriol tetranitrate-nickel. *Nanosystems: Physics, Chemistry, Mathematics*, 2014, **5**(1), P. 685–691.

[12] Alexandrov E.I., Tsipilev V.P. Effect of the pulse length on the sensitivity of lead azide to laser radiation. *Combustion, Explosion and Shock Waves*, 1984, **20**(6), P. 690–694.

[13] Kalenskii A.V., Kriger V.G., Zvekov A.A., Grishaeva E.A., Zykov I.Yu, Nikitin A.P. The Microcenter Heat Explosion Model Modernization. *Izvestija vysshih uchebnyh zavedenij. Fizika*, 2012, **55**(11-3), P. 62–65.

[14] Kriger V.G., Kalenskii A.V., Zvekov A.A., Zykov I.Yu., Aduev B.P. Effect of laser radiation absorption efficiency on the heating temperature of inclusions in transparent media. *Combustion, Explosion, and Shock Waves*, 2012, **48**(6), P. 705–708.

[15] Aduev B.P., Anan'eva M.V., Zvekov A.A., Kalenskii A.V., Kriger V.G., Nikitin A.P. Miro-hotspot model for the laser initiation of explosive decomposition of energetic materials with melting taken into account. *Combustion, Explosion and Shock Waves*, 2014, **50**(6), P. 704–710.

[16] Galkina E.V., Radchenko K.A. The model of initiation of composites PENT – Tin by the pulse Nd: YAG laser. *Nauka-Rastudent.ru*, 2015. `http://nauka-rastudent.ru/21/2917/`.

[17] Aleksandrov E.I., Tsipilev V.P. Characteristics of the optical regime in the volume of a semiinfinite layer of diffusely scattering medium under illumination by a directed beam with finite aperture. *Russian Physics Journal*, 1989, **31**(10), P. 789–794.

[18] Zvekov A.A., Kalenskii A.V., Aduev B.P., Ananyeva M.V. Calculation of the optical properties of pentaerythritol tetranitrate–cobalt nanoparticle composites. *Journal of Applied Spectroscopy*, 2015, **82**(2), P. 213-220.

[19] Aduev B.P., Nurmukhametov D.R., Belokurov G.M., Zvekov A.A., Kalenskii A.V., Nikitin A.P., Liskov I.Yu. Integrating sphere study of the optical properties of aluminum nanoparticles in tetranitropentaerytrite. *Technical Physics*, 2014, **59**(9), P. 1387–1392.

[20] Aduev B.P., Nurmukhametov D.R., Liskov I.Yu., Kalenskii A.V., Anan'eva M.V., Zvekov A.A. Characteristics of the initiation of the explosive decomposition of PETN by the second-harmonic pulsed radiation of a neodymium laser. *Russian Journal of Physical Chemistry B*, 2015, **9**(6), P. 915–920.

[21] Ananyeva M.V., Zvekov A.A., Zykov I.Yu., Kalenskii A.V., Nikitin A.P. Promising compounds for the cap of optical detonator. *Perspektivnye materialy*, 2014, **2**, P. 5–12.

[22] Lukatova S.G. Calculation of the PETN-gold composites' absorptivity for the second harmonic of the Nd:YAG laser. *Mezhdunarodnoe nauchnoe izdanie Sovremennye fundamental'nye i prikladnye issledovanija*, 2014, **1**(12), P. 95–98.

[23] Ivashenko G.J. The regularities of light scattering from the Nd:YAG first harmonic of nickel nanoparticles in PETN. *Actualscience,* 2015, **1**(3), P. 63–67.

[24] Kriger V.G., Kalenskii A.V., Zykov I.Y., Nikitin A.P., Zvekov A.A. Heat-transfer processes upon laser heating of inert-matrix-hosted inclusions. *Thermophysics and Aeromechanics*, 2013, **20**(3), P. 367–374.

[25] Glushkov D.O., Kuznetsov G.V., Strizhak P.A. Ignition of a composite propellant by a hot particle under conditions of a nonideal thermal contact. *Russian Journal of Physical Chemistry B*, 2015, **9**(4), P. 631–636.

[26] Chumakov Yu.A., Knyazeva A.G. Initiation of reaction in the vicinity of a single particle heated by microwave radiation. *Combustion, Explosion, and Shock Waves*, 2012, **48**(2), P. 144–150.

[27] Odincova O.V., Ivashenko G.J. Temporal impulse shape of the first harmonic of the ND:YAG laser. *Mezhdunarodnoe nauchnoe izdanie Sovremennye fundamental'nye i prikladnye issledovanija*, 2015, **2**(17), P. 43–48.

[28] Zykov I.Yu., Kalenskii A.V. Application program package to simulate the kinetics of the explosive decomposition initiated by laser pulse in energetic material containing metal nanoparticles. *Aspirant*, 2015, **2**, P. 73–77.

[29] Kalenskii A.V., Zvekov A.A., Nikitin A.P., Anan'eva M.V., Aduev B.P. Specific features of plasmon resonance in nanoparticles of different metals. *Optics and Spectroscopy*, 2015, **118**(6), P. 978–987.

[30] Blaber M.G., Arnold M.D., Harris N., Ford M.J., Cortie M.B. Plasmon absorption in nanospheres: A comparison of sodium, potassium, aluminium, silver and gold. *Physica B: Condensed Matter*, 2007, **394**(2), P. 184–187.

[31] Radchenko K.A. The effect of the relative error on the accuracy of mathematical modeling. *Nauka-rastudent.ru*, 2015. `http://nauka-rastudent.ru/24/3131/`.

NANOSYSTEMS: PHYSICS, CHEMISTRY, MATHEMATICS, 2016, 7 (6), P. 1024–1030

Synthesis and studies on structural and optical properties of zinc oxide and manganese-doped zinc oxide nanoparticles

S. Ajin Sundar[1], N. Joseph John[2]

[1]Department of Physics, Government Arts College, Udhagamandalam, Tamilnadu, India. Pin – 643002

[2]Department of Physics, Sethupathy Government Arts College, Ramanathapuram, Tamilnadu, India. Pin – 623502

njosephjohn@gmail.com

DOI 10.17586/2220-8054-2016-7-6-1024-1030

Wet chemical techniques have been used to synthesize undoped and Mn-doped nanoparticles at room temperature. Highly stable pure and 5.0 weight% Mn-doped ZnO nanoparticles have been prepared. The morphologies, structures and optical properties of the as-prepared samples were characterized by X-ray powder diffraction, scanning electron microscopy, energy dispersive X-ray spectroscopy and UV-Vis spectra. The results clearly reveled that both the pure and doped samples had a wurtzite hexagonal phase. The SEM studies illustrated that grain size decreases with Mn doping, with average diameter ∼30 nm, which is in good agreement with the average crystalline size calculated by Scherrer's formula. The strong absorption band in the UV region for the prepared samples can be attributed to the band edge absorption of the wurtzite hexagonal ZnO.

Keywords: nanoparticles, X-ray techniques, structural, FTIR, SEM, EDX.

Received: 1 March 2016

Revised: 25 August 2016

1. Introduction

Due to its wide band gap (∼3.37 eV) and large exciton binding energy (∼60 meV), ZnO is of great interest for photonic applications and its optical properties have been studied in detail. In recent years, due to prediction of possible ferromagnetic properties in transition metal-doped ZnO with Curie temperatures (Tc) above room temperature, studies of transition metal doped ZnO have attracted much interest [1, 2]. Multifunctional materials come on stage accompanied with magnetic properties in diluted magnetic semiconductors (DMS), in which non-magnetic ions replace some of the magnetic and non-magnetic cations. The origin of ferromagnetic properties in diluted semiconductors have been theoretically and experimentally studied [3, 4].

Among DMS materials, ZnO-based DMS has remarkable features: (i) Direct wide band gap at room temperature, (ii) access to the large bulk and high-quality single crystals of ZnO and (iii) large exciton binding energy. The latter is useful for having lasers with high efficiencies at room temperature [5, 6]. In addition, ZnO is useful in solar cells and sensors as it is transparent conductive and piezoelectric [7]. Pure ZnO nanostructures show weak optical features that result from point defects such as oxygen vacancy or interstitial Zn; therefore, they cannot be used directly in the industry [7]. As a result, doping ZnO with a convenient element is a method for engineering optical and magnetic properties. Furthermore, in order to make optoelectronic devices, n-type and p-type states are needed. It is relatively difficult to achieve p-type doping and this limitation is considered an obstacle to using ZnO in these applications [8].

Additionally, ZnO is lower in cost and is environmental friendly as compared to other metal oxides [9]. Normally, ZnO is studied in nanoscale; this is probably due to the fact that the high surface area to mass ratio of nanoparticles could enhance the adsorption of organic pollutants on the surface of particles as compared to the bulk materials [10]. Thus, in order to enhance the optical, magnetic, and electrical properties of ZnO, transition metal-doped ZnO nanoparticles have been introduced. The modification of ZnO nanoparticles by impurity incorporation leads to possible application in UV optoelectronic and spin electronics [11]. Among the transition elements, Mn shows the maximum magnetic behaviors with electron effective mass $\sim 0.3me$ (me= free electron mass); a doping of Mn into the ZnO semiconductor host lattice may result in large injected spins and carrier which make it suitable to be applied as diluted magnetic semiconductor (DMSs) [12].

ZnO has penetrated far into industry, and is one of the critical building blocks in modern society. Zinc oxide is in all likelihood one of the most abundant forms of any known material. The properties of ZnO are strongly dependent on its structure, including the morphology, aspect ratio, size, orientation, and crystal density. Due to its potential application in many areas, such as optoelectronic devices, solar cells, chemical sensor, and photocatalyst hence, ZnO has attracted much attention from researchers and scientists to develop it for technological applications.

The term "doped" is used to modify the optical or magnetic properties of the host by adding impurities ions which become incorporated into the host lattice. Doping with $3d$ metals such as Mn, Ni, Fe, Co, and Cr will increase the surface area and reduce the particle size of ZnO nanoparticles [13]. Mn is preferred for the doping of ZnO because the d electron of Mn at t_{2g} level can easily overlap with the ZnO's valence bond, as compared with other transition elements. Among nanomaterials of transition metal oxides, ZnO is considered as a significant material for multiple applications, including catalytic, optical, magnetic, electrical, electrochemical and biological uses. These properties makes ZnO as a multifunctional material that finds applications in solar cell, biosensors, field effect transistors, light emitting diodes, diluted and ferromagnetic materials for spintronics, photocatalysis and anti-bacterial activity [13]. There are various studies which have shown that Mn-doped semiconductors have influenced the physical, chemical, and structural properties of undoped ZnO nanoparticles. For example, the optical properties of undoped ZnO nanoparticles especially on the tuning of the band gap can be greatly improved at the nanoscale by optimum Mn doping content [14, 15].

It was observed that doping with $3d$ metals reduced the Eg of semiconductors by forming interband-gap localized levels [16]. The charge-transfer transition between the d-electron of dopant (t_{2g} levels) and the conduction band (CB) or valence band (VB) was reported [17]. Conversely, the metal's d-orbitals are mixed with the CB and VB of the semiconductors [18]. This overlap is because wide VB or CB directly decreases Eg. Recently, there has been much attention focused on modifying ZnO by doping with transition metals, such as Ag [19], Ni [20], Cu [21], Co [22], Cr [23], Ti [24]. These studies demonstrated that the metals can change the Eg of ZnO, and that the dopants can alter the ZnO grain size. This also demonstrated the presence of the d-electron because the t_{2g} of manganese (Mn) is very close to the VB [17, 25]. More recently, the synthesis of a Mn-doped ZnO nano-crystal (not powder) was reported by wet-chemical techniques [26]. Moreover, ZnO nanocrystalline powders doped with 1, 3 and 5% Mn were prepared using a sol-gel process [27].

Zinc oxide is a II-VI compound semiconductor. Its properties, such as wide bandgap, large excitation binding energy and low threshold power for optical pumping are considered to be the eminent features of ZnO. Thus, ZnO is said to be an efficient phosphor [28–31]. Type II–VI semiconductors, as a class of materials, have been and still are the subject of much intensive investigation. The growth of semiconductor technology in the early 1950's highlighted the limitations of silicon and germanium, which perhaps the character and the magnitude of the forbidden energy gap were the most disadvantageous. At first the extension in the range of energy gaps was sought in these III–V semiconductors, where considerable success has been achieved with InSb and GaAs in the low and high energy gap areas respectively. GaAs is today probably the most developed and well understood compound in existence. Concurrently with the later developments in the III-V semiconductors, systematic studies were made for several of these compounds.

The results of these studies have revealed much about the general nature of the II-VI semiconductors and the feature of chemical stability of the higher energy gap materials at room temperature offers an immediate advantage over the unstable III–V phosphides. Type II–VI semiconductors, in their broadest sense, include compounds formed from elements of group II and group VI of the periodic table. Zinc oxide has a wide band gap large excitation energy of 60 meV, high chemical stability, good piezo-electric properties, nontoxicity and biocompatibility. To synthesize ZnO nanoparticles with transition metals, several different methods have been employed, such as wet chemical methods like sol-gel [32], co-precipitation [33], combustion [34] etc. These nanoparticles have been used in a wide range of applications, such as sensors, varistors, piezoelectric, transducers, surface acoustic wave devices, phosphors, transparent conducting oxides, optoelectronic devices, ferromagnetic devices, and heterogeneous photo catalysts [35–40]. In this paper we report the synthesis and characterization of Mn doped and undoped zinc oxide via wet chemical method as well as the effect of 5.0 wt% Mn doping in ZnO on its structural, morphological and optical properties.

2. Experimental

2.1. Materials Used

Analytical Reagent (AR) grade Zinc acetate dehydrate, Sodium Dodecyl sulfate, Sodium hydroxide and manganese chloride were used for synthesis of pure and manganese doped zinc oxide nanoparticles. Reagents were purchased from Merck India and used as received without any further purification.

2.2. Synthesis of ZnO Nanoparticles

For the synthesis of pure zinc oxide nanoparticles 10.966 g of zinc acetate dihydrate was added to 250 ml water with vigorous stirring until an homogeneous solution was obtained. Next, 10.974 g of NaOH was added to the solution under stirring and to this solution 14.4 g of sodium dodecyl sulfate was added under continuous stirring until a pH of 12 was reached. This solution was was dried in a hot air oven at 160 °C overnight. The material was then ground in a mortar and pestle and the powder thus obtained was washed several times using ethanol and deionized water. The product was then dried at 60 °C overnight and the obtained product was calcined at 500 °C for 4 hours.

2.3. Synthesis of Mn-Doped ZnO Nanoparticles

For the synthesis of 5.0 weight% manganese doped ZnO, 0.7916 g manganese chloride was added to 250 ml of water under vigorous stirring and 10.966 g zinc acetate was then added. Next, 10.974 g of sodium hydroxide was added to the solution with 14.4 g sodium dodecyl sulfate added under continuous stirring till the pH value reached 12 and the solution was dried in a hot air oven at 160 °C overnight. Then the material was taken and ground using a mortar and pestle and the obtained powder was washed several times using ethanol and deionized water. The product was dried at 60 °C for 2 days and the obtained product was then calcined at 500 °C for 4 hours.

2.4. Characterization Studies

The pure and manganese doped Zinc oxide nanoparticles thus obtained were characterized by UV, FTIR, XRD, SEM and EDAX. The seven synthesized samples were characterized using UV-visible spectroscopy by dissolving 0.1 g of each sample in 100 ml doubly distilled water. The absorption data was recorded as a function of wavelength using a UV-visible spectrophotometer model-2202, India. XRD (X-ray Powder Diffraction) is rapid analytical technique primarily used for phase identification of crystalline material. The average crystallite size was determined from XRD peaks using Scherer's formula. The field emission Scanning Electron Microscopy (SEM) is one of the most versatile and well known analytical techniques, offering advantages like high magnification, large depth of focus, great resolution. Electrons generated from an electron gun enter a surface of sample and generate many low energy secondary electrons. The intensity of these secondary electrons is governed by the surface topography of the same. An image of the sample surface is therefore constructed by measuring secondary electron intensity as a function of the position of the scanning primary electron beam. EDX analysis is a useful tool widely used for chemical analysis. The intensity of backscattered electrons generated by electron bombardment can be correlated to the atomic number of the element within the sampling volume. Hence, qualitative elemental information can be revealed. The characteristic X-rays emitted from the sample serve as fingerprints and give elemental information for the samples, including semi-quantitative analysis, quantitative analysis, line profiling and spatial distribution of elements.

3. Results and Discussion

3.1. UV-Visible Studies

Figure 1 shows the UV-Visible spectra for zinc oxide and 5.0 wt% Mn-ZnO. These graphs show absorption peaks at 381.62 nm and 379 nm respectively. The strong absorption band in UV region for Zinc oxide and manganese doped zinc oxide can be attributed to the band edge absorption of wurtzite hexagonal ZnO, blue shift relative to its bulk 380 nm. The zinc oxide sample that is doped with Mn also shows the absorption band similar to zinc oxide. When Mn doped in ZnO nanoparticles, the position of the absorption spectra is shifted towards the lower wavelengths or known as blue-shifted which correlated to the change in the optical band gap value. Generally, blue-shifting in the bandgap was due to Mn doping in the ZnO nanoparticles with replacement of the Zn ions in the ZnO lattice by Mn ions. This indicates that the band gap of ZnO nanoparticles increases when doped with Mn. Furthermore, the blue-shifting of the band gap energy with increased Mn doping concentration can be defined as the separation in the energy between the top of the valence band and the unoccupied energy states in the conduction band [41].

3.2. FTIR Analysis

FTIR studies were performed in order to determine the presence of functional groups and chemical bonding, as well as to study the surface changes on the particles. These analyses can reveal the quality or consistency of sample. FTIR transmission spectra were obtained using a Bruker, Alpha T; Germany spectrometer from 500–4000 cm^{-1} using 2 cm^{-1} resolution. Various peaks corresponding to the main absorption bands can be seen from the FTIR spectrum on figure 2. The broad absorption bands at 3577 cm^{-1} and 3578 cm^{-1} represent the O-H stretching of the hydroxyl group. The band around 3100 cm^{-1} represents the O-H stretching [42]. The absorption bands observed between 1456 and 1330 cm^{-1} correspond to the asymmetric and symmetric stretching of the carbonyl group C=O. The small band at 879.97 and 628.104 cm^{-1} clearly indicate Zn-O stretching. From these studies, the stretching mode of undoped ZnO is at 628.104 cm^{-1}. When doped with Mn, the absorption values were found to

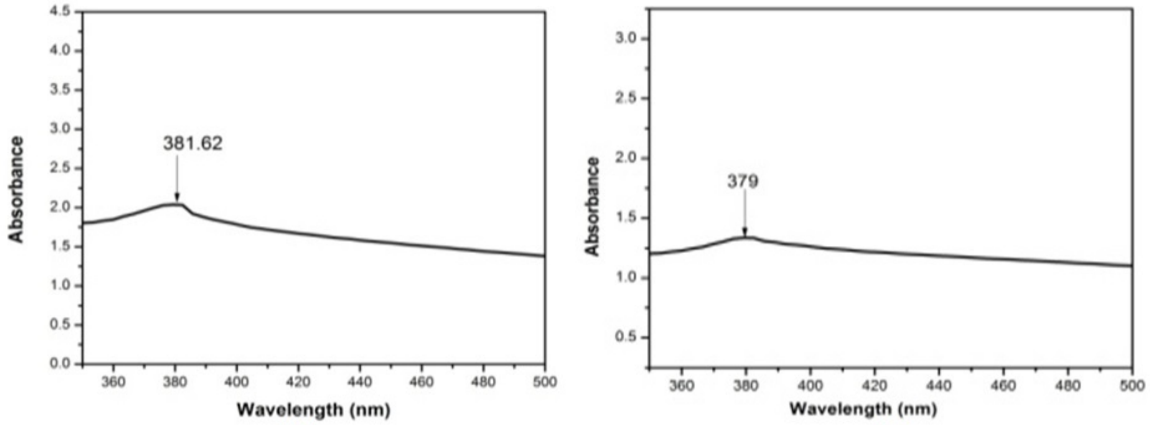

(a) (b)

FIG. 1. UV spectra of (a) pure and (b) Mn-doped ZnO

be blue-shifted at 618.8 and 595.30 cm^{-1} and were due to the Mn-O stretching and bending. Undoubtedly, this proves that the Zn-O-Zn network was perturbed by the presence of Mn in its environment as shown by the changes in the positions of the ZnO absorption bands [43].

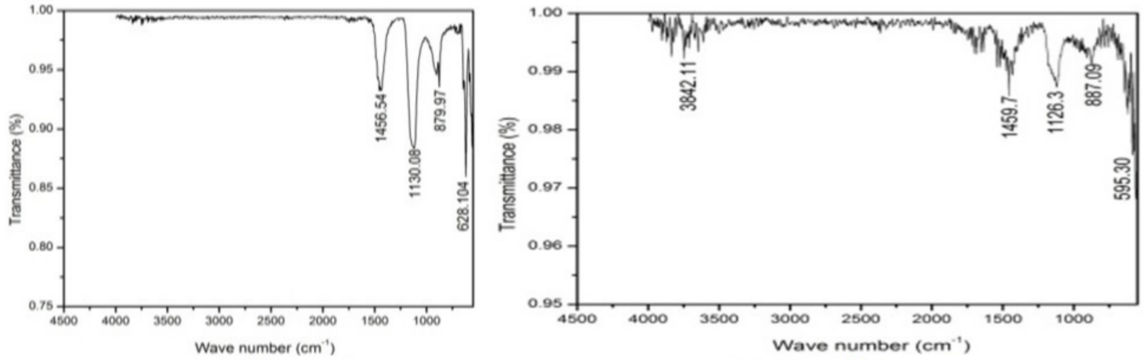

(a) (b)

FIG. 2. FTIR Spectra (a) pure and (b) Mn doped ZnO

3.3. XRD Analysis

Figure 3 illustrates ZnO and manganese doped ZnO. (a) shows the XRD spectrum of ZnO. The eleven major peaks were seen at 23.3, 25.3, 31.7, 34.6, 36.2, 47.6, 56.5, 62.9, 67.9, 68.0 and 69.8 which can be assigned to diffraction from (-112), (310), (100), (002), (101), (102), (110), (103), (200), (112) and (201) planes respectively, which is in good agreement with the standard value JCPDS no, 36-1451. (b) shows the XRD spectrum of Mn doped ZnO. The twelve major peaks were seen at 23.3, 25.3, 31.7, 34.6, 36.2, 37.8, 47.6, 56.5, 62.9, 67.9, 68.0 and 69.8 which can be assigned to diffraction from (-112), (310), (100), (002), (101), (521), (102), (110), (103), (200), (112) and (201) planes respectively. The sharp intense peaks of ZnO confirm the well-defined crystalline nature of ZnO and diffraction peak can be indicative of a hexagonal wurtize structured zinc oxide. The average crystallite size can be estimated using the Debye-Scherrer formula:

$$2d = \frac{0.9\lambda}{\beta \cos\theta}, \tag{1}$$

where, β is the full width at half maximum intensity [FWHM] corresponding to the diffraction angle 2θ in radian, and λ is the wave length of Cu-kα radiation. The average crystallite size for the prepared nanocomposite was found to be 30.587 nm for pure sample and 28.510 nm for doped sample.

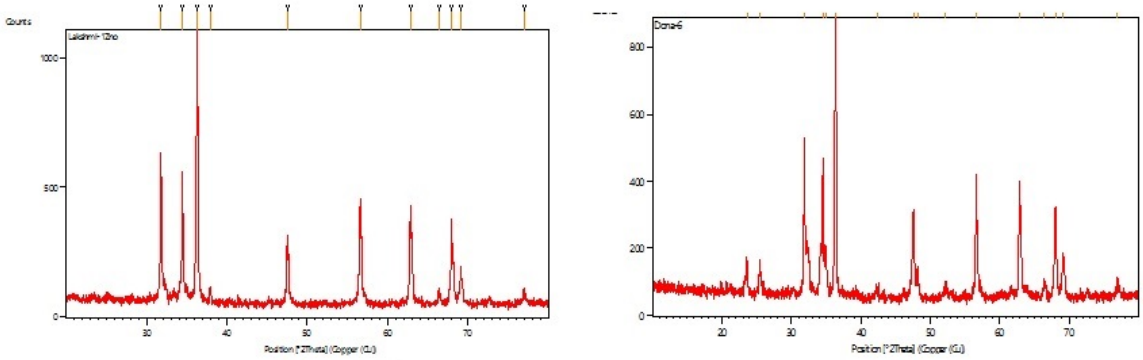

(a) **(b)**

FIG. 3. XRD Pattern of (a) pure and (b) Mn doped ZnO

3.4. Particle Morphology

Figure 4(a) shows the SEM image of undoped ZnO nanoparticles and the corresponding EDX is given in 5(a). The SEM image reveals that the particles are spherical in shape and mono dispersed with sizes less than 40 nm. The SEM and EDX images of Mndoped ZnO are shown in 4(b) and 5(b) respectively. These clearly indicate the transformation of spherical rod shape with the particle size confinement with the result of Mndoping. In elemental analysis of zinc oxide, the peaks at 1.6 keV, 8.6 keV and 9.6 keV confirm the presence of zinc and the peak at 0.53 keV shows the presence of oxygen. The EDX spectra for the manganese-doped sample also confirmed the presence of zinc, oxygen and manganese. The peaks at 0.6 keV and 5.9 keV show the presence of manganese. The peak values at 1.6 keV and 8.6 keV, confirm the presence of zinc and the peak at 0.53 keV shows the presence of oxygen in the EDS spectra of manganese-doped ZnO.

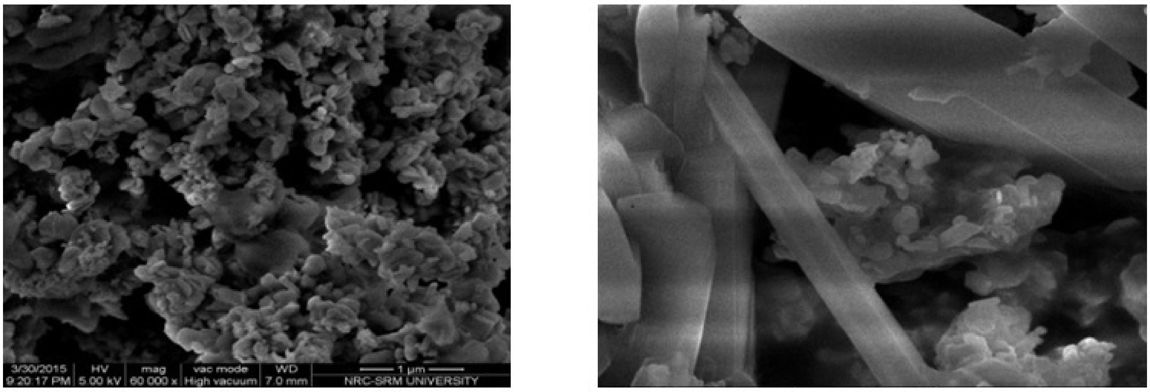

(a) **(b)**

FIG. 4. SEM images of (a) pure and (b) Mn-doped ZnO nanoparticles

4. Conclusion

In summary, zinc oxide (ZnO) and the transition metal manganese doped at various percentages of zinc oxide was synthesized by using zinc acetate dihydrate as a precursor. The characterization of the samples was done using FTIR, UV-Visible spectrophotometer, XRD, SEM and EDX. The presence of functional groups and chemical bonding was determined by FTIR. The absorption peaks for all the synthesized samples were determined by UV-Visible spectrophotometry. The average crystallite sizes for all the samples were determined using XRD. The XRD peaks corresponded to the hexagonal wurtize structure. The SEM images were taken to determine the of the sample morphology. These analyses showed, the nanoparticles which were formed ranged from 75–90 nm. The EDX spectra were taken to determine the qualitative elemental information for zinc, oxygen and manganese in the synthesized particles.

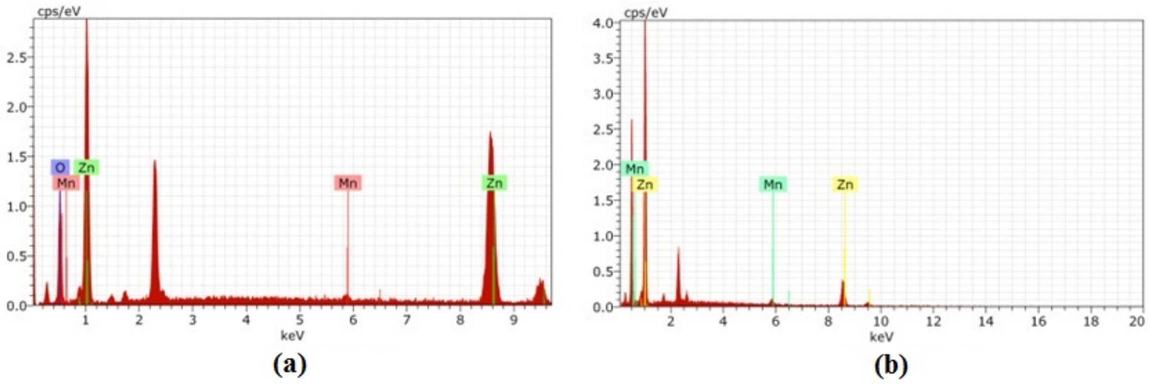

FIG. 5. EDS Spectra of (a) pure and (b) Mn-doped ZnO

Acknowledgement

The author N. Joseph John acknowledges the University Grants Commission for providing financial support (No. F-MRP-4962/14 (MRP/UGC-SERO)).

References

[1] Dietl T., Ohno H., Matsukura F., Cibert J., and Ferrand D. Zener model description of ferromagnetism in zinc-blende magnetic semiconductors. *Science*, 2000, **287**, P. 1019–1027.

[2] Sato K. and Katayama-Yoshida H. Low-dimensional Systems and Nanostructures. *Physica E Amsterdam*, 2001, **10**, P. 251–258.

[3] Pemmaraju C.D., Hanafin R., Archer T., Braun H.B., Sanvito S. Impurity-ion pair induced high-temperature ferromagnetism in co-doped ZnO. *Phys. Rev. B*, 2008, **78**, P. 452–461.

[4] Sarsari I.A., Pemmaraju C.D., Salamati H., Sanvito S. Many-body quasiparticle spectrum of co-doped ZnO: A GW perspective. *Phys. Rev. B*, 2013, **87**, P. 781–790.

[5] Tsukazaki A., Ohtomo A., Onuma T., Ohtani M., Makino T., Sumiya M., Ohtani K., Chichibu S.F., Fuke S., Segawa Y., et al. Repeated temperature modulation epitaxy for p-type doping and light-emitting diode based on ZnO. *Nat. Mater.*, 2004, **1**, P. 42–46.

[6] Ozgur U., Alivov Y.I., Liu C., Teke A., Reshchikov M., Doğăn S., Avrutin V., Cho S.-J., Morkoc H. A comprehensive review of ZnO materials and devices. *J. Appl. Phys.*, 2005, **98**(4), P. 341–352.

[7] Ahmad M., Zhao J., Iqbal J., Miao W., Xie L., Mo R., Zhu J. Conductivity enhancement by slight indium doping in ZnO nanowires for optoelectronic applications. *J. Phys. D: Appl. Phys.*, 2009, **42**(16), P. 158–165.

[8] Teklemichael S.T., Oo W.H., McCluskey M., Walter E.D., Hoyt D.W. Acceptors in ZnO nanocrystals. *Appl. Phys. Lett.*, 2011, **98**(23), 232–422.

[9] Iqbal J., Liu X., Majid A., and Yu R. Synthesis and physical properties of Mn doped ZnO dilute magnetic semiconductor nanostructures. *Journal of superconductivity and Novel Magnetism*, 2011, **24**(1-2), P. 699–704.

[10] Raval H.D. and Gohil J.M. Nanotechnology in water treatment:an emerging trend. *International Journal of Nuclear Desalination*. 2010, **4**(2), P. 184–188.

[11] Wang L.W., Xu Z., Zhang F.J., Zhao S.L., and Lu L.F. Structure, optical, and magnetic properties of Mn-doped ZnO films prepared by sputtering. *International Journal of Minerals,Metallurgy and Materials*, 2010, **17**(4), 475–480.

[12] Shi-Wei W., Ming-Yuan Z., Min Z., et al. Effects of pulsed magneticfield onMn-doped ZnO diluted magnetic semiconductorprepared by hydrothermalmethod. *Acta Physica Sinica*, 2012, **61**(19), P. 873–881.

[13] Yan X.X. and Xu G.Y. Effect of sintering atmosphere on the electrical and optical properties of (ZnO)1-x(MnO2)x NTCRceramics. *Physica B*, 2009, **404**(16), P. 2377–2381.

[14] Abdollahi Y., Abdullah A., Zainal Z., and Yusof N. Synthesisand characterization of Manganese doped ZnO nanoparticles. *International Journal of Basic and Applied Sciences*, 2011, **4**, P. 62–69.

[15] Soni B., Deshpande M.P., Bhatt S., Garg N., Pandya N., and Chaki S.H. Influence ofMn doping on optical properties of ZnOnanoparticles synthesized by microwave irradiation. *Journal of Optics*, 2013, **42**(4), P. 328–334.

[16] Campet G., Jakani M., Doumerc J.P., Claverie J., Hagenmuller P. Photoconduction mechanisms in titanium and rare earth n-type semiconducting electrodes with pyrochlore and perovskite structures. *Solid State Communications*, 1982, **42**(2), P. 93–6.

[17] Choi W., Termin A., Hoffmann M. The role of metal ion dopants in quantum-sized TiO_2: correlation between photoreactivity and charge carrier recombination dynamics. *The Journal of Physical Chemistry*, 1994, **98**(51), P. 13669-13679.

[18] Umebayashi T., Yamaki T., Itoh H., Asai K. Analysis of electronic structures of 3d transition metal-doped TiO_2 based on band calculations. *Journal of Physics and Chemistry of Solids*, 2002, **63**(10), P. 1909–1920.

[19] Wang R., Xin J.H., Yang Y., Liu H., Xu L., Hu J. The characteristics and photocatalytic activities of silver doped ZnO nanocrystallites. *Applied Surface Science*, 2004, **227**(1-4), P. 312–317.

[20] Cong C.J., Hong J.H., Liu Q.Y., Liao L., Zhang K.L. Synthesis, structure and ferromagnetic properties of Ni-doped ZnO nanoparticles. *Solid State Communications*, 2006, **138**(10-11), P. 511–515.

[21] Kanade K.G., Kale B.B., Baeg J.-O., Lee S.M., Lee C.W., Moon S.-J., Chang H. Self-assembled aligned Cu doped ZnO nanoparticles for photocatalytic hydrogen production under visible light irradiation. *Materials Chemistry and Physics*, 2007, **102**(1), P. 98–104.

[22] Volbers N., Zhou H., Knies C., Pfisterer D., Sann J., Hofmann D.M., Meyer B.K. Synthesis and characterization of ZnO:Co_2+nanoparticles. Applied Physics A: Materials Science &amp. *Processing*, 2007, **88**(1), P. 153–5.

[23] Li L., Wang W., Liu H., Liu X., Song Q., Ren S. First principles calculations of electronic band structure and optical properties of Cr-doped ZnO. *The Journal of Physical Chemistry C*, 2009, **113**(19), P. 8460–8464.

[24] Samaele N., Amornpitoksuk P., Suwanboon S. Morphology and optical properties of ZnO particles modified by diblock copolymer. *Materials Letters*, 2010, **64**(4), P. 500–502.

[25] Halperin B., Lax M. Impurity-band tails in the high-density limit. I. Minimum counting methods. *Physical Review*, 1966, **148**(2), P. 722–740.

[26] Ullah R., Dutta J. Photocatalytic degradation of organic dyes with manganese-doped ZnO nanoparticles. *Journal of Hazardous materials*, 2008, **156**(1-3), P. 194–200.

[27] Tsuzuki T., Smith Z., Parker A., He R., Wang X. Photocatalytic activity of manganese-doped ZnO nanocrystalline powders. *Journal of the Australian Ceramic Society*, 2009, **45**(1), P. 58–62.

[28] Yang Z.K., Yu P., Wang G.K.L., Kawasaki M., Ohtomo A., Koinuma H. and Segawa Y. Ultraviolet Spontaneous and Stimulated Emission from ZnO Microcrystallites at Room Temperature. *Solid State Commun.*, 1997, **103**, P. 459–461.

[29] Bagnall D.M., Chen Y.F., Zhu Z., Yao T., Koyama S., Shen M.Y. and Goto G. Optically pumped lasing of ZnO at room temperature. *Appl. Phys. Lett.*, 1997, **70**, P. 2230–2232.

[30] Kawasaki M., Ohtomo A., Ohkubo I., Koinuma H., Tang Z.K., Yu P., Wong G.K.L., Zhang B.P. and Segawa Y. Room temperature ultraviolet emission fromself assembled ZnOmicrocrystalline thin films. *Mater. Sci.*, 1998, **B56**, P. 239.

[31] Ohtomo A., Kawasaki M., Ohkubo I., Koinuma H., Yasuda Y. and Segawa Y. Structural and optical properties of ZnO/MgO_0.2MgO super lattics. *Appl. Phys. Lett.*, 1999, **75**, P. 980.

[32] Brus L.E., Harkless J.A.W., and Stillinger F.H. Theoretical Metastability of Semiconductor Crystallites in High Pressure Phases, with Application to Beta-Tin Structure Silicon. *J. Am. Chem. Soc.*, 1996, **118**, P. 4834–4840.

[33] Abrishami M.E., et. al. Structural and optical properties of zinc oxide nano powders doped with Mn. *Phys. Status Solidi C*, 2010, **7** , P. 1595–1601.

[34] Yadav R.S., Pandey A.C., and Sanjaya S.S. *Chalcogenide Lett.*, 2009, **6**, P. 233–240.

[35] Riahi-Noori N., et. al. Optical properties of europium doped bunches of ZnO nanowires synthesized by co precipition method. *J. Ceram. Process. Res.*, 2008, **9**,P. 246–252.

[36] He J.H., Hsin C.L., Liu J., Chen L.J. and Wang Z.L. Piezoelectric Gated Diode of a Single ZnO Nanowire. *Adv. Mater.*, 2007, **19**, P. 781–788.

[37] Lee C.V., Haung Y.T., Su W.F., Lin C.F. Electroluminescence from ZnO nanoparticles/ organic nanocomposites. *Appl. Phys. Lett.*, 2006, **89**(23), P. 11–16.

[38] Garcia M.A., et. al. Magnetic properties of ZnO nanoparticles. *Nano Lett.*, 2007, **7**, P. 1489.

[39] Fonoberov V.A. and Balandin A.A. *J. Nanoelectron Optoe.* 2006, **119** , P. 78–86.

[40] Kwon S.S., et. al. ZnO quantum dots: Physical properties and optoelectronic applications. *Adv. Mater.*, 2008 ,**20**, P. 4557–4565.

[41] Visvanatha R., Sapra S., Gupta S.S., et. al. Synthesis and characterization of Mn doped ZnO nanocrystals. *Journal of Physical Chemistry B*, 2004,**108**(20), P. 6303–6310.

[42] Hao M.Y., Lou S.Y., Zhou S.M., Yuan R.J., Zhu G.Y. and Li N. Structural, optical, and magnetic studies of manganese doped zinc oxide hierarchical microspheres by self assembly of nanoparticles. *Nanoscale Research Letters*, 2012,**7**(100), P. 111–113.

[43] Wu D., Huang Z., Yin G., et. al. Preparation structure and properties of Mn-doped ZnO rod arrays. *CrystEngComm*, 2010, **12**(1), P. 192–198.

NANOSYSTEMS: PHYSICS, CHEMISTRY, MATHEMATICS, 2016, 7 (6), P. 1031–1049

Formation and structural transformations of nanoparticles in the TiO_2–H_2O system

O. V. Almjasheva

Saint Petersburg Electrotechnical University "LETI",
ul. Professora Popova 5, 197376 St. Petersburg, Russia

almjasheva@mail.ru

PACS 64.60.A-; 64.70.Nd **DOI 10.17586/2220-8054-2016-7-6-1031-1049**

Results thermodynamic analysis of processes in the TiO_2 – H_2O system in a wide range of variation of parameters determine the regions of sustainable existence of titanium dioxide in the form of rutile and anatase modification. The results of thermodynamic prediction on the possibility and conditions of sustainable existence of TiO_2 with the rutile structure have been confirmed in experiments.

Keywords: nanoparticles, TiO_2, anatase, retile, thermodynamic analyses, structural transformations.

Received: 20 August 2016

Revised: 11 November 2016

1. Introduction

Despite the large number of works on formation, technology, structure and properties of compounds of different composition and structure in the TiO_2-H_2O system (for instance, see [1]), by now, there is no consensus on the stability, composition and structure of a significant number of compounds in this system. Such compounds include hydrated forms of titanium oxide. As mentioned in [2], such uncertainty exists even at the level of names for hydrated forms of TiO_2. This is determined by the uncertainty of the composition of hydrated titanium dioxide that depends on the synthesis conditions and changes with time [2, 3].

Data on the phase and chemical transformations in the TiO_2-H_2O system in the $P - T$-coordinates is quite limited by now. In particular, there is a diagram of transformations proposed in [4]. In addition to this work, there are a number of studies on phase transformations in titanium dioxide.

For instance, in [5–12], the structural states of titanium dioxide in a wide range of temperature and pressure changes summarized in [13] were studied. Along with the literature data, it includes the obtained data as $P - T$ constitutional diagram for TiO_2. Previous research [13], in addition to the rutile structure, which is equilibrium in a wide range of temperatures, showed the constitutional diagrams include a region for the existence of a high-pressure phase – TiO_2-II, which has a structure similar to α-PbO_2 [7]. In addition, these $P-T$-diagrams include P-T-regions for the existence of anatase and brookite titanium dioxide structures. However, in [13], it was noted that these phases were used as precursors for further studies of phase transitions in them with increasing temperature and pressure, i.e. reverse transition of rutile or TiO_2 with a structure of α-PbO_2 (TiO_2-II) into the anatase or brookite structure was not observed. In further studies, this allowed many authors [1] to conclude that the phases of anatase and brookite were metastable. However, the unusual coincidence of the $P - T$-boundary of transition for anatase to rutile shown by different authors and marked on the $P - T$-constitutional diagram of titanium dioxide in [13] should be noted.

In [4], on the $P-T$-diagram, where the state of the substance was studied under hydrothermal conditions, i.e., actually – the state of TiO_2 in the TiO_2-H_2O system, only the phase transition of anatase titanium dioxide to the rutile modification was observed. The absence of information on chemical transformation $Ti(OH)_4 \rightarrow TiO_2 + H_2O$ in the diagram is apparently associated with the ambiguity of the information on the temperature of this transition. For example, in [15], it was stated that, during the thermal treatment of freshly prepared titanium gels without separating the solid phase from the mother liquor, crystallization of the amorphous gel of $TiO_2 \cdot nH_2O$ with the formation of the anatase structure can begin at 60–100 °C. However, in [14], it was shown that the gel based on titanium dioxide is in the amorphous state up to $\sim$200 °C, and the crystallization starts only when the temperature rises to 250–350 °C. The crystallization onset temperature can be decreased by hydrothermal treatment of hydrated titanium dioxide [16].

The $Ti(OH)_4$ composition is often ascribed only to freshly precipitated hydrated titanium dioxide. Freshly precipitated $Ti(OH)_4$ (α-form) is subject to aging, which occurs rapidly, even at room temperature. The final product of aging, according to [2], is hydrated titanium dioxide (β-form), to which the conditional formula of

H_2TiO_3 is attributed. Heating accelerates its aging. It is supposed that ignition can induce not only dehydration, but also partial reduction of titanium dioxide. The progress of the latter process in air is in doubt due to the stability of titanium in the Ti (IV) oxidation state, which is mentioned in many works [1,3].

Along with a variety of structural modifications of hydrated titanium dioxide, there is morphological diversity of particles – from particles of isometric shape to particles of plate-like and nanotubular shapes, which are characteristic, for example, for $H_2Ti_3O_7$ [17].

Thus, the uncertainty in the dependence of chemical, structural, and morphological transformations in the TiO_2–H_2O system on external conditions, especially the temperature, resulting from the analysis of the literature data, suggests the need for further study of these processes, including thermodynamic analysis of these transformations.

2. Thermodynamics of chemical and structural phase transformations in the TiO_2-H_2O system

The thermodynamic analysis of the conditions for the stable existence of titanium oxide, in which titanium has an oxidation state of less than 4+, conducted with the use of the Ivtanthermo thermodynamic database [18], depending on the temperature and oxygen partial pressure (Fig. 1), shows that the equilibrium existence of such compounds is thermodynamically possible only in a reducing atmosphere and at a sufficiently high temperatures. According to the results of thermodynamic calculations (Fig. 1), in a reducing atmosphere and at increased temperatures, the following chain of redox processes is observed:

$$\begin{aligned}\mathrm{TiO_2} \Rightarrow \frac{1}{n}\mathrm{Ti}_n\mathrm{O}_{2n-1} + \frac{1}{n}\mathrm{O_2}\\ \Rightarrow \frac{1}{2}\mathrm{Ti_2O_3} + \frac{1}{2}\mathrm{O_2}\\ \Rightarrow \mathrm{TiO} + \frac{1}{2}\mathrm{O_2}.\end{aligned}$$

Reduction to TiO requires the use of significantly more stringent reducing conditions than reduction to Ti_nO_{2n-1} and Ti_2O_3, as can be concluded based on the analysis of the calculation results (Fig. 1).

During calculation, the impact of particle size upon the thermodynamics of redox reactions was not taken into account. It seems that these effects can not significantly change the results presented in Fig. 1, at least for particles with a size of tens of nanometers. Thus, for the temperature range below that of the recrystallization processes, i.e. below the melting point of surface (nonautonomous) phase based on TiO_2–T_{m2n} [19,20]), there is a potential possibility to obtain nanoparticles of titanium oxide in different oxidation states, less than 4+, by redox reactions.

The thermodynamic analysis of the possibility for forming titanium dioxide of different polymorph modifications during decomposition of hydrated titanium dioxide is of interest. Thermodynamic calculations were carried out with the assumption that hydrated titanium dioxide has a composition of $Ti(OH)_4$ and is in the crystalline or amorphous state.

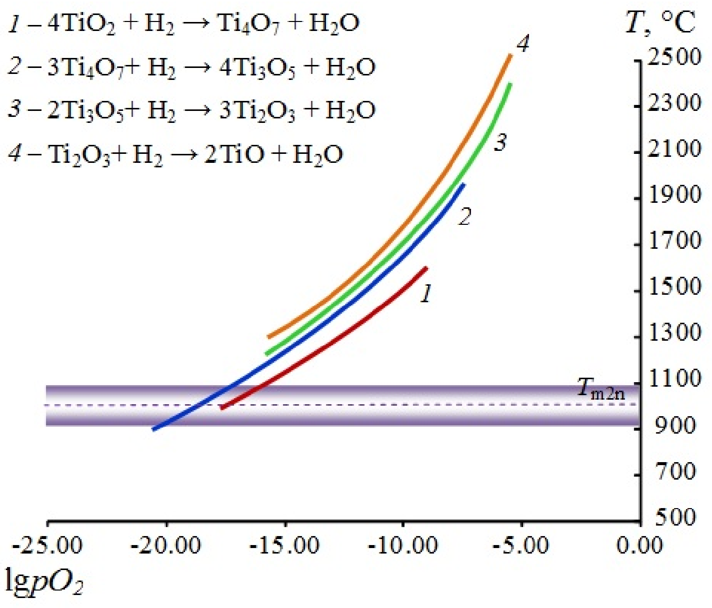

FIG. 1. T-lgp_{O2} regions of existence of titanium oxide in the "hydrogen-water vapor" atmosphere

Due to the fact that the thermodynamic data on formation enthalpy, entropy and heat capacity for Ti(OH)$_4$ ($\Delta H(T)$, $S(T)$, $c_p(T)$) are absent in the literature, this data was obtained with the use of various approximate calculation methods. In particular, the method of comparative calculation proposed by Karapetyants [21] was used, which showed good agreement with the experimental data in the evaluation of the thermodynamic properties of a similar compound – Zr(OH)$_4$ [22]. This method is based on a comparison of the relevant characteristics of two similar rows (I and II). To assess H_{298}(Ti(OH)$_4$), S_{298}(Ti(OH)$_4$) and c_p(Ti(OH)$_4$), thermodynamic data for the following compounds were used: AlX$_3$, MgX$_2$, CaX$_2$, SrX$_2$, FeX$_2$, ZrX$_4$, where X= F$^-$, Cl$^-$, Br$^-$, OH$^-$ [23]. The results of the calculations are shown in Table 1.

TABLE 1. Thermodynamic data for Ti(OH)$_4$

Thermodynamic property	**Value**	**Note**
H_{298}, kJ/mol	-1358.98	calculation according to [21]
	-1084	calculation according to [24]
S_{298},kJ/mol·K	164.75	calculation according to [21]
	127.9	calculation according to [25]
c_p,kJ/mol·K	125.52	calculation according to [21]
	131.1	calculation according to [25]

Due to the fact that the structure of the substance in an amorphous state, at least in the first coordination sphere, is close to the melt structure [26, 27], the enthalpy of amorphization of hydrated titanium dioxide was evaluated based on empirical correlation proposed in [27].

$$\Delta H_{298\,amorphization} = 0.3 - 0.5\Delta H_{melt},$$

where $\Delta H_{298\,amorphization}$– amorphization enthalpy, kJ/mol; ΔH_{melt} – melting enthalpy, kJ/mol. Thus, the enthalpy of TiO$_2 \cdot n$H$_2$O (n=2) in an amorphous state can be taken as:

$$\Delta H^0_{298\,am} = \Delta H^0_{298\,cr} + 0.4\Delta H_{melt} = -1331 \pm 10 \text{ kJ/mol},$$

ΔH_{melt} is taken as ΔH_{melt} = 68 kJ/mol (data according to the IVTANTHERMO database [18]).

Based on Gibbs energy calculations for the reaction of dehydration of titanium hydroxide, shown in Fig. 2, it can be concluded that the formation of both anatase and rutile modifications of TiO$_2$ is possible throughout the whole calculated temperature and pressure range. This was the case, regardless of whether crystalline or amorphous Ti(OH)$_4$ was considered as the starting material.

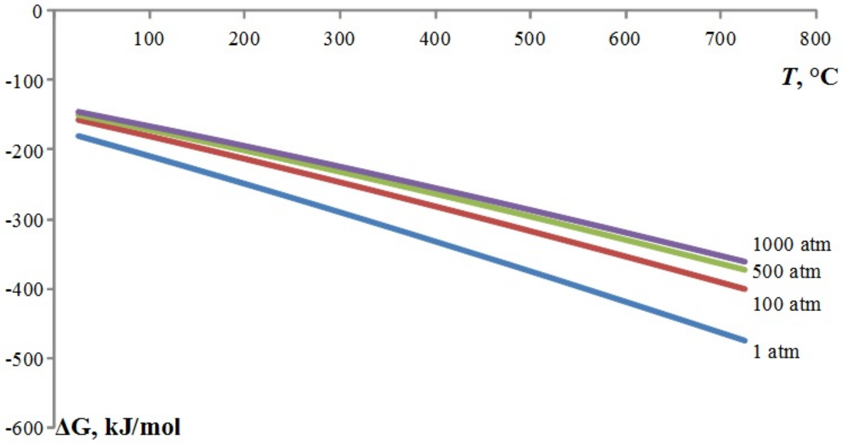

FIG. 2. Dependence of the Gibbs energy of dehydration of Ti(OH)$_{4cr}$ on the temperature and pressure for reaction Ti(OH)$_4$=TiO$_2$+2H$_2$O

The inaccuracy in the determination of the thermodynamic properties of Ti(OH)$_4$, apparently, can not affect the quality of conclusion on the instability of the hydrated form of titanium dioxide, since the ΔG value of the dehydration reaction in absolute value significantly exceeds the possible errors in its calculation in the entire range of considered temperatures and pressures. Thus, the hydrated form of titanium dioxide (Ti(OH)$_4$) in the considered range of $P - T$-conditions is unstable and can be transformed into both rutile and anatase forms.

Conclusion on thermodynamic instability of the hydrated form of titanium dioxide is supported by the results of experimental studies [1–3], in which it is shown that under certain conditions, even at temperatures close to room temperature, crystallization of amorphous gel of $TiO_2 \cdot nH_2O$ occurs with the formation of titanium dioxide with the anatase structure. Thus, based on the results of the analysis, it can be concluded that the kinetic factors, instead of thermodynamic factors, are determining in the dehydration process.

In addition to temperature and pressure influencing the possibility of the formation of a crystalline modification of TiO_2 in the dehydration of Ti(OH)$_4$, the influence of the size effect should be taken into account. To assess the effect of the size factor, the dependence between the Gibbs energy of the reaction of decomposition of titanium hydroxide and the size of formed particles of TiO_2 was calculated. The calculation was carried out based on the known relations (for instance, see [28]).

The surface energy values for rutile and anatase titanium dioxide given in the literature are quite different. Based on the theoretical analysis given in [29, 30], the surface energy value of rutile was assumed to be 1.5 J/m^2 and 1.42 J/m^2, respectively. Whereas, based on the results of experimental measurement of the excess enthalpy of grain boundaries [31], the value of surface energy for the rutile modification of titanium dioxide ranges from 1.3 to 1.7 J/m^2. In [32, 33], the rutile surface energy was taken as 1.5 J/m^2, which is the average of these values, and the anatase surface energy was taken as 0.85 of the rutile surface energy, i.e. 1.275, that was associated with a corresponding increase in the molar volume of anatase compared to rutile. A more thorough analysis carried out in [34] allowed determination of the temperature dependence of the surface energy for both rutile and anatase as:

$$\sigma_{rutil} = 1.91 - 1.48 \cdot 10^{-4}(T - 298),$$

$$\sigma_{anatase} = 1.32 - 1.48 \cdot 10^{-4}(T - 298),$$

where σ_{rutil}, $\sigma_{anatase}$ – surface energy of anatase and rutile, respectively, J/m^2; T – temperature, K. It should be noted that the value of the surface energy of rutile, determined according to [34], is much higher than the values given in [29–32], while $\sigma_{anatase}$ remains almost unchanged (Table 2). This may be due to higher difficulty of determining the influence of the relaxation processes on the surface energy of rutile having a higher density than titanium dioxide anatase.

In further thermodynamic calculations, the data given in [34] are used, which are more founded and can be presented as:

$$\sigma_{rutil} = 1.9541 - 1.48 \cdot 10^{-4}T, \tag{1}$$

$$\sigma_{anatase} = 1.364 - 1.48 \cdot 10^{-4}T, \tag{2}$$

where the first term describes mainly the enthalpy component of the surface free energy, and the coefficient in front of temperature describes mainly the entropy component.

The dependence between the size of critical nuclei of anatase and rutile formed during dehydration of Ti(OH)$_4$ and different values of temperature and pressure in the TiO_2–H_2O system was calculated (Figs. 3, 4).

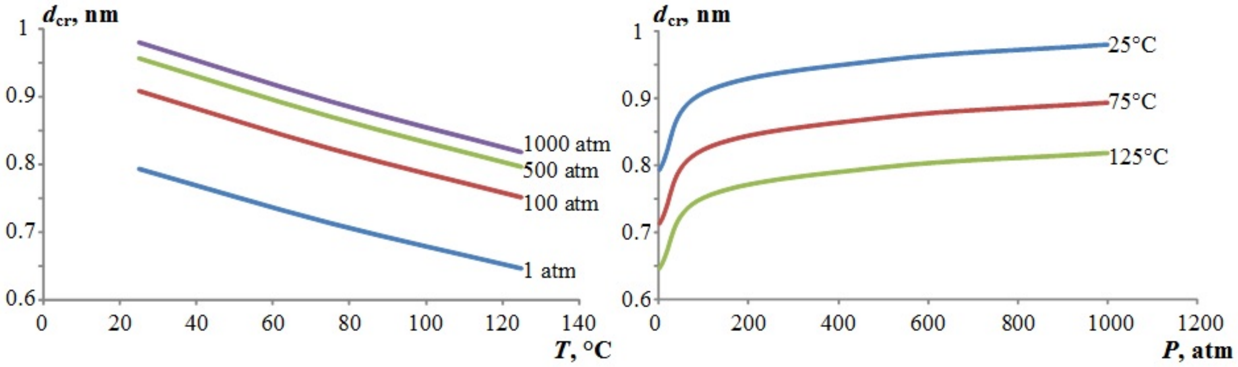

FIG. 3. Dependence of the size of the critical nucleus of TiO_2 (rutile) on the pressure and temperature during dehydration of Ti(OH)$_4$

The obtained values for the critical nucleus sizes in the temperature range of nanocrystal formation according to the analysis of the calculation results shown in Fig. 3 and 4 range from 0.5 to 1 nm. Additionally, the lowest values

TABLE 2. Values of the surface energy of rutile (σ_{rutil}) and anatase ($\sigma_{anatase}$) modifications of titanium dioxide

Value, J/m^2		References
σ_{rutil}	$\sigma_{anatase}$	
1.5	-	[29]
1.42	-	[30]
1.3-1.7	-	[31]
1.5	1.275	[32]
1.5	0.85	[32]
1.91-1.865	1.32-1.275	[34]
“clean surface” (100) – 0.60 (011) – 0.95 (110) – 0.47 “hydrated surface” (100) – 1.57 (011) – 1.79 (110) – 1.08	“clean surface” (001) – 0.51 (100) – 0.39 (101) – 0.35 “hydrated surface” (001) – 1.55 (100) – 1.13 (101) – 1.03	“clean surface” – [35] “hydrated surface ” – [33]
0.47 – 0.95	0.35 - 0.81	[36]
0.31-1.65	0.44 – 1.09	[36]

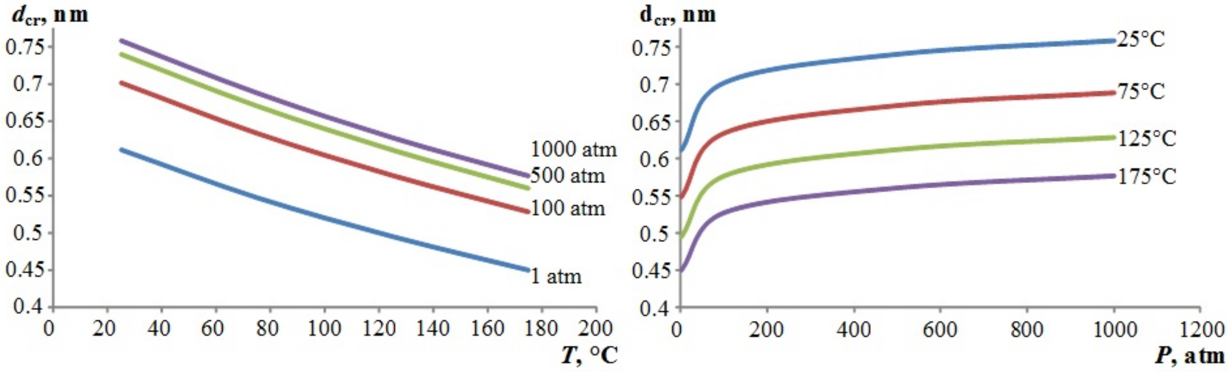

FIG. 4. Dependence of the size of the critical nucleus of TiO_2 (anatase) on the pressure and temperature during dehydration of $Ti(OH)_4$

for critical nuclei are observed at minimum values of pressure and maximum values of dehydration temperature for $Ti(OH)_4$. It should be noted that the calculated values of the critical nucleus size are beyond the applicability of the approach used. In particular, for surfaces with such curvature, it is necessary to take into account the dependence between the surface energy and the radius of curvature [37–39], and the term of crystalline titanium dioxide particle at such values of d does not make sense.

Comparison of sizes for the critical nuclei of anatase and rutile shows that the size of the critical nucleus for the TiO_2 anatase modification is somewhat less than that of rutile one. In addition, it should be noted that the very small values for the size of the critical nucleus of rutile and anatase show an extremely weak trend in the formation of anatase nuclei compared to the formation of rutile nuclei, and the possibility of forming TiO_2 of any of these modifications already at room temperature during the dehydration of $Ti(OH)_4$.

Thermodynamic analysis of the phase transition:

$$\mathrm{TiO_2(anatase)} \rightarrow \mathrm{TiO_2(rutil)} \tag{3}$$

showed that in different variants of thermodynamic data used (IVTANTHERMO database [18], JANAF reference book [40], data given in Table 3) the bulk phase with the rutile structure is thermodynamically stable throughout solid phase titanium dioxide's range of existence (Fig. 5).

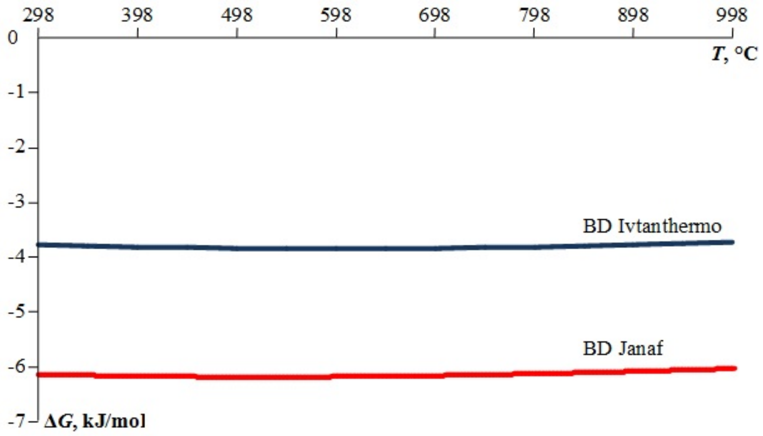

FIG. 5. Dependence of a change in the molar Gibbs energy in transition (3) on the temperature: 1) calculation based on the IVTANTHERMO data [18]; 2) calculation based on the JANAF data [40]

However, since the surface energy of anatase is lower than the surface energy of rutile (Table 2), based on the analysis of ratio:

$$\Delta G^{m}_{anatase\to rutil} = \Delta G^{m}_{b.p.(anatase\to rutil)}\left(T;P\right) + \left(\sigma_{rutil}\cdot S_{rutil} + \sigma_{anatase}\cdot S_{anatase}\right), \tag{4}$$

where, $\Delta G^{m}_{anatase\to rutil}$ – change in molar Gibbs energy during transition of particles from anatase to rutile structure; $\Delta G^{m}_{b.p.(anatase\to rutil)}$ – change in molar Gibbs energy of bulk phases of TiO_2 during transition of titanium dioxide from anatase to rutile structure; $\sigma_{rutil(anatase)}$ – specific surface energy of rutile (anatase); $S_{rutil(anatase)}$ – surface of one mole of titanium dioxide with the rutile (anatase) structure. It can be expected that in the presence of a certain amount of particles of anatase, this phase will be more thermodynamically stable than the phase with the rutile structure.

Assuming that the particles have a shape close to spherical, expression (4) can be presented as:

$$\Delta G^{m}_{anatase\to rutil} = \Delta G^{m}_{b.p.(anatase\to rutil)} + 6\left(\frac{\sigma_{rutil}\cdot V^{m}_{rutil}}{d_{rutil}} + \frac{\sigma_{anatase}\cdot V^{m}_{anatase}}{d_{anatase}}\right), \tag{5}$$

where $V^{m}_{rutil(anatase)}$ – molar volume of TiO_2 with a rutile (anatase) structure; $d_{rutil(anatase)}$ – diameter of the rutile (anatase) particles.

For the case when one anatase particle is transformed into one rutile particle, expression (2) can be presented as:

$$\begin{gathered}\Delta G^{m}_{anatase\to rutil}\left(T,P,d_{anatase}\right) = \Delta G^{m}_{b.p.(anatase\to rutil)}\left(T,P\right) + \\ 6\frac{\sigma_{anatase}\cdot V^{m}_{anatase}}{d_{anatase}}\left(\frac{\sigma_{rutil}\cdot}{\sigma_{anatase}}\left(\frac{V^{m}_{rutil}}{V^{m}_{anatse}}\right)^{2/3} - 1\right)\end{gathered} \tag{6}$$

Expression (6) does not take into account the effects of particle compression due to surface forces. This approximation can be used for larger particles [38], for example, having sizes of a few tens of nanometers or more. For small particles, taking into account the surface compression will lead to the transformation of expression (5) to the following:

$$\begin{gathered}\Delta G^{m}_{anatase\to rutil}\left(T,P,d_{anatase}\right) = \Delta G^{m}_{b.p.(anatase\to rutil)}\left(T,P\right) + \\ \left(6+4t\right)\frac{\sigma_{anatase}\cdot V^{m}_{anatase}}{d_{anatase}}\left(\frac{\sigma_{rutil}\cdot}{\sigma_{anatase}}\left(\frac{V^{m}_{rutil}}{V^{m}_{anatse}}\right)^{2/3} - 1\right),\end{gathered} \tag{7}$$

TABLE 3. Enthalpy of polymorphic transitions of TiO_2

ΔH, kJ/mol	**T, K**	**References**
Anatase→Rutile		
-3.761	298.15	IVTANTHERMO [18]
-3.743	948.15	
-6.14	298.15	JANAF [40]
-2.61±0.41 $^{1)}$	298	[41]
-0.42±0.21	903	[42]
-2.93±1.26	1360	[43]
-3.26±0.84	971	
-6.57±0.79	968	[44]
-8.37±5.92	298	[45]
0.42 $^{2)}$	298	[46]
11.67 $^{2)}$	1183	[10]
Brucite→Rutile		
-0.71±0.38	971	[43]
-0.42±0.31	715	[42]
-0.84±0.42	930	[43]
41.84±9.36 $^{2)}$		[45]
Amorphous TiO_2 →Rutile		
-20.4to-34.0 $^{3)}$	298	Calculation according to depend of [27]
-24.25±0.88 $^{4)}$	298	[41]
Rutile→Melt		
68	2185	IVTANTHERMO [18]

Note:

1) – values recommended in [41];

2) – values indicated in [41] as causing doubt;

3) – $\Delta H_{298\,amophization} = 0.3 - 0.5\Delta H_{melt}$, [27]; ΔH_{melt}(TiO_2rut) = 68 kJ/mol IVTANTHERMO [18]

4) – S_{surf}= 34596 m^2/mol [41]

where $t = 1 + \frac{\partial \ln \sigma}{\partial \varepsilon}$ (ε – surface deformation), in accordance with [34] with reference to the data presented in [47], in this case it can be $1 \lesssim t \lesssim 2$.

The results of thermodynamic calculation of limit values $d_{anatase}$, up to which the anatase polymorph modification of TiO_2 is thermodynamically stable, for various input data options $\Delta G^m_{anatase \to rutil}\,(T, P, d_{anatase})$, $\sigma_{rutil}\,(T)$, $\sigma_{anatase}\,(T)$, t (Table 2, 3) are presented in Fig. 6. The analysis of the calculated results for the limit values for anatase crystallite sizes, to which this polymorph modification is thermodynamically stable, shows that depending on possible values $\Delta G^m_{anatase \to rutil}\,(T, P, d_{anatase})\,, \sigma_{rutil}\,(T)\,,\ \sigma_{anatase}\,(T)$, t, as well as on taking into account the compression of the particles due to the surface tension forces (expression (7)), limit values $d_{anatase}$ can vary widely – from $\sim$ 5 to $\sim$ 37 nm (Fig. 6). It should be noted that these calculations do not take into account dependence $\sigma(d)$, which was mentioned, for example, in [37–39]. Taking this dependence into account is appropriate in cases where the particle size is several nanometers [28, 47]. In this case, as shown by the results of calculations of $d_{anatase}$, dependence $\sigma(d)$ can be neglected.

Despite the wide range of variability for the possible limit values of $d_{anatase}$, associated with the choice of various thermodynamic parameters (Table 4), it is possible to determine the sensitivity of $d_{anatase}$ to changes of these parameters and narrow the range of the most probable values of $d_{anatase}$. First, it should be noted that insensitivity of limit values of $d_{anatase}$ o temperature dependencies of values of $\Delta G^{m}_{b.p.(anatase\to rutil)}(T)$ and $\sigma_{rutil(anatase)}(T)$, both in the calculation $\Delta G^{m}_{b.p.(anatase\to rutil)}(T)$ according to the data of IVTANTHERMO [18], and according to the data of JANAF [40] (Fig. 6 a and b). In addition, the use of thermodynamic data from IVTANTHERMO and JANAF databases give substantially different limit values for $d_{anatase}$ (compare Fig. 6 a and 6b, Fig. 6 c and 6d). Due to the fact that the thermodynamic data from IVTANTHERMO were checked for self-consistency [18], and due to the higher compliance $\Delta H_{(anatase\to rutil)}$ (IVTANTHERMO) with values recommended in [41] (see Table 3), in comparison with calculated according to JANAF [40], the results obtained using the IVTANTHERMO database should be considered as more reliable.

Limit values of $d_{anatase}$ are sensitive to measurement of particle compression by surface tension (Fig. 6 b, c, d). Higher influence on the accuracy limit values of $d_{anatase}$ is observed for uncertainty in the data on the values of the surface energy of the particles (Fig. 6 e). If we take into account the results of the analysis of the reliability of data according on $\sigma_{rutil(anatase)}$ and $\Delta G^{m}_{b.p.(anatase\to rutil)}$, the range of possible limit values of $d_{anatase}$ is narrowed to a range of $\sim$16 nm $\lesssim d_{anatase} \lesssim$ 37 nm.

TABLE 4. Limit values for the sizes of the anatase particles ($d_{anatase}$) for various calculation parameters for cases in which one particle of TiO_2 with the rutile structure is formed from one particle of TiO_2 with the anatase structure

The parameters for calculating	d_{anatse}, nm
Calculation according IVTANTHERMO excluding compression surface tension forces at different temperatures	15.7
Calculation according JANAF excluding compression surface tension forces at different temperatures	9.6
Calculation according IVTANTHERMO based compression of the surface tension forces	
$t = 1$	26.25
$t = 1.5$	31.55
$t = 2$	36.80
Calculation according JANAF based compression of the surface tension forces	
$t = 1$	14.37
$t = 1.5$	17.24
$t = 2$	20.1
Calculation according IVTANTHERMO based compression forces of surface tension ($t = 1$) depending on the values of σ	
$\sigma_{rutil} = 0.71$ $\sigma_{anatase} = 0.58$	4.9
$\sigma_{rutil} = 1.91$ $\sigma_{anatase} = 1.32$	26.3

The thermodynamic analysis of the possibility of anatase particles transforming into rutile particles, in the case of changes in the total number of particles in the system is of interest. Such mechanism is possible, for example, in the case of merger of several anatase particles into a crystallite with rutile structure, or alternatively, in the case of crushing the crystallite of anatase into several crystallites of rutile, as was observed, in particular, in [47] dedicated to the analysis of structural transformation of t-$ZrO_2 \to m$-ZrO_2 during cooling. By designating

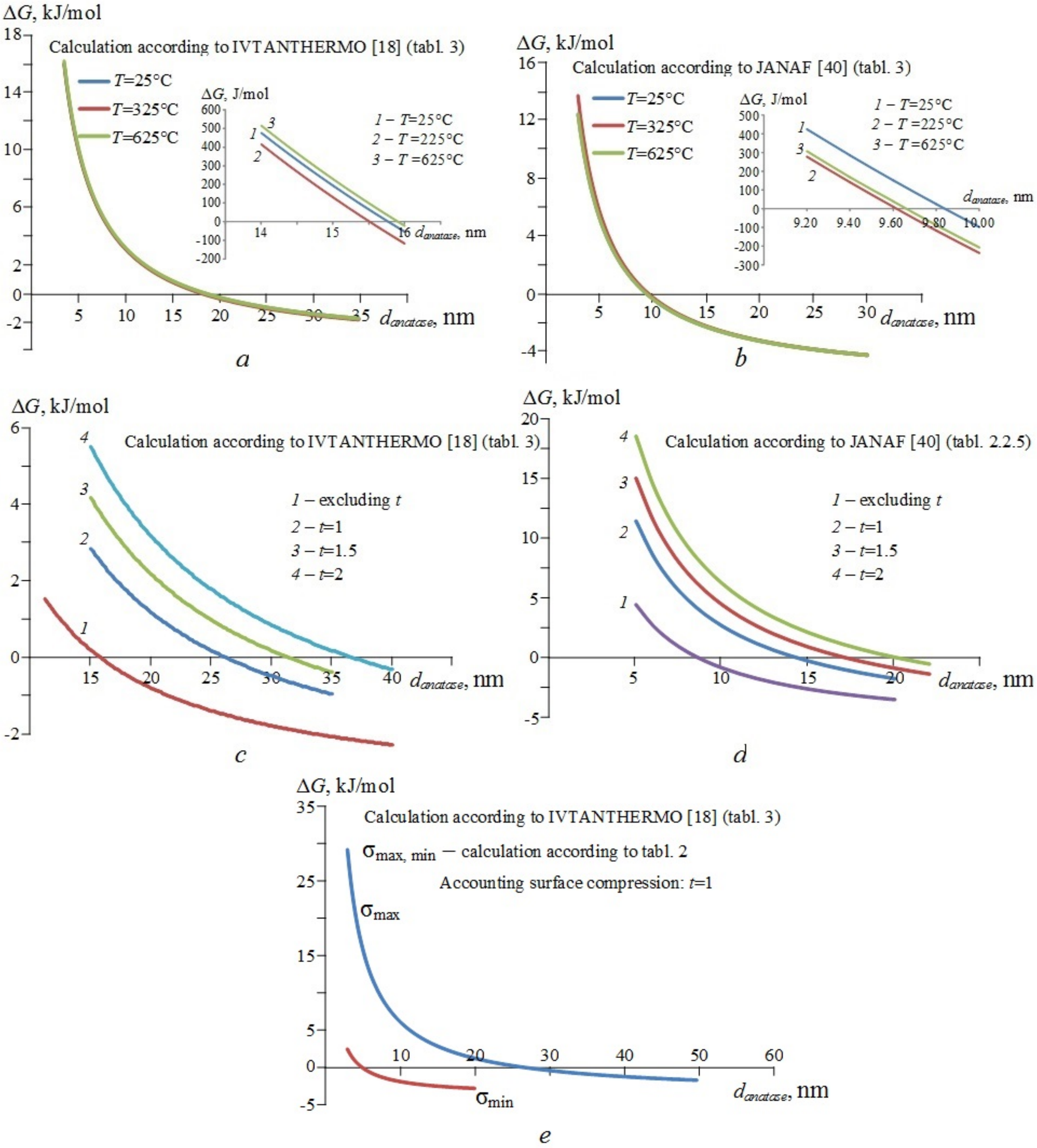

FIG. 6. Gibbs energy change in phase transition (3) depending on the anatase particle size ($d_{anatase}$) for different initial data (Table 4)

$\nu = N_{anatase}/N_{rutil}$, in the approximation of a spherical particle shape, expression (4) can be presented as:

$$\Delta G^{m}_{anatase\to rutil}\left(T,P,d_{anatase},\nu\right) = \Delta G^{m}_{b.p.(anatase\to rutil)}\left(T,P\right) + 6\frac{\sigma_{anatase}(T)\cdot V^{m}_{anatase}}{d_{anatase}}\left(\frac{\sigma_{rutil}(T)\cdot}{\sigma_{anatase}(T)}\left(\frac{V^{m}_{rutil}}{V^{m}_{anatse}}\right)^{2/3}\nu^{-\frac{1}{3}}-1\right) \tag{8}$$

In Fig. 7 and Table 5 the calculated results for the thermodynamic conversion possibilities of titanium dioxide with anatase structure into a rutile structure for different values of ν are presented: 1 (no changes in the number of particles in the system); 2, 3, 4 (fusion of 2, 3 and 4 particles of anatase into one rutile crystallite); 1/2, 1/3, 1/4 (anatase particle fragmentation during phase transition). The mechanism of such phase transitions for ν=1/4, 1/3, 1/2, 1, 2, 3, 4 is presented in Fig. 8.

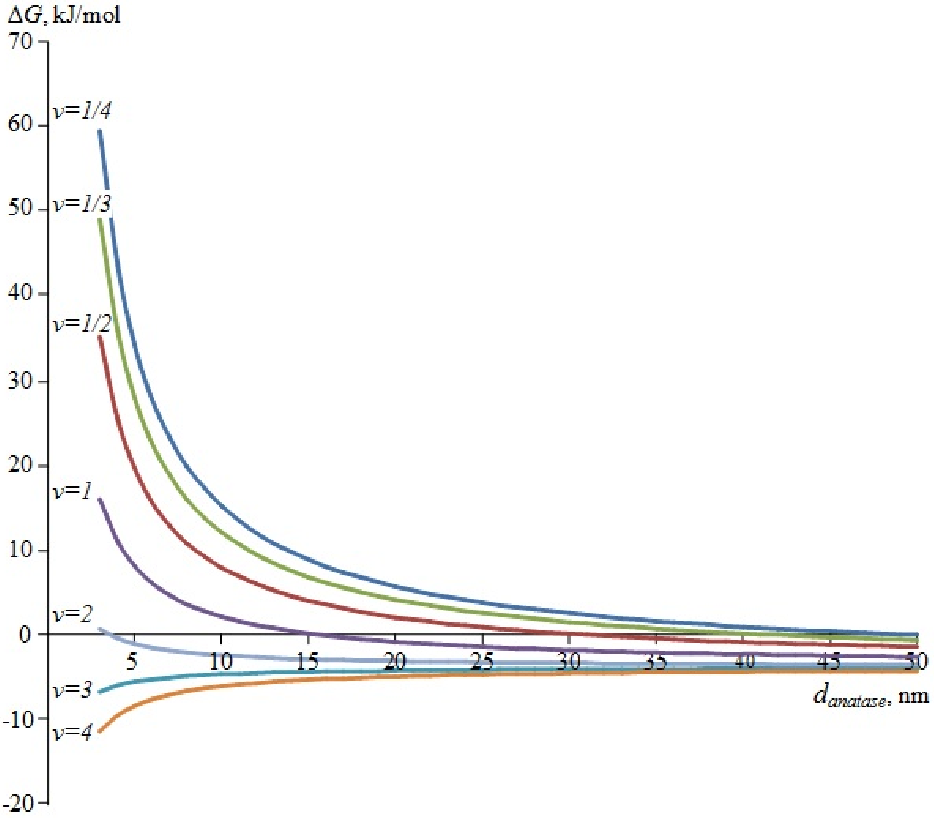

FIG. 7. Results of calculation of changes in the Gibbs energy during structural transformations (3), associated with crushing or fusion of anatase particles (for calculations, IVTANTHERMO was used, surface energy values were calculated based on expressions (1) and (2), the effect of the surface compression of the particles was not taken into account)

Calculations of dependencies $d_{anatase}(\nu)$ were carried out for Gibbs energy values for bulk phases taken from the IVTANTHERMO database, and vales $\sigma_{rutil}\left(T\right)$, $\sigma_{anatase}\left(T\right)$ presented in the form of dependencies (1) and (2), as the most reliable, as it was shown earlier, and for the calculation option, in which the compression of particles by forces of surface tension is not considered. The results of calculations as a chart of the possible structural transformations depending on the particle size of titanium dioxide and various options crushing or fusing of particles during structural transformations are presented in Fig. 8. The results of calculations (Fig. 7, Table 5) show that if crushing of particles of anatase with the formation of several particles of rutile is possible only in the case of high values of $d_{anatase}$, which are significantly higher than the limit sizes of anatase particles, at which this modification of TiO_2 is stable, the fusion of several particles of anatase with the formation of one particle of rutile, except for $\nu = 2$, is possible almost at all $d_{anatase}$ values. In addition, the formed rutile particles can be unstable and undergo transition to the anatase structure (Fig. 8). In a real situation, the presence or absence of a structural transition can be influenced by the kinetic simplicity or difficulty of structural transition and growth of the particles, allowing their transition to a potentially stable, from a thermodynamic point of view, state of the rutile modification, starting with certain particle size values.

TABLE 5. Dependence of limit values for the sizes of anatase and rutile particles in cases of crushing ($\nu < 1$) and fusion ($\nu > 1$) of anatase particles according to the data of calculations given in Fig. 7

ν	**The limits of particle size (d), nm**	
	$d_{anatase}$	d_{rutil}
1/4	51	31
1/3	42	28
1/2	31	24
1	16	16
2	3.6	4.0
3	for any values	
4	for any values	

Thus, according to the thermodynamic calculation carried out, during dehydration of $Ti(OH)_4$, there is no significant thermodynamic preference to the formation of certain structural modification of titanium dioxide. The analysis of the size of the critical anatase and rutile nucleus formed during dehydration does not give reasons for discussing the preference of forming the anatase or rutile modifications of TiO_2, i.e. thermodynamically and kinetically dehydration of $Ti(OH)_4$ can lead to formation of TiO_2 in both anatase and rutile modifications. In this situation, the preference in the formation of certain structural modifications of TiO_2 will be observed for the modification, the genetic precursor of which is the substance, which is its structural analog, as was observed, for instance, for the formation of zirconium dioxide nanocrystals [48, 49], or on the surface of the substance, which is structurally similar [50]. Analysis of the dependence between the stable state of anatase and rutile modifications and the particle size shows that in the case of formation of rutile particles during dehydration of $Ti(OH)_4$ with a size below the limit values (Fig. 6, 7, Table 4, 5), i.e. for one of variants of calculation – less than $\sim$ 15 nm (Fig. 8), transition TiO_2(rutile) $\rightarrow$ TiO_2(anatase) becomes possible, in contrast, for example, to zirconium dioxide, the transition of which from the thermodynamically stable monoclinic modification (m-ZrO_2) to metastable modification t-ZrO_2 is not possible for all particle sizes and for all $P-T$-conditions, up to (P, T), at which t-ZrO_2 becomes equilibrium bulk phase. It should be noted that, in general, structural transitions are not always expected in the case of achieving the limit values of particle sizes,

$$\mathrm{TiO_2(rutile)} \underset{d_{anatase} > d_{anatase(\lim)}}{\overset{d_{rutil} < d_{rutil(\lim)}}{\rightleftarrows}} \mathrm{TiO_2(anatase)},$$

since the existence of non-equilibrium structure of nanoparticles due to kinetic reasons is possible [47–49].

Due to the possibility of influencing the phase formation by sizes and shapes of space constraints [48, 51, 52], as well as the composition and structure of the wall material of these constraints, it is of interest to examine the formation of titanium dioxide taking into account these factors. Let's consider options of localization of titanium dioxide in "infinite cylinder" type channel and on the flat surface [48]. The two cases of solid phase contacts will be analyzed: coherent fusion of the material forming walls of spatial confinement with 1) the rutile form and 2) the anatase form of TiO_2.

Calculations made for regions of thermodynamically stable TiO_2 as rutile and anatase for the idealized cases of spatial constraints described above have shown that in the case of coherent fusion of the material of the spatially-constraining walls of "cylindrical channel" or "flat surface" types with the rutile structure, the latter will stably exist without any possibility of transformation into the anatase structure. In the cases of coherent fusion of the material of the constraining walls with the anatase structure, depending on the size of the particles of TiO_2, it can exist as both anatase and rutile (Fig. 9, *a*, *b*). In addition, the stability of these structures is almost independent of temperature. It should be noted that this conclusion explains the literature data on the effect of the substrate structure and the thickness of the deposited layer on the structure of the titanium dioxide layer deposited by molecular layering [50].

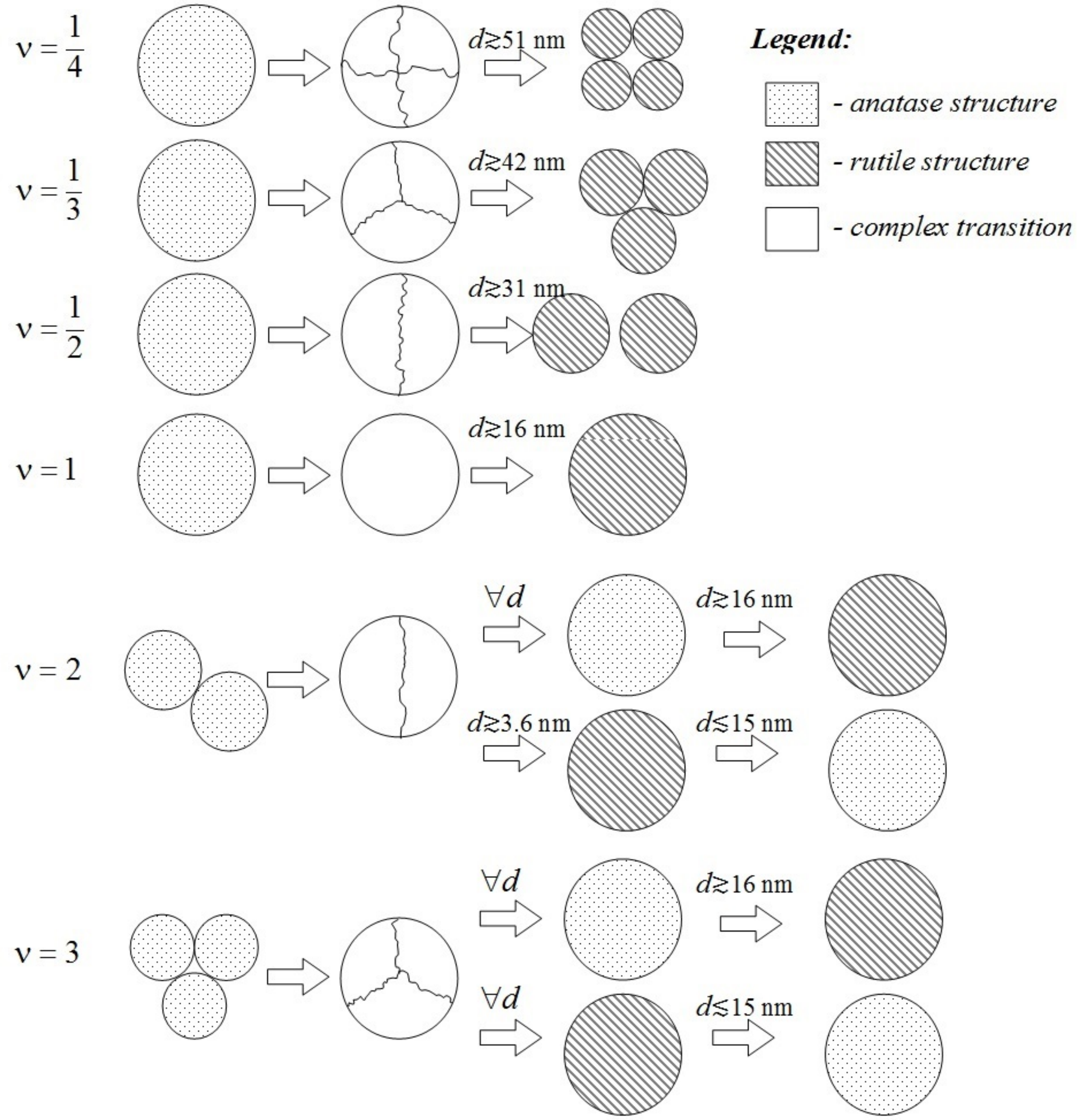

FIG. 8. Chains of possible structural transformations in titanium dioxide depending on the anatase and rutile particle size based on the results of calculation presented in Fig. 7

3. Formation of TiO_2 nanocrystals under hydrothermal synthesis and aerobic thermal treatment conditions

As the starting material for the experimental study of methods for titanium dioxide nanocrystal formation, X-ray amorphous hydrated titanium oxide obtained by direct precipitation with 25% ammonia solution NH_4OH (extra pure grade) from diluted solution of titanium tetrachloride $TiCl_4$ (0.3 mol/l) was used. Completeness of precipitation was controlled by pH of the solution (~ 10). The obtained precipitate was washed with distilled water in order to remove excess ammonia and chloride ions by decantation and filtration. According to elemental analysis, the obtained precipitate did not contain any traces of chloride ions or other impurities.

The hydrothermal treatment was carried out at 200 and 250 °C, 70 MPa, and isothermal time ranged from 10 to 240 minutes.

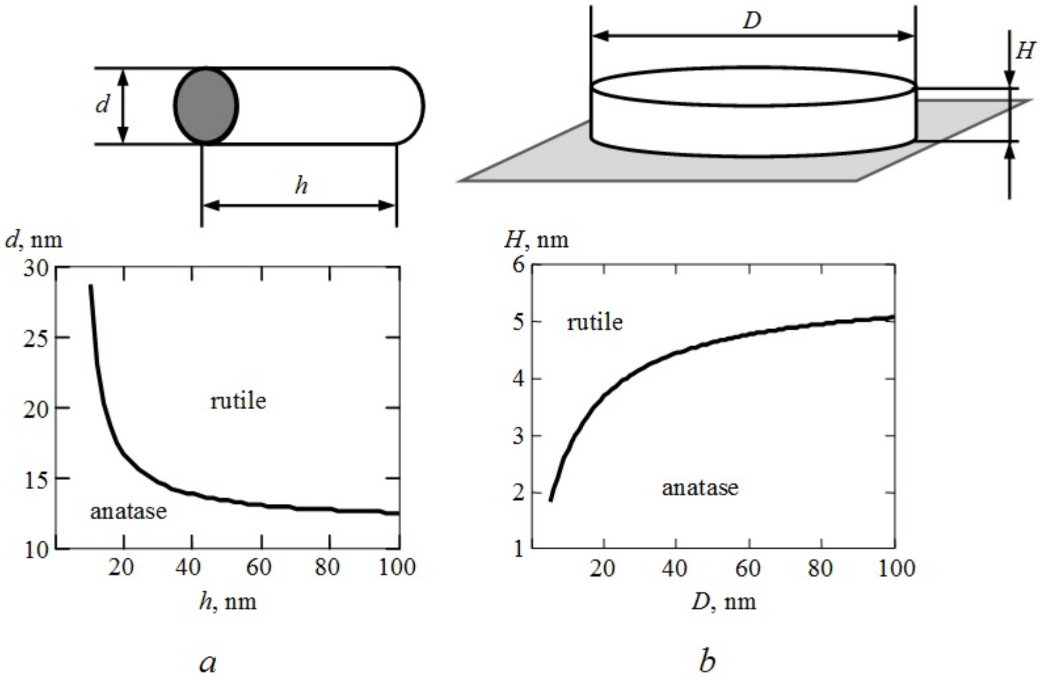

FIG. 9. Dependence of the steady state of structural modifications of TiO_2 on the nanoparticles' linear dimensions in varying types of spatially-constrained conditions: a) in "infinite cylinder" type channel b) and on the flat surface, with the assumption that the the material of the spatially-constraining walls is coherently fused with the anatase structure

The results of X-ray analysis are given in Fig. 10. According to X-ray diffraction data (Fig. 10), throughout the whole range of the hydrothermal treatment parameters, the formation of anatase crystalline titanium oxide is observed. Additionally, the size of crystallites formed is of not more than 16 nm (Fig. 11), which is consistent with the data obtained by thermodynamic analysis on the possibility of sustainable existence for the metastable anatase modification.

Analysis of X-ray diffraction data (Fig. 11) suggests that hydrothermal treatment of X-ray amorphous hydrated titanium oxide ($TiO_2 \cdot nH_2O$) at 200 °C for 10 min leads to crystallization of about 0.2 (20%) of titanium dioxide in the anatase form. Whereas, at 250 °C, for the same time, the conversion reaches 0.85 (Fig. 10b, Fig. 10). It should be noted that the change in the crystallite size change is symbatical to the change in the conversion (Fig. 11), i.e. at 200 °C a significant increase of the size of the TiO_2 crystallites occurs during a period of rapid increase in the conversion (Fig. 11), and when the conversion reaches about 0.8, the growth rate of the crystal phase and the size of the TiO_2 crystallites with the anatase structure significantly decrease.

A comparison of the curve of changes in the conversion and the curve corresponding to changes in the relative values of the average volume of crystallites (ν) (Fig. 12) suggests that at a temperature of 200 °C the formation of TiO_2 nanocrystals in the anatase form from amorphous hydrated titanium oxide in the initial stage of hydrothermal treatment is mainly associated with the formation of new crystallites of anatase from the amorphous phase. In the case of increasing the isothermal time, the amount of amorphous phase decreases, which leads to a change in the predominant mechanism of crystallite growth. Upon reaching a conversion of 0.8, an increase in the TiO_2 crystallite size is mainly due to an increase in their volume during the recrystallization process. A change in the prevailing process greatly reduces the growth rate of TiO_2 crystallites (Fig. 11). At a temperature of hydrothermal treatment of 250 °C, the process for forming titanium oxide nanocrystals takes place so rapidly that after 10 minutes of isothermal time the conversion is higher than 0.80 (Fig. 11), and therefore, a further increase in the size of the crystallites takes place apparently due to the recrystallization process.

It should be noted that in the case of hydrothermal treatment of amorphous hydrated TiO_2 and at a temperature of 200 °C and 250 °C, when the conversion is about 0.85, the size of crystallites is about 11 nm (Fig. 11). Also, the speed of their growth and increase in size during further isothermal treatment are very low. The low crystallite growth rate, and therefore a small change in their sizes appears to be related to the fact that in conditions of

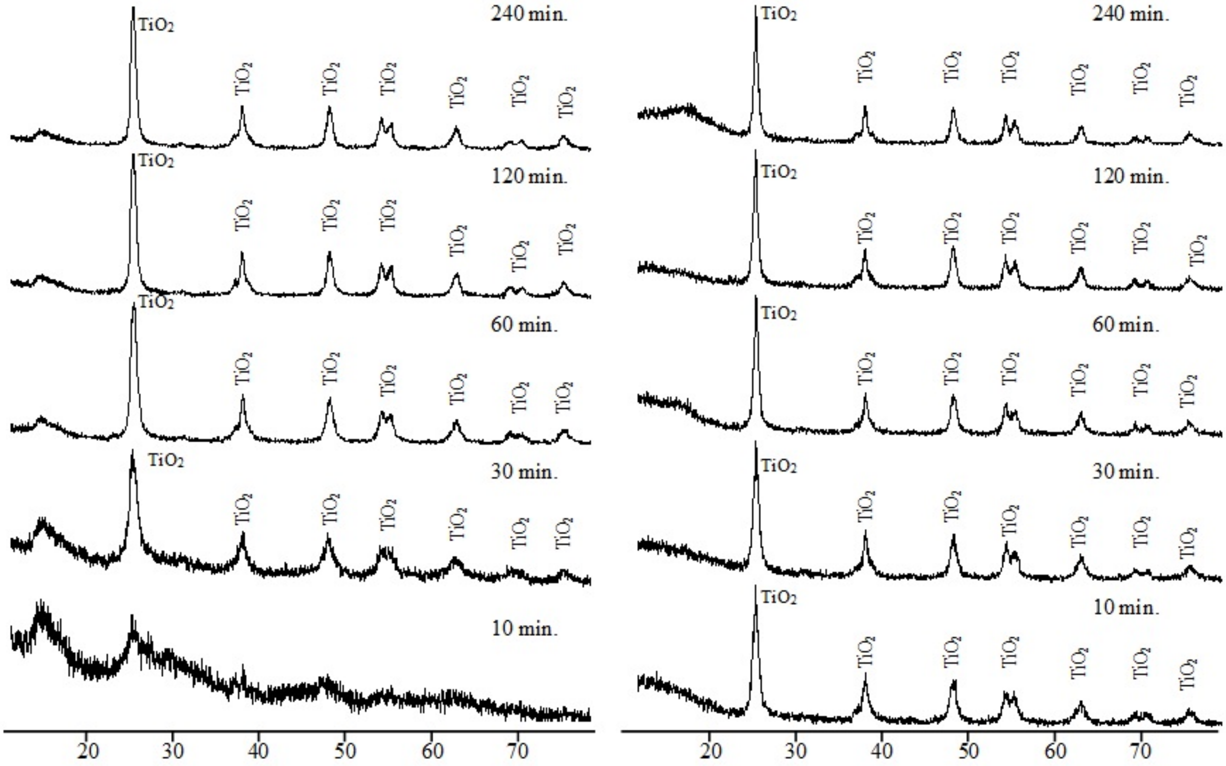

FIG. 10. X-ray diffraction patterns for samples obtained by hydrothermal treatment of hydrated titanium oxide at T=200 °C () and T=250 °C (b) and $P = 70$ MPa

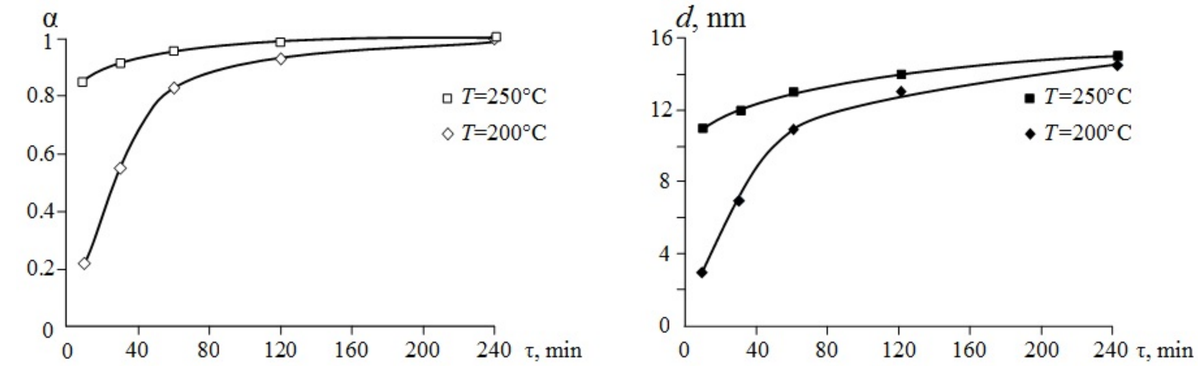

FIG. 11. Dependence of the conversion (α) and crystallite size (d) on the duration of the hydrothermal treatment of hydrated titanium oxide at =200 °C and =250 °C, P=70 MPa

practically avalanche-like crystallization of TiO_2 nanoparticles, they are characterized by relatively narrow particle size distribution, similarly to formation of ZrO_2 nanoparticles [50, 51].

For the samples obtained at hydrothermal treatment temperature of 250 °C, a change in the specific surface of samples has been analyzed depending on the isothermal treatment time (Fig. 13). According to the data shown in (Fig. 13), specific surface area of TiO_2 nanoparticles obtained during hydrothermal treatment significantly decreases when the isothermal treatment time was changed from 30 minutes to 60 minutes. A further increase in the duration of treatment leads to a monotonic, but not significant decrease in the specific surface area of TiO_2 nanoparticles.

Based on the data for the specific surface area of the titanium dioxide nanoparticles (Fig. 13), their size has been calculated assuming that the shape of particles is close to spherical. In the case of comparison of the crystallite sizes and sizes of anatase titanium dioxide particles, it can be observed that the crystallite sizes obtained based on the X-ray diffraction data are systematically lower than those of the TiO_2 particles obtained based on the data on the specific surface (Fig. 14).

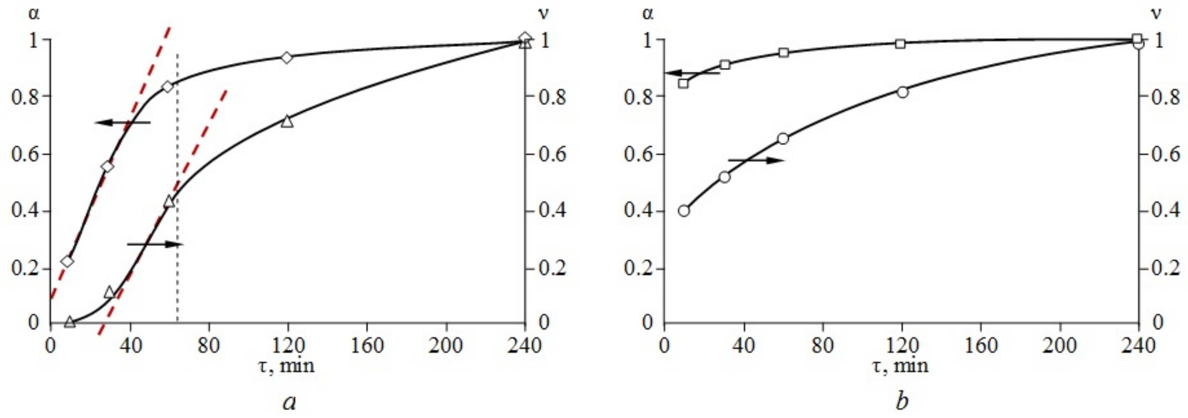

FIG. 12. Dependence of changes of the relative values of the average crystallite volume (ν) and the degree of conversion (α), on the duration of the hydrothermal treatment at T=200 °C (a) and T=250 °C (b), P=70 MPa

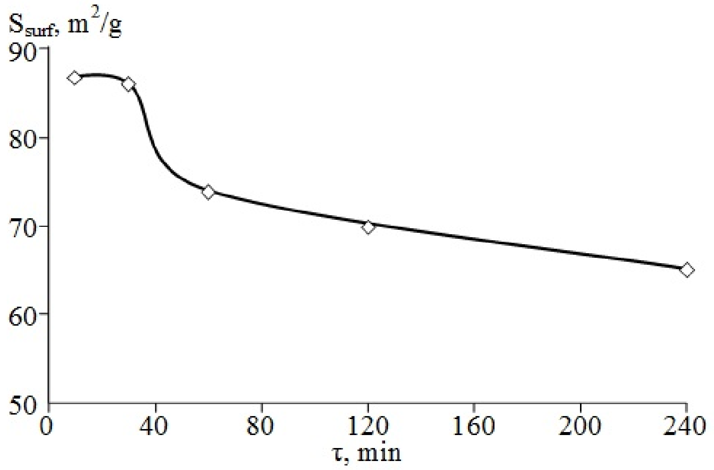

FIG. 13. Dependence of of the specific surface (S_{sp}) on the duration of the hydrothermal treatment of hydrated titanium oxide at T=250 °C, P=70 MPa

This can be be due, for example, to the fact that the obtained particles contain a crystalline core, the size of which is determined based on broadening of X-ray diffraction lines and X-ray amorphous coating, the presence of which is taken into account during specific surface area determination. Such explanation of the difference in sizes of particles and crystallites is possible in cases when the proportion of the amorphous states in the system is large, i.e. at low temperatures and times of phase formation. When the temperature and time of hydrothermal treatment are T=250 °C, $\tau \geq$60 min as follows from the analysis of the data presented in Fig. 12, the proportion of the amorphous phase in the system is low. In this case, the difference between sizes of particles and crystallites is likely determined by the fact that the anatase TiO_2 crystallites formed dense polycrystalline aggregates composed of 3–4 crystallites, as can be concluded based on the analysis of the d^3_{part}/d^3_{cryst} ratio.

The results of complex differential thermal analysis of the TiO_2 nanoparticles obtained during hydrothermal treatment of the hydrated titanium oxide are given in Fig. 15. On the DSC curve, a set of thermal effects accompanied by a change in the mass of the sample is determined (Fig. 15, Table 6).

The analysis of data presented in Fig. 16 shows that the observed exothermic heat effects in the range of 200–510 °C are not accompanied by a marked change in the structural state of TiO_2 nanoparticles. Up to 600 °C, in the X-ray diffraction patterns, peaks corresponding to titanium oxide in the anatase structural modification are observed. Only after heat treatment to temperatures in the area of 1000 °C, the anatase → rutile transition is observed. According to this data, the structural state of titanium dioxide is shown in Table 6. The dependence of the size of crystallites on the treatment temperature is shown in Fig. 16.

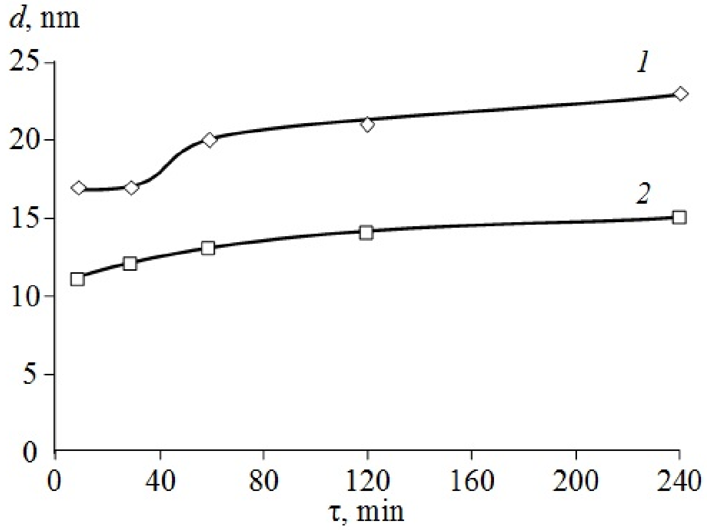

FIG. 14. Dependence of the size of TiO_2 nanoparticles calculated based on the data on the specific surface area (1) and the size of crystallites of TiO_2(anatase) calculated based on X-ray diffraction data (2) on the duration of the hydrothermal treatment of hydrated titanium oxide at T=250 °C, P=70 MPa

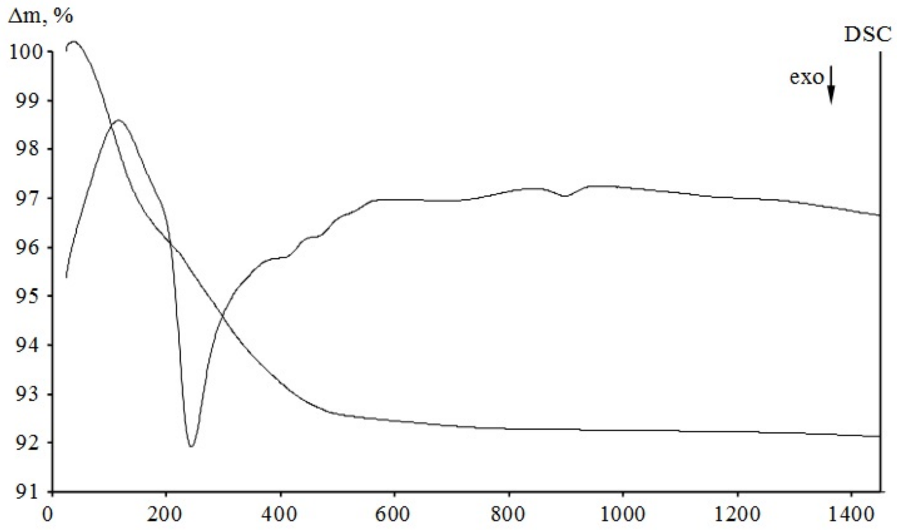

FIG. 15. Results of complex thermal analysis of TiO_2 nanoparticles obtained during hydrothermal treatment of amorphous hydrated titanium oxide at T=200 °C, P=70 MPa, and 120 min isothermal treatmen

TABLE 6. Thermal effects and changes in the weight of the sample obtained by hydrothermal treatment of amorphous hydrated titanium dioxide at T=200 °C, P=70 MPa, and 120 min isothermal treatment

Temperature range, °C	Nature of the thermal effect	Weight loss, %	Phase composition
25-200	endo	4	anatase
200-510	exo	3.7	anatase
850-950	exo	0.1	rutile

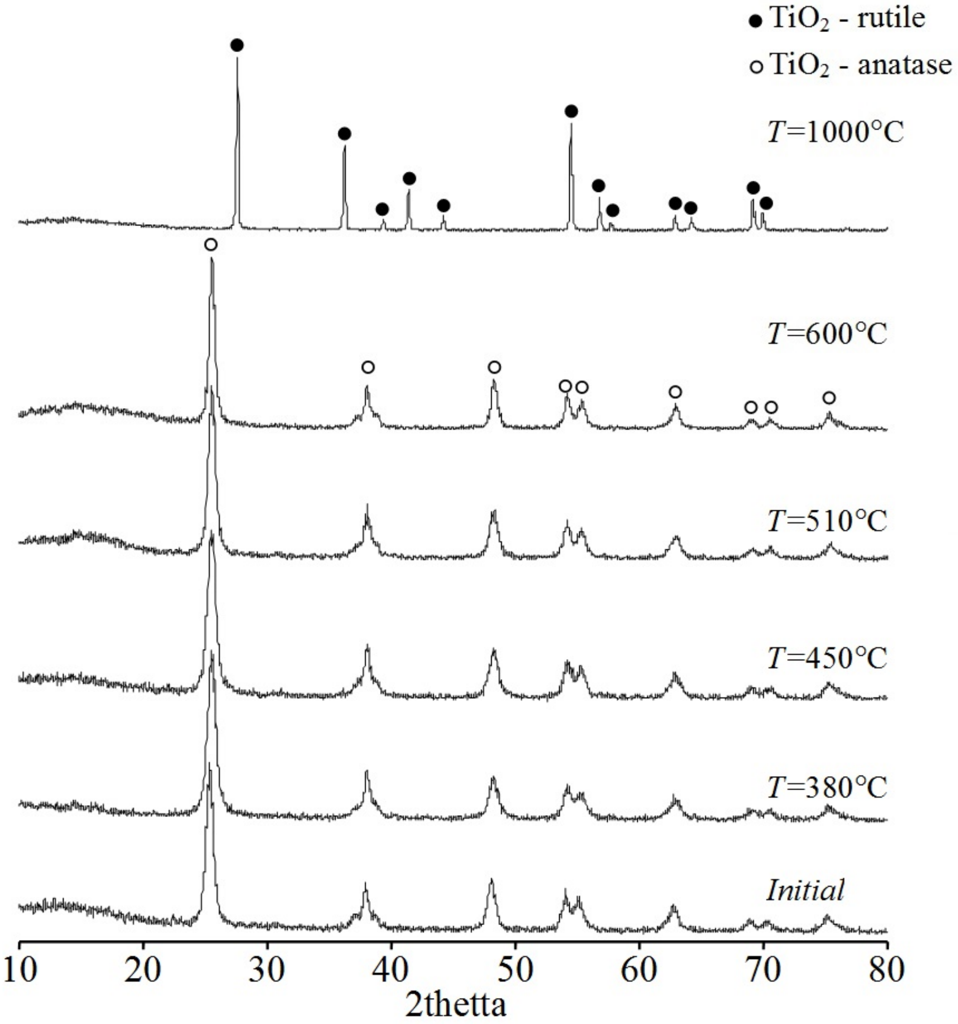

FIG. 16. X-ray diffraction patterns of the samples obtained during heating of titanium dioxide nanoparticles in air under conditions similar to used in the DSC heating mode

Thus, it seems that in the temperature range of 200–510 °C two processes occur: dehydration of remaining amorphous hydrated titanium oxide and its crystallization in the form of the anatase modification that leads to corresponding thermal effects on the thermogram (Fig. 15, Table 6). Based on the data on the weight loss in the temperature range of 200–510 °C, it can be assumed that amorphous hydrated titanium oxide component remaining after dehydration at 25–200 °C has the following formula: $TiO_2 \cdot 0.18\ H_2O$.

In the high-temperature region, the exothermic effect is accompanied by a negligible change in the weight of the sample and is associated with the TiO_2-anatase→TiO_2-rutile phase transformation. It should be noted that the size of the crystallites of titanium dioxide sharply increases during the transition from anatase to rutile modification and is about 50 nm.

4. Conclusion

Thermodynamic analysis of processes in the TiO_2–H_2O system over a wide range of varying conditions (temperature, pressure, oxygen potential and crystalline particle size), as well as the presence of various types of space constraints allowed us to determine the regions of sustainable existence for titanium dioxide in the form of rutile and anatase modification. The results of thermodynamic prediction on the possibility and conditions for the sustainable existence of TiO_2 with the rutile structure have been experimentally confirmed. The conditions and mechanisms for the formation of rutile and anatase nanocrystals during thermal treatment of amorphous hydrated titanium oxide in air and hydrothermal environments have been determined. It has been shown that the transition of titanium dioxide from the anatase to the rutile phase occurs by fusion and recrystallization of agglomerate consisting of three or four anatase particles with an average size of 50 nm.

Acknowledgements

The author would like to thank Prof. V. V. Gusarov for interest in the work and help in the interpretation of results. This work was supported by the Russian Foundation for Basic Research (project No 16-03-00532).

References

[1] Chemseddine A., Moritz T. Nanostructuring titania: control over nanocrystal structure, size, shape, and organization. *Eur. J. Inorg. Chem.*, 1999, **2**, P. 235–245.

[2] Denisova T.A. Status of proton groups sorbents based oxyhydrated, geteropolimetallatnyh and tsianoferratnyh phases. Thesis for the degree of Doctor of Science. Institute of solid state chemistry of the Ural Branch of the Russian Academy of Sciences. Ekaterinburg, 2009. (in Russian)

[3] Pletnev R.N., Ivakin A.A., Kleshchev D.G., Denisova T.A., Burmistrov V.A. Hydrated oxides of group IV and V.M. *Nauka*, 1986, 186 p. (in Russian).

[4] Osborn E.F. System H_2O-TiO_2: conversion of anatase to rutile in the presence of water. *J. Am. Ceram. Soc.*, 1953, **36**(5), P. 147–151.

[5] Dachille F., Roy R. A new high pressure form of titanium dioxide. *Am. Ceram. Soc. Bull*, 1962, **41**, P. 225.

[6] Simons P.Y., Dachille F. The structure of TiO_2II, a high pressure phase of TiO_2. *Acta Crystallogr.*, 1967, **23** (Pt. 2), P. 334–335.

[7] Bendeliany N.A., Popova S.V., Vereschagin L.F. A new modification of titanium dioxide stable at high pressure. *Geochem. Int.*, 1966, **5**, P. 387–391.

[8] McQueen R.G., Jamieson J.C. Marsh S.P. Shock wave compression and X-ray studies of titanium dioxide. *Science*, 1967, **155**(3768), P. 1401–1404.

[9] Carli P.S, Linde R.K. Residual effects of shock waves in rutile. Meteorit. Soc., 30-th Ann Meet., Mofett Field, Calif, October, 1967.

[10] Vahldiek F.W. Phase transitions of titanium dioxide under various pressures. *J. Less Common Metals*, 1966, **11**, P. 99–110.

[11] White W.B., Dachille F. Roy R High pressure high temperature polymorphism of the oxides of lead. *J. Am. Ceram. Soc.*, 1961, **44**, P. 170–175.

[12] Azzaria L., Dachille F. High pressure polymorphism of manganous fluoride. *J. Phys. Chem.*, 1961, **65**, P. 889–890.

[13] Dachille F., Simons P.Y, Roy R. Pressure-temperature studies of anatase, brookite, rutile and TiO_2-II. *Am. Mineralogist*, 1968, **53**, P. 1929–1938.

[14] El-Akkad T.M. Effect of thermal dehydration on surface characteristics of titania gel. *Thermochim. cta.*, 1980, **37**(3), P. 269–277.

[15] Hakonov A.I., Kontorovich S.I., Shchukin E.D. Thermal aging study "titanic acid" in the mother liquor. Izvestiya Academy Nauk USSR. *Neorganicheskie materialy*, 1974, **10**(11), P. 2095–2096 (in Russian).

[16] Kolen'ko Yu.V., Burukhin A.A., Churagulov B.R., Oleynikov N.N. Synthesis of nanocrystalline TiO_2 powders from aqueous $TiOSO_4$ solutions under hydrothermal conditions. *Mater. Lett.*, 2003, **57**, P. 1124–1129.

[17] Zhang S., Peng L.M., Chen Q., Du G.H., Dawson G., Zhou W.Z. Formation mechanism of $H_2Ti_3O_7$ nanotubes. *Phys. Rev. Lett.*, 2003, **91**(25), P. 256103.

[18] Iorish V.S., Belov G.V. IVTANTHERMO/WIN - database and software for high temperature chemical processes modeling. 9-th Int. Conf. on High Temperature Materials Chemistry: Proceedings.- Pennsylvania (USA), 1997, P. 42.

[19] Gusarov V.V. Fast Solid-Phase Chemical Reactions. *Russ. J. Gen. Chem.*, 1997, **67**(12), P. 1846–1851.

[20] Gusarov V.V. The thermal effect of melting in polycrystalline systems. *Thermochim. Acta*, 1995, **256**(2), P. 467–472.

[21] Karapetyanc M.H. *Methods for calculating the comparative physicochemical properties*. .: Nauka, 1965. (in Russia)

[22] Almjasheva O.V. Hydrothermal synthesis, structure and properties of crystals and nanocomposites based on the system ZrO_2-Al_2O_3-SiO_2. Thesis for the degree of PhD. Saint-Peterburg, 2007. (in Russian)

[23] Thermal constants of substances. Directory of 10 issues (Vol. VII). ed. Acad. VP Glushko. M., 1974. (in Russian)

[24] Hishman M.W., Benson S.W. *J. Phys. Chem.*, 1987, **91**(5), P. 5998–6009.

[25] Kumok V.N. *Direct and inverse problems of chemical thermodynamics*. Novosibirsk: Nauka, 1987, P. 108–128. (in Russian)

[26] Reznitsky L.A., Filippova S.E. The enthalpies of crystallization of the amorphous zirconia and solid solutions with M_2O_3 (M-Y, Sc, Pr, Nd, Eu, Tb, Yb). *Izvestiya Academy Nauk USSR. Neorganicheskie materialy*, 1991, *27*(9), P. 1841–1844. (in Russian)

[27] Reznitsky L.A. *Chemical bonding and converting oxides*. M.: MSU, 1978, 168 p. (in Russian)

[28] Almjasheva O.V., Gusarov V.V. Metastable clusters and aggregative nucleation mechanism. *Nanosystems: Physics, Chemistry, Mathematics*. 2014, **5**(3), P. 405–417.

[29] Moinov S.G., Reznichenko V.A. *Problemy mettalurgii titania*, 1967, Moscow, USSR.

[30] Brace W.F., Walsh J.B. Some direct measurements of the surface energy of quartz and orthoclase. *Am. Mineralogist*, 1962, **47**, P. 1111–1122.

[31] Terwilliger C.D., Chiang, Y. Measurements of excess enthalpy in ultrafine-grained titanium dioxide. *J. Am. Ceram. Soc.*, 1995, **78**, P. 2045–2055.

[32] Gribb A.A., Banfield J.F. Particle size effects on transformation kinetics and phase stability in nanocrystalline TiO_2. *Am. Mineralogist*, 1997. 82, P. 717–728.

[33] Barnard A.S., Zapol P., Curtiss L.A. Modeling the morphology and phase stability of TiO_2 nanocrystals in water. *J. Chem. Theory Comput.*, 2005, **1**, P. 107–116.

[34] Zhang H., Banfield J.F. Thermodynamic analysis of phase stability of nanocrystalline titania. *J. Mater. Chem.*, 1998, **8**(9), P. 2073–2076.

[35] Barnard A.S., Zapol P. Curtiss L.A. Modeling the morphology and phase stability of TiO_2 nanocrystal in water. *J. Chem. Theory Comput.*, 2005, **1**, P. 107–116.

[36] Hoang V.V. The glass transition and thermodynamics of liquid and amorphous TiO_2 nanoparticles. *Nanotechnology*, 2008, **19**(10), P. 105706.

[37] Tolman R.C. The effect of droplet size on surface tension. *J. Chem. Phys.*, 1949, **17**(3), P. 333.

[38] Phasengleichgewichte und grenzflächenerscheinungen by A.I. Rusanov, German edition by W. Schirmer, Akademie-Verlag, Berlin, 1978, 465 p.

[39] Samsonov V.M., Bazulev A.N., Sdobnyakov N.Yu. Rusanov's linear formula for the surface tension of small objects. *Dokl. Phys. Chem.*, 2003, **389**(1-3), P. 83–85.

[40] NIST-JANAF Thermochemical Tables. http://kinetics.nist.gov/janaf/.

[41] Ranade M.R., Navrotsky A., Zhang H.Z., Banfild J.F., Elder S.H., Zaban A. Borse P.H., Kulkarni S.K., Doran G.S., Witfield H.J. Energetic of nanocrystalline TiO_2. PNAS, 2002, **99**(2), P. 6476–6481.

[42] Rao C.N.R. Kinetics and thermodynamics of the crystal structure transformation of spectroscopically pure anatase to rutile. *Can. J. Chem.*, 1961, **39**, P. 498–500.

[43] Mitsuhashi T., Kleppa O.J. Transformation enthalpies of the TiO_2 polymorphs. *J. Am. Ceram. Soc.*, 1979, **62**(7-8), P. 356–357.

[44] Navrotsky A., Kleppa O.J. Enthalpy of the anatase - rutile transformation. *J. Am. Ceram. Soc.*, 1967, **50**(11), 626 p.

[45] Margrave J.L., Kybett B.D. Tech.Rep. No AFMO-TR-65, 1965, 123 p.

[46] Robie R.A., Waldum D.R. Thermodynamic properties of mineral and related substances at 298.15 °K(25.0 °C) and one atmosphere (1.013 bars) pressure and at higher temperature. *U.S. Geol. Surv. Bull.*, 1968, **1259**, 256 p.

[47] Cammarata R.C., Sieradzki K. Surface and Interface Stresses. *Annu. Rev. Mater. Sci.*, 1994, **24**, P. 215–234.

[48] Gusarov V.V., Almjasheva O.V. The role of non-autonomous state of matter in the formation of structure and properties of nanomaterials. Chapter 13 in the book Nanomaterials: properties and promising applications. Ed A.B. Yaroslavtsev. Scientific World Publishing House, Moscow, 2014, P. 378–403. (in Russian)

[49] Vasilevskay A.K., Almjasheva O.V., Gusarov V.V. Peculiarities of structural transformations in zirconia nanocrystals. *Journal of Nanoparticle Research*, 2016, **18**(7), P. 188.

[50] Pozhidaeva O.V., Korytkova E.N., Romanov D.P., Gusarov V.V. Formation of ZrO_2 nanocrystals in hydrothermal media of various chemical compositions. *Russ. J. Gen. Chem.*, 2002, **72**(6), P. 849–853.

[51] Sharikov F.Yu., Almjasheva O.V., Gusarov V.V. Thermal analysis of formation of ZrO_2 nanoparticles under hydrothermal conditions. *Russ. J. Inorg. Chem.*, **51**(10), P. 1538–1542.

[52] Gusarov V.V., Malkov A.A., Malygin A.A. Suvorov S.A. Aluminum titanate formation in compositions with a high level of spatial and structural coupling components. *Russ. J. Gen. Chem.*, 1994, **64**(4), P. 554.

[53] Al'myasheva O.V., Gusarov V.V. Nucleation in media in which nanoparticles of another phase are distributed. *Dokl. Phys. Chem.*, 2009, **424**(2), P. 43–45.

[54] Al'myasheva O.V., Gusarov V.V. Features of the phase formation in the nanocomposites. *Russ. J. Gen. Chem.*, 2010, **80**(3), P. 385–390.

NANOSYSTEMS: PHYSICS, CHEMISTRY, MATHEMATICS, 2016, 7 (6), P. 1050–1054

Successive ionic layer deposition of Fe_3O_4@$H_xMoO_4 \cdot nH_2O$ composite nanolayers and their superparamagnetic properties

L. I. Kuklo, V. P. Tolstoy

Institute of Chemistry, Saint Petersburg State University,
26 University Pr., St. Peterhof, Saint Petersburg, 198504, Russia

lenkuklo@mail.ru, v.tolstoy@spbu.ru

PACS 75.70.Ak **DOI 10.17586/2220-8054-2016-7-6-1050-1054**

The Fe_3O_4@$H_xMoO_4 \cdot nH_2O$ nanolayers were synthesized on the solid surface for the first time by Successive Ionic Layer Deposition (SILD) method with using an aqueous Fe_3O_4 suspensions and $(NH_4)_2MoO_4$ solutions. The obtained nanolayers were investigated by XRD, SEM, EDX, FTIR spectroscopy and magnetization measurement techniques. SEM images showed that the nanolayers formed by nanoparticles of size approximately 15–20 nm. The synthesized nanolayers exhibited superparamagnetic properties with the saturation magnetization value of 55 emu/g.

Keywords: magnetite, SILD, nanolayers, core-shell nanoparticles, superparamagnetism.

Received: 5 December 2016

1. Introduction

It is known that iron oxide nanomaterials are very important in a big number applications because of their magnetic properties. Iron oxides particles are prepared with solid-state reactions [1], coprecipitation from solutions [2], hydrothermal treatment [3–5], oxidation of solutions of iron (II) salt [6], combustion method [7] and etc. Iron oxides in nano-scale have a great potential for their applications as ion exchangers, adsorbents, catalytic materials, magnetic data storage devices, superparamagnetic materials and etc. The nanoparticles and nanolayers with superparamagnetic properties are very important for fabrication of new advanced materials in MRI diagnostics [8], drug delivery [9], mixture separation [10], hyperthermia [11], as well as new multi-functional materials, in particular luminescent and magnetic materials [12] and etc.

The Layer-by-Layer (LbL) method is used for such nanolayers obtaining as one of the best methods among other [13].This method of synthesis based on a successive and multiple treatments of substrate in salt solutions and polyelectrolytes, forming an insoluble layer of new compound at interaction on the surface. The SILD method is one of LbL synthesis methods without the using of polyelectrolite solutions. It has been used previously to synthesize nanolayers of metal oxides [14], noble metal nanoparticles [15], hydroxides [16] and etc. The SILD method is based on a sequential adsorption of anions and cations or colloid particles on the substrate surface with formation of nanolayer of insoluble compounds [17].

The major advantages of this method is a simplicity of the process and equipment, the application of substrates with irregular shapes and sizes and precision control of the thickness of the multilayer. These special features of the SILD method give a possibility to obtain nanolayers of wide number of substances, which can be applied in optics, microelectronics, energy storage devices.

In this paper, we describe a novel simple route for SILD synthesis of the Fe_3O_4@$H_xMoO_4 \cdot nH_2O$ composite nanolayers with using a Fe_3O_4 suspensions and $(NH_4)_2MoO_4$ solutions, as well as their magnetic properties study.

2. Experimental methods

The single crystalline silicon plates of size $10 \times 25 \times 0,3$ mm with $< 100 >$ orientation were used as substrates for synthesis of nanolayer. All substrates were cleaned in an ultrasonic acetone bath for 10 minutes before synthesis. Then plates were sequentially treated for 10 minutes in 40 % HF, distilled water, 70 % HNO_3, distilled water, 0.1 M KOH solution and flushed out by deionized water.

For SILD synthesis we used an aqueous Fe_3O_4 suspensions ($C_{Fe_3O_4} = 0,01$ M, pH 4,0) and $(NH_4)_2MoO_4$ solutions (C = 0.01 M, equilibrium pH). The Fe_3O_4 suspension was prepared by the method [18] from 0.01 M $FeCl_2$ and 0.0202 M $FeCl_3$ mixed solution. The $HClO_4$ was added in mixed solution to pH = 4.0 to enhance the suspension stability. All reagents used were of analytical grade. Deionized water with resistively 18.2 MΩ cm (Mili-Q) was used for preparation of reagent suspensions and solutions.

$Fe_3O_4@H_xMoO_4{\cdot}nH_2O$ nanolayers were synthesized by SILD. First, plates were sequential immersed for 60 second into Fe_3O_4 suspension, then washed in distilled water. Then plates were dipping for 30 second in solution of $(NH_4)_2MoO_4$ and again washed in water. The sequence corresponds to one SILD cycle, which is repeated 30 times to obtain desired nanolayer thickness.

The composition and morphology of $Fe_3O_4@H_xMoO_4{\cdot}nH_2O$ layers were investigated by energy-dispersive X-ray spectroscopy (EDX) using Oxford INCA350 detector and scanning electron microscopy (SEM) using Zeiss EVO-40EP microscope. X-ray diffraction (XRD) was carried out on Rigaku Miniflex II diffractometer with CoK_α radiation, 30 kV voltage, and 10 mA current. FT-IR transmission spectra of synthesized nanolayers on silicon surface were registered by FSM-2201 spectrophotometer using differential scheme related to spectra of bare silicon.

Magnetization measurement of the Fe_3O_4/molybdate nanocomposite nanolayers was performed with a vibrating sample magnetometer VSM Lake Shore-741 in the ±17.8 kOe window at room temperature.

The sizes of Fe_3O_4 particles in aqueous suspensions were determined with the help of Dynamic Light Scattering (DLS) method. The measurements were carried out with a Zetasizer Nano ZS analyzer in a DTS 1060 universal capillary U-shaped cell at 20°C. The electrokinetic potential was calculated by the Smoluchowski equation. The values of the ζ potential were corrected within the approximation of the Overbeek-Booth-Wiersema model [19].

3. Result and discussion

DLS experiments demonstrated that average particle size of Fe_3O_4 suspension is 16 nm. Their ζ potential equals +47,1 m.

SEM investigation of synthesized layers showed that they formed by nanoparticles with sizes about 15–20 nm (Fig. 1). The dispersive X-ray spectroscopy research has determined the significant energy signal intensity of Fe, Mo, and O elements in the sample (Fig. 2). The concentration ratio of Fe : Mo corresponds $13,5 : 1,0$.

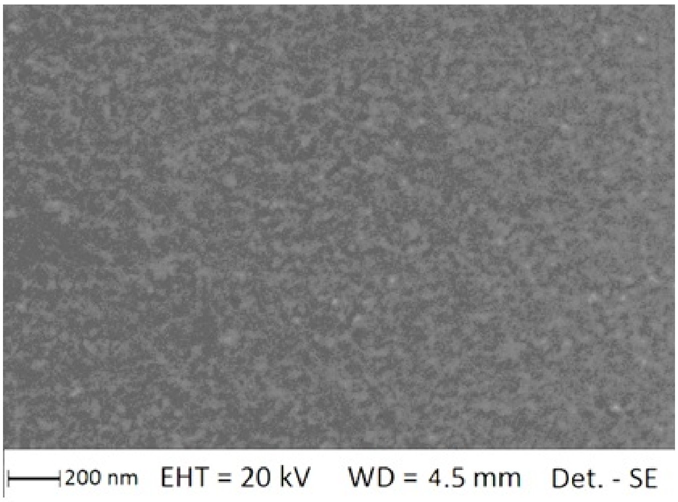

FIG. 1. SEM image of $Fe_3O_4@H_xMoO_4{\cdot}nH_2O$ nanolayer on silicon

The XRD pattern of synthesized sample is presented in Fig. 3. Five diffraction peaks at 35.2, 41.5, 50.6, 67.4, and 74.3° can be indexed as the diffractions of magnetite Fe_3O_4 (ICDD PDF # 01-071-6336).

As can be seen from the experimental FT-IR spectra (Fig. 4) a water molecules are included in composition of nanolayer, which can be identified by the valence band (3400 cm^{-1}) and the deformation band (1640 cm^{-1}). The band at 594 cm^{-1} may be assigned to valence vibrations of Fe-O bonds in magnetite Fe_3O_4 [20], and bands at 950–750 cm^{-1} region connected with valence vibrations of Mo-O bonds in molybdate-anions [21].

For the explanation the obtained results it can be suggested the following schemes of chemical reactions on the surface of silicon. At the first SILD cycle after dipping in the Fe_3O_4 suspension and wash in distilled water on the surface silicon the layer of Fe_3O_4 nanoparticles (NP) is formed:

$$\equiv \mathrm{Si-OH} + (\mathrm{Fe_3O_4})_{\mathrm{NP}} \rightarrow \equiv \mathrm{Si-OH} \cdot (\mathrm{Fe_3O_4})_{\mathrm{NP}}, \tag{1}$$

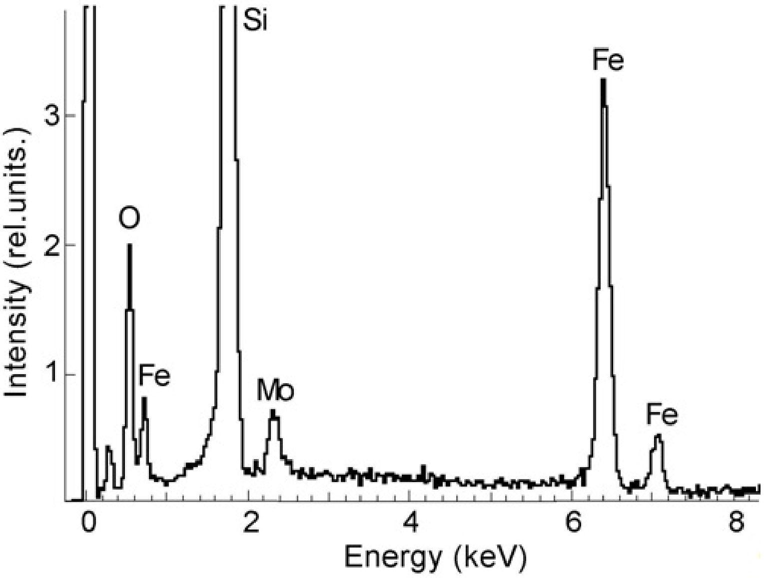

FIG. 2. EDX spectrum of $Fe_3O_4@H_xMoO_4 \cdot nH_2O$ nanolayer on silicon

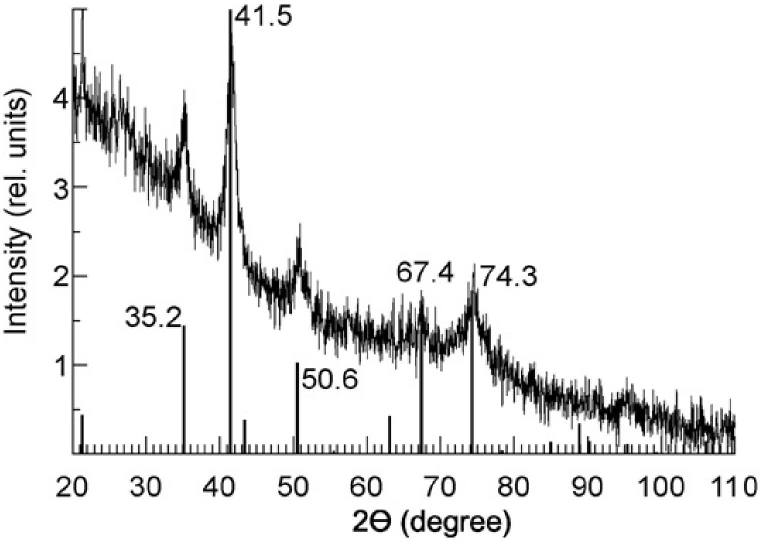

FIG. 3. XRD pattern of synthesized sample

Then after treatment in the excess of $(NH_4)_2MoO_4$ solution and washing the MoO_4^{2-}-anions adsorbed on Fe_3O_4 surface and core-shell nanoparticles layer is formed:

$$\equiv \mathrm{Si-OH} \cdot (\mathrm{Fe_3O_4})_{\mathrm{NP}} + \mathrm{MoO_4^{2-}} + \mathrm{H_2O} \rightarrow \equiv \mathrm{Si-OH} \cdot (\mathrm{Fe_3O_4@H_xMoO_4})_{\mathrm{CS}}. \quad (2)$$

On the second SILD cycle during the treatment in the Fe_3O_4 suspension, the nanoparticles of Fe_3O_4 are adsorbed on the substrate surface again:

$$\equiv \mathrm{Si-OH} \cdot (\mathrm{Fe_3O_4@H_xMoO_4})_{\mathrm{CS}} + (\mathrm{Fe_3O_4})_{\mathrm{NP}} \rightarrow \equiv \mathrm{Si-OH} \cdot (\mathrm{Fe_3O_4@H_xMoO_4})_{\mathrm{CS}} \cdot (\mathrm{Fe_3O_4})_{\mathrm{NP}} \quad (3)$$

Thus, as a result of multiple repetitions of SILD cycles the $Fe_3O_4@H_xMoO_4 \cdot nH_2O$ omposite nanolayer is created on the surface. It is evident that thickness of this layer can be control by number of SILD cycles.

Magnetic characterization of the $Fe_3O_4@H_xMoO_4 \cdot nH_2O$ nanolayer is shown in Fig. 5. The analyzed sample demonstrated superparamagnetic properties with the saturation of magnetization value of 55 emu/g and very low remanence magnetization (Mr∼4 emu/g) and coercivity (Hc∼30 Oe).

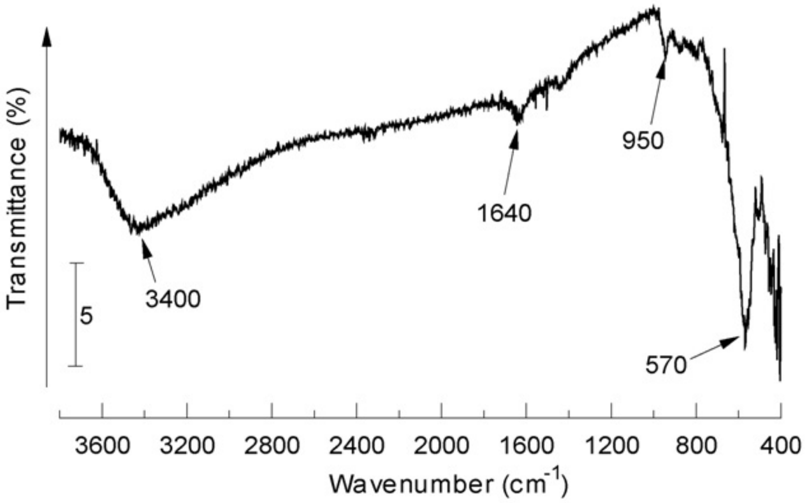

FIG. 4. FT-IR transmission spectrum of $Fe_3O_4@H_xMoO_4\cdot nH_2O$ layer on silicon surface

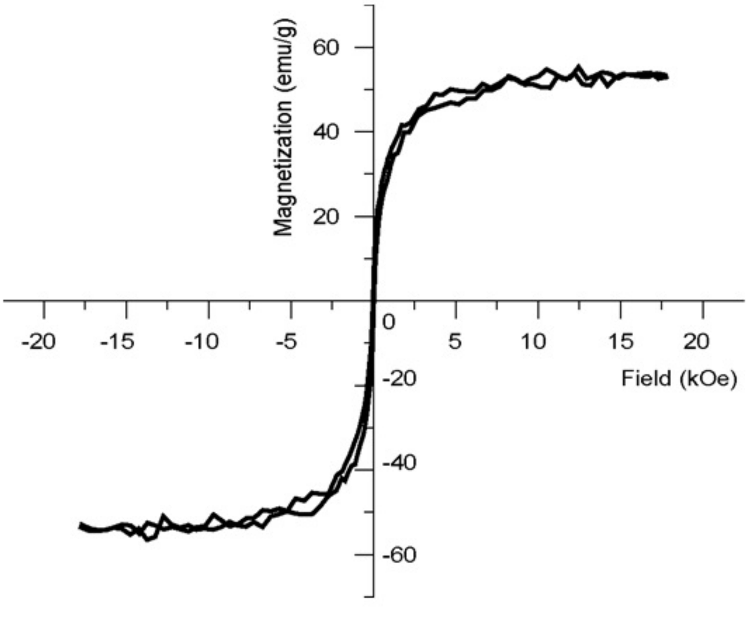

FIG. 5. Magnetization curves of $Fe_3O_4@H_xMoO_4\cdot nH_2O$ nanolayer synthesized on silicon surface in result 30 SILD cycles

We believe that nanolayers with such composition and morphology can be apply as superparamagnetic materials for separation of mixtures. The promoted approach to the synthesis provides a good opportunity to adjust the properties of the new multilayered materials in the synthesis process by changing the number of SILD cycles.

4. Conclusion

In this work, we obtained the $Fe_3O_4@H_xMoO_4\cdot nH_2O$ nanolayers by SILD method using a Fe_3O_4 suspension and $(NH_4)_2MoO_4$ solution as reagents. These nanolayers exhibit superparamagnetic behavior with saturation magnetization value of 55 emu/g.

Acknowledgement

This research was supported by grant of the Saint-Petersburg State University (# 12.38.259.2014). The authors are grateful acknowledge to the SPbSU Centres for X-ray diffraction studies and for Innovative Technologies of Composite Nanomaterials.

References

[1] Lomanova N.A., Pleshakov I.V., Volkov M.P., Gusarov V.V. Magnetic properties of Aurivillius phases $Bi_{m+1}Fe_{m-3}Ti_3O_{3m+3}$ with m = 5.5, 7, 8. *Materials Science and Engineering: B*, 2016, **214**, P. 51–56.

[2] Lomanova N.A., Gusarov V.V. Influence of synthesis temperature on $BiFeO_3$ nanoparticle formation. *Nanosystems: Physics, Chemistry, Mathematics*, 2013, **4**(5), P. 696–705.

[3] Almjasheva O.V., Gusarov V.V. Prenucleation formations in control over synthesis of $CoFe_2O_4$ nanocrystalline powders. *Russ. J. Appl. Chem.*, 2016, **89**, P. 851–855.

[4] Popkov V.I., Almjasheva O.V. Formation mechanism of $YFeO_3$ nanoparticle under the hydrothermal conditions. *Nanosystems: Physics, Chemistry, Mathematics*, 2014, **5**(5), P. 703–708.

[5] Tugova E.A., Zvereva I.A. Formation mechanism of $GdFeO_3$ nanoparticles under the hydrothermal conditions. *Nanosystems: physics, chemistry, mathematics*, 2013, **4**(6), P. 851–856.

[6] Zherebtsov D.A., Mirasov V.Sh., Kleschev D.G., Polyakov E.V. Nanodisperse oxide compounds of iron formed in the $FeSO_4$–KOH–H_2O–H_2O_2 system (4.0_pH_13.0). *Nanosystems: Physics, Chemistry, Mathematics*, 2015, **6**(4), P. 593–604.

[7] Lomanova N.A., Tomkovich M.V., Sokolov V.V., Gusarov V.V. Special Features of Formation of Nanocrystalline $BiFeO_3$ via the Glycine-Nitrate Combustion Method. *Russian Journal of General Chemistry*, 2016, **86**(10), P. 2256–2262.

[8] Su Hong-Ying, Wu Chang-Qiang, Li Dan-Yang, and Ai Hua. Self-assembled superparamagnetic nanoparticles as MRI contrast agents. – A review. *Chin. Phys. B*, 2015, **24**, P. 127506.

[9] Haining Cao, Jiang He, Li Deng, Xiaoqing Gao. Fabrication of cyclodextrin-functionalized superparamagnetic Fe_3O_4/amino-silane core-shell nanoparticles via layer-by-layer method. *Applied Surface Science*, 2009, **255**, P. 7974–7980.

[10] Liqin Xie, Shaohua Ma, Qi Yang, Fang Lan, Yao Wu and Zhongwei Gu. Double-sided coordination assembly: superparamagnetic composite microspheres with layer-by-layer structure for protein separation. *RSC Adv.*, 2014, **4**, P. 1055–1061.

[11] Yong Seok Kim, Ui Seok Chung, Jung Hyun Kim, Byoung Wook Choi, Won-Gun Koh, and Woo-Dong Jang. Fabrication of Multifunctional Layer-by-Layer Nanocapsules toward the Design of Theragnostic Nanoplatform. *Biomacromolecules*, 2014, **15**, P. 1382–1389.

[12] Bin Sun, Yang Zhang, Ke-Jun Gu, Qun-Dong Shen, Yan Yang, and Heng Song. Layer-by-Layer Assembly of Conjugated Polyelectrolytes on Magnetic Nanoparticle Surfaces. *Langmuir*, 2009, **25**, P. 5969–5973.

[13] Hua Ai. Layer-by-layer capsules for magnetic resonance imaging and drug delivery. *Advanced Drug Delivery Reviews*, 2011, **63**, P. 772–788.

[14] Bogdanova L.P., Tolstoi V.P., Aleskovskii V.B. Synthesis and properties of multilayer chromate films on the surface of carbon steel. *Protection of Metals* (English translation of Zaschita Metallov). 1991, **26**, P. 375–377.

[15] Gulina L.B., Tolstoi V.P., Tolstobrov E.V. Ag_x-SnO_2 nanocomposite layers synthesized by ionic layer deposition onto silica surface. *Russian Journal of Applied Chemistry*, 2010, **83**, P. 1525–1528.

[16] Lobinsky A.A., Tolstoy V.P. Red-ox reactions in aqueous solutions of $Co(OAc)_2$ and $K_2S_2O_8$ and synthesis of CoOOH nanolayers by the SILD method. *Nanosystems: Physics, Chemistry, Mathematics*, 2015, **6**, P. 843–849.

[17] Tolstoi V.P. Synthesis of thin-layer structures by the ionic layer deposition method. *Russian Chemical Reviews*, 1993, **62**, P. 237–242.

[18] Massart R. Preparation of Aqueous Magnetic Liquids in Alkaline and Acidic Media. *IEEE Transactions on Magnetics*, 1981, **17**, P. 1247–1248.

[19] Wiersema P.H., Loeb A.L., and Overbeek J.T.G. Calculation of the electrophoretic mobility of a spherical colloid particle. *J. Colloid Interface Sci.*, 1966, **22**, P. 78–99.

[20] Márquez F., Campo T., Cotto M., Polanco R., Roque R., Fierro P., and all. Synthesis and Characterization of Monodisperse Magnetite Hollow Microspheres. *Soft Nanoscience Letters*, 2011, **1**, P. 25–32.

[21] T. Nagyné Kovács, Hunyadi D., A.L.A. de Lucena, Szilágyi I.M. Thermal decomposition of ammonium molybdates. *Journal of Thermal Analysis and Calorimetry*, 2016, **124**, P. 1013–1021.

NANOSYSTEMS: PHYSICS, CHEMISTRY, MATHEMATICS, 2016, 7 (6), P. 1055–1058

Resistance of composite films based on polystyrene and graphene oxide

A. R. Khairullin[1], M. N. Nikolaeva[1], A. N. Bugrov[1,2]

[1]Institute of macromolecular compounds RAS, Bolshoy pr. 31,
199004 Saint Petersburg, Russia

[2]Saint Petersburg Electrotechnical University "LETI",
ul. Professora Popova 5, 197376 St. Petersburg, Russia

ahairullin@hotmail.com, marianna_n@mail.ru, alexander.n.bugrov@gmail.com

PACS 36.20.-r; 68.65.Pq; 71.20.Rv; 72.80. Tm; 74.78.-w

DOI 10.17586/2220-8054-2016-7-6-1055-1058

Polystyrene films prepared by radical polymerization can conduct electric current in metal-polymer-metal structures with film thicknesses of up to 20 nanometers. Films of polystyrene and graphene oxide composite with thickness up to 3 micrometers, synthesized in similar conditions have the same electric properties. This effect is explained by presence of highly conductive graphene oxide inclusions in the dielectric polystyrene matrix.

Keywords: graphene oxide, polystyrene, composite, conductivity.

Received: 23 August 2016

Revised: 1 September 2016

1. Introduction

The interest in the study of conducting polymers with dielectric properties can be explained by the possibility their use as components of electronic devices in various fields [1–4]. It is known [1–8] that thin films of dielectric polymers are able to conduct electricity below the electric field breakdown. Whereas doped polymers have conductivity levels similar to semiconductors. It is shown that films of such materials have metallic type conductivity [8–14]. Considering chemical structure of the polymers, conductivity of such polymer films can be selectively altered. It is necessary to vary the physicochemical properties of polymeric films to determine the factors influencing on conductive properties of dielectric polymers. Different additives were introduced into polymer films during their syntheses. The aim of this work was to create a new polymeric composite material with high conductivity. Polystyrene was used as a polymer matrix because electrization is most pronounced for polymers with high resistivity [15, 16]. The conductivity in polystyrene films appears in its turn due to the electrization of polymer by a metal substrate. In this instance, graphene oxide (GO) was used as the conducting additive. This material after heat treatment in an aqueous medium [17] becomes a semiconductor, and may even have zero bandgap. After further special treatment as it was done for zirconium oxide in [18], GO may form covalent bonds with polystyrene [19]. It is well known, that a high-conductivity state is observed in such composite films [19]. Also, according to Josephson, the current-voltage characteristics phenomenon of superconductivity was also shown [20, 21].

2. Experimental

Hummers wet chemical method was used to produce graphene oxide [22]. Graphite was used as an initial material for GO production. After series of chemical reactions in liquid medium, the prepared GO was extracted from an aqueous suspension by aerobic drying at room temperature. Surface modification of GO was carried out using the method described in our previous work [19]. Polystyrene and polymer-inorganic composites were synthesized under identical conditions by free radical polymerization in solution. Styrene in an amount of 0.5 ml and 1 % of 2,2′-azobis(2-methylpropionitrile) (AIBN) by weight of the monomer were dissolved in 0.5 ml of toluene. In the case of the composite, we took 0.47 g of styrene and 4.9 mg of AIBN as an initiator, and then added them to the dispersion of GO particles in toluene. Then the reaction mixtures with the initial GO content of 1 wt.% and without filler were placed into ampoules, which were purged with argon for 10 min and sealed. Polymerization was carried out for 35 hours at 70°C, every hour for 15 minutes the ampoules were sonicated. Part of the polymerization mixture was precipitated by methanol and dried in vacuo to constant weight. This was done to determine polystyrene yield, which reached 90 % by weight. The molecular weight of the synthesized polystyrene determined by intrinsic viscosity values was 38000.

The distribution and agglomeration of GO particles in polystyrene matrix was investigated by Zeiss Supra 55VP field emission scanning electron microscope (Germany).

Films of the polymer composite were deposited on copper electrodes through the dispenser by casting from a solution of 1 % by weight. The thicknesses of the films were controlled by the interference microscope using the method described in [2–4]. Current-voltage characteristics of the metal-composite-metal structures were obtained by the modified two-probe method [2–4]. The area of the lower electrode was 1 cm^2, and the upper one – 1 mm^2. Measurements were carried out at a pressure not more than 1 kg/cm^2. The resistive nature of obtained current-voltage characteristics exclude the presence of a breakdown in films which have been investigated.

3. Results and discussion

It was found that the amount of GO particles covalently coupled to polystyrene matrix is about 0.02 wt.% (4 vol.%), according to the SEM data of the composite films (Fig. 1). The distance between individual GO particles in polymer matrix ranges from tens to hundreds of microns. The inclusions of GO are distributed rather evenly in the polystyrene matrix due to the formation of chemical bonds between the vinyl groups of modified graphene and polystyrene. It should be noted that the lengths of individual GO particles reach more than 10 micrometers and few hundred nanometers in width. Furthermore, GO particles do not overlap, as can be seen in SEM micrographs (Fig. 1). The particles of GO are arranged parallel to the substrate and do not form a multilayer assemblies, which typical for graphene due to $\pi - \pi$-stacking [23]. This fact explains the little thickness of the composite at which conductivity is observed. As a result, high conductivity can be seen nearby GO particles. Composite films with thicknesses less than 3 μm conduct electrical current, at larger thicknesses, the composite material has dielectric behavior, even in areas with GO inclusions. Polystyrene without graphene oxide, synthesized under the same conditions, conducts only with thickness up to 0.02 μm.

Temperature dependences for the resistance, which were obtained for the composite films at thicknesses up to 0.2 μm, indicate that the samples have metallic conductivity on the entire surface area (Fig. 2).

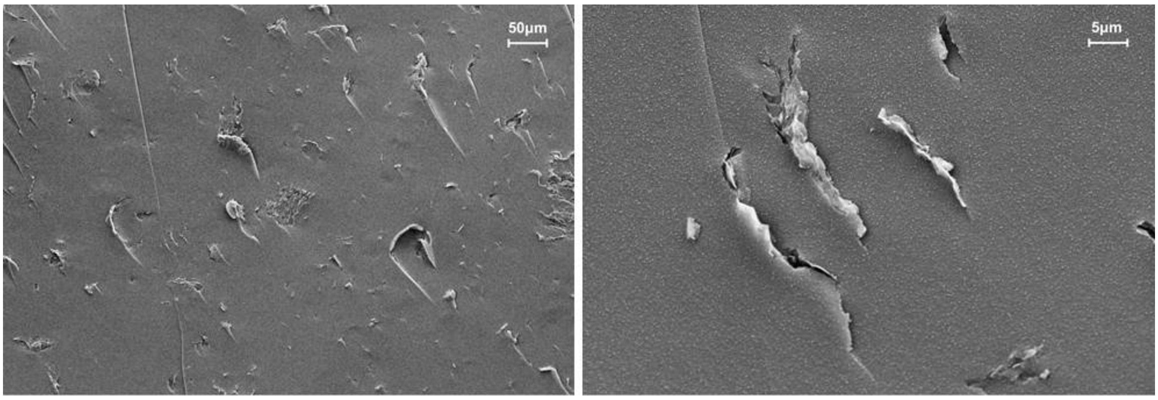

FIG. 1. Micrograph of the composite surface

Films with thickness 0.2 μm and above (up to 3 μm) are non-uniform in conductivity values. Areas of the films close to GO particles have low resistivity, but larger part of the surface without inclusions has higher resistance from a few ohms to hundreds of kilo-ohms and higher. So resistance temperature dependences were radically different for various parts of the film. Polystyrene surfaces without GO demonstrated infinite resistance at liquid nitrogen temperatures, while areas filled GO were changed into a highly-conductive state. The resistance decreased by 5–6 orders of magnitude when the temperature was lowered from room temperature to the boiling point of liquid nitrogen (Fig. 3). Such resistance-temperature dependences for film areas with GO particles are anomalous. This effect requires further investigation. It should also be noted that composite films based on polystyrene and GO particles have Josephson current-voltage characteristics over a wide temperature range from liquid helium to room temperature, according to results obtained previously [20, 21]. This effect indicates the possible existence of superconducting channels in the composite films. Since in our case in-situ introduced graphene oxide undergoes various deformations, then it seems to be possible manifestation of the previously theoretically predicted effect of superconductivity in graphite [24–27].

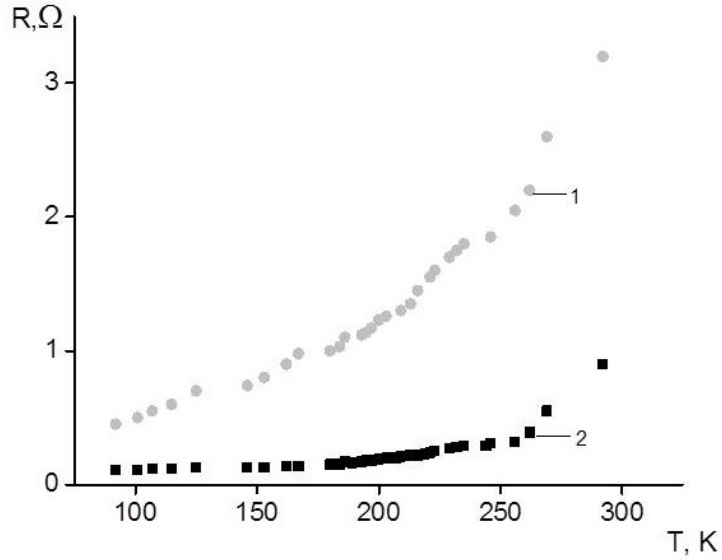

FIG. 2. Temperature dependences of the resistance for the composite films with a thickness of 0.2 μm: 1–areas of the polystyrene film without graphene oxide inclusions; 2–areas of the polystyrene film with particles of graphene oxide

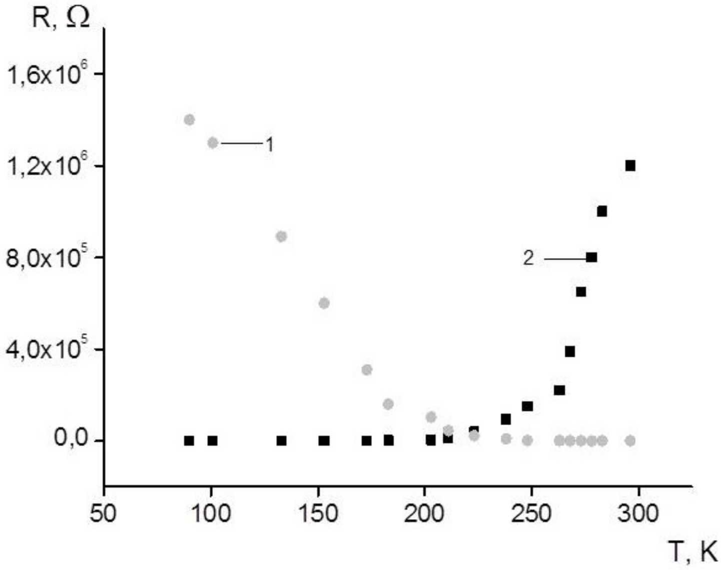

FIG. 3. Temperature dependences of resistance for the composite films: 1–areas of 0.3 μm thick polystyrene films without graphene oxide inclusions; 2–areas of 2 μm thick polystyrene films with particles of graphene oxide

4. Conclusions

As a result of chemical synthesis, composite films based on polystyrene covalently linked to 0.02 wt.% of graphene oxide particles were obtained.

The resulting composite films have high conductivity in areas adjacent to graphene oxide inclusions, while the remaining film areas are highly-resistant above 0.3 μm thickness. It is important to note that decrease in resistance value near graphene oxide inclusions for the 0.2 to 3 μm composite films can vary by several orders of magnitude in the temperatures ranging from the boiling point of liquid nitrogen to room temperature. For 3 μm thick films, the resistance values can vary by 6 orders of magnitude. Thinner composite films show resistance temperature dependence similar to that of metallic type conductivity.

Acknowledgement

We are grateful to T. D. Ananeva (Institute of Macromolecular Compounds, Russian Academy of Sciences, St. Petersburg) for taking part in the synthesis of composites. We deeply appreciate E. M. Ivankova (Institute of Macromolecular Compounds, Russian Academy of Sciences, St. Petersburg) for scanning electron microscopy measurements.

References

[1] Ionov A.N., Dunaevskii M.S., et al. The dependence of polymer conductivity on the work function of metallic electrodes. *Ann. Phys.*, Berlin, 2009, **18**, P. 959–962.

[2] Nikolaeva M., BoikoY., Martynenkov A. Supramolecular structure and conductive properties of dielectric polymers in metal/polymer/metal systems. *Int. J. Polym. Mat.*, 2013, **62**(13), P. 706–710.

[3] Nikolaeva M.N., Anan'eva T.D., et al. Influence of chemical structure and chain length on conducting properties of dielectric polymers in metal/polymer/metal structures. *Rus. J. Appl. Chem.*, 2013, **86**(5), P. 756–759.

[4] Nikolaeva M.N., Martynenkov A.A., et al. Resistance of dielectric polymer films with fillers in metal-polymer-metal systems. *Rus. J. Appl. Chem*, 2014, **87**(5), P. 646–650.

[5] Deepak A., Shankar P. Exploring the properties of lead oxide and tungsten oxide based graphene mixed nanocomposite films. *Nanosystems: Physics, Chemistry, Mathematics*, 2016, **7**(3), P. 502–505.

[6] Arhangorodsky V.M., Ionov A.N., et al. Ultra-high conductivity in the oxidized polypropylene at room temperature. *JETP Letters*, 1990, **51**(1), P. 56–62. (in Russian)

[7] Ionov A.N., Nikolaeva M.N., Rentzsch R. Local distribution of high-conductivity regions in polyamidine films. *JETP Letters*, 2007, **85**, P. 636–638.

[8] Ionov A.N., Nikolaeva M.N., Rentzsch R. Metallic conductivity in a polyamidine film. *Physica C*, 2007, **460-462**, Part 1, P. 641-642.

[9] Nikolaeva M.N., Aleksandrova G.P., Martynenkov A.A. Effect of electrization on molecular mobility in gold nanocomposites based on arabinogalactan. *Rus. J. Phys.Chem. (A)*, 2012, **86**, P. 812–815.

[10] Nikolaeva M.N., Aleksandrova G.P., Ionov A.N. Correlation between the electrification and molecular mobility of noble metal nanocomposites based on arabinogalactan. *Rus. J. Appl. Chem.*, 2011, **84**, P. 450–453.

[11] Ionov A.N., Svetlichnyi V.M., Rentzsch R. Electron transport in metal-polymer-metal systems. *Physica B: Cond. Matter*, 2005, **359-361**, P. 506–510.

[12] Rentzsch R., Ionov A.N., Nikolaeva M.N. Spreading resistance microscopy study of polyamidine thin films. *Phys. Stat. Sol. (c)*, 2006, **3**(2), P. 275–279.

[13] Ionov A.N., Nikolaeva M.N., Pozdnyakov O.F., et al. Molecular structure of poly(siloxaneimide) films and the rate of charge relaxation. *Polym. Sci. (A)*, 2008, **50**, P. 174–182.

[14] Ionov A.N., Rentzsch R., Nikolaeva M.N. Metallic conductivity in a polyamidine film. *Phys. Stat. sol. (c)*, 2008, **5**, P. 730–734.

[15] Lowell J. and Rose-Innes A.C. Contact electrification. *Adv. Phys,* 1980, **29**(6), P. 947–1023.

[16] Duke C.B., Fabish T.J. Charge-induced relaxation in polymers. *Phys. Rev. Lett.*, 1976, **37**(16), P. 1075–1078.

[17] Mikoushkin V.M., Shnitov V.V., Nikonov S.Yu. et al. Controlling Graphite Oxide Bandgap Width by Reduction in Hydrogen. *Tech. Phys. Lett.*, 2011, **37**(10), P. 942–945.

[18] Bugrov A.N., Vlasova E.N., Mokeev M.V. et al. Distribution of zirconia nanoparticles in the matrix of poly(4,4/-oxydiphenylenepyromellitimide). *Polym. Sci. Ser. B.*, 2012, **54**, P. 486–495.

[19] Nikolaeva M.N., Bugrov A.N., et al. Conductive properties of the composite films of graphene oxide based on polystyrene in a metal-polymer-metal structure. *Russ. J. Appl. Chem.*, 2014, **87**(8), P. 1151–1155.

[20] Ionov A.N. Josephson current-voltage characteristic of a composite based on polystyrene and graphene oxide. *Tech. Phys. Lett.*, 2015, **41**(7), P. 651–653.

[21] Ionov A.N. Josephson-Like Behaviour of the Current-Voltage Characteristics of Multi-graphene Flakes Embedded in Polystyrene. *J. Low Temp. Phys.*, 2016, **182**(3/4), P. 107–114.

[22] Hummers W., Offeman R. Preparation of graphitic oxide *J. Am. Chem. Soc.*, 1958, **80**(6), P. 1339–1339.

[23] Hazarika M., Jana T. Graphene nanosheets generated from sulfonated polystyrene/ graphene Nanocomposite. *Cmpos. Sci. Tech.*, 2013, **87**, P. 94–102.

[24] Heikkilä T., Kopnin N.B., Volovik G. Flat bands in topological media. *JETP Lett*, 2011, **94**, P. 233–237.

[25] San-Jose P., Prada E. Helical networks in twisted bilayer graphene under interlayer bias. *Phys. Rev. B*, 2013, **88**, P. 121408.

[26] Uchoa B., Barlas Y. Superconducting states in pseudo-Landau levels of strained graphene. *Phys. Rev. Lett.*, 2013, **111**(1–5), P. 046604.

[27] Bianconi A., Jarlborg T. Lifshitz ons and zero point lattice fluctuations in sulfur hydride showing near room temperature superconductivity. *Nov. Supercond. Mater.*, 2015, **1**, P. 37–49.

NANOSYSTEMS:

PHYSICS, CHEMISTRY, MATHEMATICS

Журнал зарегистрирован
Федеральной службой по надзору в сфере связи, информационных технологий и массовых коммуникаций
(свидетельство ПИ № ФС 77 - 49048 от 22.03.2012 г.)
ISSN 2220-8054

Учредитель: федеральное государственное автономное образовательное учреждение высшего образования
«Санкт-Петербургский национальный исследовательский университет информационных технологий, механики и оптики»

Издатель: федеральное государственное автономное образовательное учреждение высшего образования
«Санкт-Петербургский национальный исследовательский университет информационных технологий, механики и оптики»

Отпечатано в Учреждении «Университетские телекоммуникации»
Адрес: 197101, Санкт-Петербург, Кронверкский пр., 49

Подписка на журнал НФХМ
На второе полугодие 2017 года подписка осуществляется через
ОАО Агентство «Роспечать»
Подписной индекс 57385 в каталоге «Издания органов научно-технической информации»